Paula Isabel Pereira Soares

Mestrado Integrado em Ciências Farmacêuticas

Chitosan-based magnetic nanoparticles for osteosarcoma theranostic

Dissertação para obtenção do Grau de Doutor em

Nanotecnologias e Nanociências

Orientador:	Doutor João Paulo Miranda Ribeiro Borges, Professor Auxiliar, Faculdade de Ciências e Tecnologia da Universidade Nova de Lisboa
Co-orientador:	Doutora Isabel Maria das Mercês Ferreira, Professora Associada, Faculdade de Ciências e Tecnologia da Universidade Nova de Lisboa
	Doutor Carlos Manuel Mendes Novo, Investigador Auxiliar, Instituto de Higiene e Medicina Tropical da Universidade Nova de Lisboa

Júri:

Presidente:	Prof. Doutora Elvira Maria Correia Fortunato
Arguentes:	Prof. Doutor Pedro Lopes Granja
	Prof. Doutor Sérgio Jerónimo Rodrigues Dias
Vogais:	Prof. Doutora Maria Helena Mendes Gil
	Prof. Doutor José Maria Marcelino
	Prof. Doutora Elvira Maria Correia Fortunato

FACULDADE DE CIÊNCIAS E TECNOLOGIA
UNIVERSIDADE NOVA DE LISBOA

Dezembro 2015

Paula Isabel Pereira Soares

Mestrado Integrado em Ciências Farmacêuticas

Chitosan-based magnetic nanoparticles for osteosarcoma theranostic

Dissertação para obtenção do Grau de Doutor em

Nanotecnologias e Nanociências

Orientador:	Doutor João Paulo Miranda Ribeiro Borges, Professor Auxiliar, Faculdade de Ciências e Tecnologia da Universidade Nova de Lisboa
Co-orientador:	Doutora Isabel Maria das Mercês Ferreira, Professora Associada, Faculdade de Ciências e Tecnologia da Universidade Nova de Lisboa
	Doutor Carlos Manuel Mendes Novo, Investigador Auxiliar, Instituto de Higiene e Medicina Tropical da Universidade Nova de Lisboa

Júri:

Presidente:	Prof. Doutora Elvira Maria Correia Fortunato
Arguentes:	Prof. Doutor Pedro Lopes Granja
	Prof. Doutor Sérgio Jerónimo Rodrigues Dias
Vogais:	Prof. Doutora Maria Helena Mendes Gil
	Prof. Doutor José Maria Marcelino
	Prof. Doutora Elvira Maria Correia Fortunato

FACULDADE DE CIÊNCIAS E TECNOLOGIA
UNIVERSIDADE NOVA DE LISBOA

Dezembro 2015

– This page is intentionally blank –

Chitosan-based magnetic nanoparticles for osteosarcoma theranostics

– This page is intentionally blank –

“A dor é passageira mas a glória é eterna!”

Paulo Pereira

– This page is intentionally blank –

Acknowledgements

Although the acknowledgements is the less scientific part of a PhD thesis, in my opinion it is the most important part. Science as well as life, is made by people, and a lot of people helped me during this journey.

First of all, I want to acknowledge my supervisors: Prof. Dr. João Paulo Borges, Prof. Dr. Isabel Ferreira and Dr. Carlos Novo. The three of you given me the opportunity to accomplish one of the points of my bullet list: a PhD! To Prof. JPB who is always busy with his classes, a thousand students and the late paperwork, but can always have five minutes to unblock a messy mind or to have a brilliant idea. To Prof. Isabel that never gives up and is an inspiration, always giving me the support I needed. Thanks for all the correction during these four years, even the most boring ones. To Prof. Carlos for opening the doors to immunology and helping I re-learn every day the knowledge that was almost forgotten. To all of you, thank for helping me survive in the 'science world', it was a pleasure to learn from you every day!

To Prof. Elvira Fortunato and Prof. Rodrigo Martins for the opportunity to work in such an exceptional research center, such as CENIMAT.

I would like to acknowledge all of those who directly collaborated with me and provided crucial contributions to this work. I am extremely grateful to MSc. Ana Alves, MSc Frederik Löchte, BSc. Rafaela Boaventura, BSc. Francisco Ferreira, MSc. Diana Machado and MSc. Ana Isabel Sousa. I am also grateful to have had the opportunity to work along other master students that I will not list here. Although you weren't my students, it was wonderful to share the lab with you. Your ideas, motivation and interest in each of your works were wonderful to see. Without you all, this would not have been possible. Thank you!

To Prof. Dr. Paula Videira and all her team of the Glycoimmunology group at the Center of Chronic Diseases at Nova Medical School, I'm much grateful for welcoming me and letting me use your lab for the immunology studies. A special thanks to Mylène Carrascal for all the help, time and ideas shared during this work.

To Prof. Jorge Silva thank you so much for letting me use your cell culture lab like it was mine. Your dedication is impressive and inspiring!

To Dr. Alexandra Carvalho for the NMR measurements presented in this thesis. To Dr. Laura Pereira for all the SQUID measurements and the important contributions in the published papers. To Dr. César Laia for sharing his knowledge about DLS with me and believing in my work. Thank you!

To MSc. Alexandra Gonçalves for always being available with a smile on her face. Dr. Ana Pimentel thank you for all the DSC measurements.

This section would not be complete without acknowledging my lab colleagues. To the ones that are far away, MSc. Esther Merino and MSc. Joana Vasconcelos, thank you for your friendship, your support, and for making me feel like a superwoman!! It was a pleasure to have met you both. To the people of the gin' bar, aka "gente jovem" MSc. Rita Pontes, MSc. Teresa Kullberg, MSc. Joana Fernandes, and MSc. Alex Grüninger, thank you for the wonderful moments sharing a gin or not. To the ones that are still here to see me finish this, MSc. Carlos João, Dr. Ana Batista, Dr. Sumita Nandy, Dr. Susete Fernandes, and Augusta Gonçalves thank you for all the motivation, the long conversations, the loud laughter's, and the promptness to help me along this research. Finally, a special acknowledge to my colleague that became a wonderful friend, Dr. Coro Echeverria, you cannot image what I have learned from you in this two years. I am extremely grateful to have met you, and to share a "meia de leite" with you every day!

I would also like to thank two other friends that share this "burden" with me, MSc. Sofia Almeida and MSc. Raquel Varela. Sofi you are the most extraordinary person that I have ever met, and I just grateful to be a part of your life! Raquelita we know each other for 12 years now, since we were just "caloiras na FFUL". So above everything thank you for your friendship during these years. We are almost "doutoras a sério" now!

Thank you also to Sara Oliveira and to Sónia Seixas from DCM secretariat and Susana Mendes from CENIMAT secretariat for all the administrative support given during this thesis.

I am extremely grateful for the financial support provided by Fundação para a Ciência e a Tecnologia (FCT-MCTES) under the grant SFRH/BD/79302/2011 which allowed this research to be accomplished.

A special thanks to all my running friends, you make me forget all the problems and just focus on the next run! Running is a part of me now!

Finally and more important, thank you to my wonderful family, my parents Paulo and Isabel, my brother MSc. Miguel, and to my sister Daniela, for your unconditional love and support. Mom and Dad you are responsible for who I am today. I cannot express in words how grateful I am to all of you. Without you, I would not be here, and none of this would make sense. Miguel and Dani I am so proud of both of you. It has been a wonderful journey to grow up with the two of you. Thank you! I love you all! Also, to my dogs that can also find a way to make me happy.

A special thanks to my dear husband, Luís Carlos, for all your love, support, and patience. You make me a better person! I love you!

Abstract

Cancer is a well-known disease with a significant impact in society not only due to its incidence, more evident in more developed countries, but also due to the expenses related to medical treatments. Cancer research is considered an increasingly logical science with great potential for the development of new treatment options. Advances in nanomedicine have resulted in rapid development of nanomaterials with considerable potential in cancer diagnostics and treatment. The combination of diagnosis and treatment in a single nano-platform is named theranostic. In this PhD thesis a theranostic system for osteosarcoma was proposed, composed by a magnetic core, a polymeric coating, and a chemotherapeutic drug. The presence of a specific targeting agent, in this case a monoclonal antibody, provides high specificity to the proposed theranostic system.

For the core of the proposed theranostic system, stable aqueous suspensions of superparamagnetic iron oxide nanoparticles with an average diameter of 9 nm were produced. Chitosan-based polymeric nanoparticles with a hydrodynamic diameter around 150 nm were successfully produced. Incorporation of iron oxide nanoparticles into the polymeric ones increased their hydrodynamic diameter to at least 250 nm. A monoclonal antibody specific for a transmembranar protein (carbonic anhydrase IX) present in solid tumors was developed by hybridoma technology. Functional hybridomas producing the desired monoclonal antibodies were obtained.

The proposed theranostic system functionality was evaluated in separated parts of its components. Uncoated and coated iron oxide nanoparticles with chitosan-based polymers generated heat under the application of an external alternating magnetic field. Uncoated iron oxide nanoparticles stabilized with oleic acid were able to enhance contrast in magnetic resonance imaging. Drug delivery studies were conducted in chitosan-based polymeric nanoparticles without and with the incorporation of iron oxide nanoparticles, demonstrating to be an effective drug delivery platform for doxorubicin.

The theranostic system proposed in this PhD thesis is very promising for cancer theranostic, demonstrating to be applicable in solid tumors such as osteosarcoma.

Keywords: Cancer, Chitosan, Iron oxide nanoparticles, Magnetic hyperthermia, Theranostic.

– This page is intentionally blank –

Resumo

O cancro é uma doença bem conhecida a nível mundial e com um elevado impacto na sociedade, não só pela sua elevada incidência mas também devido aos custos médicos que acarreta. Como consequência, a investigação científica nesta área é considerada bastante promissora para o desenvolvimento de novas opções terapêuticas. Por outro lado, o avanço na nano-medicina tem permitido o rápido desenvolvimento de nano-materiais com grande potencial para o diagnóstico e tratamento de cancro. A combinação de diagnóstico e tratamento num único nano-dispositivo chama-se teragnóstico. Nesta tese de doutoramento foi proposto o desenvolvimento de um sistema de teragnóstico para o osteossarcoma composto por um núcleo magnético, um revestimento polimérico e um fármaco quimioterapêutico. A presença de um anticorpo monoclonal torna o sistema altamente específico.

Para o núcleo do dispositivo de teragnóstico proposto foram desenvolvidas nanopartículas de óxido de ferro superparamagnéticas estáveis em suspensões aquosas, com um diâmetro médio de 9 nm. Foram também produzidas nanopartículas poliméricas à base de quitosano com um diâmetro hidrodinâmico de 150 nm. A incorporação de nanopartículas de óxido de ferro nas nanopartículas poliméricas aumentou o diâmetro hidrodinâmico destas últimas para 250 nm. Por último, foi produzido um anticorpo monoclonal específico para uma proteína transmembranar (anidrase carbónica IX) presente em tumores sólidos usando a tecnologia do hibridoma. Foram obtidos hibridomas funcionais capazes de produzir os anticorpos desejados.

A funcionalidade do dispositivo de teragnóstico proposto foi testada em cada uma das suas partes isoladamente. As nanopartículas de óxido de ferro com e sem o revestimento polimérico foram capazes de gerar calor sob a aplicação de um campo magnético externo alternado. As mesmas nanopartículas de óxido de ferro estabilizadas com ácido oleico melhoraram o contraste da ressonância magnética de imagem. Os estudos de libertação de fármaco foram feitos usando nanopartículas poliméricas com e sem óxido de ferro, tendo demonstrado a sua eficácia na libertação controlada de doxorubicina.

O sistema de teragnóstico desenvolvido nesta tese de doutoramento é bastante promissor para o teragnóstico do cancro, podendo ser aplicado em tumores sólidos como o osteossarcoma.

Palavras-chave: Cancro, Hipertermia magnética, Nanoparticulas de óxido de ferro, Quitosano, Teragnóstico.

– This page is intentionally blank –

Contents

List of Figures

List of Tables

Abbreviations

3D	Three-Dimensional
Ab	Antibody
AC	Alternating Current
ACF	Auto-Correlation Function
ADCC	Antibody-Dependent Cellular Toxicity
AMF	Alternating Magnetic Field
AML	Acute Myeloid Leukemia
ANLL	Acute Non-Lymphocytic Leukemia
ATR	Attenuated Total Reflectance
Bax	Bcl-2 Associated X-protein
BCRP	Breast Cancer Resistance Protein
bFGF	Basic Fibroblast Growth Factor
BSA	Bovine Serum Albumin
CA	Carbonic Anhydrase
CARP	CA Related Protein
cDNA	Complementary DNA
CDR	Complementary Determining Regions
CLL	Chronic Lymphocytic Leukemia
CMC	Complement Mediated Cytotoxicity
CS	Chitosan
CSC	Cancer Stem Cell
CTLA-4	Cytotoxic T-Lymphocyte Antigen 4
DA	Degree of Acetylation
DC	Direct Current
DD	Degree of Deacetylation

D_H	Hydrodynamic Diameter
DLS	Dynamic Light Scattering
DLVO	Derjaguin-Landau-Verwey-Overbeek
DMEM	Dulbecco's modified Eagle's medium
DNA	Deoxyribonucleic acid
DNR	Daunorubicin
DOX	Doxorubicin
DSC	Differential Scanning Calorimetry
DTA	Differential thermal analysis
DTPA	DiethyleneTriaminePentaacetic Acid
EE	Encapsulation Efficiency
EGF	Epidermal Growth Factors
EGFR	Epidermal Growth Factor Receptor
EMA	European Medicines Agency
EpCAM	Epithelial Cell Adhesion Molecule
EPI	4'-*epi*-doxorubicin
EPR	Enhanced Permeability and Retention
FC	Field-cooled
FCS	Fetal Calf Serum
FDA	Food and Drug Agency
FTIR	Fourier Transform Infrared spectrometer
GTMAC	Glycidil TriMethyl Ammonium Chloride
HA	Hydroxyapatite
HAMA	Human Anti-Mouse Antibodies
HIF	Hypoxia Induced Factor
HIV	Human Immunodeficiency Virus
HRE	HIF-Responsive Element

HTCC	Trimethyl ammonium Chitosan Chloride
IARC	International Agency for Research of Cancer
IC50	Half-maximum Inhibitory Concentration
IDA	Idarubicin
IFN	Interferon
Ig	Immunoglobulin
ISO	International Organization of Standardization
JNK	c-Jun N-terminal Kinase
KS	Kaposi Sarcoma
LD50	Lethal dose 50%
LDH	Lactate Dehydrogenase
mAb	Monoclonal Antibody
MDR	Multidrug Resistance
MFI	Mean Fluorescence Intensity
MHC	Myosin Heavy Chain
MHS	Mark-Houwink-Sakurada
MMAE	Monomethyl Auristatin E
MRI	Magnetic Resonance Image
mRNA	Messenger Ribonucleic Acid
MRP	Multidrug Resistance-associated Protein
M_w	Molecular Weight
NCAM	Neural Cell adhesion Molecule
NHL	Non-Hodgkin Lymphoma
NIR	Near Infrared
NMR	Nuclear magnetic resonance
NOS	Nitric Oxide Synthase
NP	Nanoparticle

OA	Oleic Acid
***O*-HTCC**	*O*-(2-Hydroxyl) propyl-3-Trimethyl ammonium Chitosan Chloride
PBS	Phosphate Buffer Saline
PEG	Polyethylene glycol
PEO	Poly (Ethylene Oxide)
PET	Positron Emission Tomography
PVA	Polyvinyl Alcohol
pVHL	Von Hippel-Lindau tumor supressor Protein
PZC	Point of Zero Charge
RANKL	Receptor Activator of NFκB ligand
RCC	Renal Cell Carcinoma
RES	Reticulo Endothelial System
ROS	Reactive Oxygen Species
SAM	Self-Assembled Monolayers
SAR	Specific Absorption Rate
SEM	Scanning Electron Microscopy
SPECT	Single-Photon Emission Computed Tomography
SQUID	Superconducting Quantum Interference Device
TC	Tri-sodium Citrate
TD	Thermal Decomposition
TEM	Transmission Electron Microscopy
TGA	Thermogravimetric Analysis
TPP	Tripolyphosphate
TREG	Triethylene glycol
TREM	Triethanol amine
TX	Triton X-100
US	United States

UV	Ultra-violet
VEGF	Vascular Endothelial Growth Factor
VIS	Visible
w/o	Water-in-oil
XRD	X-Ray Diffraction
ZFC	Zero field-cooled

– This page is intentionally blank –

Symbols

C	Concentration
D	Diffusion coefficient
H_c	Coercivity
H	Magnetic field
η	Viscosity
m	Magnetic moment
M	Magnetization
μ_0	Magnetic permeability of free space
μ	Ionic strength
T	Temperature
T_1	Transverse relaxation
T_2	Longitudinal relaxation
τ	Relaxation time
V	Volume
χ	Magnetic susceptibility
ζ	Zeta potential
∇	Gradient
λ	Wavelength

– This page is intentionally blank –

Chapter 1. Motivation

The present chapter introduces the cancer problem around the world and the need for new treatment options. Nanotechnology is presented as a reliable solution for this problem. The thesis' objectives are subsequently presented as a result of nanotechnology development and its application in cancer treatment and diagnostic. At the end of this chapter, the outline of the thesis is presented, followed by the scientific contributions that resulted from this PhD.

1.1. Scientific context

Cancer is a devastating disease of the present days with a huge incidence and related deaths. Everyone knows someone that had, have or will have cancer. It is estimated that each year more than 11 million new cases of cancer are diagnosed, and more than 7 million people die from this devastating disease. If current trends continue, in 2020 new cancer cases will increase to 17 million, an increase of 30% compared to 2009.

In the past 20 years, the total medical costs of cancer have nearly doubled as a direct consequence of the increasing number of cancer cases. The dramatic increase in the number of cancer cases is because of new cases diagnosed among the aging population base, as well as increasing cancer prevalence [1].

Current cancer treatments, such as radiotherapy and chemotherapy, although effective for some cases, did no cover all of them. In addition, cancer treatment is exhaustive and expensive because of the multi-therapeutic approaches and constant admissions for treatments and side effects management. The majority of cancer treatments are not specific for the type of cancer and for the patient, and treatment monitoring is not accurate.

Osteosarcoma is a relatively uncommon malignancy, with an overall incidence of five cases per million persons per year. However, among childhood malignancies, osteosarcoma is the eighth most common. Only leukemia, lymphomas, and neurological malignancies are more common.

Osteosarcoma accounts for 8-9% of cancer-related deaths in children and carries an overall 5-year survival rate of 60–70% [2]. Current chemotherapy regimens comprise a group of chemotherapeutic agents in which doxorubicin are included. However, tumor resistance to anthracyclines and cardiotoxicity are limiting factors for its usage. Liposomal formulations of doxorubicin improve its anti-cancer effects but are still insufficient.

Consequently, a method that possesses enough versatility to be adapted to the cancer type within a group of cancer types but that, when is applied, has a high specificity for cancer cells, dramatically decreasing the side effects, is required. Moreover, if this method allows cancer diagnose and treatment monitoring, although may seem ambitious and expensive at a first glance, will become economically favorable for the patient and for the medical institution. By reducing the side effects, reduces the number of hospital admissions and the costs of side effects management. By increasing treatment effectiveness, reduces the number of treatments required and improves patients' quality of life.

Nanotechnology is a recent technology with a huge potential for medicine, among other applications. Properties like increased surface area, optical, electronic, magnetic, and structural properties at nanometer scale are not available for bulk solids or individual molecules, making these materials unique. The development of new materials based on multi-functional magnetic nanoparticles can open a window of opportunity for a new therapeutic approach to osteosarcoma treatment. There is currently significant interest in designing new drug delivery systems with the objective of achieving targeted drug delivery.

1.2. Objective

The main objective of this PhD thesis is to obtain chitosan-based magnetic nanoparticles for osteosarcoma treatment (drug delivery and magnetic hyperthermia) and monitoring (contrast agents for targeted magnetic resonance imaging). These nanoparticles are composed of a magnetic core and a chitosan-based coating that will encapsulate a chemotherapeutic drug. In addition, a highly specific monoclonal antibody is attached to the nanoparticle surface conferring specificity to the whole system. It is expected that these highly specific nanoparticles promote specifically tumor cell death, opening a new therapeutic approach for osteosarcoma treatment and monitoring. The therapeutic effectiveness of these nanoparticles is achieved by: specificity for tumor cells due to the presence of a monoclonal antibody specific for CA IX, a transmembranar protein present in several tumor cells; specific drug delivery, using the produced nanoparticles as a carrier; and

sensitization or death of tumor cells by magnetic hyperthermia. In addition, the magnetic core provides the basis for the treatment monitoring through magnetic resonance imaging.

To achieve this objective, several tasks were developed:

1. Production and characterization of superparamagnetic iron oxide nanoparticles with diameters in the nanometric range, stable in physiological conditions and able to generate heat by the application of an alternating external magnetic field.

2. Production and characterization of chitosan and *O*-HTCC nanoparticles with diameters in the nanometric range, stable in physiological conditions. Further, both polymers were used to coat iron oxide nanoparticles produced in task 1.

3. Production of a highly specific monoclonal antibody for CA IX (a glycoprotein over expressed in osteosarcoma).

4. Study the suitability of the produced nanoparticles for application in magnetic hyperthermia, as a contrast agent for magnetic resonance image, and as a drug delivery system for doxorubicin.

1.3. Thesis outline

The following section is an outline of the chapters in this thesis:

Chapter 1: Motivation – This chapter presents the motivation and the objectives of the present PhD thesis.

Chapter 2: General Introduction – This chapter reviews some of cancer' bullet points, such as current treatments and statistics. A brief insight on osteosarcoma is also given. Finally, nanotechnology is presented as an alternative for cancer treatment and diagnosis.

Chapter 3: Iron oxide nanoparticles – This chapter starts with an introduction to iron oxide nanoparticles synthesis, colloidal stability, and properties. The detailed methodology for the production and characterization of the studied iron oxide nanoparticles is provided, and the main results obtained are presented and discussed.

Chapter 4: Chitosan-based coating – Chitosan and chitosan's derivatives properties and applications are summarized in this chapter. Methods for producing chitosan nanoparticles are reviewed and a detailed methodology for the production and characterization of chitosan and *O*-HTCC nanoparticles is presented. Moreover, are provided in this chapter the main results and discussion of the coated iron oxide nanoparticles with both polymers.

Chapter 5: Monoclonal antibody production – A summary of state of the art concerning monoclonal antibodies' properties and their production is provided in the beginning of this chapter, that also includes a detailed methodology for production and evaluation of monoclonal antibodies anti-CA IX, and the obtained results are presented and discussed.

Chapter 6: Theranostic part I: Magnetic hyperthermia, MRI, and cytotoxicity – This chapter contains a brief overview on magnetic hyperthermia and magnetic resonance imaging, presents and discuss the results obtained in both techniques, and the cytotoxic behavior of the produced nanoparticles.

Chapter 7: Theranostic part II: Drug release studies – This chapter is related to doxorubicin as a model drug, giving an insight on its usage and drawbacks. Moreover, the potential of chitosan as a drug delivery system and the mathematical models used are reviewed. Drug delivery studies are presented and discussed, and mathematical models are fitted to the experimental data to evaluate the release behavior of the produced nanoparticles.

Chapter 8: Conclusions and Perspectives – In this final chapter are presented the main conclusions of this PhD thesis and provides new perspectives for future work.

1.4. Scientific contribution

The main contributions of this PhD thesis were published in peer-reviewed journals, as book chapters, and presented in international conferences.

The list of publications supporting this thesis is the following:

- **Paula Soares**, Isabel Ferreira, Rui Igreja, Carlos Novo, João Paulo Borges. Application of hyperthermia for cancer treatment: recent patents review. Recent patents on anti-cancer drug discovery, 7(1): 64-73, 2012.
- **Paula Soares**, Sérgio Dias, Carlos Novo, Isabel Ferreira, João Paulo Borges. Doxorubicin vs. ladirubicin: methods for improving osteosarcoma treatment. Mini reviews in medicinal chemistry, 12 (12): 1239-1249, 2012.
- Ana Baptista, **Paula Soares**, Isabel Ferreira, and João Paulo Borges. Nanofibers and nanoparticles in biomedical applications, Chapter 4. Bioengineered Nanomaterials book edited by Atul Tiwari and Ashutosh Tiwari, CRC Press (Taylor & Francis Group), USA, 2013.
- **Paula Soares**, Ana Alves, Laura Pereira, Joana Coutinho, Isabel Ferreira, Carlos Novo, João Paulo Borges. Effects of surfactants on the magnetic properties of iron oxide colloids. Journal of colloid and interface science. 419, 46-51, 2014.

- **Paula Soares**, Isabel Ferreira, João Paulo Borges. Application of Hyperthermia for Cancer Treatment: Recent Patents Review, Chapter 9. Topics in Anti-Cancer Research, Vol. 3, book edited by Atta-ur-Rahman and Khurshid Zaman, Bentham Science Publishers, USA, 2014.
- **Paula Soares**, Frederik Lochte, Coro Echeverria, Laura Pereira, Joana Coutinho, Isabel Ferreira, Carlos Novo, João Paulo Borges. Thermal and Magnetic Properties of Iron Oxide Colloids: influence of surfactants. Nanotechnology, 26, 425704, 2015.
- **Paula Soares**, César Laia, Alexandra Carvalho, Laura Pereira, Joana Coutinho, Isabel Ferreira, Carlos Novo, João Paulo Borges. Iron oxide nanoparticles stabilized with a bilayer of oleic acid for magnetic hyperthermia and MRI applications, submitted.
- **Paula Soares**, Diana Machado, César Laia, Laura Pereira, Joana Coutinho, Isabel Ferreira, Carlos Novo, João Paulo Borges. Thermal and magnetic properties of chitosan-coated iron oxide nanoparticles, submitted.
- **Paula Soares**, Ana Isabel Sousa, Jorge Silva, Isabel Ferreira, Carlos Novo, João Paulo Borges. Chitosan-based nanoparticles as drug delivery systems for doxorubicin: optimization and modelling, submitted.
- **Paula Soares**, Ana Isabel Sousa, Isabel Ferreira, Carlos Novo, João Paulo Borges. Composite chitosan-based iron oxide nanoparticles as drug delivery systems for doxorubicin: optimization and modelling. Under preparation.

Other publications

- Vanessa Zamora-Mora, **Paula Soares**, Coro Echeverria, Rebeca Hernández, Carmen Mijangos. Composite Chitosan/Agarose Ferrogels for Potential Applications in Magnetic Hyperthermia. Gels, 1, 69-80, 2015.
- Coro Echeverria, **Paula Soares**, Ana Robalo, Laura Pereira, Carlos Novo, Isabel Ferreira, João Paulo Borges. One-pot synthesis of dual-stimuli responsive hybrid PNIPAAm-chitosan microgels. Materials and Design. 86, 745-751, 2015.

Conference contributions

Oral presentation

- **Paula Soares**, Isabel Ferreira, João Paulo Borges. Studies on Thermal and Magnetic Properties of Iron Oxide Nanoparticles for Magnetic Hyperthermia Application. NanoBio&Med 2014 International Conference, 18-21 November 2014, Barcelona, Spain.

- **Paula Soares**, Isabel Ferreira, João Paulo Borges. Multifunctional Nanoparticles for Cancer Theranostic. 4th World Congress on Cancer Science & Therapy, October 20-22, 2014, Chicago, USA.

Poster presentation

- **Paula Soares**, Isabel Ferreira, Carlos Novo, João Paulo Borges. Chitosan and *O*-HTCC nanoparticles. *NanoPortugal International Conference 2013*, 13-15 February 2013, Porto, Portugal.
- **Paula Soares**, Isabel Ferreira, João Paulo Borges. Iron oxide colloids as Hyperthermia agents. *26th Annual Conference of ESB*, 31 August – 3 September 2014, Liverpool, England.

1.5. References

1. F. K. Tangka, J. G. Trogdon, L. C. Richardson, D. Howard, S. A. Sabatino, E. A. Finkelstein, Cancer treatment cost in the United States: has the burden shifted over time?, Cancer, 116 (2010), 3477-3484.

2. M. L. Broadhead, J. C. M. Clark, D. E. Myers, C. R. Dass, P. F. M. Choong, The molecular pathogenesis of osteosarcoma: a review., Sarcoma, 2011 (2011), 959248.

Chapter 2. General introduction

The present chapter gives a brief overview of the cancer problem, illustrating the gaps in its treatment options. Some cancer statistics are shown for better understanding of the global burden of cancer. Theranostic systems are a reliable alternative for management of cancer in men. As such, the basic structure of a theranostic system is presented and discussed. Finally, the most recent applications of both magnetic nanoparticles and chitosan nanoparticles in cancer treatment and diagnostic are reviewed.

2.1. Cancer

Cancer is a generic term used for a group of more than 100 diseases that can affect any part of the body. It is defined as a disease in which a group of abnormal cells grows uncontrollably, disregarding the signals that regulate cell cycle of normal cells. In some cases, cancer cells become able to invade other tissues, a process referred to as metastasis [1, 2].

Cancer can be caused by either genetic factors or environmental factors. Environmental factors include not only carcinogens such as tobacco smoke, alcohol, and infectious diseases, but also age, diet, excess body weight, among others. Carcinogens are by definition any substance, radionuclide, or radiation that is an agent directly involved in the promotion of cancer or in the facilitation of its propagation. These substances have the ability to damage the genome or to disrupt cellular metabolic processes after prolonged or excessive exposure [1].

On the other hand, cancer can also be caused by the inclusion of mutations in certain genes that are responsible for proliferation, maturation, and apoptosis of the cells (tumor suppressor genes or oncogenes). A small proportion of many cancers are due to inherited mutations in genes, which result in a high risk to the individual of developing specific cancers. However, familiar clustering of cancer is relatively common. This is likely to occur due to a combination of environmental factors, rare gene mutations with high penetrance, and common lower penetrance gene variants

acting together to change disease susceptibility. These usually occur at a young age and are frequently aggressive [2, 3].

Certain viruses can also cause cancer by persistent mucosal or epithelial cell colonization, which leads to chronic inflammation. Hepatitis B and C can cause hepatocellular cancer, human papilloma viruses can cause cervical cancer, and the bacterium *Helicobacter pylori* is responsible for gastric cancer. The combined effects of increased inflammation and epithelial cell turnover can promote the phenotypic and genotypic changes that may ultimately progress to malignant transformation. In the inflammatory process, some mediators are release, such as cytokines, chemokines and free radicals, which play an important role in carcinogenesis [4].

2.1.1. The hallmarks of cancer

Although there are several factors that can lead to tumor development, all cancer cells have defects in the regulatory circuits that govern normal cell proliferation and homeostasis. The deregulation of the production and release of growth-promoting signals, cancer cells become masters of their own destinies [5]. Taking the basic teachings of cell biology into account in which all mammalian cells carry a similar machinery to regulate their proliferation, differentiation and death, Hanahan and Weinberg [5] defined rules that govern the transformation of normal human cells into malignant cancers. These six essential alterations in cell physiology are manifested as different cancer genotypes, although they are shared in common by most or even all human tumors. The six hallmarks of cancer defined by these authors in 2000 are the following:

- Self-sufficiency in growth signals: tumor cells are able to stimulate their own growth;
- Insensitivity to anti-growth signals: the inhibitory signals that normally govern normal cells proliferation and homeostasis do not have affect tumor cells;
- Evasion of programmed cell death (apoptosis): tumor cells are able to evade apoptosis and survive;
- Limitless replicative potential: contrary to normal cells, tumor cells are able to replicate indefinitely;
- Sustained angiogenesis: tumors are able to stimulate the growth of blood vessels to supply nutrient to their own cells;
- Tissue invasion and metastasis: tumor cells are able to invade local tissues and spread to distant sites.

The acquisition of each of these hallmarks capabilities explain the evolution of normal cells to progressively become tumoral cells. With the combination of these traits, tumor cells are able to

survive, proliferate, and disseminate. However, a decade of research later led to a change in the notion that tumor development was exclusively dependent on the tumor cells. Instead, to a better understanding of the biology of tumors, one must consider the contribution of the tumor microenvironment. Tumors are complex tissues composed of multiple distinct cell types that participate in heterotypic interactions with one another [6].

2.1.1.1. Tumor microenvironment

In the last decade, the tumor microenvironment was recognized to be of critical importance for the understanding of fundamental cancer biology. Nowadays, cancer is known to be composed not only by a mass of malignant cells, but also by other cells that are recruited and that can be corrupted by the transformed cells. The close interaction between malignant and non-transformed cells create the tumor microenvironment [7, 8].

The non-malignant component of the tumor microenvironment often has a dynamic and tumor-promoting function at all stages of cancer development. For example, intracellular communication is achieved by a complex and dynamic network of cytokines, chemokines, growth factors, and inflammatory and matrix remodeling enzymes. The evolution, structure and activities of the tumor microenvironment has many similarities with the wound healing and inflammation process [8]. In fact it is well demonstrated that human tumors are generally infiltrated by inflammatory cells, which demonstrates that the host is not ignorant of the developing tumor; instead, the host tries to interfere with tumor progression, a process referred as immune surveillance [9].

The tumor microenvironment of a developing tumor is composed of proliferating tumor cells, the tumor stroma, blood vessels, infiltrating inflammatory cells and a variety of associated tissue cells [9]. The non-malignant cells of the tumor microenvironment can comprise over 50% of the mass of primary tumors and their metastasis, although in some cases their biology and function is still unclear. However, it is clear that in both hematological cancers and solid tumors there is a Darwinian evolution of malignant cells, leading to heterogeneous mutations within single tumors and at different sites of metastasis [8].

2.1.1.2. The next generation of cancer hallmarks

The above-described hallmarks of cancer are acquired functional capabilities that allow cancer cells to survive, proliferate, and disseminate. These functions are acquired in different tumor types via distinct mechanisms and at various times during the course of multistep tumorigenesis. The acquisition of such characteristics is made possible by two enabling characteristics:

- Genomic instability and mutation in cancer cells;
- Inflammatory state of premalignant and frankly malignant lesions.

In addition, two other attributes of cancer cells have been proposed to be functionally important for the development of cancer and were therefore added to the list of core hallmarks:

- Deregulating cellular energetics;
- Avoiding immune destruction.

The first attribute is a consequence of the need to support continuous cell growth and proliferation, which involves a major reprogramming of cellular energy metabolism. In this case, the metabolic program that operates in most normal tissues and fuels the physiological operations of the associated cells is replaced. The second attribute is related to an active evasion by cancer cells from attack and elimination by immune cells. In both cases, these two attributes may facilitate the development and progression of many forms of human cancers [6].

The six core hallmarks defined in 2000 provide a solid framework for understanding the complex biology of cancer. Nevertheless, the extended concept of cancer hallmarks and the definition of the emerging hallmark capabilities and enabling characteristics have provided the basis for the development of new means to treat human cancer. The understanding of the tumor microenvironment functionality and importance during tumorigenesis is crucial for the development of new and more effective cancer treatments.

2.1.2. Current treatments

There are several treatments available for cancer including surgery, i.e., removal of tumor cells, radiotherapy that uses radiation to kill tumor cells, chemotherapy with cytotoxic drugs and biotherapy that is usually targeted therapy.

2.1.2.1. Surgery

The majority of long-term cancer survivors have been treated largely because of the surgical removal of their solid tumor. Even in the disseminated stages of disease, the surgical removal of isolated organ metastases may offer a realistic chance for cure, for example, following resection of liver or lung metastases in patients with colorectal or other types of cancer [10].

The spectrum of cancer surgery ranges from very minor procedures (polypectomy, lumpectomy) to ‘mega-operations' such as regional pancreatectomy, pelvic exenterating, or liver transplantation. The type of surgery performed depends on the biology and natural history of the tumor, the

expected functional and cosmetic outcome, the skill of the individual surgeon, the efficacy and availability of other treatment modalities, the morbidity and mortality of the operation itself, and the patient's willingness to accept the associated risk(s) [10].

2.1.2.2. Radiotherapy

Radiation therapy (RT) is based upon use of ionizing radiation as part of cancer treatment to control malignant cells. Radiotherapy may be used for curative or adjuvant cancer treatment. Today, more than 50% of newly diagnosed cancer patients receive radiation therapy, typically as a part of curative combined modality treatment with surgery and/or chemotherapy. Additionally, a majority of patients who present with metastatic disease or who develop metastases following initial cancer treatment require palliative radiation therapy [11].

The interaction of ionizing radiation with various types of biologic materials or media (e.g., air, soft tissue, bone) is a random process, with frequency and density of energy deposition. As human cells and tissues (as well as tumors) are mainly considered dilute aqueous solutions containing biomolecules, the localized but randomly distributed energy depositions from ionizing radiation can have either direct effects on important biomolecules such as DNA or indirect effects produced by intermediate radiation products resulting from interactions with water. This interactions produce highly reactive species like the hydroxyl radical (•OH) among many other types of free radicals produced by ionizing radiation, including DNA free radicals resulting from direct ionizations that cause chemical damage to DNA [11].

Radiation side effects can be divided into acute and chronic. Acute radiation sequel such as skin desquamation, mucositis, and diarrhea, occur during or immediately following treatment. Such side effects are believed to be due to the interruption of repopulation of rapidly proliferating tissues. The type of reaction is dependent on the site irradiated. Chronic reactions, such as, fibrosis, fistula, and necrosis, occur months to years following treatment and are due, in part, to damage in slowly proliferating tissues. Chronic reactions, like acute ones, are dependent upon the irradiated site; chronic reactions, however, are often permanent. Overall, the risk of a second malignancy following RT is low. The notable exception is osteosarcoma arising in irradiated bones in children treated for retinoblastoma, particularly the hereditary type [12].

2.1.2.3. Chemotherapy

Chemotherapy uses chemical drugs to destroy cancer cells, keep them from growing, and spreading, shrink the size of a tumor or relieve cancer symptoms. Cancer chemotherapy has mainly been used in the management of advanced or metastatic disease, following failed local therapies, or in

disease for which no alternative therapy is effective [13]. In the majority of patients with cancer, chemotherapy will be considered for use at some time during the course of their illness, either aiming at cure, prolongation of life, and/or palliation [10].

Chemotherapy is curative for several advanced human cancers, such as gestational trophoblastic disease, certain hematologic malignancies, or germ cell testicular cancer. However, most common solid tumors are not curable with current chemotherapeutic regimens when metastatic [13].

Chemotherapy can be used as a primary therapy or as adjuvant. Induction chemotherapy denotes its use as primary therapy when there is no alternative treatment available or subsequently suitable even with tumor response, such as in hematologic malignancies, where disease is systemic. On the other hand, chemotherapy as an adjunct in combined modality therapy is applied after the tumor has been controlled by an alternative modality, such as surgery and/or radiotherapy, or neoadjuvant (primary) chemotherapy [13].

Conventional chemotherapy, although directed toward certain macromolecules or enzymes, typically does not discriminate effectively between rapidly dividing normal cells and tumor cells, thus leading to several toxic side effects. Important common side effects include (dependent on the agent): nausea and vomiting, hair loss, immunosuppression and mielossupression, among others. Tumor responses from cytotoxic chemotherapy are usual partial, brief, and unpredictable [14]. Recently, chemotherapy has been combined with targeted therapies that interfere with molecular targets that have a role in tumor growth or progression.

2.1.1. Cancer statistics

Cancer is a leading cause of death worldwide in both more and less developed countries. The most concerning part is that the burden is expected to grow worldwide due to the growth and aging of the population, mainly in less developed countries, which accounts for around 82% of the world's population. Changes in the lifestyle behaviors such as smoking, poor diet, physical inactivity, and reproductive changes have further increased the cancer burden in less economically developed countries. GLOBOCAN 2012 worldwide estimates cancer incidence and mortality using data produced by the International Agency for Research on Cancer (IARC) for 2012. According to this, an estimated 14.1 million of new cancer cases and 8.2 million cancer deaths occurred in 2012 worldwide. The most frequently diagnosed cancers and the leading causes of death in men and women are lung and breast, respectively, in less developed countries. In more developed countries, the number of prostate cancers in men is superior than lung ones, thus being the leading cause of death in men. The most frequent cancers in more developed countries are

prostate, colorectal, female breast, and lung cancer. On the other hand, in less developed countries the most frequently diagnosed cancers are liver, stomach, and cervical cancers, which are predominantly attributed to infection, which accounts for 77%, 75%, and 100% of cases worldwide, respectively. Although the majority of the world's population is in less developed countries, only 57% of cases and 65% of cancer deaths worldwide occur in these countries. The main reasons for this is the younger age structure, immaturity of the tobacco epidemic, and competing causes of death, such as infection. However, changes in lifestyle behaviors in less developed countries will continue to shift the global cancer burden [15].

Breast cancer is the most frequent diagnosed cancer and the leading cause of death in women worldwide, with an estimated 1.7 million cases and 521,900 deaths in 2012. Breast cancer alone causes 15% of cancer deaths in women. The main risk factors for breast cancer are reproductive and hormonal factors such as a long menstrual history, recent use of oral contraceptives, and never having children, among others. Potentially modifiable risk factors include overweight, physical inactivity, use of menopausal hormone therapy (combined estrogen and progestin), and alcohol consumption [15, 16].

Prostate cancer is the second most frequently diagnosed cancer in men worldwide, with estimated 1.1 million new cases in 2012. It is the most frequently diagnosed cancer among men in more developed countries, and is the fifth leading cause of death worldwide. Death rates due to prostate cancer have been decreasing in more developed countries mainly due to improved treatment and/or early detection. On the other hand, death rates have been increasing in less developed countries, mostly due to associated risk factors such as consumption of animal fat, obesity, and physical inactivity [15, 17].

Lung cancer was the most frequently diagnosed and the leading cause of death in men in 2012, accounting for an estimated 1.8 million new lung cancer cases, about 13% of total cancer diagnoses. Lung cancer is the leading cause of death in women in more developed countries, and the secondary cause of death in less developed countries. The risk factors for lung cancer include exposition to air pollution, exposure to occupational and environmental carcinogens such as asbestos, arsenic, radon, and polycyclic aromatic hydrocarbons, and outdoor pollution [15, 18]. Lung cancer is one of the most prevalent cancers, and most of them can be avoided by eliminating smoking initiation and increasing smoking cessation among current smokers [15].

Colorectal cancer is the third most commonly diagnosed cancer in men and the second in women, with an estimated 1.4 million cases and 693,900 deaths occurring in 2012. The decrease of incidence in more developed countries such as the United States in the last five decades is related to increase in screening and removal of precancerous adenomas. Moreover, increase incidence in

several Asian and Eastern European countries may reflect an increased prevalence of risk factors for colorectal cancer such as unhealthy diet, obesity, and smoking [15, 19, 20]. Preventive measurements for colorectal cancer include maintaining a healthy body weight, being physically active, minimizing consumption of red and processed meat and alcohol, and avoidance of smoking [21, 22].

2.1.1.1. Cancer statistics in Portugal

According to GLOBOCAN, an estimated 49,000 new cases of cancer in Portugal occurred in 2012. Moreover, around 24,100 cancer deaths occurred in 2012, for both sexes. The main causes of cancer deaths include colorectal, prostate, and breast cancers (Figure 2.1). Similarly, to more developed countries, prostate, colorectal and lung cancer are the most frequently diagnosed cancers in men in Portugal, in 2012. In women, the most diagnosed cancer in 2012 was breast, colorectal and corpus uteri cancers [23].

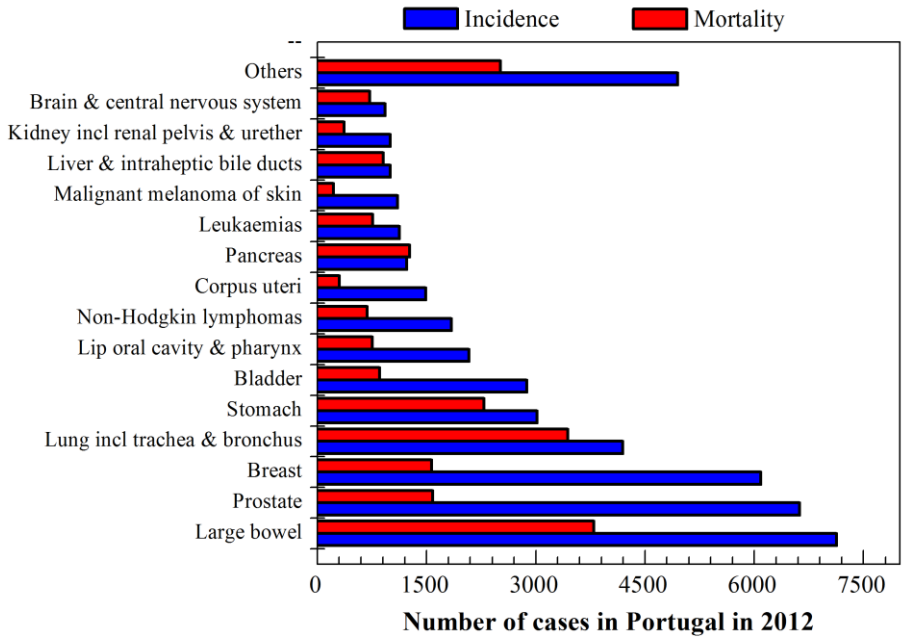

Figure 2.1. Estimated number of new cases (incidence) and deaths (mortality) of cancer for both sexes in Portugal in 2012 (adapted from [23]).

2.1.2. Osteosarcoma

Osteosarcoma is the most common primary malignant bone tumor and has a high incidence in children and adolescents, since it accounts for approximately 60% of primary malignant bone tumors diagnosed in the first two decades of life. It is characterized by an extremely aggressive

clinical route with rapid development of metastases in 40-50% of patients, occurring mainly in lung [24, 25]. Conventional therapies for osteosarcoma include surgery (frequently amputation), chemotherapy and radiotherapy [12]. Current neoadjuvant chemotherapy protocols for high-grade osteosarcoma are based on doxorubicin (DOX), high-dose methotrexate (MTX), and cis-dichloro-diamine platinum (CDDP), with the addition of ifosfamide in the post-operative phase, increasing the 5-year disease free survival rate to 70%, in patients without metastasis [25]. However, current treatments for osteosarcoma have not resulted in improved prognosis during the last decade providing incentive for the development of new treatment options [26].

The major cause of failure of chemotherapeutic regimens is multidrug resistance (MDR). MDR has been correlated with multi-factorial processes such as: enhanced detoxification of the drugs through increased metabolism; decreased drug uptake; a reaction with increased levels of intra-cellular nucleophiles; enhanced repair of the drug-induced damage to DNA; or through overex-pression of membrane-bound drug transporter proteins, such as P-glycoprotein (Pgp, ABCB1), multidrug resistance-associated proteins (MRP1, ABCC1 and MRP2, ABCC2) and the breast cancer resistance protein (BCRP, ABCG2) [24, 27].

Solid tumors such as osteosarcoma, breast cancer, and prostate cancer, among others, consist of a heterogeneous population of cells that differ in their relative states of differentiation [28]. Dur-ing the last years, the cancer stem cells (CSC) theory emerged as a model to account for the heterogeneity and renewal capacity of tumor cells. The CSC theory postulates that the greater part of a tumor mass contains more differentiated cells that are susceptible to radiation and chemo-therapy because of their close vicinity to non-tumorigenic tissues and sufficient blood flow due to induced angiogenesis, or blood vessel growth [28]. In contrast, a small subset of cells with stem-like properties that is responsible for initiating and sustaining tumor growth were termed cancer stem cells because of the properties they share with normal stem cells, including their ability to self-renew and undergo differentiation [29]. Similar to the normal tissue stem cells, in some tumors, the CSCs are believed to reside in less oxygenated areas in a quiescent state. In fact, CSCs have several features that make them naturally resistant to conventional therapies. Most of the drugs used in cancer treatment target DNA and induce irreversible damage leading to cell death. CSCs seem to have enhanced DNA repair mechanisms allowing them to resist do damage induced by conventional therapies [30]. The multidrug resistance trait of CSCs is associated with an overexpression of proteins from the BCL-2 family, which protects CSCs from apoptosis and leads to an increase in expression of membrane proteins responsible for drug resistance [31]. In addition, an increased expression of transporting proteins such as MDR1 and ABC transporters is an important factor in chemotherapy resistance [32].

Recent studies have successfully identified the presence of CSCs in osteosarcoma. Gibbs *et al.* [33] have successfully isolated the CSCs subpopulation from nine established cultures from untreated osteosarcoma biopsies and an osteosarcoma cell line (MG 63) through sphere formation assay. Sarcospheres-derived cells expressed the MSC surface markers Stro-1, CD105 and CD44 and over-expressed embryonic stem cells pluripotency markers (OCT4 and Nanog). Wang *et al.* [34] observed similar results in four more human osteosarcoma cell lines. Murase *et al.* [35] also reported the existence of a subset of CSCs in human osteosarcoma cell lines identified through the extrusion of Hoechst 33324. These cells revealed higher tumorigenic potential *in vivo* and *in vitro*. These findings strongly suggest that osteosarcoma is enriched in cells with stem-like properties, and that these cells may be responsible for drug resistance.

The high incidence of MDR in osteosarcoma and the difficulties in its treatment suggest the need for new treatment options.

2.2. The basis of a theranostic system

The latest advances in cancer nanotechnology aims at the design and engineering of targeted contrast agents that improve the resolution of cancer cells to the single cell level, and nano-devices that are capable of addressing the biological and evolutionary diversity of the multiple cancer cells that make up a tumor within an individual [36].

NP development is highly focused on the development of both therapeutic and diagnostic agents. Ideally, these two approaches should be combined in a single nano-agent, because of its potential ability to simultaneously image and treat disease at the cellular level. The term theranostics is used to define ongoing efforts to develop more specific, individualized therapies for various diseases and to combine diagnostic and therapy capabilities into a single agent. These nanostructures may present differences in size, shape, functionality, targeting mechanism, and imaging modality; however, some components are common between them (Figure 2.2):

- *Detection component* for noninvasive imaging: can be metallic or magnetic compounds for MRI, fluorescent compounds for optical imaging, and radioisotopes for positron emission tomography (PET) and single-photon emission computed tomography (SPECT).
- *Polymer coating*: this component is essential for colloidal stability and to provide functional groups for bioconjugation.

- *Drug loading capabilities*: this may be achieved by physical encapsulation in the polymeric matrix and electrostatic interaction with the other components of the nanostructure or by co-valent biding.

The rationale for theranostics arose from the fact that diseases, such as cancer, are very heterogeneous and the existing treatments are effective only in a small part of the patient population and at selective stages of disease development. The theranostic approach is expected to provide therapeutic protocols that are more specific to individuals and, therefore, more likely to improve prognostics [37]. This integration of diagnostic imaging capabilities with therapeutic intervention is crucial to overcome cancer challenges.

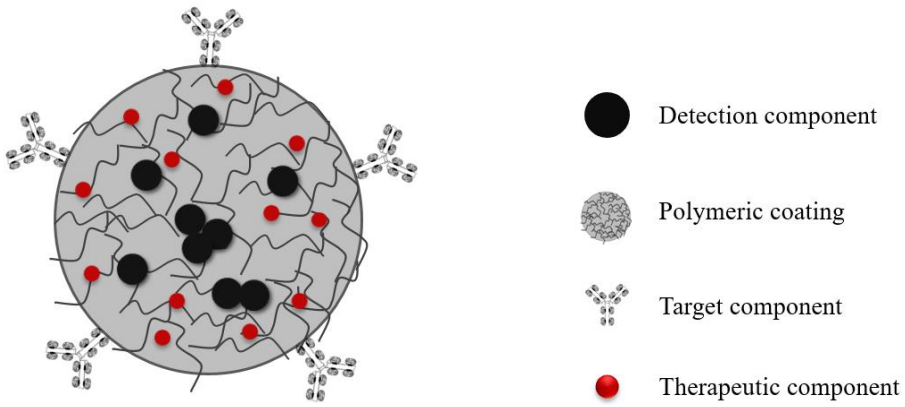

Figure 2.2. Basic components of a theranostic nanostructure.

Recent advances on cancer research have shown a huge heterogeneity among the different type, between the primary tumor and its metastasis foci, and even differences between cells that constitute individual tumors [38]. That said cancer has become one of the major applications of theranostic nanostructures.

Due to the exciting potential of these theranostic nanostructures, many researchers have focused on this issue. Theranostic nanostructures can be roughly divided by their detection and therapeutic component (Figure 2.2).

2.2.1. Detection Component

The detection component through molecular imaging allows the characterization of biological processes at cellular and subcellular level, without any damage to the living tissues. As so, by selecting a specific probe or a contrast agent, it is possible to create a powerful tool to both detect

and characterize early stage disease and monitor the treatment progress. There are vast possibilities for the detection component; however, two materials are the most used in theranostic nanostructures: iron oxide NPs and quantum dots.

2.2.1.1. Iron oxide NPs

Iron oxide NPs have been used clinically as MRI contrast agents mainly in the liver (e.g., Resovist, Feridex), due to the high magnetic moments that make them efficient in reduction T2 relaxation time, leading to signal attenuation on a T2 or T2*-weighted map.

The idea of using magnetic micro- or nanoparticles as drug carriers for cancer treatment dates back to the late 1970s [39], when magnetic micro- and nanoparticles attached to cytotoxic drugs were developed. Since then, several authors tried to improve this technique. For example, some authors have proposed nanocomposites based on the inclusion of magnetite nanocrystals into NPs constructed by self-assembling molecules of squalenoyl gemcitabine (SQgem) bioconjugate. These nanocomposites, after subcutaneous injection on mice tumor model, were magnetically guided to the target site showing high anticancer activity. The superior therapeutic activity and enhanced tumor accumulation were successfully visualized using T2-weighted imaging in MRI. This method was further actualized by the design of squalene-based NPs containing the T1 Gd^{3+} contrast agent instead of magnetite and by using different chemotherapeutic drugs such as DOX, cisplatin, and paclitaxel.

The use of MRI contrast agents has another advantage, treatment monitoring. By using oleic acid–coated iron oxide and pluronic-stabilized magnetic NPs loaded with DOX and paclitaxel, highly synergetic anti-proliferative activity in breast cancer cells was demonstrated [40], the NP accumulation and time of circulation in blood being monitored by MRI. Thus, that work showed that the incorporation of cytotoxic agents in magnetic NPs does not affect its physical (size and surface) properties or magnetization characteristics.

2.2.1.2. Quantum dots

Quantum dots are nanostructures with favorable characteristics for theranostic applications as a detector component, to identify disease via targeting ligands. However, their innate toxicity limits the applications in biomedical field [41, 42]. To overcome quantum-dot toxicity, hydrophobic quantum dots and iron oxide NPs were co-encapsulated along with DOX, into micelles formed with PEGylated phospholipid [43]. The conjugates were further coupled to a tumor-homing peptide F3 and injected into an MDA-MB-435 xenograft model. The results showed successful tumor targeting by both optical and MRI modalities.

The use of quantum dots in biomedical applications is very promising owing to their unique physicochemical properties such as broad absorption spectra, size-dependent narrow and stable emission spectra, and photostability. However, the inherent toxicity is a large limitation of their application. Moreover, there is a need to understand the quantum dot faith once they enter the body [41].

2.2.2. Coating Component

As seen by the given examples, the diagnostic component must be coated with a biocompatible material in order to be used as a theranostic agent. In the case of iron oxide NPs, these are generally coated with a biocompatible material (e.g., polysaccharide, synthetic polymer, lipid protein), creating a composite morphology often referred as core-shell structure. An ideal coating biomaterial for iron oxide NPs is the one that satisfies the following requirements [44]:

- Prevent opsonization and, consequently, increase the blood half-life of the iron oxide NPs in circulation;
- Avoid agglomeration of the NPs in physiological conditions;
- Achieve the desired surface charge for NPs' function;
- Preserve the functionalities of the NPs;
- Ensure the biocompatibility of the iron oxide NPs;
- Serve as a platform for NPs' surface functionality.

Several organic and inorganic coatings that meet these requirements have been used on the iron oxide NP surface. One example of a polysaccharide-based coating is given by chitosan. Chitosan is the *N*-deacetylated product of chitin, the second most abundant polysaccharide in nature, and possesses favorable characteristics: nontoxicity, biocompatibility, biodegradability, cationic, and hydrophilic. In addition, chitosan possesses amine and hydroxyl groups, suitable for NP functionalization with targeting, imaging, and therapeutic agents.

On the other hand, if the polymeric component is composed of a "smart" polymer, the theranostic nanostructure will only become activated when an external stimulus (temperature, pH, redox potential, or specific biomolecules) is present. For example, a theranostic nanostructure for a specific solid tumor composed by a polymer sensitive to a pH variation is capable of only releasing the therapeutic drug in the tumor microenvironment, which is characteristically more acidic than physiological conditions. This pH variation will induce changes in physical conformation (swelling or deswelling) of the polymeric coating, leading to drug release [45].

Liposomes are also used as coating, with promising results as a part of a theranostic agent. Liposomes are very versatile structures because of its capacity to incorporate pharmaceutical drugs, water-soluble macromolecules (hydrophilic), or lipid macromolecules (hydrophobic). Consequently, liposomes are a promising approach as theranostic agents [46]. Liposome application as theranostic agents was achieved by combining delivery and MRI of DOX-loaded liposomes in a Kaposi's sarcoma *in vivo* [47]. MRI was used both to determine liposome tissue distribution and to monitor DOX delivery and release. The results showed that Cd3 (high-affinity neural cell adhesion molecule [NCAM] binding ligand)-coated liposomes loaded with both DOX and gadolinium-DOTAMA(C18) were internalized and induced apoptosis of Kaposi's cells and tumor endothelial cells significantly more efficiently than did with uncoated PEG liposomes. In addition, the incorporation of DOX in PEG-coated liposomes reduced its cardiotoxicity while increasing its therapeutic efficacy. Furthermore, the use of gadolinium-labeled liposomes allowed the concomitant MRI visualization of the drug delivery in the tumor region.

Similarly, to liposomes, dendrimers are versatile structures capable of acting as drug and imaging agents with applications in tumor regression, gene delivery, and molecular imaging. However, their toxicity is a current barrier to its usage in this field [48]. To overcome this, several researchers have focused on chemical modification of dendrimers. For example, new dendrimer was designed and synthesized as based building block that is water soluble and can be functionalized in a highly controllable and orthogonal fashion [49]. This dendrimer was functionalized with an NIR-cyanine dye. The results showed fluorescence in the NIR region with a large Stokes shift and relatively high quantum yields. In addition, dendrimers showed no toxicity toward T98G human cells being promising agents for theranostic applications.

2.2.3. Target Component

After the detection component and coating of the theranostic nanostructure, another important issue is the target component. Although passive targeting is possible due to the NPs' small dimensions, it is not suitable for all diseases. As so, specific targeting is generally required. The specific targeting may be achieved using numerous biomarkers, specifically overexpressed by the target cells. Monoclonal antibodies were the first targeting agents to exploit molecular recognition to deliver magnetic NPs [50]. Magnetic nanocrystals conjugated to Herceptin were used as cancer-targeting monoclonal antibody for breast cancer treatment and successfully monitored *in vivo* selective targeting events of human cancer cells implanted in live mice [51].

Depending on NP characteristic, all types of NPs previously described may be applied for theranostics as a component of the theranostic nanostructure. Concerning this matter, iron oxide

NPs are among the most used NPs as theranostic agents. As such, iron oxide NPs may have two main functions: MRI contrast agents and hyperthermia agents.

2.3. Theranostic systems: *state of the art*

The proposed theranostic system is composed of magnetic nanoparticles with a polymeric coating based on chitosan. Iron oxide nanoparticles were chosen as the magnetic core of this theranostic system. In this section, the most recent developments for cancer treatment and/or diagnostic using both magnetic nanoparticles, especially iron oxide ones, and chitosan-based systems are reviewed.

2.3.1. Magnetic nanoparticles

Iron oxide NPs may form ideal platform for imaging of biological materials. Their mode of action is noninvasive and can be controlled remotely for drug release and cell signaling in the therapeutic field. Their superior magnetic properties allow for targeted imaging of specific receptors in disease processes and for monitoring treatment efficiency. The development of theranostic agents based on iron oxide NPs is a relatively recent approach but very promising application of these NPs. If by one hand is too early to predict its success the interest in this field has led to a larger investment in this technology, expecting consistent results soon.

Cell labeling/cell separation, magnetofection to facilitate drug delivery, as contrast agents for MRI or as drug delivery agents [39, 40, 52-55] are some of the possible applications of magnetic NPs, in particularly iron oxide nanoparticles have already been employed in clinical practice as MRI agents (e.g. Feridex®) and as magnetic hyperthermia agents (NanoTherm®). NanoTherm® is still in clinical trials for three types of tumors: glioblastoma multiform, prostate carcinoma [56-58] and pancreatic carcinoma [59].

The use of magnetic NPs as drug delivery agents for chemotherapeutic drugs is possible and promising. However, the major problems of chemotherapeutic drugs are their non-specificity and cell resistance; but with a drug carrier it is possible to overcome these problems [60]. For that, size, charge and surface chemistry of the magnetic NPs are crucial because they affect the time of circulation on the blood and the bioavailability of magnetic NPs [52]. Akiyoshi *et al.* [61] produced cholesterol-bearing pullulan hydrogel nanoparticles incorporated with doxorubicin (DOX) and, despite the loading levels were very low, encapsulated DOX-mediated cytotoxicity

was lower than with free DOX. Other authors associated DOX to polyalkylcyanoacrylate nanoparticles demonstrating reduced cardio toxicity after intravenous administration in mice [62] and increased cytotoxicity against multidrug resistance cell lines *in vitro* [63]. Janes *et al.* [64] demonstrated the viability of using chitosan nanoparticles as colloidal carriers to DOX delivery, incorporated with dextran sulfate. These particles have demonstrated a minimal burst release and the cytotoxic activity of DOX *in vitro* was retained. Sun *et al*. [65] developed iron oxide nanoparticles conjugated with chlorotoxin, a specific target for glioma and medulloblastoma cells, which are capable of delivering methotrexate to the tumor cells. They obtained improved specificity, extended particle retention and increased cytotoxicity in tumor cells. In order to improve these methods some authors used tumor-targeted magnetic NPs, e.g., DeNardo *et al.* [66] used dextran-coated magnetic nanoparticles conjugated to breast cancer targeting chimeric L6 monoclonal antibody and demonstrated its specificity in targeting cancer cells.

Another application of magnetic NPs is MRI, which is a powerful imaging tool due to its non-invasive nature, high spatial resolution, and tomographic capabilities [67]. The use of superparamagnetic iron oxide nanoparticles provides a better differentiation between healthy and pathological tissues and specifically allows for cancer cell targeting [68]. For example, some authors have used magnetic NPs to detect apoptosis, an active process of cellular self-destruction present in many disorders, such as neurodegenerative diseases (e.g. Alzheimer, Parkinson), by MRI [69-71].

The use of nanotechnology in biomedicine, particularly in cancer treatment, is becoming a real treatment option as more investigation is made in this area. Nanoparticles potential has been explored in several areas showing its advantages as adjuvant agents for chemo- and radiotherapy; moreover, magnetic NPs are already used as contrast agents for cancer detection, diagnosis, and treatment monitoring.

2.3.2. Polymeric nanoparticles

Park *et al.* [72] surveyed the use of chitosan in the area of targeted delivery of low molecular weight drugs, a category of major importance in therapeutics. This review is divided in two sections: the first related to organ-specific delivery and the subsequent one with recent developments of drug delivery carriers for cancer therapy. In colon, targeting the issue was how to protect the drug/chitosan combination as it transited the stomach and upper gastrointestinal tract to arrive the colon. Several strategies include coating, microspheres, and polyanionic micelles. Other target sites mentioned included the liver, kidney, and lung. In the second part of the review, the drug

delivery of cancer drugs using chitosan was presented. Passive targeting adopting the EPR (enhanced permeation and retention) effect included methods such as cross-linking of chitosan and polyelectrolyte complexes. Active targeting with receptor-mediated endocytosis and physical methods such as the use of chitosan-based stimuli-sensitive formulations and magnetic particles were explained.

Akbuğa *et al.* [73] prepared cisplatin loaded chitosan microspheres using a w/o emulsion system with an efficiency of about 30%. Pharmacokinetics, targeting, embolization effects, and alteration of liver function using cisplatin chitosan microspheres were evaluated after hepatic arterial embolization in dogs. A remarkable decrease in the number of arterioles in liver, necrosis of nodules and hepatic cell degeneration in the embolized region was found. Wei *et al.* [74] encapsulated paclitaxel in salicylic acid-graft chitosan oligosaccharide nanoparticle.

Chitosan structures have been used for the delivery of proteins/peptides, antibiotics, anti-inflammatory drugs and vaccines, among other molecules [75].

2.4. References

1. Known and probable human carcinogens, http://www.cancer.org/cancer/cancercauses/othercarcinogens/generalinformationaboutcarcinogens/known-and-probable-human-carcinogens, accessed on August, 26, 2015

2. S. Hodgson, Mechanisms of inherited cancer susceptibility, J Zhejiang Univ Sci B, 9 (2008), 1-4.

3. M. Hejmadi, Introduction to Cancer Biology, bookboon.com, 2010

4. S. F. Moss, M. J. Blaser, Mechanisms of disease: Inflammation and the origins of cancer, Nature clinical practice. Oncology, 2 (2005), 90-97; quiz 91 p following 113.

5. D. Hanahan, R. A. Weinberg, The hallmarks of cancer, Cell, 100 (2000), 57-70.

6. D. Hanahan, R. A. Weinberg, Hallmarks of cancer: the next generation, Cell, 144 (2011), 646-674.

7. F. Mbeunkui, D. J. Johann, Cancer and the tumor microenvironment: a review of an essential relationship, Cancer chemotherapy and pharmacology, 63 (2009), 571-582.

8. F. R. Balkwill, M. Capasso, T. Hagemann, The tumor microenvironment at a glance, Journal of cell science, 125 (2012), 5591-5596.

9. T. L. Whiteside, The tumor microenvironment and its role in promoting tumor growth, Oncogene, 27 (2008), 5904-5912.

10. R. L. Souhami, Oxford Textbook of Oncology, 2nd ed., Oxford University Press, Oxford, 2002.

11. T. J. Kinsella, J. Sohn, B. Wessels, 3 - Principles of Radiation Oncology, in: Oncology: An Evidence-Based Approach, Springer, 2006, pp. 41-57.

12. R. C. Bast, Cancer Medicine, 5th ed., B.C. Decker, Canada, 2000.

13. G. K. Dy, A. A. Adjei, 2 - Principles of Chemotherapy, in: Alfred E. Chang (Ed.) Oncology: An Evidence-Based Approach, Springer, 2006, pp. 14-40.

14. A. Arora, E. M. Scholar, Role of tyrosine kinase inhibitors in cancer therapy, The Journal of pharmacology and experimental therapeutics, 315 (2005), 971-979.

15. L. A. Torre, F. Bray, R. L. Siegel, J. Ferlay, J. Lortet-Tieulent, A. Jemal, Global cancer statistics, 2012, CA Cancer J Clin, 65 (2015), 87-108.

16. R. T. Chlebowski, J. E. Manson, G. L. Anderson, J. A. Cauley, A. K. Aragaki, M. L. Stefanick, D. S. Lane, K. C. Johnson, J. Wactawski-Wende, C. Chen, L. Qi, S. Yasmeen, P. A. Newcomb, R. L. Prentice, Estrogen plus progestin and breast cancer incidence and mortality in the Women's Health Initiative Observational Study, J Natl Cancer Inst, 105 (2013), 526-535.

17. M. M. Center, A. Jemal, J. Lortet-Tieulent, E. Ward, J. Ferlay, O. Brawley, F. Bray, International variation in prostate cancer incidence and mortality rates, Eur Urol, 61 (2012), 1079-1092.

18. G. B. Hamra, N. Guha, A. Cohen, F. Laden, O. Raaschou-Nielsen, J. M. Samet, P. Vineis, F. Forastiere, P. Saldiva, T. Yorifuji, D. Loomis, Outdoor particulate matter exposure and lung cancer: a systematic review and meta-analysis, Environmental health perspectives, 122 (2014), 906-911.

19. B. K. Edwards, E. Ward, B. A. Kohler, C. Eheman, A. G. Zauber, R. N. Anderson, A. Jemal, M. J. Schymura, I. Lansdorp-Vogelaar, L. C. Seeff, M. van Ballegooijen, S. L. Goede, L. A. Ries, Annual report to the nation on the status of cancer, 1975-2006, featuring colorectal cancer trends and impact of interventions (risk factors, screening, and treatment) to reduce future rates, Cancer, 116 (2010), 544-573.

20. M. M. Center, A. Jemal, R. A. Smith, E. Ward, Worldwide variations in colorectal cancer, CA Cancer J Clin, 59 (2009), 366-378.

21. E. Botteri, S. Iodice, V. Bagnardi, S. Raimondi, A. B. Lowenfels, P. Maisonneuve, Smoking and colorectal cancer: a meta-analysis, JAMA, 300 (2008), 2765-2778.

22. P. Ferrari, M. Jenab, T. Norat, A. Moskal, N. Slimani, A. Olsen, A. Tjonneland, K. Overvad, M. K. Jensen, M. C. Boutron-Ruault, F. Clavel-Chapelon, S. Morois, S. Rohrmann, J. Linseisen, H. Boeing, M. Bergmann, D. Kontopoulou, A. Trichopoulou, C. Kassapa, G. Masala, V. Krogh, P. Vineis, S. Panico, R. Tumino, C. H. van Gils, P. Peeters, H. B. Bueno-de-Mesquita, M. C. Ocke, G. Skeie, E. Lund, A. Agudo, E. Ardanaz, D. C. Lopez, M. J. Sanchez, J. R. Quiros, P. Amiano, G. Berglund, J. Manjer, R. Palmqvist, B. Van Guelpen, N. Allen, T. Key, S. Bingham, M. Mazuir, P. Boffetta, R. Kaaks, E. Riboli, Lifetime and baseline alcohol intake and risk of colon and rectal cancers in the European prospective investigation into cancer and nutrition (EPIC), Int J Cancer, 121 (2007), 2065-2072.

23. J. Ferlay, E. Steliarova-Foucher, J. Lortet-Tieulent, S. Rosso, J. W. Coebergh, H. Comber, D. Forman, F. Bray, Cancer incidence and mortality patterns in Europe: estimates for 40 countries in 2012, Eur J Cancer, 49 (2013), 1374-1403.

24. M. Susa, A. K. Iyer, K. Ryu, F. J. Hornicek, H. Mankin, M. M. Amiji, Z. Duan, Doxorubicin loaded Polymeric Nanoparticulate Delivery System to overcome drug resistance in osteosarcoma, BMC cancer, 9 (2009), 399.

25. M. Pasello, C. M. Hattinger, G. Stoico, M. C. Manara, S. Benini, C. Geroni, M. Mercuri, K. Scotlandi, P. Picci, M. Serra, 4-Demethoxy-3'-deamino-3'-aziridinyl-4'-methylsulphonyl-daunorubicin (PNU-159548): a promising new candidate for chemotherapeutic treatment of osteosarcoma patients, Eur J Cancer, 41 (2005), 2184-2195.

26. V. O. Lewis, What's new in musculoskeletal oncology, J Bone Joint Surg Am, 89 (2007), 1399-1407.

27. K. Moitra, H. Lou, M. Dean, Multidrug efflux pumps and cancer stem cells: insights into multidrug resistance and therapeutic development, Clin Pharmacol Ther, 89 (2011), 491-502.

28. P. Dalerba, R. W. Cho, M. F. Clarke, Cancer stem cells: models and concepts, Annual review of medicine, 58 (2007), 267-284.

29. L. Moserle, M. Ghisi, A. Amadori, S. Indraccolo, Side population and cancer stem cells: therapeutic implications, Cancer Lett, 288 (2010), 1-9.

30. S. J. Miller, R. M. Lavker, T. T. Sun, Interpreting epithelial cancer biology in the context of stem cells: tumor properties and therapeutic implications, Biochim Biophys Acta, 1756 (2005), 25-52.

31. M. Al-Hajj, M. S. Wicha, A. Benito-Hernandez, S. J. Morrison, M. F. Clarke, Prospective identification of tumorigenic breast cancer cells, Proc Natl Acad Sci U S A, 100 (2003), 3983-3988.

32. C. T. Jordan, M. L. Guzman, M. Noble, Cancer stem cells, N Engl J Med, 355 (2006), 1253-1261.

33. C. P. Gibbs, V. G. Kukekov, J. D. Reith, O. Tchigrinova, O. N. Suslov, E. W. Scott, S. C. Ghivizzani, T. N. Ignatova, D. A. Steindler, Stem-like cells in bone sarcomas: implications for tumorigenesis, Neoplasia, 7 (2005), 967-976.

34. L. Wang, P. Park, C. Y. Lin, Characterization of stem cell attributes in human osteosarcoma cell lines, Cancer biology & therapy, 8 (2009), 543-552.

35. M. Murase, M. Kano, T. Tsukahara, A. Takahashi, T. Torigoe, S. Kawaguchi, S. Kimura, T. Wada, Y. Uchihashi, T. Kondo, T. Yamashita, N. Sato, Side population cells have the characteristics of cancer stem-like cells/cancer-initiating cells in bone sarcomas, Br J Cancer, 101 (2009), 1425-1432.

36. S. M. Moghimi, A. C. Hunter, J. C. Murray, Nanomedicine: current status and future prospects, FASEB journal : official publication of the Federation of American Societies for Experimental Biology, 19 (2005), 311-330.

37. P. I. Soares, S. J. Dias, C. M. Novo, I. M. Ferreira, J. P. Borges, Doxorubicin vs. ladirubicin: methods for improving osteosarcoma treatment, Mini reviews in medicinal chemistry, 12 (2012), 1239-1249.

38. B. Sumer, J. Gao, Theranostic nanomedicine for cancer, Nanomedicine (Lond), 3 (2008), 137-140.

39. K. J. Widder, A. E. Senyel, G. D. Scarpelli, Magnetic microspheres: a model system of site specific drug delivery in vivo, Proc Soc Exp Biol Med, 158 (1978), 141-146.

40. T. K. Jain, J. Richey, M. Strand, D. L. Leslie-Pelecky, C. A. Flask, V. Labhasetwar, Magnetic nanoparticles with dual functional properties: drug delivery and magnetic resonance imaging, Biomaterials, 29 (2008), 4012-4021.

41. J. Xie, S. Lee, X. Chen, Nanoparticle-based theranostic agents, Adv Drug Deliv Rev, 62 (2010), 1064-1079.

42. J. V. Jokerst, S. S. Gambhir, Molecular imaging with theranostic nanoparticles, Acc Chem Res, 44 (2011), 1050-1060.

43. J. H. Park, G. von Maltzahn, E. Ruoslahti, S. N. Bhatia, M. J. Sailor, Micellar hybrid nanoparticles for simultaneous magnetofluorescent imaging and drug delivery, Angew Chem Int Ed Engl, 47 (2008), 7284-7288.

44. S. Laurent, S. Dutz, U. O. Hafeli, M. Mahmoudi, Magnetic fluid hyperthermia: focus on superparamagnetic iron oxide nanoparticles, Adv Colloid Interface Sci, 166 (2011), 8-23.

45. M. E. Caldorera-Moore, W. B. Liechty, N. A. Peppas, Responsive theranostic systems: integration of diagnostic imaging agents and responsive controlled release drug delivery carriers, Acc Chem Res, 44 (2011), 1061-1070.

46. W. T. Al-Jamal, K. Kostarelos, Liposomes: from a clinically established drug delivery system to a nanoparticle platform for theranostic nanomedicine, Acc Chem Res, 44 (2011), 1094-1104.

47. C. Grange, S. Geninatti-Crich, G. Esposito, D. Alberti, L. Tei, B. Bussolati, S. Aime, G. Camussi, Combined delivery and magnetic resonance imaging of neural cell adhesion molecule-targeted doxorubicin-containing liposomes in experimentally induced Kaposi's sarcoma, Cancer Res, 70 (2010), 2180-2190.

48. S. M. Janib, A. S. Moses, J. A. MacKay, Imaging and drug delivery using theranostic nanoparticles, Adv Drug Deliv Rev, 62 (2010), 1052-1063.

49. C. Ornelas, R. Pennell, L. F. Liebes, M. Weck, Construction of a well-defined multifunctional dendrimer for theranostics, Org Lett, 13 (2011), 976-979.

50. Cerdan S, Lotscher H R, Kunnecke B, S. J., Monoclonal antibody-coated magnetite particles as contrast agents in magnetic resonance imaging of tumors Mag Reson Med, 12 (1989), 151-163.

51. Y. M. Huh, Y. W. Jun, H. T. Song, S. Kim, J. S. Choi, J. H. Lee, S. Yoon, K. S. Kim, J. S. Shin, J. S. Suh, J. Cheon, In vivo magnetic resonance detection of cancer by using multifunctional magnetic nanocrystals, J Am Chem Soc, 127 (2005), 12387-12391.

52. A. K. Gupta, M. Gupta, Synthesis and surface engineering of iron oxide nanoparticles for biomedical applications, Biomaterials, 26 (2005), 3995-4021.

53. A. S. Arbab, L. A. Bashaw, B. R. Miller, E. K. Jordan, B. K. Lewis, H. Kalish, J. A. Frank, Characterization of biophysical and metabolic properties of cells labeled with superparamagnetic iron oxide nanoparticles and transfection agent for cellular MR imaging, Radiology, 229 (2003), 838-846.

54. O. Olsvik, T. Popovic, E. Skjerve, K. S. Cudjoe, E. Hornes, J. Ugelstad, M. Uhlen, Magnetic separation techniques in diagnostic microbiology, Clin Microbiol Rev, 7 (1994), 43-54.

55. Q. A. Pankhurst, J. Connolly, S. K. Jones, J. Dobson, Applications of magnetic nanoparticles in biomedicine, Journal of Physics D: Applied Physics, 36 (2003), R167-R181.

56. M. Johannsen, U. Gneveckow, K. Taymoorian, B. Thiesen, N. Waldofner, R. Scholz, K. Jung, A. Jordan, P. Wust, S. A. Loening, Morbidity and quality of life during thermotherapy using magnetic nanoparticles in locally recurrent prostate cancer: results of a prospective phase I trial, Int J Hyperthermia, 23 (2007), 315-323.

57. M. Johannsen, U. Gneveckow, B. Thiesen, K. Taymoorian, C. H. Cho, N. Waldofner, R. Scholz, A. Jordan, S. A. Loening, P. Wust, Thermotherapy of prostate cancer using magnetic nanoparticles: feasibility, imaging, and three-dimensional temperature distribution, Eur Urol, 52 (2007), 1653-1661.

58. M. Johannsen, U. Gneveckow, L. Eckelt, A. Feussner, N. WaldÖFner, R. Scholz, S. Deger, P. Wust, S. A. Loening, A. Jordan, Clinical hyperthermia of prostate cancer using magnetic nanoparticles: Presentation of a new interstitial technique, Int J Hyperther, 21 (2005), 637-647.

59. MagForce AG, accessed on May 5, 2014,

60. B. N. Gray, S. K. Jones, in, Sirtex Medical Limited, US, 2003.

61. K. Akiyoshi, I. Taniguchi, H. Fukui, J. Sunamoto, Hydrogel nanoparticle formed by self-assembly of hydrophobized polysaccharide, stabilization of adriamycin by complexation, European journal of pharmaceutics and biopharmaceutics, 42 (1996), 286-290.

62. P. Couvreur, B. Kante, L. Grislain, M. Roland, P. Speiser, Toxicity of polyalkylcyanoacrylate nanoparticles II: Doxorubicin-loaded nanoparticles, J Pharm Sci, 71 (1982), 790-792.

63. C. Cuvier, L. Roblot-Treupel, J. M. Millot, G. Lizard, S. Chevillard, M. Manfait, P. Couvreur, M. F. Poupon, Doxorubicin-loaded nanospheres bypass tumor cell multidrug resistance, Biochem Pharmacol, 44 (1992), 509-517.

64. M. D. Sapozink, T. Cetas, P. M. Corry, M. J. Egger, P. Fessenden, Introduction to hyperthermia device evaluation, Int J Hyperthermia, 4 (1988), 1-15.

65. C. Sun, C. Fang, Z. Stephen, O. Veiseh, S. Hansen, D. Lee, R. G. Ellenbogen, J. Olson, M. Zhang, Tumor-targeted drug delivery and MRI contrast enhancement by chlorotoxin-conjugated iron oxide nanoparticles, Nanomedicine (Lond), 3 (2008), 495-505.

66. S. DeNardo, G. DeNardo, L. Miers, A. Natarajan, A. Foreman, C. Gruettner, G. Adamson, R. Ivkov, Development of tumour targeting bioprobes (111In-chimeric L6 monoclonal antibody nanoparticles) for alternating magnetic field cancer therapy, Clinical cancer research, 11 (2005), 7087-7092.

67. C. C. Berry, Progress in functionalization of magnetic nanoparticles for applications in biomedicine, Journal of Physics D: Applied Physics, 42 (2009), 224003.

68. M. A. Oghabian, N. M. Farahbakhsh, Potential Use of Nanoparticle Based Contrast Agents in MRI: A Molecular Imaging Perspective, Journal of Biomedical Nanotechnology, 6 (2010), 203-213.

69. M. Zhao, D. A. Beauregard, L. Loizou, B. Davletov, K. M. Brindle, Non-invasive detection of apoptosis using magnetic resonance imaging and a targeted contrast agent, Nat Med, 7 (2001), 1241-1244.

70. H. Poptani, A. Puumalainen, O. Grohn, S. Loimas, R. Kainulainen, S. Yla-Herttuala, R. Kauppinen, Monitoring thymidine kinase and gancyclovir induced changes in rat malignant glioma in vivo by nuclear magnetic resonance imaging, Cancer Gene Ther, 5 (1998), 101-109.

71. F. G. Blankenberg, P. D. Katsikis, R. W. Storrs, C. Beaulieu, D. Spielman, J. Y. Chen, L. Naumovski, J. F. Tait, Quantitative analysis of apoptotic cell death using proton nuclear magnetic resonance spectroscopy, Blood, 89 (1997), 3778-3786.

72. J. H. Park, G. Saravanakumar, K. Kim, I. C. Kwon, Targeted delivery of low molecular drugs using chitosan and its derivatives, Adv Drug Deliv Rev, 62 (2010), 28-41.

73. J. Akbuga, N. Bergisadi, Effect of formulation variables on cis-platin loaded chitosan microsphere properties, J Microencapsul, 16 (1999), 697-703.

74. X. H. Wei, Y. P. Niu, Y. Y. Xu, Y. Z. Du, F. Q. Hu, Y. Hong, Salicylic Acid-grafted Chitosan Oligosaccharide Nanoparticle for Paclitaxel Delivery, Journal of Bioactive and Compatible Polymers, 25 (2010), 319-335.

75. M. Dash, F. Chiellini, R. M. Ottenbrite, E. Chiellini, Chitosan—A versatile semi-synthetic polymer in biomedical applications, Progress in Polymer Science, 36 (2011), 981-1014.

– This page is intentionally blank –

Chapter 3. Iron oxide nanoparticles

This chapter starts with the most important concepts related to iron oxide nanoparticles, their magnetic properties, synthesis, colloidal stability, and toxicity. The used methodology for the production of iron oxide nanoparticles as well as the detailed characterization are further described and discussed in this chapter. At the end of this chapter, the produced iron oxide nanoparticles are suitable to compose the core of the theranostic system developed during this PhD thesis.

3.1. Introduction

In a general approach, nanostructures have at least one dimension in a range of 1–100 nm and can be classified according to their dimension. Further, these nanostructures exhibit new or enhanced size-dependent properties compared with larger particles of the same material. Some regulatory agencies have tried to standard the definitions of nanoparticle (NP). The first published standard to provide this definition was given by an International Organization of Standardization (ISO) standard, ISO/TS 27687:2008 "Nanotechnologies - Terminology and definitions for nano-objects - nanoparticle, nanofiber and nanoplate" [1]. According to this standard, a NP is defined as a "nano-object with all three dimensions in the nanoscale" being the nanoscale a "size range from approximately 1 nm to 100 nm." Two notes accompany this nanoscale definition: "Properties that are not extrapolations from a larger size will typically, but not exclusively, be exhibited in this size range. For such properties the size limits are considered approximate" and "The lower limit in this definition (approximately 1 nm) is introduced to avoid single and small groups of atoms from being designated as nano-objects or elements of nanostructures, which might be implied by the absence of a lower limit."

3.1.1. Magnetic nanoparticles

Within the last decades, magnetic NPs have been extensively investigated for biomedical applications (Figure 3.1). These applications include magnetic resonance image (MRI) contrast agents for diagnosis [2] and magnetic hyperthermia agents for cancer treatment [3, 4]. In general, all materials respond to applied magnetic fields. However, those that have a strong response to magnetic fields are called magnetic. Magnetic nanoparticles are a class of nanoparticles that can be manipulated using a magnetic field. These NPs possess unique physical properties and ability to function at cellular and molecular level of biological interactions [2].

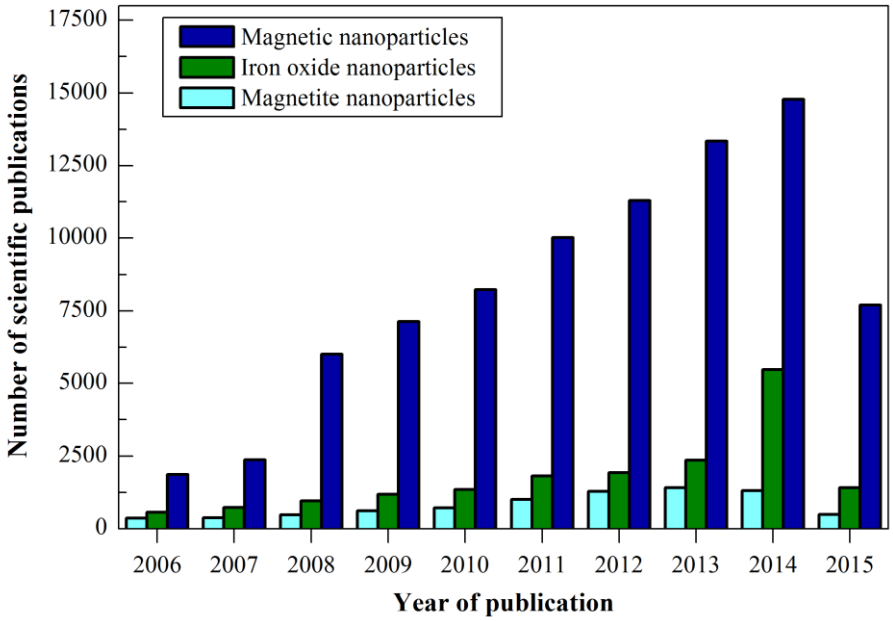

Figure 3.1. Evolution in the number of scientific papers published related to magnetic nanoparticles, iron oxide nanoparticles and magnetite nanoparticles. (Source: ISI Web of Knowledge © the Thompson Corporation. Search terms: 'magnetic nanoparticles', 'iron oxide nanoparticles', and 'magnetite nanoparticles'. Date of search: June 2015).

Magnetic NPs are generally composed of pure metals, metal alloys or metal oxides [5]. Metallic NPs have larger magnetization compared to metal oxides but they are not stable in air and are easily oxidized. Metal NPs may be composed of iron, cobalt, or nickel, and due to their instability are typically protected by coating such as gold or silica, forming a core-shell structure. Despite the difficulty in synthetize these types of magnetic NPs, research continues due to the unique advantages some of these NPs can offer. For example, iron NPs have a high magnetic moment density and are able to maintain their superparamagnetism at larger particle sizes, when compared to their oxides [2, 5]. Metal alloy NPs or bimetallic NPs are usually composed of one metallic

material and platinum or of two metallic materials. These nanoparticles can also exhibit superparamagnetic behavior and have shown extremely high saturation magnetization values [2, 6].

3.1.1.1. Iron oxide nanoparticles

Iron oxides are compounds available in nature and easily synthetize in laboratory. Iron oxide NPs are superior to other metal oxide NPs for their biocompatibility and stability and are the most commonly employed magnetic NPs for biomedical applications [7]. From all the iron oxides, Fe_3O_4 (magnetite) has the most interesting magnetic properties due to the presence of iron cations in two valence states, Fe^{2+} and Fe^{3+} [5]. In the bulk form, this material is ferromagnetic due to the antiferromagnetic coupling among Fe (III) in its inverse spinel structure. However, at nanoscale (< 20 nm), iron oxide NPs are superparamagnetic at room temperature, that is, when the size of the particle is reduced enough, magnetite NPs become a single magnetic dipole and therefore maintain one large magnetic moment. Consequently, these NPs are easily magnetized under the application of an external magnetic field and unmagnetized once the field is removed. Another interesting property of iron oxide NPs is their ability to generate heat when subjected to an alternating magnetic field (AMF). This thermal phenomenon may be due to energy losses during the demagnetization process (specific loss power). This property is crucial for hyperthermia applications [2, 8, 9].

The need to improve magnetic properties of these materials has generated the development of metal-doped iron oxides. These materials with a composition of MFe_2O_4, where M may be Mn, Fe, Co or Ni, have a remarkably similar spinel structure to magnetite [2, 10].

3.1.2. Magnetic properties

Macroscopic objects possess a large number of atoms ($> 10^{23}$ particles) and therefore their magnetic properties should be calculated using methods of solid-state physics. On the other hand, nanoparticles are composed of several hundred up to $\approx 10^5$ atoms and consequently their magnetic properties can be determined by methods common to quantum chemistry and solid state physics [5].

The magnetic effects are caused by particles with both mass and electric charges such as electrons, holes, protons, positive and negative ions. The spinning of an electric-charged particle causes a magnetic dipole – a magneton. A ferromagnetic material is composed of magnetic domains, i.e., a magnetic domain is a portion of the ferromagnetic material in which all magnetic dipoles are

aligned in the same direction by the exchange forces [11]. Bulk ferromagnetic materials are composed of thousands of magnetic domains separated by boundaries called domain walls, forming the so-called grains. This domain wall is a defect in the material that takes energy to form, and have significant width, generally in the tens to hundreds of nanometers. In these cases the reversal of the magnetization is controlled by the nucleation and motion of domain walls through the material [12]. When the size of the particles is reduced, the state of lowest energy has uniform magnetization and the particle is composed of a single domain. The critical size of the single domain is affected by several factors, such as the value of the saturation magnetization (M_s), the strength of the crystal anisotropy and exchange forces, the surface or domain-wall energy, and the shape of the particles [11].

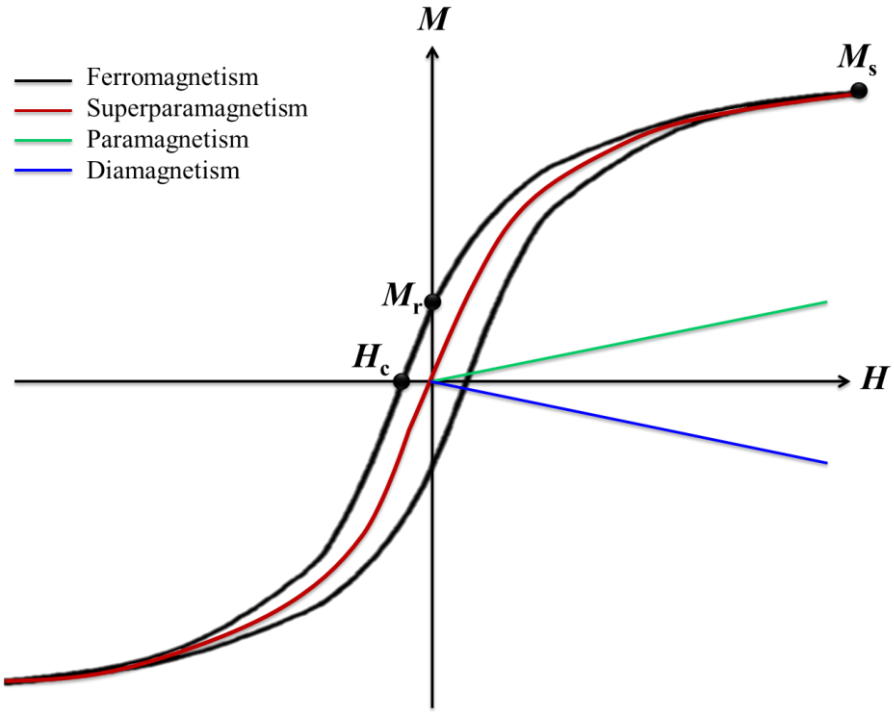

Figure 3.2. Schematic representation of hysteresis loops (magnetization versus applied magnetic field) for ferromagnetic, superparamagnetic, diamagnetic, and paramagnetic nanoparticles. (H_c – Coercivity; M_r – Remanent magnetization; M_s – Saturation magnetization) (Adapted from [12, 13]).

The properties of magnetic materials are classified according to the magnetic susceptibility (χ), which is defined by the ratio of the induced magnetization (M) to the applied magnetic field (H) [2, 14]. This ratio is well described by a hysteresis loop (Figure 3.2), which is characterized by two main parameters: remanence (M_r) and coercivity (H_c). The remanence or remanent magnetization is the magnetization that remains after an applied field has been removed. The coercivity or coercive field is related to the 'thickness' of the curve and is the applied magnetic field required

for reduction of a saturated magnetic material to zero magnetization. The coercivity has been found to be size-dependent for small particles, i.e., as the size of the particle is reduced, the coercivity increases to a maximum and then decreases toward zero (Figure 3.3) [11, 12].

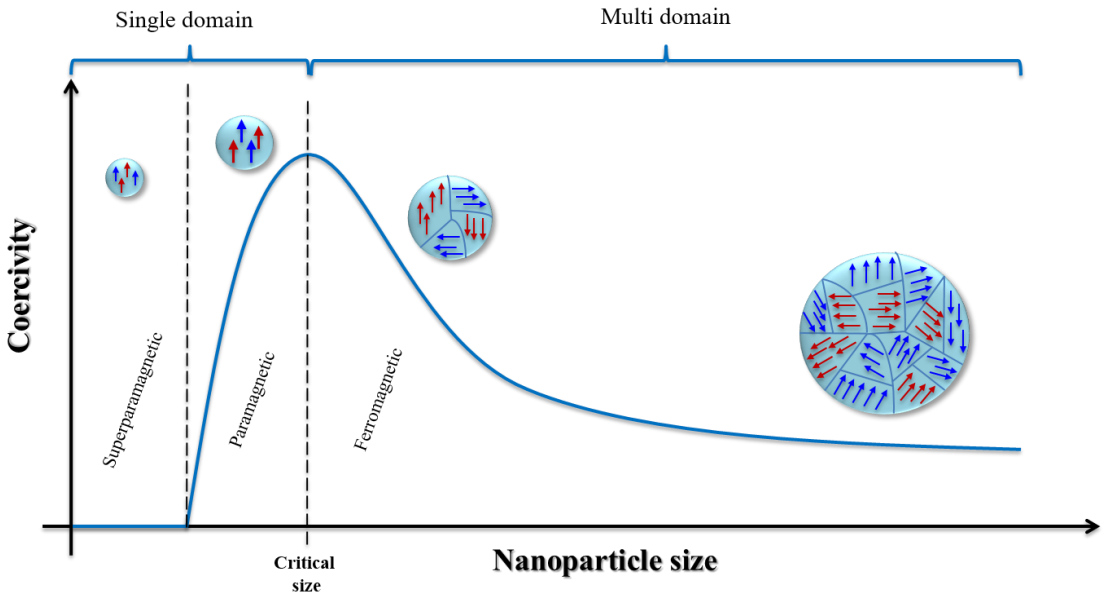

Figure 3.3. Schematic illustration of the relationship between coercivity, nanoparticles size, and magnetic domain structures. The blue and red arrows represent the magnetic dipoles (adapted from [11]).

When the size of single domain particles decreases and the coercivity becomes zero such particles become superparamagnetic. Superparamagnetic NPs have such strong thermal fluctuations to demagnetize a previously saturated assembly, i.e., these NPs become magnetic when an external magnetic field is applied; however, they are able to revert to a nonmagnetic state once the applied magnetic field is removed. Therefore, superparamagnetic nanoparticles have zero coercivity and no hysteresis [11]. The transition temperature in which the NPs become superparamagnetic is called Blocking temperature (T_B) and is defined by the Equation 3.1:

$$K = 25k_B\frac{T_B}{V} \qquad \text{Equation 3.1}$$

Where K is the magnetic anisotropy constant, k_B is the Boltzmann constant, and V is the volume of a single nanoparticle. The superparamagnetic behavior may be described by the Langevin equation:

$$\frac{M}{M_S} = \coth\alpha - \frac{1}{\alpha} \qquad \text{Equation 3.2}$$

Where M is the magnetization, M_S is the saturation magnetization and α is the ratio of magnetic to thermal energy, defined by:

$$\alpha = \frac{\mu_0 m H}{k_B T} \qquad \text{Equation 3.3}$$

Where H is the magnetic field, m is the magnetic moment, μ_0 is the permeability of free space, k_B is the Boltzmann constant, and T is the absolute temperature. At very low magnetic fields, $\alpha << 1$ and the Langevin equation becomes $M/M_S = (\mu_0 m H)/(k_B T)$ where the relationship between the magnetization and the magnetic field is linear. With the increase of the magnetic field, magnetic saturation occurs due to the very high magnetic moment of the magnetic nanoparticles ($\alpha >> 1$) [15].

Magnetic materials may be classified according the type of response to an applied magnetic field. All materials exhibit diamagnetism, a very weak repulsion to an applied magnetic field. These materials have negative susceptibility ($\chi < 0$) because the current loops created by the orbital motion of electrons respond to oppose the applied magnetic field. The effects of these atomic current loops are overcome if the material displays a net magnetic moment or has a long-range ordering of its magnetic moments. The other types of magnetic behaviors occur in materials that have at least partially unpaired electrons in their atomic shells, often in the 3*d* or 4*f* shells of each atom [11].

Paramagnetic materials possess atomic uncoupled magnetic moments and consequently their magnetic moments have no long-range order and are permanent. Therefore these materials have a small positive magnetic susceptibility ($\chi \approx 0$) [11]. Ferromagnetism occurs in particles whose unpaired electron spins align themselves spontaneously and subsequently the material can exhibit magnetization in the absence of an applied magnetic field [11, 16]. Similarly, antiferromagnetism occurs in materials with atomic magnetic moments of equal magnitude but arranged in an antiparallel fashion. Above the Néel temperature (temperature above which an antiferromagnetic material becomes paramagnetic), thermal energy is sufficient to cause the equal and oppositely aligned atomic moments to randomly fluctuate, leading to a disappearance of their long-range order, becoming a paramagnetic material [11, 12].

Ferrimagnetic materials consist of antiparallel arrangements of the magnetic moments in a zero applied field below at the Néel temperature (T_N), yet the material maintains a net magnetization. This magnetic behavior occurs due to either the number of magnetic moments being different in each direction, or the size of the magnetic moments in alternating directions being different, or both. At sufficient high temperature (above the Currie temperature, T_c), the material becomes

paramagnetic [11, 12]. It should be noted that the Currie temperature is the critical point where a material's intrinsic magnetic moments change direction. The Néel temperature is similar to Curie temperature but for antiferromagnetic materials.

3.1.3. Synthesis

The synthesis of NPs can be performed by different methods, although when choosing one it is important to consider the application, because their properties are highly dependent on the synthesis method.

3.1.3.1. Chemical co-precipitation

The co-precipitation method is probably the simplest method to produce iron oxide NPs. It is possible to use harmless and biocompatible materials and chemical agents and thus suitable for biomedical applications. A careful control of the reaction parameters, allows obtaining a fine suspension of NPs with sizes as small as 5 nm. For magnetite preparation, a strong base is added to a mixture of Fe^{2+} and Fe^{3+} solution (usually with molar ratio of 1:2) under an inert atmosphere leading to the following reaction:

$$Fe^{2+}{}_{(aq)} + 2Fe^{3+}{}_{(aq)} + 8OH^{-}{}_{(aq)} \rightarrow Fe_3O_{4(s)} + 4H_2O_{(l)} \qquad \text{Equation 3.4}$$

The controlling of particles size, distribution, and morphology is the main difficulty of this method. Although, an oxygen-free atmosphere is required to avoid oxidation of ferrous ion in the solution [10, 14], Fe_3O_4 NPs can be utilized to prepare the Fe_2O_3 NPs by oxidation or anneal treatment under oxygen atmosphere [17].

The size and shape of the obtained NPs depend on the type of salt used (such as chlorides, sulfates, nitrates, perchlorates, etc.), the ferric and ferrous ions ratio, the reaction temperature, the pH value, ionic strength of the media, and the other reaction parameters (e.g. stirring rate, dropping speed of basic solution) [17]. Gnanaprakash and coworkers [18] have studied the effect of digestion time and alkali addition rate on the size and magnetic properties of magnetite NPs produced by chemical precipitation. The M_S of the obtained NPs decreases from 60 to 46 emu.g^{-1} as the particle size decreases. More recently other authors found similar behavior but influenced by temperature, stirring rate and time, pH and concentration of precursors [19]. In general, the experimental value for M_S obtained by this method is around 30-80 emu.g^{-1} [17].

Despite the difficulty in controlling the properties of the NPs, several authors have obtained low size and narrow dispersed NPs [20-22], even without stabilizers [23-25].

3.1.3.2. Thermal decomposition

The synthesis of NPs by thermal decomposition is based on the decomposition of metal oxysalts (e.g., nitrates, carbonates, and acetates) when heated. The decomposition is made on controlled environment and so the reactions are more controlled, leading to a better size control, narrow size distribution, and crystallinity of grains. Thermolysis of $Fe(acac)_3$ in diphenyl ether in the presence of small amounts of hexadecane-1,2-diol gives very fine Fe_3O_4 NPs (around 1 nm), which can be enlarged by adding excess $Fe(acac)_3$ into the reaction mixture [5]. However, usually it is required relatively high temperature and a complicated operation [14, 17] and the NPs are generally only dissolved in nonpolar solvents [26]. However, Maity and coworkers [27, 28] have synthetized water-soluble magnetite NPs by thermal decomposition of iron (III) acetylacetonate in tri(ethylene glycol) (TREG) alone and a mixture of TREG and triethanol amine (TREM). In both cases, the obtained NPs have a M_S of 65 and 68 emu.g^{-1}, respectively, are biocompatible and have potential applicability for magnetic hyperthermia application.

3.1.3.3. Microemulsion method

Microemulsion is a thermodynamically stable isotropic dispersion of two immiscible phases (water and oil) under the surfactant present. Iron oxide NPs may be produced also through water-in-oil (w/o) microemulsion systems that are composed of fine microdroplets of the aqueous phase trapped within assemblies of surfactant molecules dispersed in a continuous oil phase. The surfactant-stabilized microcavities (of approximately 10 nm range) provide the necessary confinement to limit particle nucleation, growth, and agglomeration [14].

3.1.3.4. Hydrothermal synthesis

Hydrothermal synthesis includes various wet chemical technologies of crystalizing substance in a sealed container from the high temperature aqueous solution (usually above 100 ºC) at high vapor pressure (usually above 1 atm). This technique is prone to obtain highly crystalline iron oxide NPs, and the unusual iron oxide nanostructures such as nanocubes or iron oxide hollow spheres. The advantages of this technique include low-temperature synthesis, simple reactions, cost effectiveness, and good water dispersibility of the obtained NPs [17, 29, 30].

Several other techniques are available for the preparation of iron oxide NPs, including sonochemical synthesis [31], electrochemical synthesis [32, 33], laser pyrolysis techniques [34], microorganism or bacterial synthesis [35, 36].

3.1.4. Colloidal stability and coating

Colloidal stability of magnetic nanoparticles is crucial to obtain magnetic colloidal ferrofluids that are stable against aggregation in both a biological medium and a magnetic field [37].

When nanoparticles are in aqueous medium they may agglomerate or aggregate, forming large particles that may settle out due to gravity. This event may change the superparamagnetic properties to ferromagnetic ones due to particle size increase [16, 38].

The colloidal stability is strongly influenced by the interactions between nanoparticles and between NPs and its surrounding medium. The particle surface charges are balanced by an equal but oppositely charged region of counter-ions. Each particle has electrical charge that is responsible by the mutual electrostatic repulsion/attraction force between adjacent particles. The counter-ions form a double layer at the interface of the NPs with the medium. The double layer theory (Figure 3.4 A) describes the formation and the extension of the ionic neighborhood of a charged colloid [39, 40]. If one considers a negative charged particle in an aqueous medium, this particle would be surrounded by a layer of positive ions (counter-ions) also known as the Stern layer. Surrounding the Stern layer are positive ions that form a second layer called diffuse layer. The Stern layer together with the charged region of the diffuse layer is the so-called double layer. The presence of the double layer not only neutralizes the charged particle, but also creates an electrokinetic potential between the surface of the colloid and any point in the mass of the solution, called surface potential (Figure 3.4 B). On the other hand, the diffuse layer, or part of it, can move under the influence of tangential stress. Therefore, a slipping plane is introduced to separate the mobile fluid from fluid that remains attached to the surface. The electric potential at this plane is called the zeta potential (ζ). A value of 25-30 mV (in modulus) can be taken as a reference of the minimum potential to form a stable colloid, since it separates low charged surfaces from highly charged surfaces [39, 40].

Colloidal stability of magnetic NPs in aqueous media results from the equilibrium established between attractive and repulsive forces. Theoretically, the attractive ones are van der Waals forces, dipolar, and magnetic dipolar forces while repulsive forces come from electrostatic and steric repulsion. Van der Waals forces induce strong short-range isotropic attractions. The electrostatic repulsive forces can be partially screened by adding salt to the suspension. These repulsive forces become significant when two particles approach each other and their double layers begin to interfere. When discussing colloidal stability of magnetic nanoparticles another force must be considered, the magnetic dipolar force. This force induces anisotropic interactions, which result in globally attractive forces if the anisotropic interparticle potential is integrated over all

directions. Finally, when the nanoparticles are coated with a surfactant, a polymer, or any other type of coating, steric repulsion has to be taken into account [37, 39].

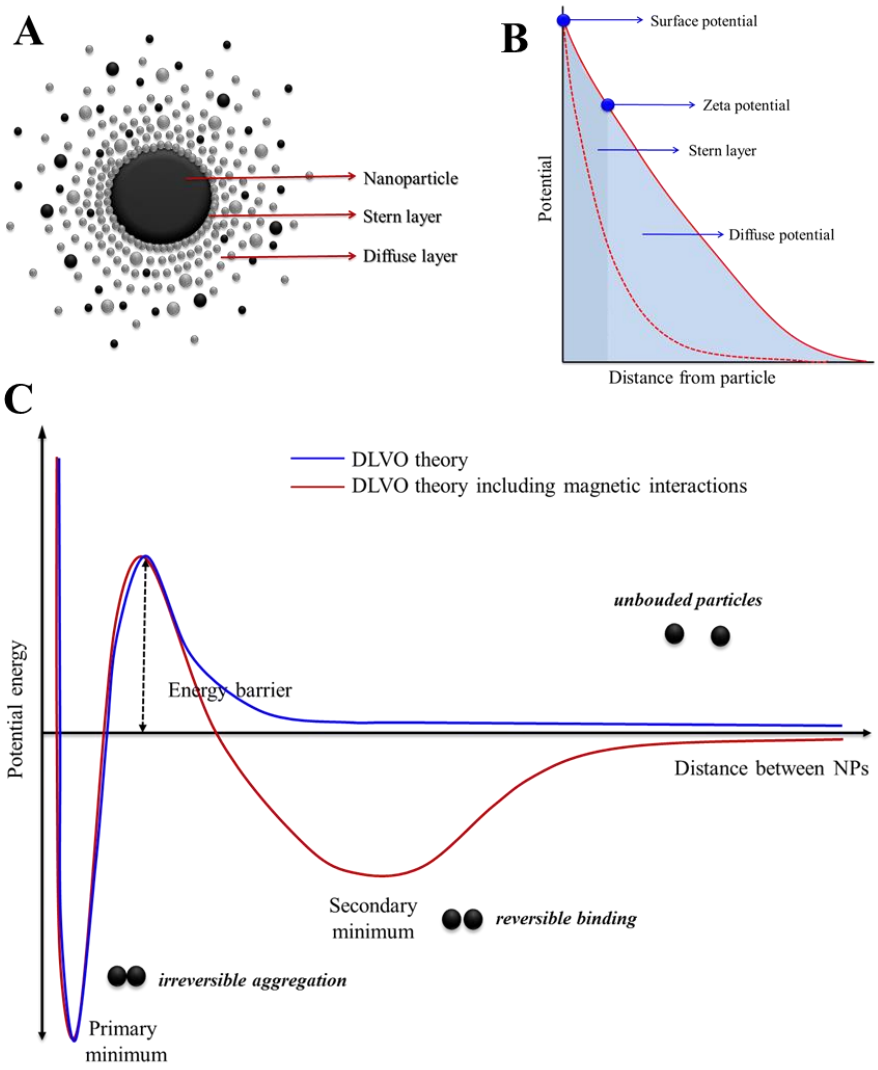

Figure 3.4. A) Schematic representation of the double layer of a nanoparticle in aqueous medium; B) Relationship between zeta potential and surface potential; C) Schematic representation of the free energy profile interaction between two superparamagnetic particles in the presence and absence of a strong magnetic field according to a generalized theory including magnetic interactions. The particles are assumed to be stabilized electrostatically (adapted from [40-42]).

A good stabilization can be achieved by controlling the strength of one or both repulsive forces (electrostatic and steric repulsion). While steric repulsion is difficult to predict and quantify, since it depends on the coating, electrostatic forces can be followed through the knowledge of the zeta potential and the Debye-Huckel length (depend upon the ionic strength and pH of the solution) [37].

Stabilization means that the particles do not aggregate at a significant rate. The rate of aggregation is generally determined by the frequency of collisions and the probability of cohesion during collision. Taking these facts into account, the Derjaguin-Landau-Verwey-Overbeek (DLVO) theory explains the tendency of colloids to agglomerate or not. The DLVO theory suggests that the stability of a particle in aqueous medium is determined by the sum of van der Waals attractive and electrical double layer repulsive forces that exist between particles. By combining the van der Waals attraction curve with the electrostatic repulsion, the DLVO theory forms a net interaction energy curve. At each distance, the smaller value is subtracted from the larger to obtain the net energy. The net value is then plotted – above if repulsive and below if attractive – and a net magnetization curve is formed. The maximum repulsive energy is called the energy barrier (Figure 3.4 C) [37, 38, 41].

When dealing with superparamagnetic nanoparticles in aqueous medium, magnetic interaction must be added. Figure 3.4 C shows a typical shape of interaction energy between two electrostatically stabilized superparamagnetic NPs in a magnetic field. When the NPs are very close from each other, there is a primary minimum due to the van der Waals attractive forces. The energy barrier created by electrostatic repulsion prevents the particles from achieving this minimum (electrostatic stabilization). A secondary minimum is present, which is responsible for the reversible aggregation of particles in the presence of the magnetic field. If the energy barrier is large enough, a NP captured in the second minimum will remain there, thus preventing irreversible aggregation. Once the magnetic field is removed, the second minimum disappears, and the particles captured in the second minimum redisperse again without adding energy to the system (e.g. sonication) [42].

Iron oxide NPs surface is covered by iron atoms that act as Lewis acids and coordinate with molecules that donate lone-pair electrons. When iron oxide NPs are placed in aqueous medium, water dissociates and the iron oxide surface gets hydroxyl functionalized. These hydroxyl groups are amphoteric and therefore may react with either acids or bases. The surface of the iron oxide NPs may be positive or negative, depending upon the pH of the solution. The isoelectric point for magnetite is around pH 6.8. Around this point of zero charge (PZC) the surface charge density is too small and the particles are no longer stable in water and flocculate. Accordingly, to obtain stable iron oxide nanoparticles it is necessary to play on both electrostatic and steric stabilization [37, 39].

Surfactants and polymers can form a single or double layer around magnetic NPs by either chemical anchoring or physical adsorption. This coating creates repulsive (mainly as steric repulsion)

forces to balance the magnetic and the van der Waals attractive forces. As a consequence, the NPs are stabilized in suspension by steric repulsion [43].

The purpose of coating iron oxide NPs is not only to stabilize the NPs, but also to provide chemical handles for the conjugation of drug molecules, targeting ligands, and reporter moieties. Furthermore, polymer coating have been engineered to enhance iron oxide NPs pharmacokinetics, endosomal release, and tailored drug loading and release behaviors [43].

3.1.4.1. Coating with inorganic materials

Iron oxide nanoparticles can be coated with silica [44-48], gold [49-52] or gadolinium (III) [37, 53].

Inert silica coating on the surface of magnetite NPs prevents their aggregation in liquid, improves their chemical stability, and provides better protection against toxicity. Silica coating stabilizes magnetite NPs through shielding the magnetic dipole interaction with the silica shell [13, 54]. Coating of magnetite NPs is difficult since its amorphous structure prohibits silica from forming a homogenous layer on the surface of magnetite NPs. The result is the formation of silica spherical particles upon the iron oxide surface with size comparable to the iron oxide NP [10]. Additionally, silica NPs are negatively charged leading to an enhancement of the Coulomb repulsion of magnetic NPs [37]. Moreover, the internal porosity of silica can be used to host a specific drug, avoiding unwanted adsorption of larger molecules [13]. One of the great advantages of using silica as a coating for iron oxide NPs is the presence of surface silanol groups that can easily react with various coupling agents to covalently attach specific ligands to these magnetic NPs [37]. Furthermore, silica and other microporous inorganic materials are heat resistant, with high surface areas and good mechanical strength [13].

Gold as a coating for magnetic NPs has the advantages of having low chemical reactivity and unique ability to form self-assembled monolayers (SAMs) on their surface using alkanethiols. Nevertheless, the chemical inertness of gold may difficult the formation of gold shells over NPs with an adequate thickness to prevent aggregation [2, 16].

The incorporation of gadolinium in magnetic NPs can help surpass the hurdle for molecular imaging with paramagnetic NPs. The problem relays on the sparseness of the molecular epitope on targeted cell surfaces (e.g. nanomolar concentration) concerning the modest signal intensity from conventional paramagnetic agents, which may result in insufficient contrast-to-noise ratio. Paramagnetic particles carrying high payloads of gadolinium enables to quantify molecular epitopes present in picomolar concentration in single cells with routines magnetic resonance imaging [16].

3.1.4.2. Coating with monomeric materials

As above stated, iron oxide surface act as a Lewis acid therefore coordinates with molecules that donate lone-pair electrons. For that reason, functional groups such as carboxylates, phosphates, and sulfates can easily bind to the surface of iron oxide NPs. This stabilization can be tailored for dispersibility into oil/hydrocarbon carrier fluids or aqueous medium.

Carboxylates such as citric acid stabilizes iron oxide NPs in aqueous dispersions. This molecule coordinates one or two of its carboxylate functionalities, depending upon the steric necessity and the curvature of the surface. This way, at least one carboxylic acid group is exposed to the solvent. This functional group is responsible for making the surface negatively charged and hydrophilic [37]. Long chain surfactants such as oleic acid are composed of a long hydrocarbon chain with a carboxylic acid at the end. These molecules are usually suitable for stabilization in oil medium (hexadecane) [16]. However, above a certain concentration oleic acid is suitable for stabilization in aqueous medium [55-57].

Phosphates [58] such as alkanesulphonic and alkanephosphoric acid are suitable to obtain thermodynamically stable dispersions of iron oxide NPs, maybe due to a quasi-bilayer structure formed by the ligands [37].

Liposomes [59] are phospholipid bilayer membrane vesicles that can range from 100 nm to 5 μm in size. These structures are very used to delivery of small molecules, proteins and peptides, DNA and MRI contrast agents (e.g. iron oxide NPs). The great advantage of using these structures is that the *in vivo* behavior has been well established with processes such as PEGylation, resulting in long circulation times. Furthermore, these structures have the ability to encapsulate a large number of magnetic NPs cores and deliver them together to a target site [2].

3.1.4.3. Coating with polymeric materials

Coating with polymeric materials provides a steric barrier to prevent NP agglomeration and avoid opsonization. Furthermore, polymeric coatings provide a means to tailor the surface properties of magnetic NPs such as surface charge and chemical functionality. The nature of the chemical structure of the polymer, the length or molecular weight and the conformation of the polymer, the type of anchoring, and the degree of particle surface coverage are critical factors that may affect the performance of the magnetic NP [2].

Natural polymers which include carbohydrates and proteins have the inherent advantage of being biocompatibility [10]. Dextran is a neutral polysaccharide composed exclusively of α-D-glucopyranosyl units with varying degrees of chain length and branching [60]. Dextran chains have a

favorable size enabling optimum polar interactions (mainly chelation and hydrogen bounding) with iron oxide surfaces. Although hydrogen bonds are relatively weak, the total bonding energy of hydrogen bonds over the length of a polysaccharide molecule can be very high because of the large number of hydroxyl groups per molecule [37, 61]. Alginate is another natural polymer also classified as an electrolytic polysaccharide. This polymer has many carboxylic groups. It is a non-immunogenic and biocompatible polymer. Moreover, it is able to dissolve and degrade under physiological conditions [9]. Chitosan is an alkaline, non-toxic, hydrophilic, biocompatible, and biodegradable natural polymer [37]. The presence of reactive groups of –OH and $–NH_2$ allows the formation of hydrogen bounds with substrates by inter- or intramolecular hydrogen bounding [9]. This particular natural polymer will be further analyzed in Chapter 4.

Besides natural polymers, synthetic polymers can also be used as coating for iron oxide NPs. One of the most studied is polyethylene glycol (PEG) [62, 63], which is hydrophilic, water soluble, and biocompatible polymer. The presence of PEG into the surface of iron oxide NPs increase their biocompatibility and blood circulating times, and minimizes or eliminates protein adsorption onto the particle surface, thus evading the reticuloendothelial system (RES) [37, 61]. Poly (ethylene oxide) (PEO) is also widely used as a surface coating of iron oxide NPs due to its biocompatibility and non-biodegradability [61]. Polyvinyl alcohol (PVA) is a hydrophilic and biocompatible polymer that prevents coagulation, originating monodisperse particles. 61].

Only a few polymers were described in this section. However, there is an enormous list of polymers used as coating for magnetic nanoparticles. Some of them were reviewed in references [9], [37] and [64].

3.1.5. Pharmacokinetics, biodistribution and clearance

Typically, once the iron oxide NPs are administrated within the body, they are internalized by cells via endocytosis where, clustered in lysosomes, the NPs are degraded into iron ions by an array of hydrolyzing enzymes at low pH according to endogenous iron metabolism pathways. A critical factor for their success is increasing the magnetic NPs blood circulating times thus evading RES. RES is the primary physiological mechanism responsible for NPs clearance from circulation, being determinant for plasma lifetime. During RES clearance the circulating opsonin proteins adsorb to NPs surface, are recognized, and removed from the bloodstream by circulating macrophages [2, 65].

NPs physical characteristics (hydrodynamic size, surface charge, morphology, surface chemistry) determine their biodistribution in the body. Large NPs (> 200 nm) are usually retained in the

spleen via mechanical filtration followed by phagocytosis, while small NPs (< 10 nm) are rapidly removed through extravasation and renal clearance. Therefore, particles within a range diameter of 10–100 nm are optimal for intravenous administration [2, 7]. Related to surface charge, positively charged polymers and particles tend to stick to cells nonspecifically, decreasing their blood half-life. On the other hand, negatively charged particles tend to increase liver uptake. Consequently, neutral particles are optimal for extended blood circulating times [2].

3.1.5.1. Passive targeting

Passive targeting is a non-specific accumulation that occurs mainly through the enhanced permeability and retention (EPR) effect. This effect is based on the mechanism that damaged tissues (tumor, inflammation, infection) possess "leaky" vasculature, allowing macromolecules and NPs to extravasate and accumulate in these tissues. For this non-specific accumulation to occur particles must have a diameter within the range of 10 to 500 nm [2].

Passive targeting can be useful to deliver contrast agents and drug carriers to organs related to RES by the uptake of magnetic NPs by phagocytic cells (bone marrow progenitors, blood monocytes, and tissue macrophages) [2].

3.1.5.2. Active targeting

Active targeting is achieved through targeting molecules with high affinity toward unique molecular signatures found on tumor cells. The receptor-ligand or antigen-antibody interactions provide effective strategy to improve the residence time in tumoral tissues [2].

The targeting molecules may be proteins, peptides, aptamers, and small molecules. The specific binding of these molecules can facilitate internalization of the NPs by receptor mediated endocytosis [2]. However, active targeting often requires a costly synthetic production and/or complicated chemistries for their attachments to the NPs [65].

Monoclonal antibodies (mAbs) are high affinity molecules that were the first targeting agents to exploit molecular recognition to deliver magnetic NPs. The disadvantage of using these molecules is their large size and inherent immunogenicity that can cause conjugated NPs to diffuse poorly through biological barriers [2].

3.1.5.3. Active targeting with applied magnetic fields

The active targeting with applied magnetic fields, or magnetic targeting, can be very useful to deliver magnetic NPs to a specific site. The gradient (∇B) produced by an externally applied magnetic field (B) to a tumor region exerts attractive forces on magnetic NPs delivered via the circulation, according to Equation 3.5:

$$F_{mNP} = (\nabla B^2)\frac{\chi V_c}{2\mu_0} \qquad \text{Equation 3.5}$$

Where χ is the magnetic susceptibility of the magnetic core, V_c is the volume of the magnetic core, and μ_0 is the magnetic permeability of free space. According to the above equation, magnetic NPs are retained when the magnetic force is sufficient to overcome hydrodynamic drag forces exerted on the particles by blood flow. Optimal magnetic NPs for magnetic targeting must have a large core (> 100 nm in diameter) and be superparamagnetic. Nevertheless, for larger cores the magnetic forces are greater but the clearance is faster, limiting the availability for interaction with the applied field [65].

3.1.5.4. Biodistribution

An optimal biodistribution is crucial for the success of targeting and for the determination of the off-target toxicity. The majority of the administrated NPs often distribute in tissues of the RES, mostly in liver and spleen [7, 65].

After intravenous administration of magnetic NPs, the NPs enter the bloodstream and opsonization activates RES. Consequently, mononuclear phagocytes (monocytes) clear the NPs to the liver, sleep and bone marrow. The NPs retained in the liver are uptaken by Kupffer macrophage cells located in sinusoids. Some of the NPs present in the lysosomal vesicles of the Kupffer cells may incorporate bile and be removed by feces. Smaller particles are filtered in the kidneys and incorporated into urine. Finally, if NPs are biodegradable, the decomposition products can be taken by any cell by means of pinocytosis [13, 65].

Local subcutaneous injection of small particles allows them to infiltrate into the interstitial spaces and be gradually absorbed by the lymphatic capillary system. Lymphatic targeting may be useful for lymphatic tumors. However, the used particles must be small (below 60 nm). In addition this process can be limited by intra tumoral pressure caused by the fast proliferation in solid tumors [13].

Oral administration for delivery in the gastrointestinal tract has the drawbacks of particles (mainly organic ones) being degraded in gastrointestinal acid, have low absorption, being eliminated by the first-pass metabolism by the liver, and a significant initial increase in drug concentration [13].

3.1.6. Toxicity

Uncoated iron oxide NPs have shown some toxic effects, while coated iron oxide NPs have been found to be relatively nontoxic. Poly(ethylene glycol) (PEG)-coated NPs have shown biocompatibility since exposed cells remained more than 99% viable relative to control at an upper concentration of 1 $mg.ml^{-1}$ [63]. On the other hand, bare iron oxide NPs induced 25%–50% loss in fibroblast viability at 250 $\mu g.ml^{-1}$. In a more extensive study, the same group [16] found that iron oxide NPs toxicity is dose dependent. Iron oxide NPs caused a 20% reduction in cell viability at the lowest concentration tested (0.05 $mg.ml^{-1}$). Further reductions were seen at higher concentrations, with the highest concentration tested (2.0 $mg.ml^{-1}$), resulting in about 60% loss of cell viability.

The increase of body contact with magnetic NPs arouses serious concerns about their pharmacokinetics, metabolism, and toxicity. The major contributions of magnetic iron oxide NPs are usually the generation of reactive oxygen species (ROS) via Fenton reaction [66]:

$$H_2O_2 + Fe^{2+} \rightarrow Fe^{3+} + HO^- + HO^* \qquad \text{Equation 3.6}$$

This reaction is the most prevalent source of ROS in biological systems [7]. The high chemical reactivity of NPs may produce oxidative stress via four primary sources: 1) generation of ROS from the NPs surface; 2) leaching of the NPs, causing the generation of ROS; 3) altering organelle functions (mitochondrial or other); 4) induction of cell signaling [67]. Although some authors consider that uncoated iron oxide NPs are biocompatible *in vitro*, there are several studies reporting *in vitro* cytotoxicity of iron oxide NPs with and without coating [68-71].

The *in vivo* toxicity assessment of magnetic iron oxide NPs is difficult due to the complexity of the biological systems. Nevertheless, iron oxide NPs are considered biocompatible *in vivo* because iron is a natural component of the human body. Nevertheless, high concentrations of Fe (above 60 mg per kg) may lead to severe side effects. Contrast agents (for example, Endorem™) are used in a concentration of 1 mg of Fe per kg [72] and *in vivo* toxicity studies show no long-term implications when administrated at clinically relevant concentrations via relevant routes. For

example, although iron oxide NPs deposits were detected in the prostates of prostate cancer patients after one year of magnetic hyperthermia therapy in phase I clinical trials, there were no evidences of toxic effects due to this accumulation [73].

3.2. Materials and methods

All the chemical reagents used in this research work were of analytical grade and used without further purification.

3.2.1. Iron oxide nanoparticles synthesis

3.2.1.1. Chemical precipitation

Iron oxide nanoparticles were synthesized by chemical co-precipitation using an adapted method of Gnanaprakash and coworkers [18]. Ferrous and ferric chlorides (*Sigma-Aldrich*) were dissolved in deionized water to achieve a concentration of 1 M. An appropriate amount of the above-mentioned solutions was mixed in order to obtain a molar ratio of 1:2 (Fe^{2+}:Fe^{3+}) and diluted to 100 ml of deionized water with deaeration of O_2 with bubbling N_2. Further, 10 ml of NH_4OH 25% (*Panreac*) was rapidly added under vigorous stirring and kept for a fixed period of time (5, 10 or 30 min). Deionized water was added to stop the reaction, the precipitate was left to settle, and the top water layer was discarded. The magnetic NPs were washed three times with deionized water, and pH of the final suspension was adjusted to 7 with diluted HCl. A part of the suspension was freeze-dried (Vaco 2, Zirbus) in order to obtain dry nanoparticles for further characterization. These samples without further modification will be designated as "**Pristine Fe_3O_4 NPs**" from now on.

3.2.1.2. Stabilization of pristine Fe_3O_4 NPs

Pristine Fe_3O_4 NPs obtained from chemical precipitation technique form instable colloidal suspensions in water. Due to the positive charge, the NPs tend to aggregate and sediment when in an aqueous suspension. This is a crucial issue for biomedical application. One of the most effective way to stabilize these NPs is by using surfactants (surface active agents) that neutralize the superficial charge of the NPs and promote their stabilization in an aqueous medium [74]. In this work three stabilizing agents were studied: tri-sodium citrate (TC), oleic acid (OA) and triton X-100 (TX).

Tri-sodium citrate (Figure 3.5) is a carboxylate such as citric acid used in the synthesis of silver, gold and alumina nanoparticles due to its high solubility in several solvents and because it has a high degree of stabilization of the nanoparticles. Its chemical structure has three negative charged groups which facilitate the attachment to negative nanoparticles such as Fe_3O_4, enhancing the particles dispersion and stabilization in suspensions.

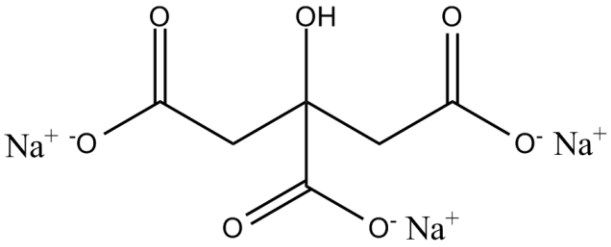

Figure 3.5. Chemical structure of tri-sodium citrate.

The chemical structure of oleic acid (Figure 3.6) makes it a very good surfactant for magnetite nanoparticles since the oleic acid chain possesses a terminal carboxylic acid with negative charge that has high affinity to magnetite nanoparticles surface due to their positive charge [56]. This compound is a monounsaturated fatty acid that can be found naturally in many plant or animal products.

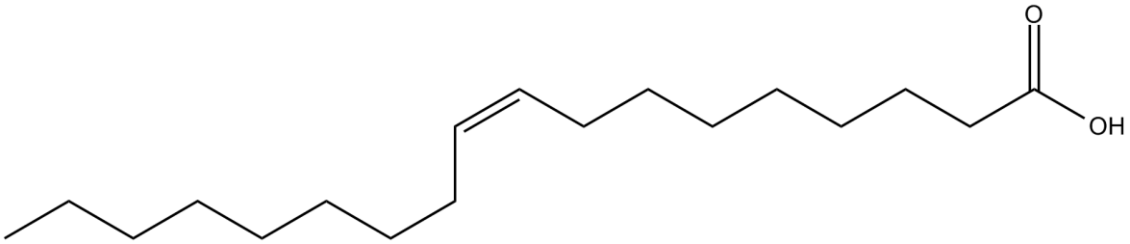

Figure 3.6. Chemical structure of oleic acid.

Triton X-100 (Figure 3.7) is a non-ionic surfactant from the class of the alkyl phenyl polyethoxylate (PEO) surfactants, composed of a PEO hydrophilic chain and a hydrophobic aromatic group. It is compatible with other surfactants non-ionic, anionic and cationic. This surfactant is utilized in the production of detergents, emulsifiers, wetting agents, solubilizers and dispersants [75].

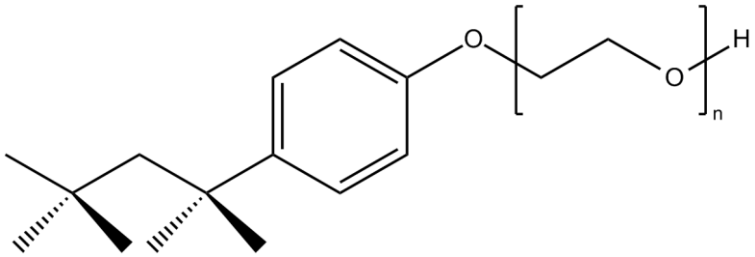

Figure 3.7. Chemical structure of triton X-100.

For the stabilization of the iron oxide nanoparticles, an appropriate amount of tri-sodium citrate, oleic acid or triton X-100 was added to a known volume of the magnetite suspension. The mixture was allowed to react for 1 h under stirring. Finally, the samples were sonicated for 5 min. These different surfactants were used in the iron colloidal solutions with the concentrations indicated in Table 3.1.

Table 3.1. Tested concentrations of the three stabilizing agents used (tri-sodium citrate, oleic acid and triton X-100).

	Tri-sodium citrate	**Oleic Acid**	**Triton X-100**
Concentration (mM)	1.25	8	17
	2.5	16	26
	5	32	34
	10	64	43
	20	96	52
	30	128	61
		192	

3.2.1.3. Thermal decomposition

Iron oxide nanoparticles synthesis using thermal decomposition (TD) technique was based on the work of Maity and his coworkers [28, 76]. This technique is based on the thermal decomposition of an iron precursor, $Fe(acac)_3$ in tri-ethylene glycol (TREG) at high temperature without the use of further stabilizers. Typically, 2 mmol of $Fe(acac)_3$ (*Sigma Aldrich*) are dissolved in 20 ml of TREG (*Alfa aesar*) and magnetically stirred under a flow of nitrogen. There are two heating stages in this synthesis method: the first stage is related to the dehydration of the solution; the second

stage is the one that leads to the decomposition of the iron source at the solvent boiling temperature. Therefore, the first stage of temperature was fixed at 120 ºC for either 30 or 60 minutes. The second stage (around 280 ºC, i.e. TREG boiling temperature) was kept for 30 min, 1 h, or 2 h. A condenser was used to prevent the high-boiling temperature solvent from evaporation. The resultant black solution was cooled to room temperature overnight by removing the heat source. The obtained nanoparticles were precipitated by addition of 20 ml of ethyl acetate (*Sigma Aldrich*), and then isolated by centrifugation (Heraeus Multifuge X1R Centrifuge) for 20 minutes at 10000 rpm. The washing process was repeated three times and finally the obtained nanoparticles were dispersed in ultrapure water. A part of the suspension was freeze-dried (VaCo 2, *Zirbus*) in order to obtain dry nanoparticles for further characterization. These samples will be designated as "**Fe_3O_4 TD**".

3.2.2. Iron content determination

The iron content of the samples was determined using the 1,10-phenantroline colorimetric method [77]. Briefly, 40 µl of diluted sample was placed into an Eppendorf, followed by the addition of 20 µl of hydrochloric acid 37% (v/v) (*Panreac*). The mixture was incubated for 1 h at room temperature to dissolve all the iron oxide NPs and obtain ferrous and ferric chloride. Next, to reduce Fe (III) to Fe (II), 100 µl of hydroxylamine hydrochloride (*Alfa aesar*) solution 100 $mg.ml^{-1}$ was added to the mixture, followed by 500 µl of phenanthroline (*Applichem*) 3 $mg.ml^{-1}$ to form the orange-red complex of tris(1,10-phenantroline) iron (II). Lastly, the samples were diluted to 1800 µl by adding ammonium acetate (*Sigma Aldrich*) 500 mM pH 4 buffer. The absorbance of the samples was measured at 510 nm using a UV-VIS spectrophotometer (T90+ UV/VIS Spectrometer PG Instruments Ltd). The concentration of iron (II) was calculated by a calibration curve obtained using Mohr's salt solution in HCl 0.01 N in a concentration range of 10 to 1000 $\mu g.ml^{-1}$.

To obtain the nanoparticles concentration the formula [Fe] = 0.7 x [NPs] was used. The ratio was obtained from control experiments.

3.2.3. Characterization

3.2.3.1. X-ray diffraction (XRD)

The crystalline phases of the samples were verified using powder X-ray diffraction. X'Pert PRO PANAlytical X-ray diffractometer was used to obtain X-ray diffraction patterns of the iron oxide

nanoparticles previously freeze-dried. The 2θ values were taken from 15º to 80º using a Cu-Kα radiation (k = 1.54060 Å) with a step size of 0.033. The Scherrer`s equation was used to measure the average crystallite size.

3.2.3.2. Fourier Transform Infrared (FTIR) spectrometry

FTIR spectra of the samples were obtained using a Nicolet 6700 – Thermo Electron Corporation Attenuated Total Reflectance-Fourier Transform Infrared spectrometer (ATR-FTIR). The spectra were acquired with a 45° incident angle in the range of 4000 – 480 cm^{-1} and with a 2 cm^{-1} resolution.

3.2.3.3. Scanning electron microscopy (SEM)

Morphology and size of the NPs was obtained using a scanning electron microscope of high resolution, Zeiss DSM-962. A drop of the diluted sample was placed into the sample holder using a carbon tape. The solvent was left to evaporate overnight.

3.2.3.4. UV-VIS spectrophotometry

UV–VIS spectrophotometer (PG Instruments model T90+) was used to perform the absorbance spectra of colloidal solutions containing iron oxide nanoparticles coated with different surfactants: oleic acid, tri-sodium citrate, and triton X-100. The measurements were acquired using a quartz cuvette with high purity water. The colloidal solutions were prepared in a dilution of 1:100 with respected to the initial concentration, where the concentration of surfactant was changed keeping the dilution constant to ensure that the absorbance spectra do not saturate. Measurements were performed at different times after sonication of the samples, using a single cuvette for each sample. Spectra were acquired using the same concentration of the surfactant used in the samples in the reference cuvette.

3.2.3.5. Transmission electron microscopy (TEM)

Transmission electron microscopy images were obtained using a Hitachi H-8100 II with thermoionic emission LaB6. TEM analysis was performed in a little quantity of nanoparticles suspended in pure water that were placed in a Kevlar 25 mesh grid.

3.2.3.6. Thermogravimetric analysis (TGA)

Thermogravimetric analysis and differential thermal analysis (DTA) studies were carried out using a Thermal Analyzer NETZSCH STA 449 F3 Jupiter® at a rate of 10 ºC.min^{-1} in a N_2 atmosphere.

3.2.3.7. Superconducting quantum Interference device (SQUID)

The DC magnetic properties were performed using a 7T SQUID magnetometer (S700X; Cryogenic Ltd.). The zero-field cooled (ZFC) and field-cooled (FC) measurements were performed by cooling the sample to 5 K at zero field or in the presence of an external field of 100 Oe, respectively. All the magnetic measurements were carried out in increasing temperature range 5–320 K. Isothermal magnetization curves were obtained for fields up to 5 T for temperatures of 10 and 320 K.

3.2.3.8. Dynamic light scattering (DLS)

Hydrodynamic diameter (D_H) of the nanoparticles was measured by means of dynamic light scattering equipment (Avid Nano) using the blade cell at 20 ºC.

Dynamic light scattering and zeta potential measurements were performed using a SZ-100 nanopartica series (Horiba, Lda) with a laser of 532 nm and controlling temperature with a Peltier system (25 ºC). DLS measurements were carried out for diluted NPs suspensions in triplicates using a disposable cell with a scattering angle equal to 90º. Data analysis was performed using cumulative statistics to measure hydrodynamic size and polydispersity unless stated otherwise. Zeta potential measurements were performed with a scattering angle equal to 173º, in a graphite electrode cell.

3.3. Results and discussion

The results section of this chapter is divided into three sub-sections: the first one shows the characterization and optimization of iron oxide nanoparticles obtained from chemical precipitation technique. The second one refers to the influence of surfactants; and the third section is related to the characterization of iron oxide nanoparticles obtained from thermal decomposition technique.

3.3.1. NPs obtained from chemical precipitation

The structure of the samples was analyzed by XRD spectra while their morphology was observed through TEM images. These characterizations were performed before and after functionalization with the stabilizers.

3.3.1.1. Structural and physical characterization

Figure 3.8 shows the XRD patterns obtained for pristine iron oxide NPs. The six characteristic 2θ peaks occurred at 30.1, 35.5, 43.2, 53.5, 57.0 and 62.8, which correspond to the diffraction planes (220), (311), (400), (422), (511) and (440), respectively. Compared to standard XRD patterns for magnetite and maghemite powders (JCPDS 00-019-0629 for magnetite and JCPDS 00-039-1346 for maghemite) the synthesized NPs have a crystalline cubic magnetite structure. The average crystallite size is around 9.75 nm, calculated from Scherrer's equation:

$$\tau = \frac{K\lambda}{\beta cos\theta} \qquad \text{Equation 3.7}$$

Where τ is equivalent of particles average core diameter; K is the grain shape factor (K = 0.94); λ is the incident X-ray wavelength; β denotes the full width at half-maximum (in radians) of the highest intensity, and θ is the corresponding diffraction angle (2θ = 35.6141).

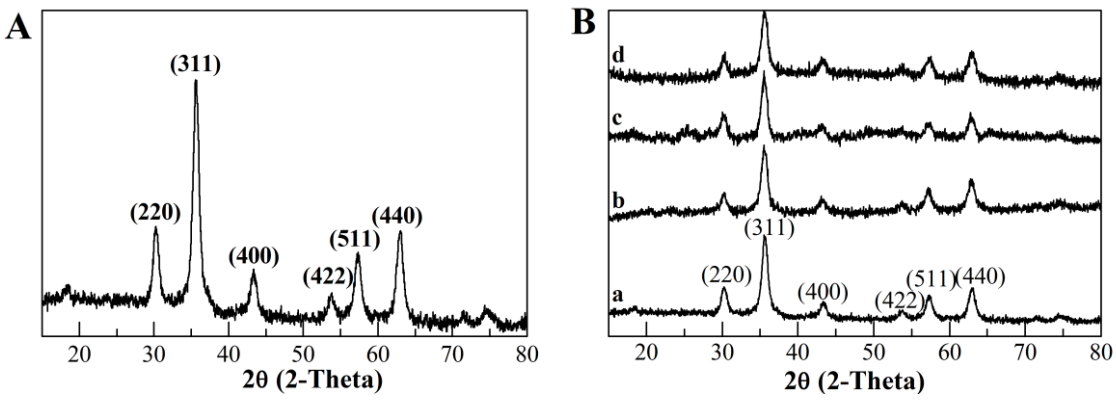

Figure 3.8. X-ray patterns of (a) pristine iron oxide nanoparticles produced by chemical precipitation technique (b) Tri-sodium citrate 5 mM coated Fe_3O_4 nanoparticles; (c) Oleic acid 64 mM coated Fe_3O_4 nanoparticles; (d) Triton X-100 17 mM coated Fe_3O_4 nanoparticles.

The iron oxide NPs stabilized with surfactants retained the crystal structure of pristine Fe_3O_4, as can be seen in Figure 3.8 (B) where pristine and coated nanoparticles XRD patterns are similar, denoting that the surfactant does not change the Fe_3O_4 nanoparticles crystalline structure.

The obtained FTIR spectrum for pristine Fe_3O_4 NPs is shown in Figure 3.9 (A). The strong absorbance band at 560 cm^{-1} is attributed to the Fe-O stretching vibration mode while the band at 1630 cm^{-1} is related to the O-H stretching vibration modes, and the broad band between 3000 cm^{-1} and 3500 cm^{-1} is related to the O-H stretching vibration mode due to water vapor [18].

The influence of surfactants in FTIR spectra is shown in Figure 3.9 (B), (C) and (D) for tri-sodium citrate, oleic acid, and triton X-100 coated Fe_3O_4 NPs, respectively. It is possible to observe the presence of the above-referred bands of Fe_3O_4 in all the spectra. By increasing the surfactants concentration, the appearance of other bands characteristic of the corresponding surfactants are also seen.

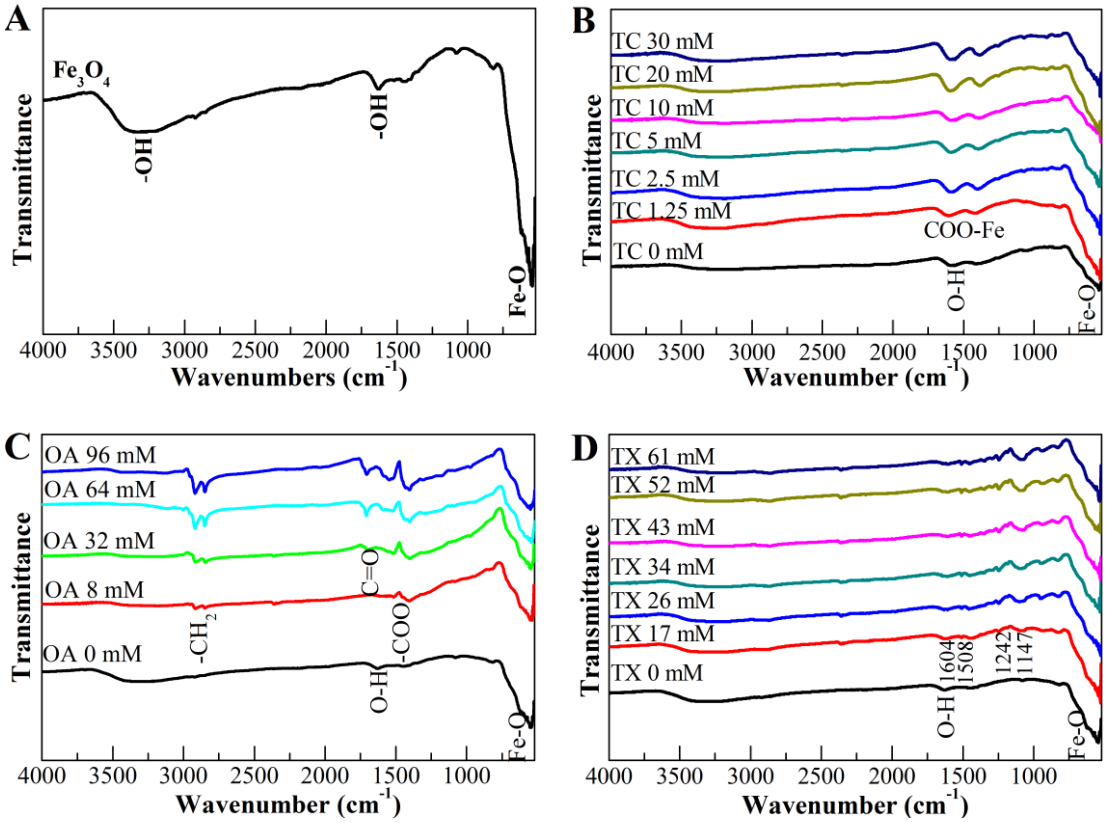

Figure 3.9. FTIR spectra of (A) pristine Fe_3O_4 nanoparticles, (B) tri-sodium citrate coated Fe_3O_4 NPs, (C), oleic acid coated Fe_3O_4 NPs (D) triton X-100 coated Fe_3O_4 NPs.

In oleic acid coated nanoparticles (Figure 3.9 (C)), the difference between the minimum and maximum concentration used is much evident. In the sample with 8 mM of oleic acid, it is possible to identify the following bands: bands at 2910 and 2840 cm^{-1} are attributed to the symmetric and asymmetric CH_2 stretch in the oleic acid molecule, respectively. The bands at 1506 and 1415 cm^{-1} are respectively due to the symmetric and asymmetric $–COO^-$ stretching vibration modes; the

band at 1398 cm^{-1} corresponding to the CH_3 umbrella mode of oleic acid. For a concentration above 32 mM of oleic acid, a sharp band at 1704 cm^{-1} appears, which corresponds to the stretching vibration of C=O in oleic acid, while the bands between 1550 and 1450 cm^{-1} tend to disappear. The differences between oleic acid samples are due to the formation of a bilayer above a concentration of 32 mM. Considering that the oleic acid molecule links to the Fe_3O_4 nanoparticle surface through the carboxylic group, when oleic acid forms a monolayer, only the COO^- group appears on FTIR spectra, since none of the COOH groups are present. However, with the addition of more oleic acid, the COOH group starts to become visible in the FTIR spectra, thus justifying the formation of the bilayer. This bilayer formed by the oleic acid molecules turns the magnetite nanoparticles hydrophilic making them more stable in aqueous solutions [56].

In the tri-sodium citrate Fe_3O_4 NPs (Figure 3.9 (B)) the absorptions bands at 1369 and 1568 cm^{-1} are characteristic of the COO-Fe bond that may be due to the reaction of hydroxide radical groups on the surface of Fe_3O_4 with carboxylate anion of tri-sodium citrate [78]. These characteristic bands prove that the tri-sodium citrate molecule is linked to the nanoparticle surface, thus providing stability in aqueous solutions.

In the FTIR spectrum of triton X-100 Fe_3O_4 NPs (Figure 3.9 (D)) the broad absorption band at 3320 cm^{-1} corresponding to the stretching vibration of hydroxyl groups (O-H). The sharp bands at 2933 and 2852 cm^{-1} are owed to the asymmetric and symmetric CH_2 stretch, respectively. The bands at 1604 and 1508 cm^{-1} are due to the stretching vibration of the benzenoid group while the peaks at 1242 and 1147 cm^{-1} are associated with the asymmetric stretch of the aromatic ether [79]. Comparing to the characteristic bands of triton X-100 [80], a shift of the characteristic bands to a lower frequency region can be observed. These could indicate that triton X-100 molecules are attached to the Fe_3O_4 NPs surface.

3.3.1.2. Morphological characterization

Chemical precipitation technique is a very versatile way to synthetize iron oxide nanoparticles since it allows controlling the properties of the obtained nanoparticles by changing the synthesis parameters. In this work, the time of reaction was evaluated to access if the size of the nanoparticles changed. To determine the appropriate time of reaction, SEM images were taken in samples with 5, 10 and 30 minutes of reaction. Figure 3.10 show the differences obtained for tri-sodium citrate and oleic acid Fe_3O_4 nanoparticles.

The obtained images do not allow to clearly identifying differences between samples. The size distribution graphs show mean diameters around 30-40 nm, with a high standard deviation. The obtained data may reflect that the time of reaction does not promote differences between samples.

Based on an exhaustive study published by Gnanaprakash [18], further on all samples produced by chemical precipitation had a reaction time of 5 minutes.

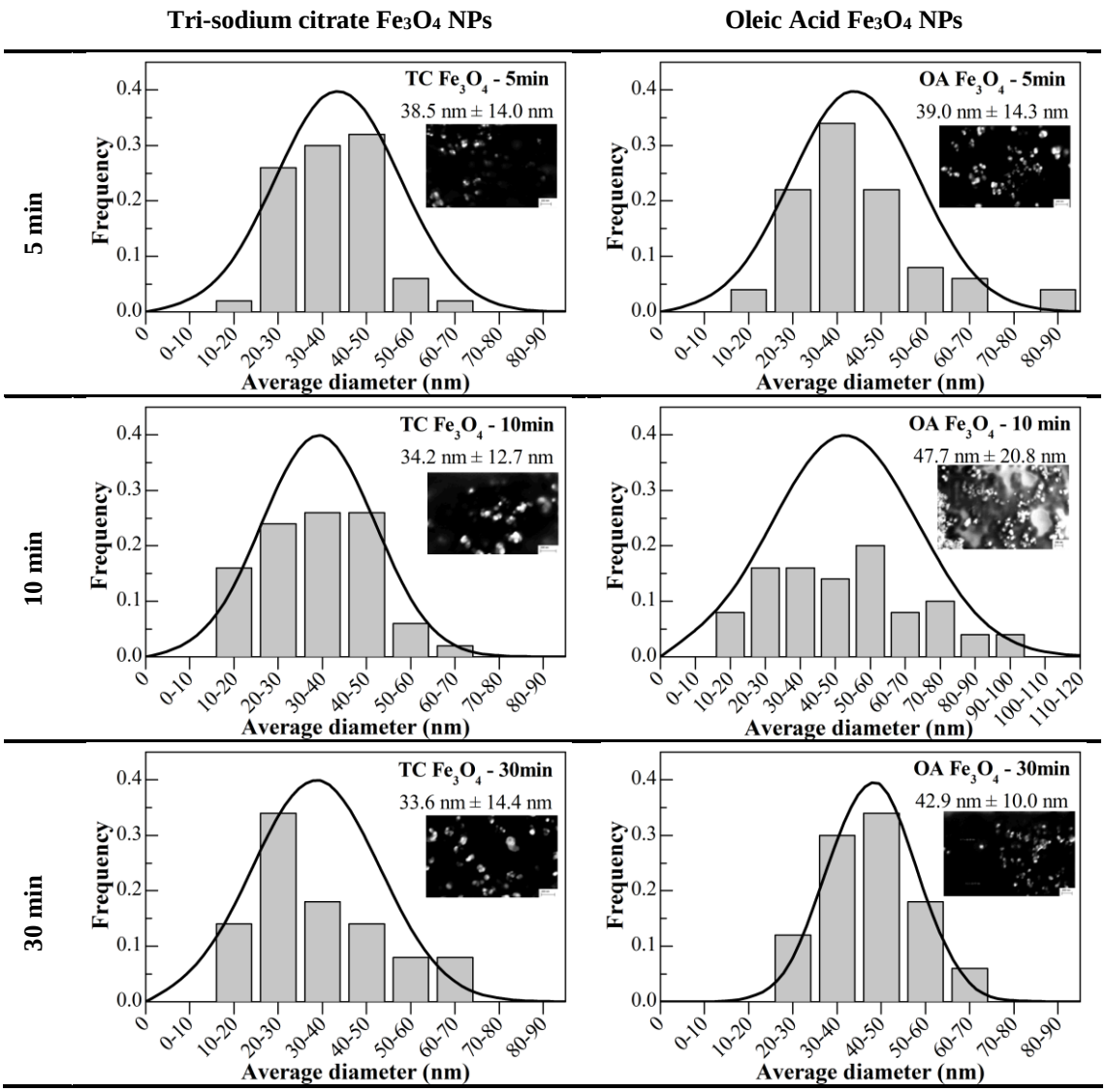

Figure 3.10. Size distribution graphs with SEM images insets of Fe_3O_4 stabilized with either tri-sodium citrate (TC) or oleic acid (OA) with 5, 10 and 30 minutes of reaction time.

Keeping the reaction time constant, a new set of samples was produced to investigate the influence of the surfactants in the nanoparticles size by TEM. Figure 3.11 (A) shows TEM image of pristine Fe_3O_4 NPs with an average diameter of 8.5 nm and a narrow size distribution. This is very interesting considering that for biomedical applications the nanoparticles must have a size below 100 nm and a narrow size distribution. In addition, for these nanoparticles to be superparamagnetic their size cannot exceed a few tens of nanometers [37]. However, the NPs show a high

aggregation state, due to the absence of stabilizers. The remaining TEM images and size distributions are relative to Fe_3O_4 NPs stabilized with the chosen molecules. In all cases, there is a common conclusion: the used stabilizers in the tested concentrations do not change the Fe_3O_4 core size, as can be seen by the average diameter of each case.

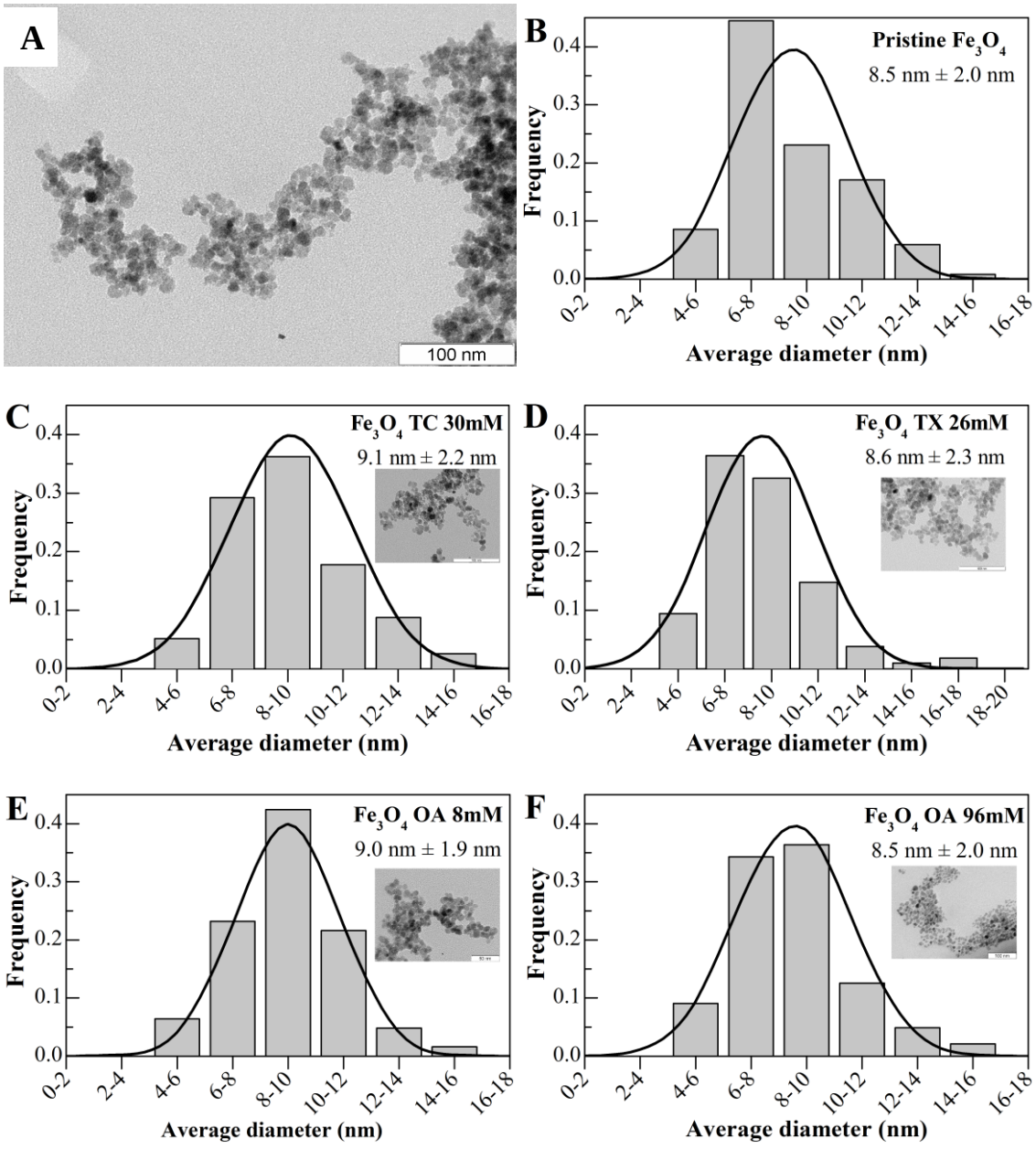

Figure 3.11. TEM image of pristine Fe_3O_4 NPs (A) and their respective size distribution graph. Size distribution graphs with TEM image inset of Fe_3O_4 NPs obtained from chemical precipitation technique and further stabilized with TC 30 mM (C), TX 26 mM (D), OA 8 mM (E) and OA 96 mM (F).

Figure 3.11 (C) and (D) are relative to Fe_3O_4 NPs stabilized with tri-sodium citrate and triton X-100, respectively. The aggregation state of the NPs seems to decrease for tri-sodium citrate, i.e., the samples seem to have fewer aggregates. The same is not observed for triton X-100. Regarding oleic acid, when a low concentration is used (8mM, Figure 3.11 E) aggregation of the NPs is observed. However, if this concentration is increased to 96 mM (Figure 3.11 F), oleic acid is the most effective stabilizer, since isolated nanoparticles are visible as well as the absence of aggregates.

3.3.1.3. Colloidal stability

The colloidal stability of Fe_3O_4 NPs with surfactants was performed using two techniques: evaluation of the UV/VIS absorbance along the time after sonication of the samples to a maximum of 24h; and evaluation of the sedimentation rate of the samples over a period of 8 weeks. Both studies were performed for concentrations that do not saturate the values of absorption. All the samples were diluted in a factor of 1:100 for pristine, TC and OA Fe_3O_4 NPs and 1:200 for TX Fe_3O_4 NPs. The hydrodynamic diameter was measured through dynamic light scattering at 0 h and 24 h after sonication.

To perform the absorbance test, the colloidal solutions with different concentrations of surfactant were placed on a quartz cuvette and the absorbance spectra was acquired immediately after the suspension preparation (t = 0 h) and after a period (t = x), keeping the suspension unruffled.

Figure 3.12 shows the obtained UV-VIS spectra for pristine Fe_3O_4 NPs in ultrapure water. The absorbance spectra of as-prepared colloids do not present a specific peak of absorbance in the UV–VIS wavelength range. However, as time passes the absorbance of the samples decreases because of the sedimentation of NPs, leading to a more transparent suspension.

The UV–VIS spectrum of pristine Fe_3O_4 nanoparticles (Figure 3.12) demonstrates that the sedimentation occurs faster within the first hours after sonication. This effect was expected due to the absence of a stabilizer in the suspension. Thus, the NPs tend to agglomerate and consequently their size increases leading to fast sedimentation. The use of a stabilizer not only avoids the nucleation of the iron oxide NPs but also prevents its growth and agglomeration.

The Fe_3O_4 nanoparticles coated with surfactants show a specific absorbance peak that follows the observed peak of surfactant.

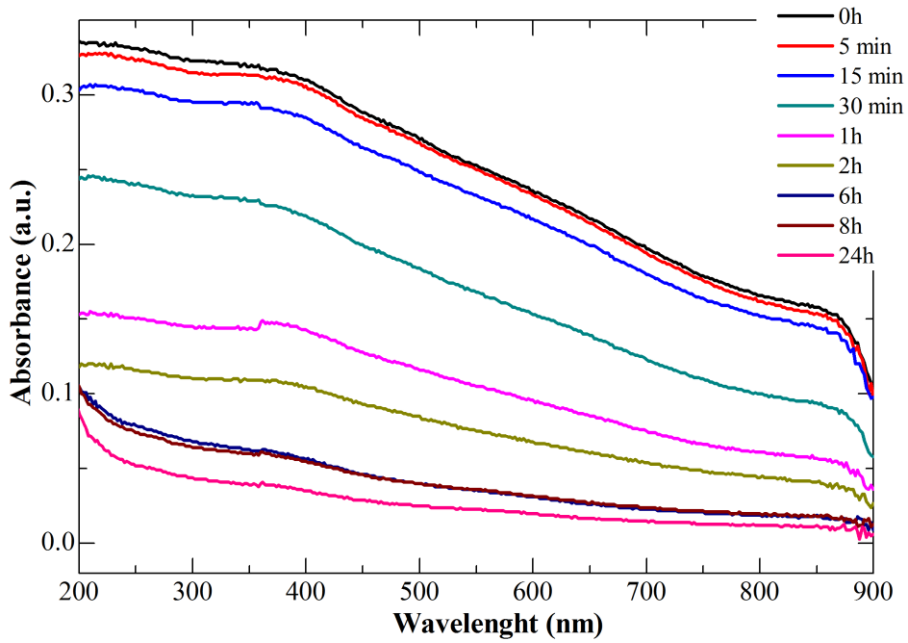

Figure 3.12. UV-VIS spectra of pristine Fe_3O_4 NPs immediately after sonication and after different periods up to 24 h.

3.3.1.3.1.Tri-sodium citrate

Figure 3.13 shows the UV-VIS spectra of tri-sodium citrate Fe_3O_4 NPs in the range of tested concentrations of tri-sodium citrate, immediately and 24 h after sonication. In each case, the absorbance of a tri-sodium citrate solution with the same concentration was also measured. The maximum absorbance is observed in the wavelength from 200 to 300 nm, and from 300 to 400 nm a hump is observed, which may be attributed to NPs with bigger size. Considering the stabilizer concentration, for tri-sodium citrate with concentrations below 5 mM, the nanoparticles are not well stabilized and a remarkable decrease in the intensity of the hump occurs after 24 h, probably due to the amount of surfactant that is insufficient to prevent agglomeration of the nanoparticles in suspension. Moreover, above a concentration of 5 mM no significant differences can be found.

To better identify the differences between samples with different stabilizer concentration, the maximum absorbance at 300 nm was taken at 0 h and 24 h after sonication. Figure 3.14 shows the obtained values. It is clear that for lower tri-sodium citrate concentrations, the NPs settle and the absorbance drastically decreases. However, for concentrations above 5 mM, no significant difference exists between the absorbance at 0 h and 24 h after sonication. Taking into account the data in Figure 3.14 it seems that the best concentration to stabilize the Fe_3O_4 NPs is between 5 and 10 mM of tri-sodium citrate.

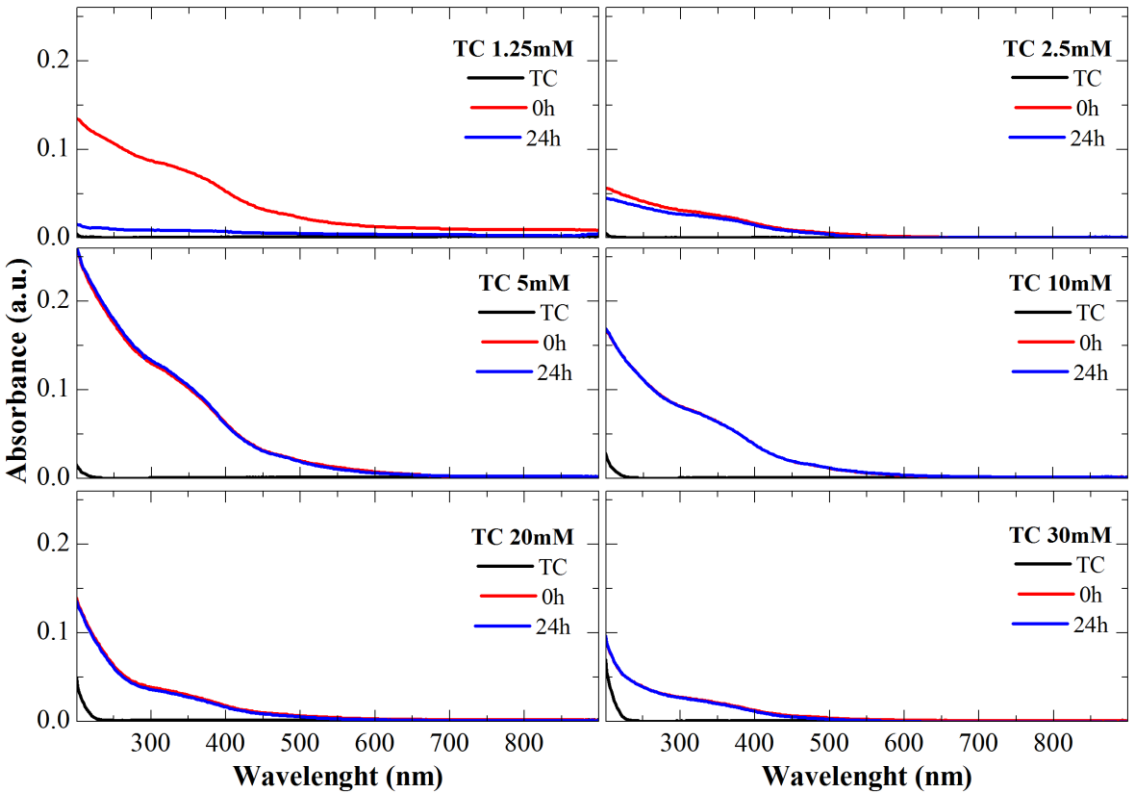

Figure 3.13. UV-VIS spectra of tri-sodium citrate Fe_3O_4 NPs immediately and after 24 h of sonication, at different tri-sodium citrate concentrations.

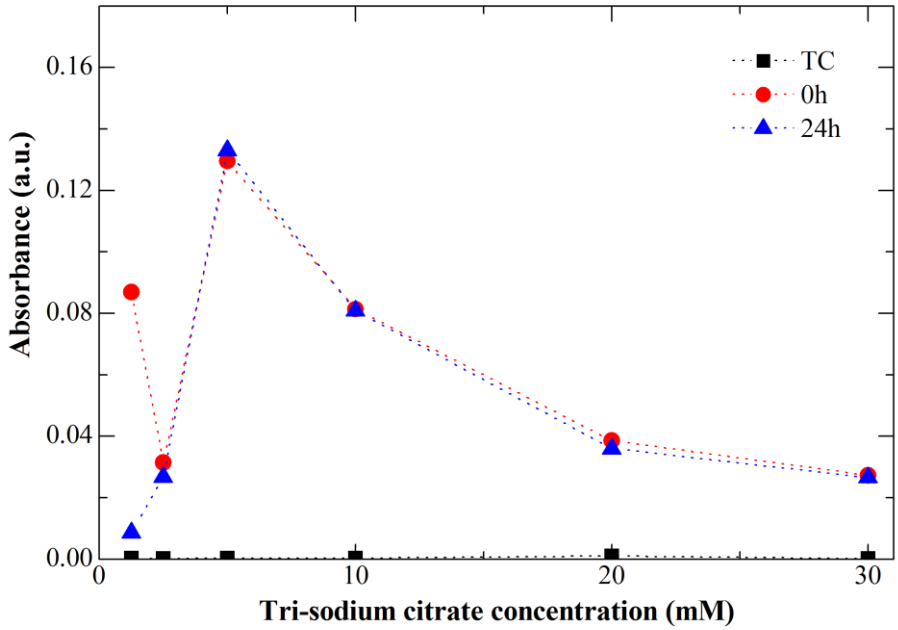

Figure 3.14. UV-Vis absorbance at 300 nm of tri-sodium citrate and Fe_3O_4 TC immediately and 24 h after sonication for different concentrations of tri-sodium citrate.

Figure 3.15 represents the sedimentation test performed for tri-sodium citrate Fe_3O_4 NPs. This test was performed for 8 weeks by weighting the sediment obtained over time. The high standard deviation observed in the graph was caused by experimental errors (small sample size and lack of precision of the balance). In the obtained results, two groups of samples are seen: the first group containing the lower concentrations of tri-sodium citrate and the second group with the three higher concentrations of tri-sodium citrate.

In UV-VIS, absorbance test the tri-sodium citrate concentration that better stabilizes Fe_3O_4 NPs in an aqueous suspension was between 5 and 10 mM. In the sedimentation test, the tri-sodium citrate concentrations that achieve a higher mass of nanoparticles in suspension along 8 weeks are above 10 mM. Therefore, the better concentration of tri-sodium citrate to stabilize iron oxide nanoparticles in an aqueous suspension is 10 mM, within the tested conditions.

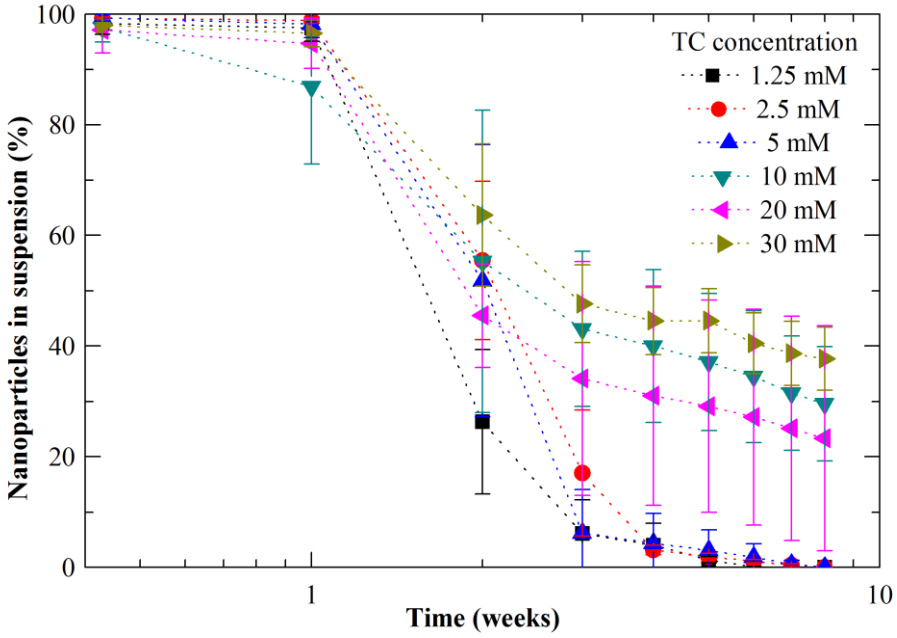

Figure 3.15. Mass of Fe_3O_4 TC NPs in suspension (%) along time for the tested tri-sodium citrate concentrations.

3.3.1.3.2.Oleic Acid

Figure 3.16 shows the UV-VIS spectra of oleic acid Fe_3O_4 NPs within the tested range of concentrations, immediately and 24 h after sonication. Similarly, to tri-sodium citrate, each graph has the equivalent oleic acid concentration absorbance spectrum without Fe_3O_4 NPs. For oleic acid Fe_3O_4 NPs spectra, a maximum absorbance peak is at 224 nm. Considering oleic acid concentration it is visible that below an oleic acid concentration of 32 mM the absorbance is very low,

leading to the conclusion that almost none of the NPs are in suspension. However, above the same concentration, oleic acid maximum absorbance peak is clearer and has a higher value, which may be associated to a higher mass of NPs in suspension. Moreover, in the OA 64 mM sample a hump is visible at 280 nm, which similarly to tri-sodium citrate case may be attributed to the presence of larges particles, possibly agglomerates of NPs. However, this hump decreases after 24 h of sonication, which reveal that the NPs agglomerates fall down, being in suspension only the small ones.

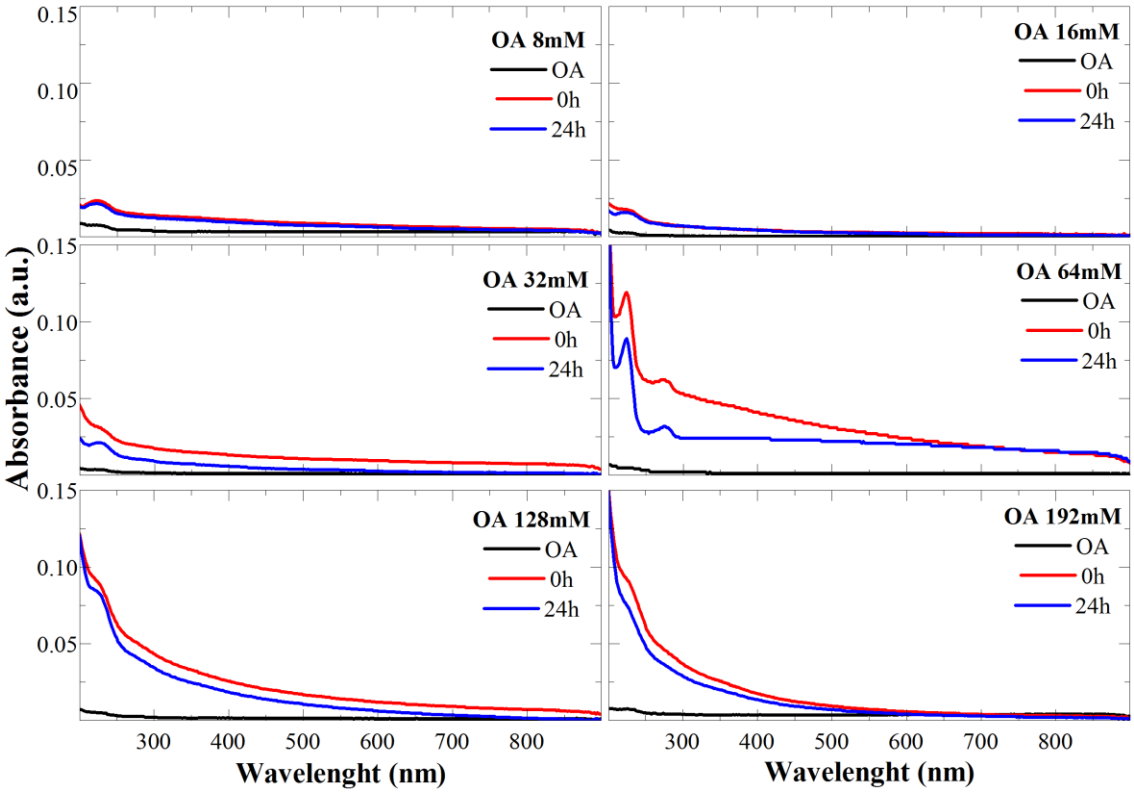

Figure 3.16. UV-VIS spectra of oleic acid Fe_3O_4 NPs immediately and after 24 h of sonication, at different oleic acid concentrations.

Figure 3.17 shows the absorbance at 224 nm taken 0 h and 24 h after sonication, for each concentration of oleic acid. Except for the lowest concentration, the tested concentrations show differences in the absorption values between 0 h and 24 h after sonication, which is attributed to the NPs settling due to agglomeration. However, the trend with the concentration is similar for both, and OA of 64 mM and above lead to the most stable suspensions.

Figure 3.18 represents the sedimentation test performed for oleic acid Fe_3O_4 NPs. Comparing to tri-sodium citrate, oleic acid is not so effective stabilizer of Fe_3O_4 NPs, leading to a complete sedimentation after four weeks, in all the tested surfactant concentrations.

Thus, the results show that any concentration above 64 mM (including) is appropriate to stabilize the Fe_3O_4 NPs in an aqueous suspension. However, this stabilization is only effective for short periods.

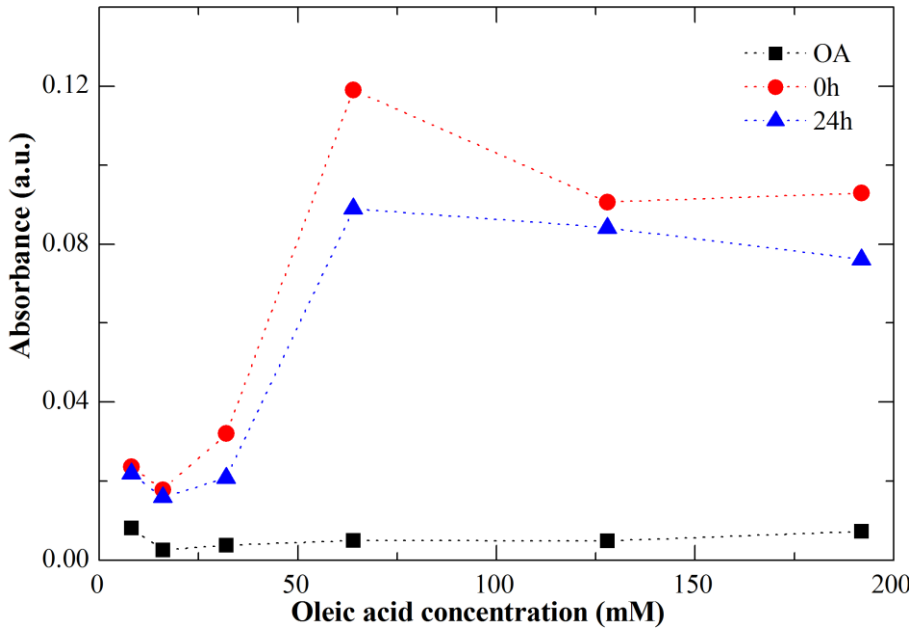

Figure 3.17. UV-VIS absorbance at 224 nm of oleic acid and Fe_3O_4 OA immediately and 24 h after sonication for different concentrations of oleic acid.

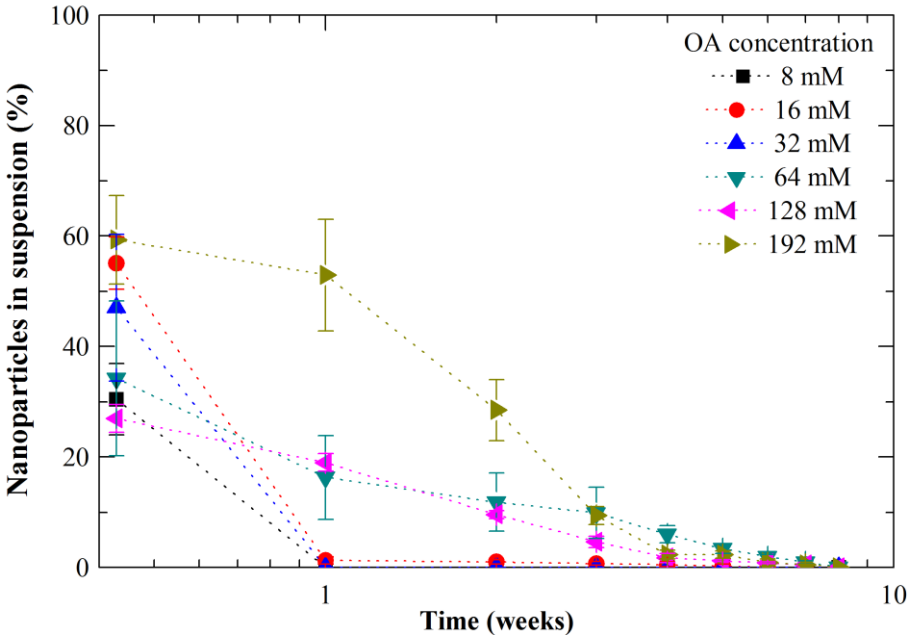

Figure 3.18. Mass of Fe_3O_4 OA NPs in suspension (%) along time for the tested oleic acid concentrations.

3.3.1.3.3.Triton X-100

The UV-VIS spectrum of triton X-100 Fe_3O_4 NPs within the tested range of concentrations, immediately and 24 h after sonication is depicted in Figure 3.19. Similarly, to tri-sodium citrate, each graph has the equivalent triton X-100 concentration absorbance spectrum without Fe_3O_4 NPs. When triton X-100 is added to the NPs, the maximum absorbance peak is at 222 nm. In this case, as the surfactant concentration increases, the absorbance at 222 nm also increases (Figure 3.20), without further changes in the curves, similarly to oleic acid case. As such, the most probable explanation is that the tested range of concentration was small and the ideal concentration was not found.

Figure 3.21 shows the UV-VIS spectra for suspensions of Fe_3O_4 NPs with different concentrations of triton X-100 along the time. Comparing to tri-sodium citrate and oleic acid samples, in triton X-100 only after 6 weeks is verified a complete sedimentation of the NPs. However, for this study the range of concentrations used for triton X-100 was not enough to found an ideal concentration. Further increase in concentration is needed.

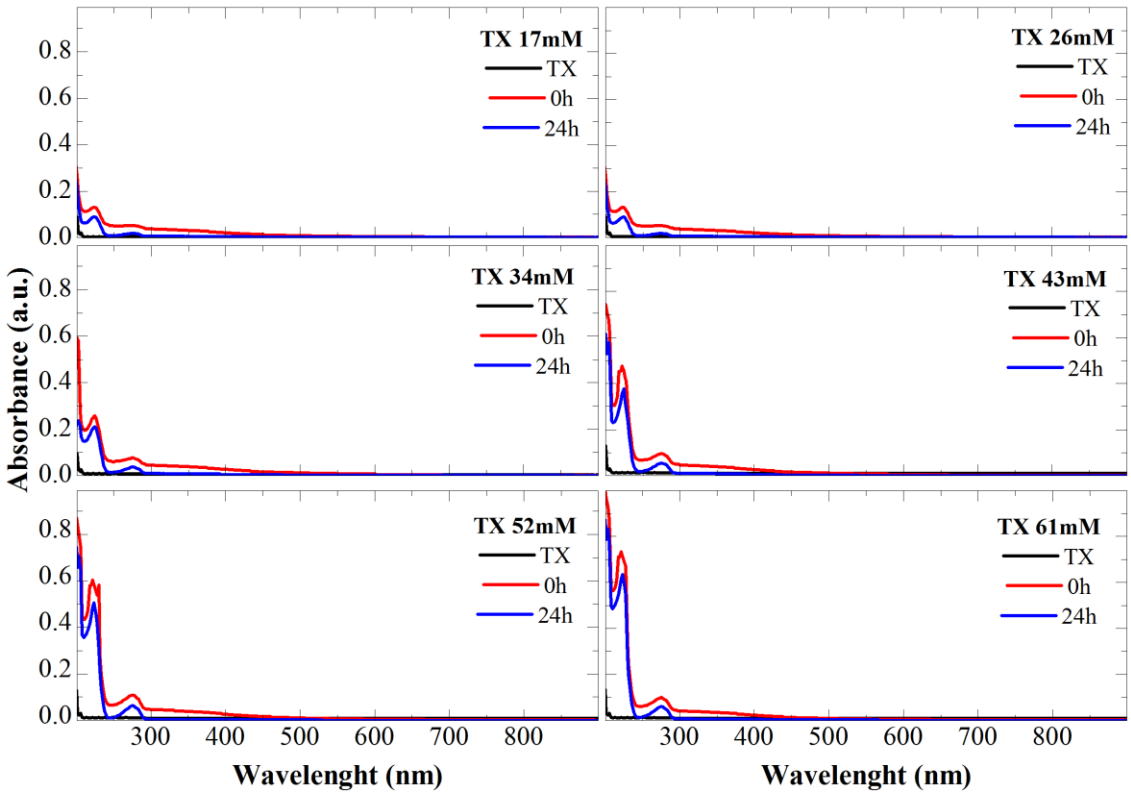

Figure 3.19. UV-VIS spectra of triton X-100 Fe_3O_4 NPs immediately and after 24 h of sonication, at different triton X-100 concentrations.

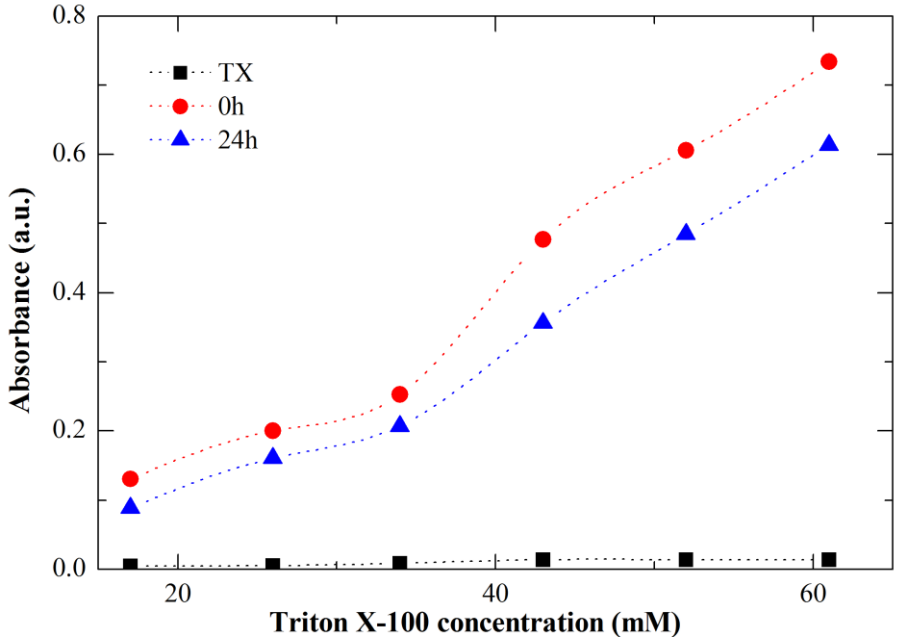

Figure 3.20. UV-VIS absorbance at 222 nm of triton X-100 and Fe_3O_4 TX, immediately and 24 h after sonication for different concentrations of triton X-100.

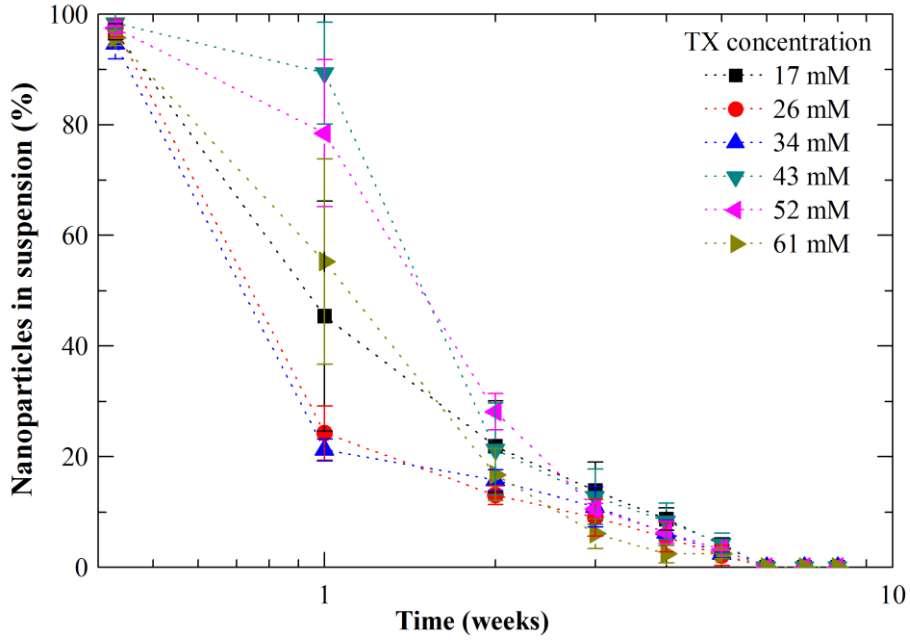

Figure 3.21. Mass of Fe_3O_4 TX NPs in suspension (%) along time for the tested triton X-100 concentrations.

In order to complement the previous study, the hydrodynamic diameter of NPs was measured at 0 h and 24 h after sonication, for all the tested concentrations of the three surfactants (Figure 3.22). Hydrodynamic measurements are important to optimize suspensions and extrapolate the biodistribution of the NPs in the body. It allows the prediction of the nanoparticles behavior in

the blood vessel, the mechanism of clearance, and the permeability of the nanoparticles out of the vasculature [81].

The average hydrodynamic diameter increases after 24 h of sonication for suspensions with tri-sodium citrate. Since tri-sodium citrate is a salt, it reduces the surface energy and dipolar attraction. As such, there is some aggregation after 24 h but the hydrodynamic diameter of the nanoparticles is not greatly increased, allowing the nanoparticles to remain in suspension.

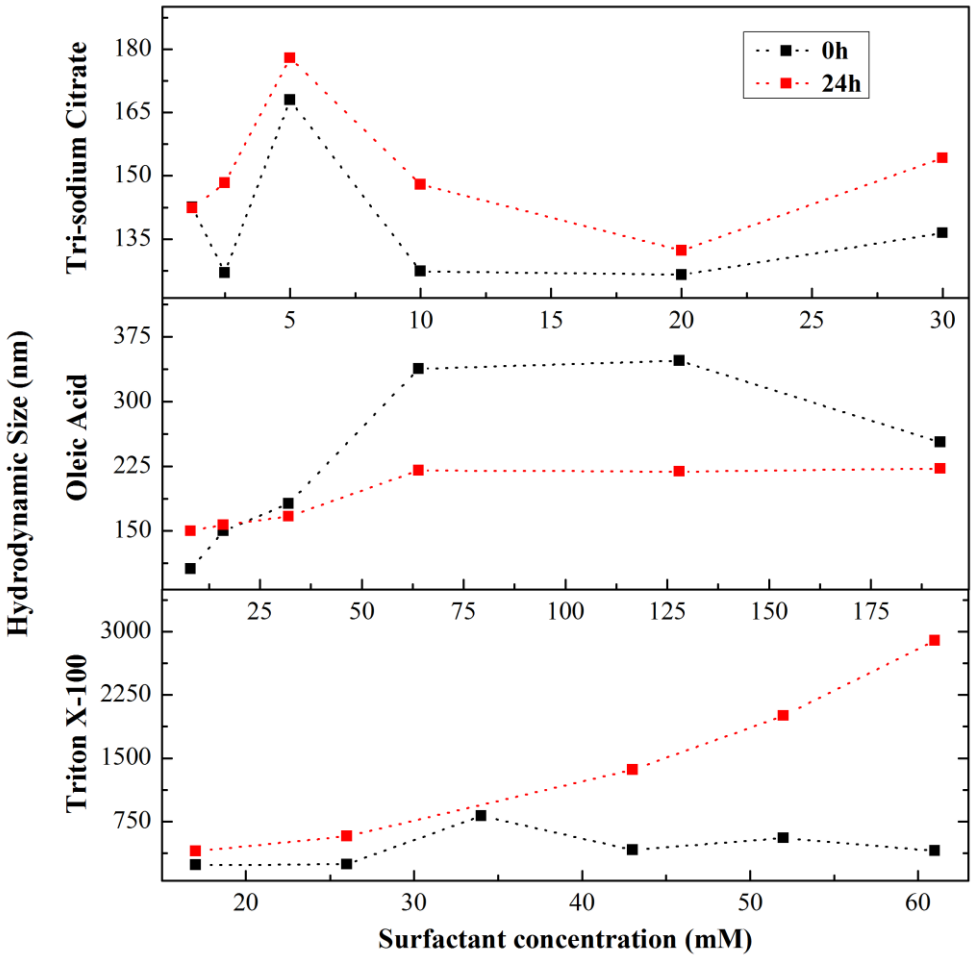

Figure 3.22. Hydrodynamic diameter of coated magnetic nanoparticles with six concentrations of each tested surfactant, 0 h and 24 h after sonication.

The average hydrodynamic diameter of the nanoparticles decreases after 24 h of sonication for concentrations of oleic acid above 16 mM. This is in agreement with the absorbance results shown previously and can be correlated with the sedimentation of the bigger agglomerates of NPs, leaving in suspension only the smaller particles. Indeed the figure shows that immediately after sonication the hydrodynamic diameter almost duplicates in OA concentrations above 64 mM. On the

other hand, for those concentrations the nanoparticles colloids are stable as the hydrodynamic diameter is constant. This behavior may be correlated with the formation of the oleic acid double layer.

The hydrodynamic diameter after 24 h sonication is much higher in suspensions made with triton X-100. Therefore, within the tested conditions, it is the surfactant with the lowest performance.

3.3.1.4. Magnetic characterization

The influence of surfactants in the magnetic properties of Fe_3O_4 NPs was evaluated by magnetometry, using a superconducting quantum interference device. The magnetization, represented as emu per gram of the whole particle (including magnetic and non-magnetic material), was evaluated in samples with and without surfactants.

Figure 3.23 (A) shows the temperature dependence of the zero-field cooled and field cooled magnetization curves of pristine Fe_3O_4 NPs measured by SQUID under an applied filed of 100 Oe. The blocking temperature (T_B) was determined as the maximum value of ZFC curve. The hysteresis loops measured at temperatures 10 and 320 K for the pristine Fe_3O_4 nanoparticles are shown in Figure 3.23 (B).

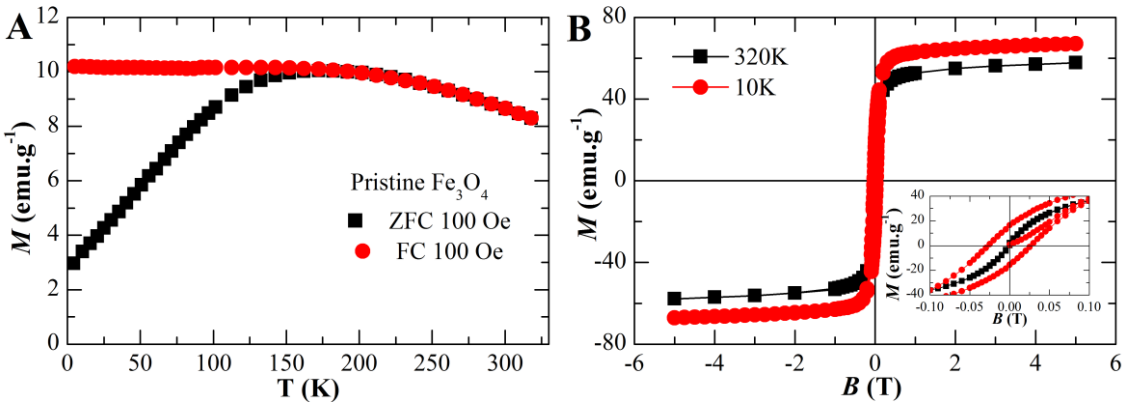

Figure 3.23. Magnetic characterization of pristine Fe_3O_4 nanoparticles: (A) Zero-field cooled and field cooled results; (B) Magnetization vs. applied magnetic field at 320 and 10 K.

The temperature dependence of magnetization of pristine Fe_3O_4 NPs exhibits a T_B around 172 K, which indicates that at room temperature the produced NPs have a superparamagnetic behavior, confirmed by the absence of coercivity and remanence at 320 K. For pristine NPs at 10 K, the saturation magnetization reaches 67 emu.g^{-1} with a coercivity of 270 Oe.

For the tri-sodium citrate, Fe_3O_4 NPs magnetic characterization was performed for the lowest and higher concentrations used. Figure 3.24 shows (A) the ZFC-FC curves obtained under an applied

field of 100 Oe and (B) the hysteresis loops measured at 320 K for both concentrations. The obtained results show that a higher concentration of tri-sodium citrate has a higher influence in blocking temperature (152 K for TC 1.25 mM and 147 K for TC 30 mM). However, in both cases, the superparamagnetic behavior above T_B remains constant. Moreover a little influence of the surfactant is observed, resulting in saturation magnetization around 60 emu.g^{-1} for both concentrations tested.

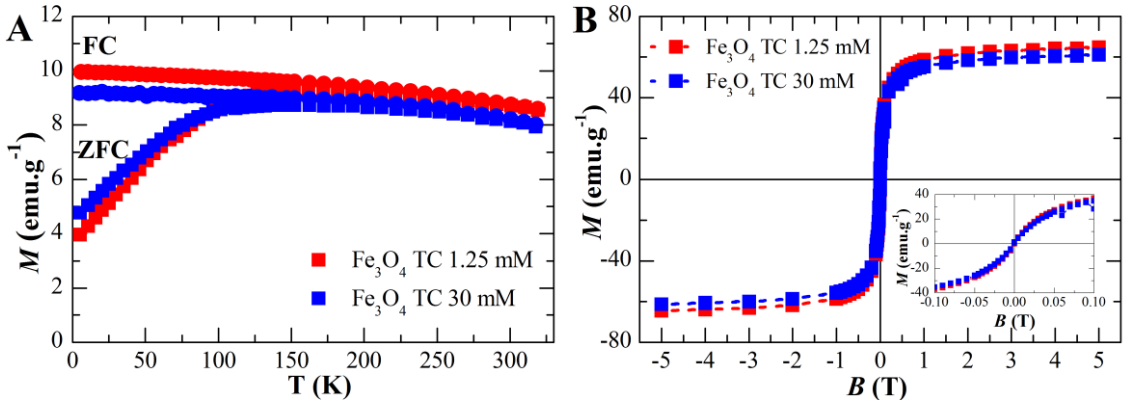

Figure 3.24. Magnetic characterization of tri-sodium citrate Fe_3O_4 nanoparticles: (A) Zero-field cooled and field cooled results for TC 1.25 mM and TC 30 mM; (B) Magnetization vs. applied magnetic field at 320 K for TC 1.25 mM and TC 30 mM.

Figure 3.25 shows the influence of oleic acid on the Fe_3O_4 NPs for concentrations of 8 and 64 mM. The influence in the T_B is small but the saturation magnetization decreases from 60 emu.g^{-1} (OA 8 mM) to 45 emu.g^{-1} (OA 64 mM). This suggests that a concentration of 8 mM of OA is so small that do not influence the magnetic properties of Fe_3O_4 NPs. When OA concentration increases the surfactant is reducing the magnetic moments at the surface of the nanoparticles probably due to the diamagnetic contribution of the surfactant volume [21]. In addition, the formation of the oleic acid bilayer must have a lower influence in the magnetic properties of the nanoparticles.

Fe_3O_4 NPs stabilized with triton X-100 (Figure 3.26) show a magnetic behavior quite similar to tri-sodium citrate, meaning that this surfactant has also very small influence over the Fe_3O_4 NPs magnetic properties.

Table 3.2 resumes the obtained data from magnetic characterization of pristine Fe_3O_4 NPs and Fe_3O_4 NP stabilized with tri-sodium citrate, oleic acid and triton X-100.

The results confirm that pristine Fe_3O_4 NPs have a superparamagnetic behavior above the blocking temperature, given by the absence of coercivity and remanence at 320 K. Moreover, for the

tested concentrations of the three surfactants, the superparamagnetic behavior is not affected, since at 320K the absence of coercivity and remanence remains. In all cases, the magnetic domains are not separate by domain walls (multi-domain state). Instead, each particle represents a single magnetic domain [82]. For magnetite the critical size is 30 nm at room temperature [83]. This observation confirms the superparamagnetic behavior of our samples. The loop areas for all samples are narrow, demonstrating very low heat generations due to hysteresis, which also correlates with the literature values [82, 84].

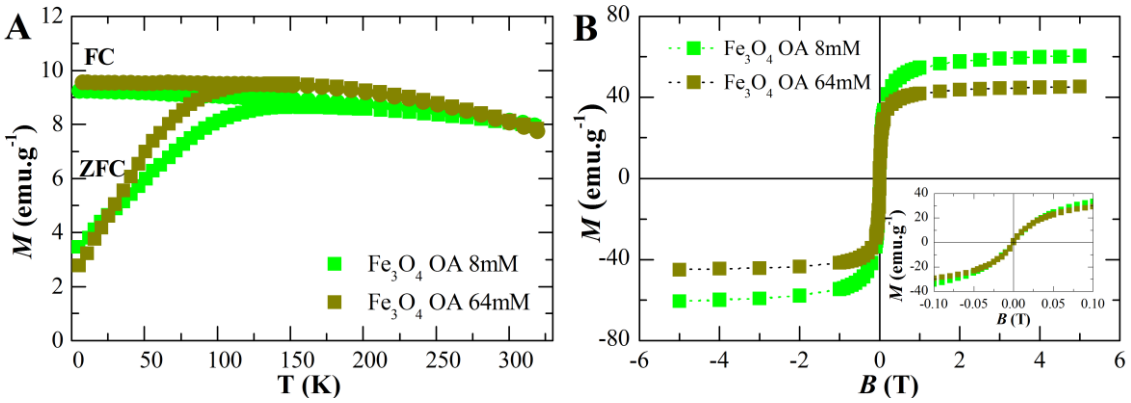

Figure 3.25. Magnetic characterization of oleic acid Fe_3O_4 nanoparticles: (A) Zero-field cooled and field cooled results for OA 8 mM and OA 64 mM; (B) Magnetization vs. applied magnetic field at 320 K for OA 8 mM and OA 64 mM.

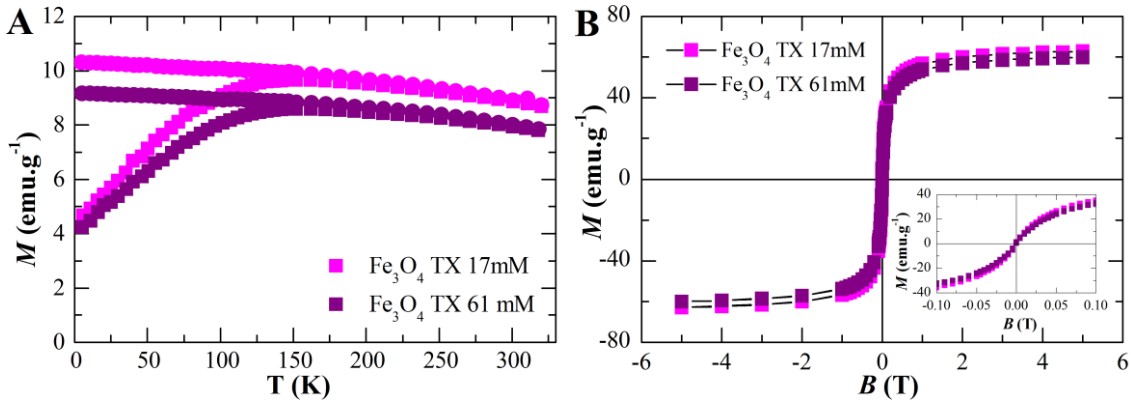

Figure 3.26. Magnetic characterization of triton X-100 Fe_3O_4 nanoparticles: (A) Zero-field cooled and field cooled results for TX 17 mM and TX 61 mM; (B) Magnetization vs. applied magnetic field at 320 K for TX 17 mM and TX 61 mM.

The characterizations performed confirm that triton X-100 has the worst performance as surfactant, both related to the aggregation and stability of the particles in suspension. Both tri-sodium citrate and oleic acid were very effective in stabilizing the iron oxide nanoparticles. Their negative

nature promotes the ideal environment for the stabilization of the iron oxide nanoparticles whose surface is usually positively charged [56, 85, 86]. Further, coating of NPs is possible with any of these surfactants since it allows obtaining a high number of small NPs stabilized in the suspensions. Furthermore, the tested surfactants do not significantly change the physicochemical and magnetic properties of the NPs except for higher concentration of oleic acid due to the formation of a bilayer.

Table 3.2. Magnetic properties of pristine Fe_3O_4 NPs and Fe_3O_4 NPs coated with a lower and higher concentration of the used stabilizers: tri-sodium citrate (TC), oleic acid (OA) and triton X-100 (TX). The magnetic properties shown are blocking temperature (T_B) obtained from the maximum value of the ZFC curve, saturation magnetization (M_S) at 10 K and 320 K, and coercivity (H_c) at 10 K (at 320 K there was an absence of coercivity for all tested samples).

Sample		T_B **(K)**	M_S **10 K (emu.g^{-1})**	H_c **(10 K) (Oe)**	M_S **(320 K) (emu.g^{-1})**
Pristine Fe_3O_4		172	67	270	58
Fe_3O_4 TC	**1.25 mM**	152	76	180	64
	30 mM	147	71	145	61
Fe_3O_4 OA	**8 mM**	152	71	188	60
	64 mM	147	52	157	45
Fe_3O_4 TX	**17 mM**	152	75	175	63
	61mM	152	71	186	60

3.3.2. Oleic acid double layer study

Oleic acid is commonly used as a surfactant to modify the surface of magnetite nanoparticles due to its high affinity to the magnetite surface. Although oleic acid is only soluble in non-polar solvents, bilayer oleic acid-coated magnetite nanoparticles can be dispersed in polar carrier liquids with the proper adjustment of pH. Though several works have been reported with oleic acid as a surfactant for magnetite nanoparticles [77, 87, 88], only few authors have reported the presence of an oleic acid bilayer that turns the iron oxide NPs soluble in aqueous solvents [56, 82, 89]. Maity *el al.* [76] have prepared iron oxide NPs coated with either a monolayer or a bilayer of oleic acid and found that they are either stable in kerosene and dodecane or water, respectively.

This is important as per their biomedical use in MRI as contrast agents and for magnetic hyperthermia as treatment agents.

Lan *et al.* [90] have synthetized bilayer surfactant stabilized nanoparticles with an average size of about 12 nm by using oleic acid as the primary and secondary layer of surfactant. In addition, the author found that the prepared NPs are applicable in preparing Pickering emulsions with controllable stability due to their sensitivity to pH and ionic strength. Other authors have found that oleic acid coated Fe_3O_4 NPs are effective to enhance hyperthermic killing ability under an AC magnetic field in mice fibrosarcoma tumoral cells.

Yang *et al.* [56] have performed an extensive study to distinguish between the monolayer and the bilayer. Based on the assumption that the amount of oleic acid necessary to form a bilayer is 20 % with respect to the Fe_3O_4 NP mass, the authors have characterized both types of samples. In the present study, the formation of the oleic acid bilayer was also studied and its influence on iron oxide nanoparticles properties was accessed.

3.3.2.1. FTIR spectroscopy and DSC/TGA

The presence of oleic acid bonded to the NPs was evaluated by FTIR spectroscopy. Figure 3.27 shows the FTIR spectra of pristine Fe_3O_4 NPs and the same particles with different percentages of oleic acid. The typical bands of pristine Fe_3O_4 NPs are present, as previously demonstrated. For low concentrations of oleic acid (below 20%) which are assumed to form a monolayer, the FTIR spectra show some characteristic bands of the surfactant.

The presence of oleic acid covering the nanoparticles was also evaluated by thermal analysis. The TGA/DTA curves of Fe_3O_4 NPs coated with oleic acid are shown in Figure 3.28. In the analyzed temperature range pristine Fe_3O_4 NPs shows only a slight decrease in the mass percentage which is related to the conversion of Fe_3O_4 to γ-Fe_2O_3 and FeO, which are the stable phase of diagram of Fe-O system above 570 ºC [91]. Fe_3O_4 NPs with 8% and 96% of oleic acid show three derivative peaks in the DTA curve corresponding to mass losses in the TGA curve. The first peak at 214ºC is close to the boiling temperature of oleic acid (b.p. 94-195 ºC/1.2 mmHg) and is common to both oleic acid samples, OA 8% and 96%, where a mass loss of about 2.3% and 7.5%, respectively, is obtained and can be correlated to the removal of free oleic acid on the Fe_3O_4 NPs. The second peak is at about 338 ºC with a mass loss of 10.6% for OA 96% and less than 2% for OA 8% and corresponds to the removal of oleic acid molecules that are bonded to Fe_3O_4 NPs surface. This peak adsorption temperature confirms stronger binding energy between the oleic acid molecules and Fe_3O_4 NPs, and happens when a bilayer is formed [58]. The third peak at 617 ºC and 712 ºC is common to both OA samples and the mass loss is of 6.8% and 32% for OA 8% and OA

96%, respectively. Above 600 ºC the carbon from the oleic acid is oxidized to CO and CO_2 during the annealing and the reduction mechanism may be as follows [92]:

$$Fe_3O_4 + CO \rightarrow 3FeO + CO_2$$ Equation 3.8

$$3FeO \leftrightarrow Fe_2O_3 + \alpha Fe$$ Equation 3.9

$$CO + \frac{1}{2}O_2 \rightarrow CO_2$$ Equation 3.10

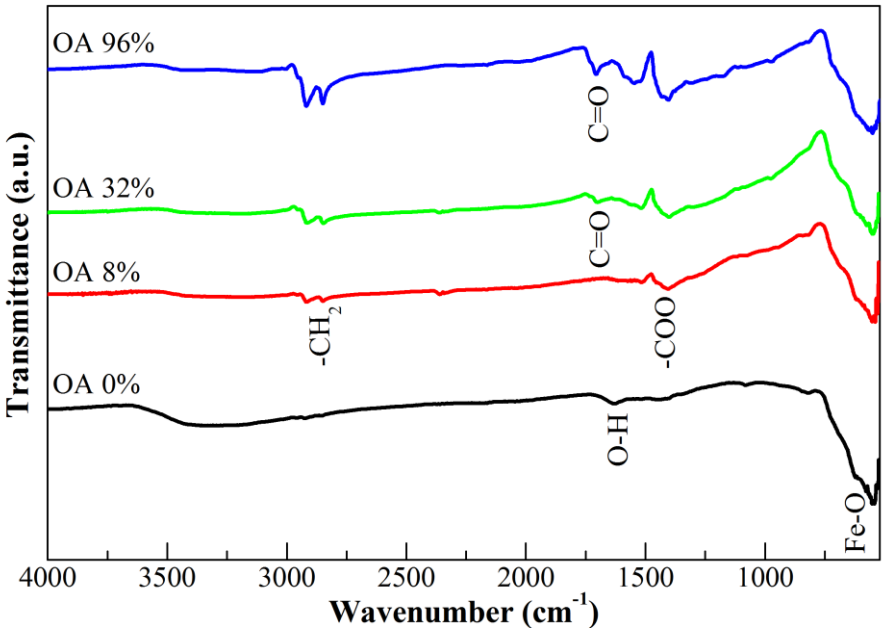

Figure 3.27. FTIR spectra of pristine Fe_3O_4 nanoparticles coated with 0% (black line), 8% (red line) 32% (green line) and 96% (blue line) of oleic acid.

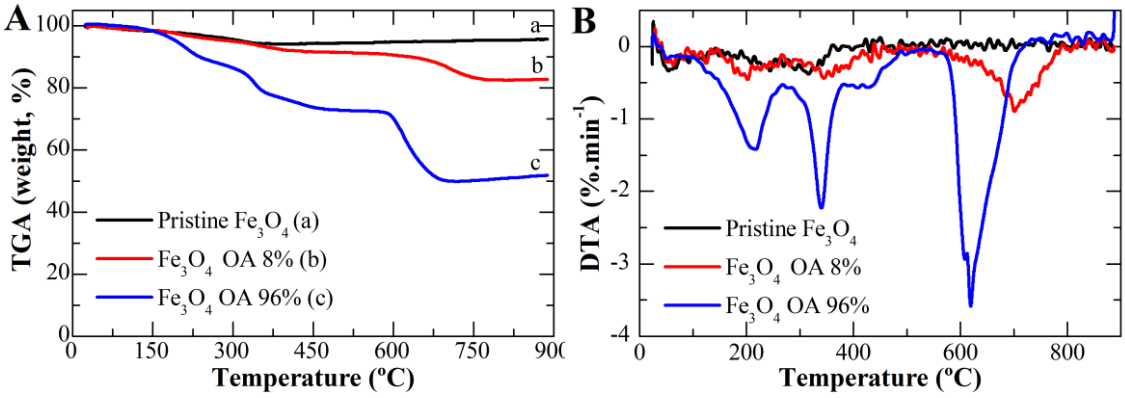

Figure 3.28. TGA (A) and DTA (B) of pristine Fe_3O_4 NPs and coated with 8% and 96% of oleic acid.

3.3.2.2. Zeta potential and DLS

The effect of the oleic acid bilayer on the stability of the Fe_3O_4 NPs suspended in water was evaluated by zeta potential and DLS. The samples with different percentages of oleic acid were prepared at different pH and measured the zeta potential of these samples in order to evaluate their stability (given by a zeta potential value above +/- 30 mV) as a function of pH. Figure 3.29 shows the variation of zeta potential as a function of pH for each NPs suspension.

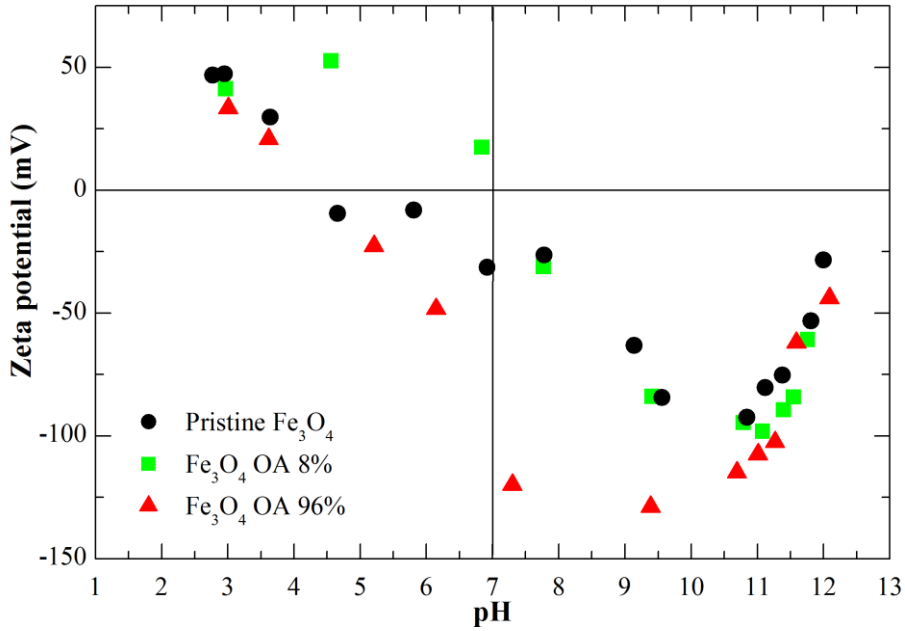

Figure 3.29. Graphical representation of zeta potential of oleic acid coated iron oxide nanoparticles as a function of pH for an iron concentration of 1.25 mM.

At neutral pH (pH = 7), the NPs have a zeta potential of around -32 mV. Moreover at basic pH (above 9) the NPs are stable in aqueous suspension for an iron concentration of 1.25 mM. When oleic acid is added to the NPs suspension, for a low concentration (8%), the zeta potential of the NPs at pH 7 shifted to positive values of zeta potential (around 17 mV). Above the critical concentration for the formation of the bilayer, the zeta potential at pH 7 shifts to more negative values, around -120 mV for 96% of oleic acid. Therefore, it is possible to achieve a stable NPs suspension at physiological pH using oleic acid as a stabilizer.

Dynamic light scattering measurements allow the probing of the diffusion dynamics of the NPs in a number of conditions and compare them with the zeta potential results. Autocorrelation functions (ACF) of pristine NPs show clearly two relaxation modes (Figure 3.30 A). Indeed a slow relaxation mode is present, here attributed to very large NPs aggregates, and contributes largely

to the overall measurement despite its zeta potential value being clearly negative at pH=9 (Figure 3.29).

Comparison between OA 8% and OA 96% at the same pH and NPs concentration shows the disappearance of the slow relaxation mode with the increase of OA concentration. Indeed, with 96% of oleic acid, it is completely absent and the ACF shows a typical single-exponential relaxation. The DLS experiments show that although the zeta potential is clearly favorable at pH=9 even without oleic acid, large aggregates persist which may compromise the long-term colloidal stability of the dispersions.

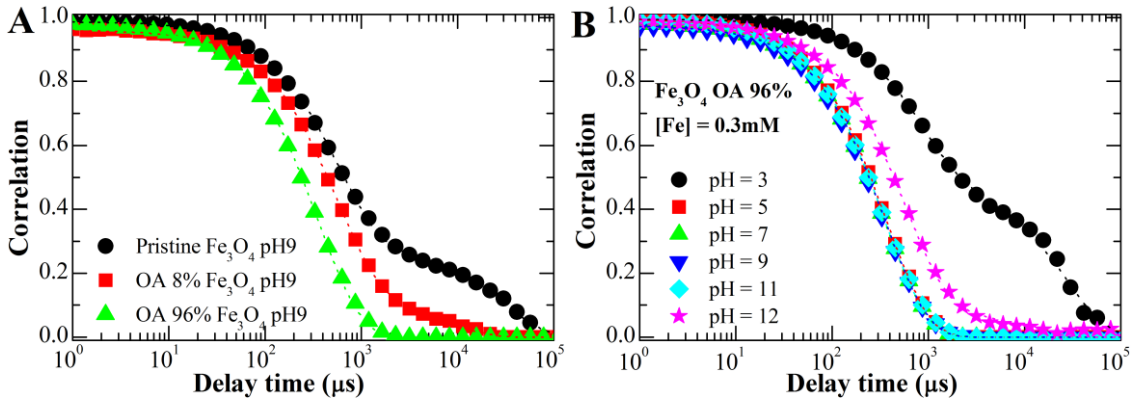

Figure 3.30. Comparison of measured (dots) and adjusted (lines) correlation curves of dynamic light scattering measurements between (A) pristine Fe_3O_4, OA 8% Fe_3O_4 and OA 96% Fe_3O_4 at pH9, and (B) OA 96% Fe_3O_4 at different pH: 3, 5, 7, 9, 11 and 12.

Using 96% of oleic acid as an optimal condition to attain stable colloidal dispersions the pH was changed in order to understand its effect on the NPs stability (Figure 3.30 B). Again, when zeta potential values approach zero (pH=3) a very slow relaxation mode is observed. However, in the range between pH=5 and 11 all ACF overlap, showing that within experimental error the system is independent of pH in this region. This includes the physiological pH. A single relaxation is obtained, which may be fitted with a single-exponential function.

In order to analyze the obtained data from dynamic light scattering measurements the method of cumulants expansion was used for every measurement described above. This method is based on the expansion in Taylor series of the expression that relates the autocorrelation curve with the experimental curve, given by Equation 3.11:

$$C(\tau) = 1 + \beta \exp(-2\Gamma\tau) \qquad \text{Equation 3.11}$$

Where τ is the delay time (μsec), C is the autocorrelation, β is a pre-exponential factor, and Γ is the decay constant, giving the average value ⟨Γ⟩. In a first order expansion: ⟨Γ⟩ = Γ and

$$\Gamma = Dq^2 \qquad \text{Equation 3.12}$$

Being *D* the diffusion coefficient and q the scattering vector that can be determined by

$$q = \frac{4\pi n}{\lambda}\sin\left(\frac{\theta}{2}\right) \qquad \text{Equation 3.13}$$

Where n is the refractive index, λ is the wavelength (532 nm) and θ is the scattering angle (90º). Finally, the hydrodynamic diameter of the samples can be calculated using the Stokes-Einstein equation given by

$$D_h = \frac{k_B T}{3\pi\eta(T)D} \qquad \text{Equation 3.14}$$

Where k_B is the Boltzmann constant, *T* is the absolute temperature and η is the fluid viscosity. Under non-optimal conditions, i.e., when ACF has more than one relaxation, this type of analysis is not valid.

Figure 3.31 shows the relation between the measured hydrodynamic diameters and the iron concentration. For each case and using the method of the cumulants expansion the hydrodynamic diameters were calculated through the ACF curves. Although this type of analysis is not valid, it is possible to see that for the cases where the ACF curve has more than one relaxation, there are two calculated diameters, probably representing the isolated NPs (smallest diameter, around 200 nm) and the larger aggregates, since these suspensions are not stable enough to prevent NPs aggregation.

Figure 3.32 shows the relation between the measured and calculated hydrodynamic diameters in the range of pH. According to ACF curves, at pH 3 and 12, the most instable ones, the measured and calculated hydrodynamic diameters are different. However, when all ACF measurements overlap the method of the cumulants is valid. For these the hydrodynamic diameter is constant over a wide range of pH and NPs concentration of 96% oleic acid. The determined size at pH 7 (physiological pH) is 164 ± 3 nm and polydispersity is 0.20 ± 0.06, indicating a fairly monodispersed suspension.

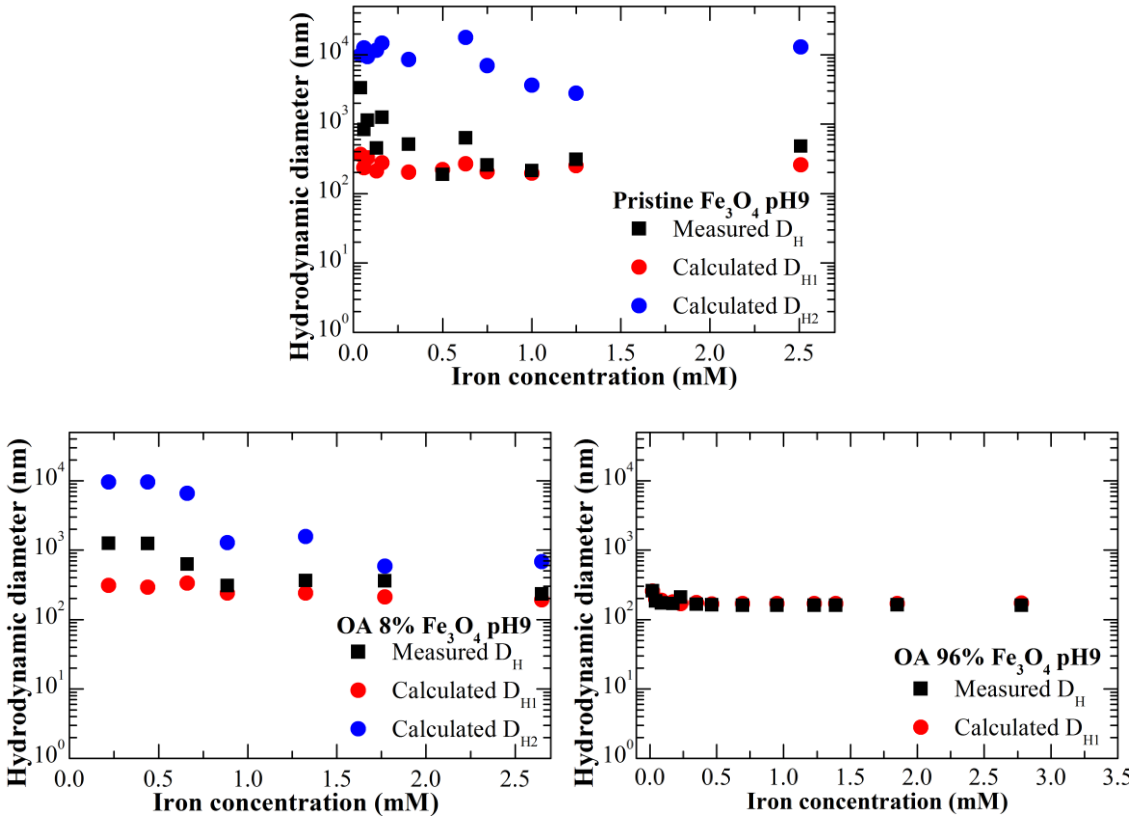

Figure 3.31. Measured vs calculated hydrodynamic diameter for pristine Fe_3O_4 NPs, OA 8% Fe_3O_4 NPs, and OA 96% Fe_3O_4 NPs at pH 9. The calculated hydrodynamic diameters were obtained using the above-described method of the cumulants expansion.

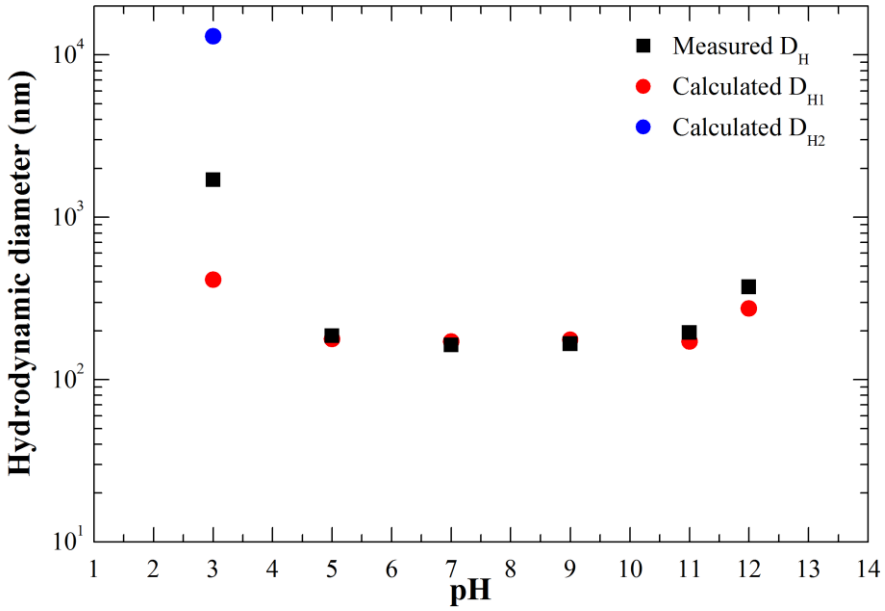

Figure 3.32. Measured vs calculated hydrodynamic diameter in the range of pH measured for OA 96% Fe_3O_4 NPs.

A difference between the size of NPs obtained by TEM and the D_h is observed. In TEM image, the oleic acid coating is not visible; therefore, the measured diameters correspond to the single core of the NP. When the NPs are in suspension with oleic acid, the hydrodynamic diameter was measured with DLS, which incorporates also the oleic acid bilayer. Still accounting with the bilayer leads to a discrepancy of one order of magnitude between the two experiments. The most plausible explanation is that even at very low concentrations, the Fe_3O_4 NPs are agglomerated in larger particles with a size of about 164 nm. Interestingly, this effect is pH independent between 5 and 11. At pH=12 this size increases to about 390 nm and becomes again dependent of NPs concentration. Therefore, the structure of the agglomerates is dependent of the ionization degree of the oleic acid.

3.3.2.3. Magnetic characterization

DC magnetic measurements were performed to access the influence of oleic acid in pristine iron oxide NPs magnetic properties. Magnetic saturation values are presented in emu per gram of the whole particle (magnetic and non-magnetic material). Pristine iron oxide NPs exhibit a saturation magnetization of around 59 emu.g^{-1} at 320 K. When oleic acid is incorporated, M_S of the nanoparticles is greatly reduced (around 27 emu.g^{-1} for OA 96%). The reduction of Fe_3O_4 M_S is dependent upon oleic acid' percentage.

Figure 3.33 represents the hysteresis loops of pristine NPs and Fe_3O_4 NPs coated with oleic acid 8%, 64%, and 96%, measured at 320 K. Inset corresponds to the magnification of the same hysteresis loops. For all samples it is evident the absence of coercivity and remanence at 320 K, which confirms superparamagnetic behavior of all samples above the blocking temperature. Accordingly, it is possible to conclude that oleic acid does not change the superparamagnetic behavior of the Fe_3O_4 NP. However, with the increase in the oleic acid concentration the magnetic saturation of the NPs decreases, which may be attributed to surface effects. Larger oleic acid concentration decreases aggregation of NPs, the surface atoms to volume ratio in NPs increases and consequently reduces the saturation of magnetization [4, 93].

The formation of a bilayer of oleic acid on the surface of Fe_3O_4 NPs was studied and its influence on the NPs properties was assessed. Using FTIR and TGA/DTA analysis, the presence of an oleic acid bilayer was confirmed. This bilayer formation is a major factor for the Fe_3O_4 NPs stabilization in physiological conditions. An oleic acid concentration of 96% is able to prevent the formation of larger aggregates at physiological pH, as demonstrated by TEM and DLS measurements. The average size of the Fe_3O_4 cores is around 9 nm while the average hydrodynamic diameter is around 170 nm, not only due to the presence of oleic acid but also probably because the

oleic acid bilayer incorporated small aggregates of Fe_3O_4 NPs. Furthermore zeta potential measurements confirmed that at physiological conditions (pH = 7) OA 96% Fe_3O_4 NPs are stable (~ -120 mV).

The magnetic studies confirmed the presence of oleic acid bilayer since the magnetic saturation of the NPs is inferior to the values obtained when a bilayer is not present. Additionally, this surfactant does not change the superparamagnetic nature of the Fe_3O_4 NPs, as shown by the absence of coercivity and remanence magnetization at 320 K.

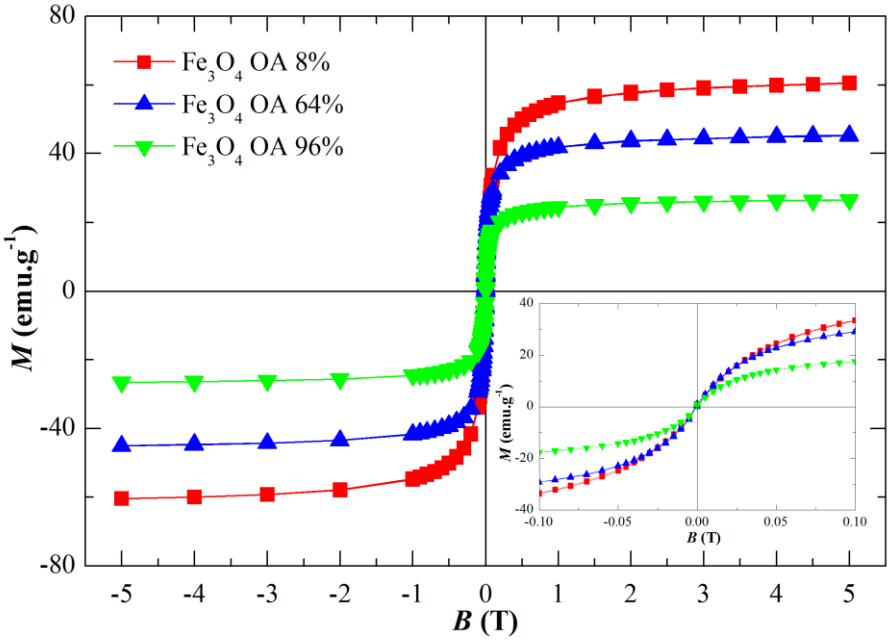

Figure 3.33. Magnetization vs. applied magnetic field of oleic acid coated iron oxide NPs, for different surfactant concentration: 8%, 64%, and 96%.

3.3.3. NPs obtained from thermal decomposition

The structure of the NPs synthetized by thermal decomposition method is shown in Figure 3.34. The XRD patterns obtained for pristine iron oxide nanoparticles have the 2θ six characteristic peaks at 30.1, 35.4, 43.2, 53.6, 57.2, and 62.8, which correspond to (220), (311), (400), (422), (511) and (440), diffraction planes, respectively. Comparison of XRD pattern of NPs with standard diffraction spectrum for magnetite and maghemite powders (JCPDS 00-019-0629 for magnetite and JCPDS 00-039-1346 for maghemite) for the synthesized product we clearly identify the diffraction peaks of crystalline cubic magnetite structure. The average crystallite size was calculated to be 9.74 nm using the Scherrer's equation (Equation 3.7).

FTIR measurements were performed to identify the main chemical bonds of Fe_3O_4 TD NPs. The obtained spectrum for Fe_3O_4 TD NPs is shown in Figure 3.35 that shows the presence of specific absorbance bands. A strong absorbance band at 538 cm^{-1} is attributed to the Fe-O stretching vibration mode. The bands at 1421 cm^{-1} and 1626 cm^{-1} are related to the C-H bending and O-H stretching vibration modes, respectively. The broad band between 3000 cm^{-1} and 3500 cm^{-1} is related to the O-H stretching vibration mode due to water vapor [18].

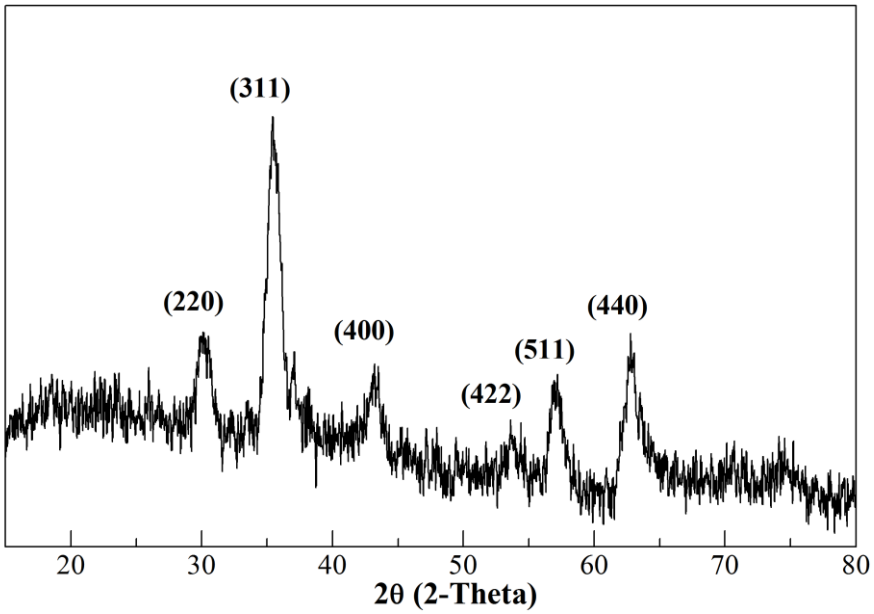

Figure 3.34. X-ray patterns of iron oxide nanoparticles produced thermal decomposition technique.

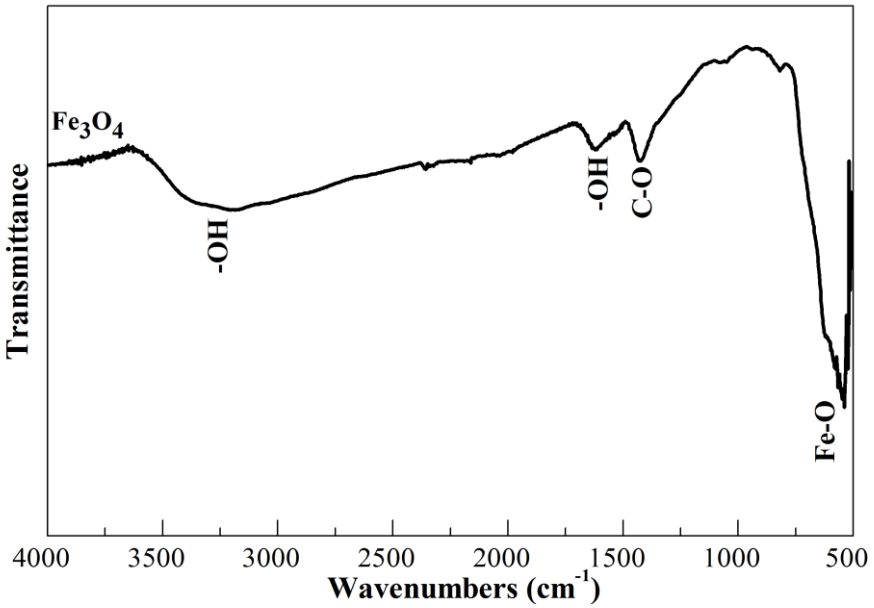

Figure 3.35. FTIR spectra of Fe_3O_4 nanoparticles produced by thermal decomposition technique.

The average diameter of the Fe_3O_4 TD nanoparticles was obtained from TEM images (Figure 3.36). The synthetized NPs show an average diameter of 8 nm with a narrow size distribution, which is similar to the average diameter obtained for pristine Fe_3O_4 NPs.

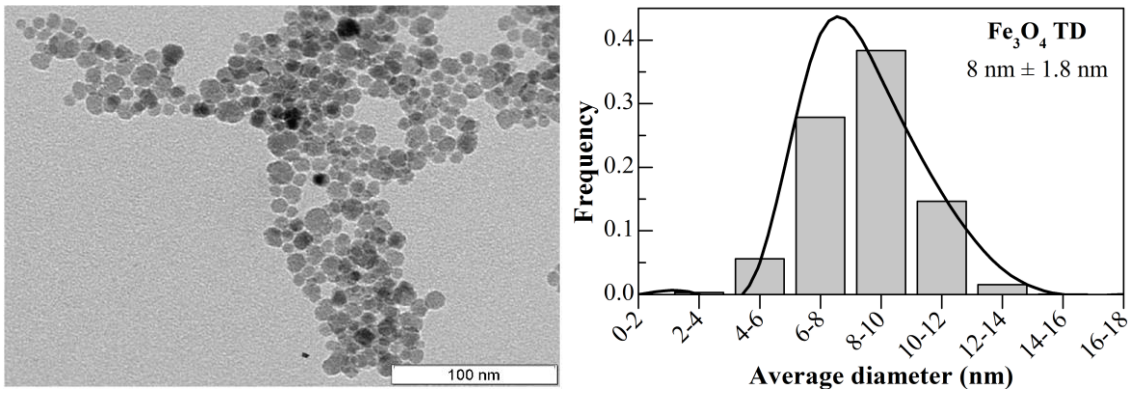

Figure 3.36. TEM image of pristine Fe_3O_4 TD NPs and their respective size distribution graph.

Figure 3.37 shows the temperature dependence of the zero-field cooled and field cooled magnetization curves of Fe_3O_4 TD NPs measured by SQUID under an applied field of 100 Oe. The blocking temperature (T_B) was determined as the maximum value of ZFC curve. The hysteresis loops measured at temperatures 10 and 320 K for the pristine Fe_3O_4 nanoparticles are shown in Figure 3.37.

The temperature dependence of magnetization of Fe_3O_4 TD NPs exhibits a T_B around 182 K, confirming that the produced NPs have a superparamagnetic behavior, due to the absence of coercivity and remanence at 320 K. For Fe_3O_4 TD NPs at 10 K, the saturation magnetization reaches 72 emu.g^{-1} with a coercivity of 250 Oe and at 320 K the saturation magnetization is around 61 emu.g^{-1}.

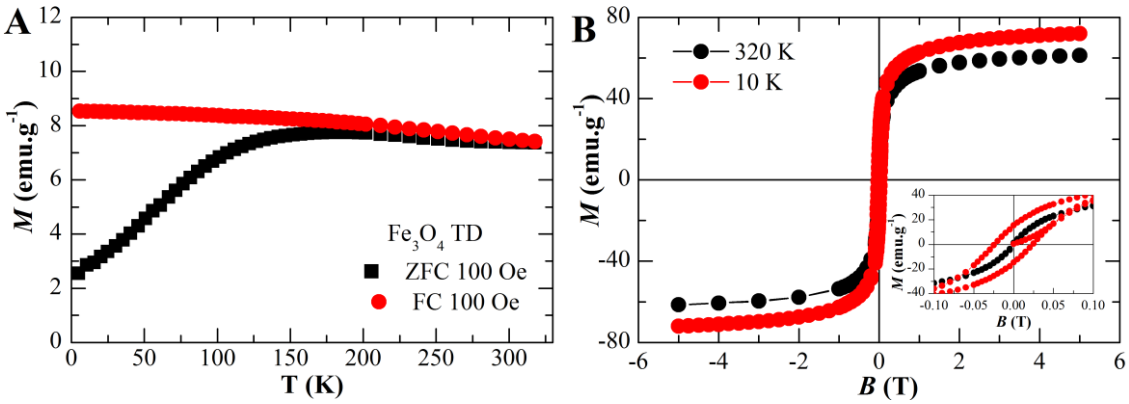

Figure 3.37. Magnetic characterization of Fe_3O_4 TD NPs: (A) Zero-field cooled and field cooled results; (B) Magnetization vs. applied magnetic field at 320 and 10 K.

The obtained results of Fe_3O_4 TD NPs characterization are very similar to the ones obtained for Fe_3O_4 NPs produced by chemical precipitation method. As such, both techniques allow obtaining superparamagnetic NPs suitable for biomedical applications.

3.4. Summary

Magnetic nanoparticles have been extensively investigated for biomedical applications in the last decades. Among the different types of magnetic nanoparticles, iron oxides are the most interesting due to their biocompatibility and stability. Their superparamagnetic properties provide them advantage face to ferromagnetic materials due to the absence of magnetization once an externally applied magnetic field is removed. Colloidal stability of iron oxide NPs in aqueous medium is crucial for biomedical applications. The stabilization of colloids can be achieved by controlling the strength of one or both repulsive forces (electrostatic and steric repulsion). In most cases, stabilizing agents such as surfactants or polymers are used to control these forces and obtain highly stable colloids.

In this chapter the core of the theranostic system developed in this PhD thesis was studied. Synthesis and characterization of iron oxide colloids produced by either chemical precipitation or thermal decomposition technique was described and discussed. The characterization of the produced iron oxide colloids evolves the most significant properties for biomedical applications. Morphology of the produced Fe_3O_4 NPs was evaluated by TEM and SEM, while crystalline phases and chemical composition was evaluated by XRD and FTIR, respectively. The stability of iron oxide colloids in aqueous medium was also evaluated and the magnetic properties of the produced NPs were accessed.

The iron oxide NPs produced by either chemical precipitation or thermal decomposition were identified to be magnetite due to its characteristic crystalline cubic structure. Using Scherrer's equation, the average crystallite size was found to be 9.75 and 9.74 nm for chemical precipitation and thermal decomposition, respectively. The obtained size correlates with TEM diameter that was found to be 8.5 ± 2.0 nm and 8.0 ± 1.8 nm, respectively. FTIR spectra demonstrated the presence of typical absorbance bands for iron oxides.

Iron oxide NPs produced by chemical precipitation are typical hydrophilic but not very stable in aqueous medium, having a tendency to agglomerate. Therefore, the particles obtained by this technique were stabilized using three different agents: tri-sodium citrate, oleic acid, and triton X-100. The three of them possess at least one negative charge that is attracted to the positively

charged magnetite surface. In order to evaluate the influence of the stabilizers upon the properties of the NPs, XDR, FTIR and TEM were again performed. XDR showed that the presence of the surfactant do not change the crystalline phase of the compound, while FTIR, although show the presence of the typical absorbance bands for each stabilizer also show the presence of the iron oxide. Morphology analysis demonstrated that the average size of the iron oxide core is not altered by the presence of surfactants; however, in some cases, the agglomeration of the NPs decreases significantly.

The colloidal stability of the iron oxide colloids in aqueous medium was evaluated by UV-VIS absorbance through time dependence and by sedimentation rate, using different stabilizer concentration. An optimal concentration was found for tri-sodium citrate and oleic acid stabilized NPs. Tri-sodium citrate appears to have the best performance for long-term stability (up to 8 weeks), while oleic acid is better for short-term stability (24 hours). Triton X-100 showed the worst performance in both stability tests performed.

Magnetic characterization tests were performed in pristine Fe_3O_4 NPs and Fe_3O_4 NPs stabilized with the three tested stabilizers. In all cases, the NPs are superparamagnetic at room temperature, confirmed by the absence of coercivity and remanence at this temperature. The saturation magnetization of pristine Fe_3O_4 NPs at 320 K (58 $emu.g^{-1}$) decreases when the surfactant is present. The surfactant that mostly affects the saturation magnetization is oleic acid.

Oleic acid is a particular surfactant that has high affinity to the magnetite surface. Although oleic acid is only soluble in non-polar solvents, bilayer oleic acid-coated magnetite NPs can be dispersed in polar carrier liquids with the proper adjustment of pH. The presence of the mono- and bilayer of oleic acid was studied using FTIR, DSC/TGA, zeta potential, and DLS. Finally the influence on the magnetic properties of the iron oxide core was evaluated. FTIR spectra demonstrated the presence of the typical bands for the monolayer and the bilayer, which was confirmed by DSC/TGA measurements. An oleic acid concentration of 96% is able to prevent the formation of larger aggregates at physiological pH, as demonstrated by TEM and DLS measurements. The average diameter of the Fe_3O_4 cores is around 9 nm while the average hydrodynamic diameter is around 170 nm, not only due to the presence of oleic acid but also probably because the oleic acid bilayer incorporated small agglomerates of Fe_3O_4 NPs. Furthermore zeta potential measurements confirmed that at physiological conditions (pH = 7) OA 96% Fe_3O_4 NPs are extremely stable (~ -120mV). The magnetic studies demonstrated that the presence of the oleic acid bilayer reduces the magnetic saturation of the NPs. Additionally this surfactant does not change the superparamagnetic nature of the Fe_3O_4 NPs, as shown by the absence of coercivity and remanence magnetization at 320 K.

In this chapter nanometric iron oxide colloids that are stable in aqueous medium and have superparamagnetic properties were studied. These iron oxide colloids were fully characterized, providing the basis to evaluate their potential in biomedical applications such as magnetic hyperthermia, drug delivery and MR imaging contrast agents. Moreover, cytotoxicity evaluation and biomedical applications are further studied in Chapter 6 and Chapter 7.

3.5. References

1. I. S. O. (ISO), in, ISO Standards, Geneva 20, Switzerland, 2008.

2. C. Sun, J. S. Lee, M. Zhang, Magnetic nanoparticles in MR imaging and drug delivery, Adv Drug Deliv Rev, 60 (2008), 1252-1265.

3. T. Kobayashi, Cancer hyperthermia using magnetic nanoparticles, Biotechnol J, 6 (2011), 1342-1347.

4. I. Obaidat, B. Issa, Y. Haik, Magnetic Properties of Magnetic Nanoparticles for Efficient Hyperthermia, Nanomaterials, 5 (2015), 63-89.

5. S. P. Gubin, Magnetic Nanoparticles, WILEY-VCH Verlag GmbH & Co., Federal Republic of Germany, 2009.

6. J. Bai, J.-P. Wang, High-magnetic-moment core-shell-type FeCo–Au⁄Ag nanoparticles, Applied Physics Letters, 87 (2005), 152502.

7. V. I. Shubayev, T. R. Pisanic, 2nd, S. Jin, Magnetic nanoparticles for theragnostics, Adv Drug Deliv Rev, 61 (2009), 467-477.

8. D. Ho, X. Sun, S. Sun, Monodisperse magnetic nanoparticles for theranostic applications, Acc Chem Res, 44 (2011), 875-882.

9. A. M. G. C. Dias, A. Hussain, A. S. Marcos, A. C. A. Roque, A biotechnological perspective on the application of iron oxide magnetic colloids modified with polyssacharides, Biotechnological advances, 29 (2011), 142-155.

10. S. C. McBain, H. H. Yiu, J. Dobson, Magnetic nanoparticles for gene and drug delivery, Int J Nanomedicine, 3 (2008), 169-180.

11. A. Akbarzadeh, M. Samiei, S. Davaran, Magnetic nanoparticles: preparation, physical properties, and applications in biomedicine, Nanoscale Res Lett, 7 (2012), 144.

12. M. A. Willard, L. K. Kurihara, E. E. Carpenter, S. Calvin, V. G. Harris, Chemically prepared magnetic nanoparticles, International Materials Reviews, 49 (2004), 125-170.

13. M. Arruebo, R. Fernández-Pacheco, M. R. Ibarra, J. Santamaría, Magnetic nanoparticles for drug delivery, Nano Today, 2 (2007), 22-32.

14. T. K. Indira, P. K. Lakshmi, Magnetic Nanoparticles – A Review, 3 (2010).

15. N. Lee, T. Hyeon, Designed synthesis of uniformly sized iron oxide nanoparticles for efficient magnetic resonance imaging contrast agents, Chemical Society reviews, 41 (2012), 2575-2589.

16. A. K. Gupta, M. Gupta, Synthesis and surface engineering of iron oxide nanoparticles for biomedical applications, Biomaterials, 26 (2005), 3995-4021.

17. W. Wu, Q. He, C. Jiang, Magnetic iron oxide nanoparticles: synthesis and surface functionalization strategies, Nanoscale Res Lett, 3 (2008), 397-415.

18. G. Gnanaprakash, J. Philip, T. Jayakumar, B. Raj, Effect of digestion time and alkali addition rate oh physical properties of magnetite nanoparticles, The journal of physical Chemistry B, 111 (2007), 7978-7986.

19. U. S. Khan, N. S. Khattak, A. Manan, A. Rahman, F. Khan, A. Rahim, Some Properties of Magnetite Nanoparticles Produced Under Different Conditions, Journal of Elec Materi, 44 (2014), 303-312.

20. D. Ling, N. Lee, T. Hyeon, Chemical synthesis and assembly of uniformly sized iron oxide nanoparticles for medical applications, Acc Chem Res, 48 (2015), 1276-1285.

21. D. K. Kim, Y. Zhang, W. Voit, K. V. Rao, M. Muhammed, Synthesis and characterization of surfactant-coated superparamagnetic monodispersed iron oxide nanoparticles, Journal of Magnetism and Magnetic Materials, 225 (2001), 30-36.

22. Y. S. Kang, S. Risbud, J. F. Rabolt, P. Stroeve, Synthesis and Characterization of Nanometer-Size Fe3O4 and γ-Fe2O3 Particles, Chemistry of Materials, 8 (1996), 2209-2211.

23. J.-H. Wu, S. P. Ko, H.-L. Liu, S. Kim, J.-S. Ju, Y. K. Kim, Sub 5 nm magnetite nanoparticles: Synthesis, microstructure, and magnetic properties, Materials Letters, 61 (2007), 3124-3129.

24. S. Wu, A. Sun, F. Zhai, J. Wang, W. Xu, Q. Zhang, A. A. Volinsky, Fe3O4 magnetic nanoparticles synthesis from tailings by ultrasonic chemical co-precipitation, Materials Letters, 65 (2011), 1882-1884.

25. I. Martínez-Mera, M. E. Espinosa-Pesqueira, R. Pérez-Hernández, J. Arenas-Alatorre, Synthesis of magnetite (Fe3O4) nanoparticles without surfactants at room temperature, Materials Letters, 61 (2007), 4447-4451.

26. N. C. Bigall, E. Dilena, D. Dorfs, M.-L. Beoutis, G. Pugliese, C. Wilhelm, F. Gazeau, A. A. Khan, A. M. Bittner, M. A. Garcia, M. Garcia-Hernandez, L. Manna, T. Pellegrino, Hollow Iron Oxide Nanoparticles in Polymer Nanobeads as MRI Contrast Agents, The Journal of Physical Chemistry C, 119 (2015), 6246-6253.

27. D. Maity, D. C. Agrawal, Synthesis of iron oxide nanoparticles under oxidizing environment and their stabilization in aqueous and non-aqueous media, Journal of Magnetism and Magnetic Materials, 308 (2007), 46-55.

28. D. Maity, S. N. Kale, R. Kaul-Ghanekar, J.-M. Xue, J. Ding, Studies of magnetite nanoparticles synthesized by thermal decomposition of iron (III) acetylacetonate in tri(ethylene glycol), Journal of Magnetism and Magnetic Materials, 321 (2009), 3093-3098.

29. J. Li, X. Shi, M. Shen, Hydrothermal Synthesis and Functionalization of Iron Oxide Nanoparticles for MR Imaging Applications, Particle & Particle Systems Characterization, 31 (2014), 1223-1237.

30. M. Daschner de Tercero, C. Röder, U. Fehrenbacher, U. Teipel, M. Türk, Continuous supercritical hydrothermal synthesis of iron oxide nanoparticle dispersions and their characterization, Journal of Nanoparticle Research, 16 (2014), 1-27.

31. R. Dolores, S. Raquel, G. L. Adianez, Sonochemical synthesis of iron oxide nanoparticles loaded with folate and cisplatin: effect of ultrasonic frequency, Ultrason Sonochem, 23 (2015), 391-398.

32. S. Mosivand, L. M. A. Monzon, K. Ackland, I. Kazeminezhad, J. M. D. Coey, Structural and magnetic properties of sonoelectrocrystallized magnetite nanoparticles, Journal of Physics D: Applied Physics, 47 (2014), 055001.

33. C. Pascal, J. Pascal, F. Favier, M. Moubtassim, C. Payen, Electrochemical Synthesis for the Control of γ-Fe2O3 Nanoparticle Size. Morphology, Microstructure, and Magnetic Behavior, Chem. Mater., 11 (1999), 141-147.

34. F. Dumitrache, I. Morjan, C. Fleaca, A. Badoi, G. Manda, S. Pop, D. S. Marta, G. Huminic, A. Huminic, L. Vekas, C. Daia, O. Marinica, C. Luculescu, A. M. Niculescu, Highly magnetic Fe2O3 nanoparticles synthesized by laser pyrolysis used for biological and heat transfer applications, Applied Surface Science, 336 (2015), 297-303.

35. A. Bharde, R. Parikh, M. Baidakova, S. Jouen, B. Hannoyer, T. Enoki, 2008.

36. R. Sakuma, H. Hashimoto, Y. Kusano, Y. Ikeda, M. Nakanishi, T. Fujii, M. Takano, J. Takada, Characterization of Microtubule Material Consisting of Iron Oxide Nanoparticles Produced by Bacteria, Journal of the Japan Society of Powder and Powder Metallurgy, 61 (2014), S90-S92.

37. S. Laurent, D. Forge, M. Port, A. Roch, C. Robic, L. Vander Elst, R. N. Muller, Magnetic iron oxide nanoparticles: synthesis, stabilization, vectorization, physicochemical characterizations, and biological applications, Chem Rev, 108 (2008), 2064-2110.

38. W. Yu, H. Xie, A Review on Nanofluids: Preparation, Stability Mechanisms, and Applications, Journal of Nanomaterials, 2012 (2012), 1-17.

39. R. Qiao, C. Yang, M. Gao, Superparamagnetic iron oxide nanoparticles: from preparations to in vivo MRI applications, Journal of Materials Chemistry, 19 (2009), 6274.

40. V. Tandon, S. K. Bhagavatula, W. C. Nelson, B. J. Kirby, Zeta potential and electroosmotic mobility in microfluidic devices fabricated from hydrophobic polymers: 1. The origins of charge, ELECTROPHORESIS, 29 (2008), 1092-1101.

41. K. Hidehiro, I. Motoyuki, Surface modification and characterization for dispersion stability of inorganic nanometer-scaled particles in liquid media, Science and Technology of Advanced Materials, 11 (2010), 044304.

42. J. Faraudo, J. S. Andreu, J. Camacho, Understanding diluted dispersions of superparamagnetic particles under strong magnetic fields: a review of concepts, theory and simulations, SOft Matter, 9 (2013), 6654.

43. A.-H. Lu, E. L. Salabas, F. Schüth, Magnetic Nanoparticles: Synthesis, Protection, Functionalization, and Application, Angewandte Chemie International Edition, 46 (2007), 1222-1244.

44. M. E. Khosroshahi, L. Ghazanfari, Preparation and characterization of silica-coated iron-oxide bionanoparticles under N2 gas, Physica E: Low-dimensional Systems and Nanostructures, 42 (2010), 1824-1829.

45. M. Chastellain, A. Petri, A. Gupta, K. V. Rao, H. Hofmann, Superparamagnetic Silica-Iron Oxide Nanocomposites for Application in Hyperthermia, Advanced Engineering Materials, 6 (2004), 235-241.

46. J. Yang, F. Zhang, W. Li, D. Gu, D. Shen, J. Fan, W. X. Zhang, D. Zhao, Large pore mesostructured cellular silica foam coated magnetic oxide composites with multilamellar vesicle shells for adsorption, Chem Commun (Camb), 50 (2014), 713-715.

47. W.-Y. Rho, H.-M. Kim, S. Kyeong, Y.-L. Kang, D.-H. Kim, H. Kang, C. Jeong, D.-E. Kim, Y.-S. Lee, B.-H. Jun, Facile synthesis of monodispersed silica-coated magnetic nanoparticles, Journal of Industrial and Engineering Chemistry, 20 (2014), 2646-2649.

48. L. Jia, Y. Kitamoto, Influence of silica coating process on fine structure and magnetic properties of iron oxide nanoparticles, Electrochimica Acta, (2015).

49. J. Gautier, E. Allard-Vannier, E. Munnier, M. Souce, I. Chourpa, Recent advances in theranostic nanocarriers of doxorubicin based on iron oxide and gold nanoparticles, J Control Release, 169 (2013), 48-61.

50. P. Quaresma, I. Osório, G. Dória, P. A. Carvalho, A. Pereira, J. Langer, J. P. Araújo, I. Pastoriza-Santos, L. M. Liz-Marzán, R. Franco, P. V. Baptista, E. Pereira, Star-shaped magnetite@gold nanoparticles for protein magnetic separation and SERS detection, RSC Adv., 4 (2014), 3690-3698.

51. K. Niemirowicz, I. Swiecicka, A. Z. Wilczewska, I. Misztalewska, B. Kalska-Szostko, K. Bienias, R. Bucki, H. Car, Gold-functionalized magnetic nanoparticles restrict growth of Pseudomonas aeruginosa, Int J Nanomedicine, 9 (2014), 2217-2224.

52. A. Ahmadi, H. Shirazi, N. Pourbagher, A. Akbarzadeh, K. Omidfar, An electrochemical immunosensor for digoxin using core-shell gold coated magnetic nanoparticles as labels, Mol Biol Rep, 41 (2014), 1659-1668.

53. A. Szpak, S. Fiejdasz, W. Prendota, T. Straczek, C. Kapusta, J. Szmyd, M. Nowakowska, S. Zapotoczny, T-T Dual-modal MRI contrast agents based on superparamagnetic iron oxide nanoparticles

with surface attached gadolinium complexes, Journal of nanoparticle research : an interdisciplinary forum for nanoscale science and technology, 16 (2014), 2678.

54. N. Erathodiyil, J. Y. Ying, Functionalization of inorganic nanoparticles for bioimaging applications, Acc Chem Res, 44 (2011), 925-935.

55. Q. Lan, C. Liu, F. Yang, S. Liu, J. Xu, D. Sun, Synthesis of bilayer oleic acid-coated Fe3O4 nanoparticles and their application in pH-responsive Pickering emulsions, J Colloid Interface Sci, 310 (2007), 260-269.

56. K. Yang, H. Peng, Y. Wen, N. Li, Re-examination of characteristic FTIR spectra of secundary layer in bilayer oleic acid-coated Fe_3O_4 naoparticles, Applied Surface Science, 256 (2010), 3093-3097.

57. E. D. Smolensky, H. Y. Park, T. S. Berquo, V. C. Pierre, Surface functionalization of magnetic iron oxide nanoparticles for MRI applications - effect of anchoring group and ligand exchange protocol, Contrast media & molecular imaging, 6 (2011), 189-199.

58. Y. Sahoo, H. Pizem, T. Fried, D. Golodnitsky, L. Burstein, C. N. Sukenik, G. Markovich, Alkyl Phosphonate/Phosphate Coating on Magnetite Nanoparticles: A Comparison with Fatty Acids, Langmuir, 17 (2001), 7907-7911.

59. W. T. Al-Jamal, K. Kostarelos, Liposomes: from a clinically established drug delivery system to a nanoparticle platform for theranostic nanomedicine, Acc Chem Res, 44 (2011), 1094-1104.

60. D. G. You, G. Saravanakumar, S. Son, H. S. Han, R. Heo, K. Kim, I. C. Kwon, J. Y. Lee, J. H. Park, Dextran sulfate-coated superparamagnetic iron oxide nanoparticles as a contrast agent for atherosclerosis imaging, Carbohydr Polym, 101 (2014), 1225-1233.

61. M. M. Lin, K. Kim do, A. J. El Haj, J. Dobson, Development of superparamagnetic iron oxide nanoparticles (SPIONS) for translation to clinical applications, IEEE Trans Nanobioscience, 7 (2008), 298-305.

62. X. L. Liu, H. M. Fan, J. B. Yi, Y. Yang, E. S. G. Choo, J. M. Xue, D. D. Fan, J. Ding, Optimization of surface coating on Fe3O4 nanoparticles for high performance magnetic hyperthermia agents, Journal of Materials Chemistry, 22 (2012), 8235.

63. A. K. Gupta, A. S. Curtis, Surface modified superparamagnetic nanoparticles for drug delivery: interaction studies with human fibroblasts in culture, J Mater Sci Mater Med, 15 (2004), 493-496.

64. A. H. Lu, E. L. Salabas, F. Schuth, Magnetic nanoparticles: synthesis, protection, functionalization, and application, Angew Chem Int Ed Engl, 46 (2007), 1222-1244.

65. A. J. Cole, V. C. Yang, A. E. David, Cancer theranostics: the rise of targeted magnetic nanoparticles, Trends Biotechnol, 29 (2011), 323-332.

66. A. Baptista, P. Soares, I. Ferreira, J. P. Borges, Nanofibers and Nanoparticles in Biomedical Applications, in: Atul Tiwari, Ashutosh Tiwari (Eds.) Bioengineered Nanomaterials, CRC Press, New York, 2013, pp. 98-100.

67. D. Ling, T. Hyeon, Chemical design of biocompatible iron oxide nanoparticles for medical applications, Small, 9 (2013), 1450-1466.

68. M. Dan, D. F. Scott, P. A. Hardy, R. J. Wydra, J. Z. Hilt, R. A. Yokel, Y. Bae, Block copolymer cross-linked nanoassemblies improve particle stability and biocompatibility of superparamagnetic iron oxide nanoparticles, Pharm Res, 30 (2013), 552-561.

69. A. R. Murray, E. Kisin, A. Inman, S. H. Young, M. Muhammed, T. Burks, A. Uheida, A. Tkach, M. Waltz, V. Castranova, B. Fadeel, V. E. Kagan, J. E. Riviere, N. Monteiro-Riviere, A. A. Shvedova, Oxidative stress and dermal toxicity of iron oxide nanoparticles in vitro, Cell Biochem Biophys, 67 (2013), 461-476.

70. A. M. Kruse, S. A. Meenach, K. W. Anderson, J. Z. Hilt, Synthesis and characterization of CREKA-conjugated iron oxide nanoparticles for hyperthermia applications, Acta Biomater, 10 (2014), 2622-2629.

71. R. Mejías, L. Gutiérrez, G. Salas, S. Pérez-Yagüe, T. M. Zotes, F. J. Lázaro, M. P. Morales, D. F. Barber, Long term biotransformation and toxicity of dimercaptosuccinic acid-coated magnetic

nanoparticles support their use in biomedical applications, Journal of Controlled Release, 171 (2013), 225-233.

72. J. Gallo, N. J. Long, E. O. Aboagye, Magnetic nanoparticles as contraste agents in the diagnosis and treatment of cancer, Chem. Soc. Rev, 42 (2013), 7816.

73. M. Johannsen, U. Gneveckow, K. Taymoorian, B. Thiesen, N. Waldofner, R. Scholz, K. Jung, A. Jordan, P. Wust, S. A. Loening, Morbidity and quality of life during thermotherapy using magnetic nanoparticles in locally recurrent prostate cancer: results of a prospective phase I trial, Int J Hyperthermia, 23 (2007), 315-323.

74. P. I. Soares, A. M. Alves, L. C. Pereira, J. T. Coutinho, I. M. Ferreira, C. M. Novo, J. P. Borges, Effects of surfactants on the magnetic properties of iron oxide colloids, J Colloid Interface Sci, 419 (2014), 46-51.

75. J. Saien, Z. Ojaghloo, A. R. Soleymani, M. H. Rasoulifard, Homogenous and heterogenous AOPs for rapid degradation of Triton X-100 in aqueous media via UV light, nano titania hydrogen peroxide and potassium persulfate, Chemical Engineering Journal, 167 (2011), 172-182.

76. D. Maity, D. Agrawal, Synthesis of iron oxide nanoparticles under oxidizing environment and their stabilization in aqueous and non-aqueous media, Journal of Magnetism and Magnetic Materials, 308 (2007), 46-55.

77. M. Talelli, C. J. Rijcken, T. Lammers, P. R. Seevinck, G. Storm, C. F. van Nostrum, W. E. Hennink, Superparamagnetic iron oxide nanoparticles encapsulated in biodegradable thermosensitive polymeric micelles: toward a targeted nanomedicine suitable for image-guided drug delivery, Langmuir, 25 (2009), 2060-2067.

78. Y. Wei, B. Han, X. Hu, Y. Lin, X. Wang, X. Deng, Synthesis of Fe_3O_4 nanoparticles and their magnetic properties, Procedia Engineering, 27 (2012), 632-637.

79. L. Yang, J. Zhu, D. Xiao, Microemulsion-mediated hydrothermal synthesis of ZnSe and Fe-doped ZnSe quantum dots with different luminescence characteristics, RSC Advances, 2 (2012), 8179.

80. A. R. Biris, Y. Xu, D. Wang, in, 2014.

81. O. Veiseh, J. W. Gunn, M. Zhang, Design and fabrication of magnetic nanoparticles for targeted drug delivery and imaging, Adv Drug Deliv Rev, 62 (2010), 284-304.

82. X. Liu, M. D. Kaminski, Y. Guan, H. Chen, H. Liu, A. J. Rosengart, Preparation and characterization of hydrophobic superparamagnetic magnetite gel, Journal of Magnetism and Magnetic Materials, 306 (2006), 248-253.

83. D. R. Lucas, Osteoblastoma, Arch Pathol Lab Med, 134 (2010), 1460-1466.

84. A. S. Lubbe, C. Alexiou, C. Bergemann, Clinical applications of magnetic drug targeting, J Surg Res, 95 (2001), 200-206.

85. J. Gass, P. Poddar, J. Almand, S. Srinath, H. Srikanth, Superparamagnetic polymer nanocomposites with uniform Fe_3O_4 nanoparticle dispersions, Advanced Functional Materials, 16 (2006), 71-75.

86. R.-Y. Hong, J.-H. Li, S.-Z. Zhang, H.-Z. Li, Y. Zheng, J.-m. Ding, D.-G. Wei, Preparation and characterization of silica-coated Fe_3O_4 nanoparticles used as percursor of ferrofluids, Applied Surface Science, 255 (2009), 3485-3492.

87. L. Zhang, R. He, H.-C. Gu, Oleic acid coating on the monodisperse magnetite nanoparticles, Applied Surface Science, 253 (2006), 2611-2617.

88. M. Bloemen, W. Brullot, T. T. Luong, N. Geukens, A. Gils, T. Verbiest, Improved funcionalization of oleic acid-coated iron oxide nanoparticles for biomedical applications, Journal of Nanoparticle Research, 14 (2012).

89. M. Mahdavi, M. Ahmad, M. Haron, F. Namvar, B. Nadi, M. Rahman, J. Amin, Synthesis, Surface Modification and Characterisation of Biocompatible Magnetic Iron Oxide Nanoparticles for Biomedical Applications, Molecules, 18 (2013), 7533.

90. Q. Lan, C. Liu, F. Yang, S. Liu, J. Xu, D. Sun, Synthesis of bilayer oleic acid-coated Fe_3O_4 nanoparticles and their application on pH-responsive Pickering emulsions, Journal of colloid and interface science, 310 (2007), 260-269.

91. L. S. Darken, R. W. Gurry, The System Iron—Oxygen. II. Equilibrium and Thermodynamics of Liquid Oxide and Other Phases, J Am Chem Soc, 68 (1946), 798-816.

92. S. Ayyappan, G. Gnanaprakash, G. Panneerselvam, M. P. Antony, J. Philip, Effect of Surfactant Monolayer on Reduction of Fe3O4 Nanoparticles under Vacuum, The Journal of Physical Chemistry C, 112 (2008), 18376-18383.

93. R. H. Kodama, Magnetic nanoparticles, Journal of Magnetism and Magnetic Materials, 200 (1999), 359-372.

– This page is intentionally blank –

Chapter 4. Chitosan-based coating

This chapter introduces chitosan and its derivatives as the coating for the theranostic system developed in this thesis. Their biological activity and toxicity are reviewed, as well as some of their applications. The methodology chitosan and *O*-HTCC coating are described, and the most important results are presented and discussed.

4.1. Introduction

Chitosan (CS) was first discovered in the 19th century when Rouget found that boiling chitin in potassium hydroxide rendered a material soluble in organic acids. However, only five decades later it was first named chitosan. Moreover, only in 1950 the structure of chitosan was finally stablished [1, 2]. Chitosan is a biopolymer obtained from naturally occurring sources, for example, exoskeleton of crustacean, arthropod and fungi [1, 3, 4]. It is a linear copolymer composed of β-(1-4) linked 2-acetamino-2-deoxy-β-D-glycopyranose and 2-amino-2-deoxy-β-D- glycopyranose subunits (Figure 4.1).

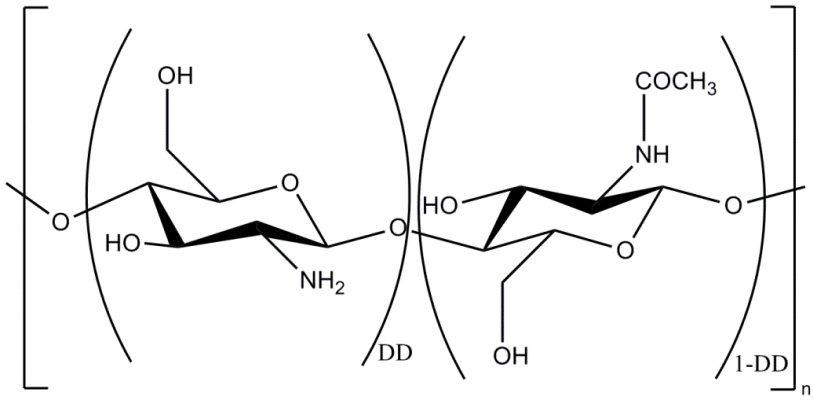

Figure 4.1. Chemical structure of chitin or chitosan, depending on the deacetylation degree (DD). Chitin is present when DD < 50%, while chitosan has a DD > 60%. Besides the deacetylation degree, the structure of both biopolymers is similar.

Chitosan is non-toxic, hydrophilic, biocompatible, biodegradable and anti-bacterial, and has been widely used as a biomaterial and a pharmaceutical excipient in drug formulations [1, 3].

4.1.1. Chitosan and chitin

4.1.1.1. Source, structure and physicochemical properties

Chitosan is obtained from the thermochemical deacetylation of chitin in the presence of alkali. Several other alkali methods are available, most of them involving the hydrolysis of the acetate position using sodium or potassium hydroxide solution as well as a mixture of anhydrous hydrazine and hydrazine sulfate. Chitin is the second most abundant polysaccharide in nature, cellulose being the most abundant. The main commercial sources of chitin are shell waste of shrimps, lobsters, krill, and crabs, being a cheap and readily available source. Chitin is highly hydrophobic and is insoluble in water and most organic solvents. On the other hand, chitosan is soluble in diluted acids such as acetic acid, among others [1].

Being obtain from chitin deacetylation, chitosan is a polycationic polymer with one amino group and two hydroxyl groups in the repeating glycosidic residue. The carbohydrate backbone contributes to the rigid crystalline structure obtained after chitosan refinement. This structure is dependent on inter- and intra-molecular hydrogen bounding [1].

Both the source of chitin and the chosen method for chitin deacetylation influence the degree of deacetylation (DD) and polymer molecular weight [1]. The degree of acetylation (DA = 1 – DD) is the amount of nitrogen sites occupied by acetyl groups (each nitrogen atom can react with one acetyl group) [5]. Chitosan is often considered when the DD is above 60%, while its molecular weight typically ranges from 50 to 2000 kDa. On the other hand, chitin typically has a DD below 50% (Figure 4.1) [2, 6].

Chitosan solubility in water medium depends not only upon the DD, but also with the ionic concentration, the pH, the nature of the acid used for protonation, and the distribution of acetyl groups along the chain, as well as the conditions of isolation and drying of the polysaccharide. Moreover, it is also important to consider the intra-chain hydrogen bonds involving the hydroxyl groups [7].

4.1.1.2. Structure-propriety relationship

The presence of amino groups in the chitosan structure differentiates chitosan from chitin. Chitosan has a pKa in the range of 6 to 6.5. Below this range, the amino groups are protonated and become positively charged, i.e., chitosan becomes a water-soluble cationic polyelectrolyte. Above

6.5 the amino groups get deprotonated and thus the polymer becomes insoluble in water medium. Since the amino groups are the ones that determine chitosan solubility, pKa value is highly dependent on the degree of N-acetylation [1, 6].

Moreover, the presence of the amino groups gives chitosan the capacity to complex various species, such as metal ions. As such, chitosan is often used for the treatment of waste waters, purifying them by recovering heavy metals [6]. In its protonated state, chitosan is able to form ionic complexes with a wide variety of natural or synthetic anionic species such as lipids, proteins, DNA and some negative charged synthetic polymers [6].

Chitosan shows crystallinity and polymorphism, depending on the origin of the polymer and its treatment during extraction process. In acidic environment, chitosan behaves as a pseudoplastic material and decreases viscosity with increasing shear rates. Viscosity of chitosan solution increases with an increase in concentration, decreases with temperature and with increasing DD [1].

The degradation rate of chitosan augments when DD decreases, it is inversely related to the degree of crystallinity and also affected by the polymer molecular weight [1].

Other notable intrinsic properties of chitosan are: antibacterial activity [8-10]; antifungal [11-14]; mucoadhesive [15-17]; analgesic [18, 19] and hemostatic properties [20, 21]; is biodegradable into non-toxic residues [1].

4.1.1.3. Biological activity

As above-mentioned, chitosan has remarkable properties that make it an interesting material for developing biomedical applications. These properties are controllable and a consequence of the protonable amino groups in chitosan' structure [6].

The mucoadhesion results from negatively charged residues (sialic acid) in the glycoprotein that composes the mucus, the mucin. The protonated amino groups of chitosan in acidic medium interact with the mucin, since the number of protonable amino groups is directly related to the DD, higher DD leads to improved mucoadhesion properties [6, 22].

The hemostatic property of chitosan is also related with the presence of the protonated amino groups of chitosan. When in contact with blood, positively charged chitosan tends to attract circulating plasma proteins, resulting in platelet adhesion and activation on the surface of the material and then thrombus formation [2, 6, 23].

Some studies also have proven that chitosan is only able to open the cellular membrane tight junctions in its protonated form due to the negative part of cellular membrane [24, 25].

The antibacterial activity of chitosan is partially explained by the presence of the amino groups. Microorganisms' surface has predominantly anionic components (such as Gram-negative lipopolysaccharide and cell surface proteins) for which the chitosan has a high affinity. This ionic interaction alters cell permeability and prevents essential materials to enter the cells and/or leak fundamental solutes out of the cell. The other possible mechanism occurs for low molecular weight water-soluble chitosan and ultrafine nanoparticles that could penetrate cell wall of bacteria and combine with DNA inhibiting the synthesis of mRNA and DNA transcription [2, 26].

Other biological attributes of chitosan have been proved, such as anti-ulcerogenic, anti-tumor, immune modification, renal protective and osteogenic actions, analgesic effect, and scaffold to allow skin or bone cell growth [27, 28].

4.1.1.4. Biodegradability

Chitin and chitosan are partially biodegradable in the presence of human enzymes and are non-toxic and beneficial to the human body [29]. It is important to consider that chitosan is a polysaccharide and consequently contains breakable glycosidic bonds [6]. Glucosamine is the major component of chitosan and is a natural substance produced in the body from glucose. Glucosamine is involved in the manufacture of glycosaminoglycan, which forms cartilage tissue in the body; this molecule is also present in tendons and ligaments [2].

Chitosan can undergo chemical and enzymatic degradation. Chemical degradation, also mentioned as acid catalyzed degradation can occur in the stomach. Enzymatic degradation can occur by several proteases, and mainly lysozyme. Other degradation fates can also occur such as oxidation-reduction reaction and free radical degradation. However, these are unlikely to play an important role in chitosan' degradation *in vivo* [1, 6].

Chitosan degradation depends upon the DD of the polymer. If a fully deacetylation of chitosan (DD of 100%) is achieved its structure changes from semi-crystalline to a crystalline polymer enhancing the biodegradation rate. Furthermore, the reduction of molecular weight also increases its biodegradation rate, since smaller chains are more rapidly degraded into oligosaccharides [1, 6].

4.1.2. Chitosan derivatives

Chitosan has three types of reactive functional groups, the amino group and the primary and secondary hydroxyl groups. The presence of these groups provide many possibilities for covalent

and ionic modifications of chitosan [30]. Consequently, chitosan derivatives can be roughly divided according the site of functionalization: 1) specific reactions involving the NH_2 group; and 2) nonspecific reactions of the –OH groups (mainly esterification and etherification).

Chitosan typically undergoes amines reactions such as *N*-acylation and Schiff reaction. *N*-acylation with acid anhydrides or acyl halides introduces amide groups at the chitosan nitrogen [31], through the quaternization of the amino group or a reaction in which an aldehyde function reacts with $–NH_2$ by reductive amination. The latter reaction can happen in aqueous solution under very mild conditions to obtain randomly distributed substituents in a controlled amount along the chitosan chain [7]. Linear aliphatic *N*-acyl groups above propionyl allow rapid acetylation of hydroxyl groups [31]. Chitosan and simple aldehydes produce *N*-alkyl chitosan upon hydrogenation. The presence of bulky substituent weakens the hydrogen bonds of chitosan; therefore *N*-alkyl chitosan swell in water in spite of the hydrophobicity of the alkyl chains, but they retain the film forming property of chitosan [31].

Consequently, a large number of chitosan derivatives have been produced. In the next paragraphs some examples of chitosan derivatives are detailed.

4.1.2.1. *O*- and *N*-Carboxymethyl chitosan

O- and *N*-carboxymethyl chitosan is a chitosan derivative having carboxymethyl substituents on some or both the amino and primary hydroxyl sites of chitosan backbone [32]. This is an amphoteric polymer with solubility dependent on the pH used [32-36]. Under controlled reaction conditions with sodium monochloroacetate in the presence of NaOH, the substitution in both the *N*- and the *O*-site can be obtained [7].

N-carboxymethyl chitosan is obtained from glyoxylic acid in the presence of a reducing agent [31]. This derivative is water soluble in a wide range of pH, with the condition of being prepared from fully acetylated chitin [7].

4.1.2.2. *N*-methylene phosphoric chitosan

This anionic derivative of chitosan shows some amphoteric character and can be synthetized from several precursors. It has proven to have good complexing efficiency with cations such as Ca^{2+} and those of transition metals (Cu (II), Cd (II), Zn (II), among others). This complexation provides corrosion protection for metal surfaces, among other applications [7, 37-40].

4.1.2.3. Trimethylated chitosan

N-trimethyl chitosan is a water-soluble chitosan derivative that can be prepared by reductive methylation of amine groups of chitosan. The degree of quaternization directly influences the water solubility and the mucoadhesive properties [4, 41].

This chitosan derivative increases the permeation of hydrophilic macromolecules (like peptides and proteins) in neutral and basic environments, being applicable in intestinal delivery of peptide drugs. Moreover, effects are caused by opening the tight junctions [4, 41].

4.1.2.4. HTCC and *O*-HTCC

Ammonium quaternary chitosan derivatives have a permanent positive charge, that enables its full solubility in a large range of pH, and allows its interaction with cellular membranes [25]. The first quaternized chitosan was synthetized by alkylation of the primary amine groups of chitosan with various aldehydes using sodium borohydrate as reducing agent [4].

Other quaternary derivatives of chitosan have been synthetized by attaching a quaternary ammonium moiety to the amine group of chitosan. Xu *et al.* synthetized a quaternary derivative of chitosan, *N*-(2-hydroxyl) propyl-3-trimethyl ammonium chitosan chloride (HTCC), by reaction of chitosan with glycidyl trimethyl ammonium chloride (GTMAC) [42]. This chitosan derivative has excellent water solubility over wide pH range, besides maintaining its antibacterial and antifungal properties, anti-tumoral activity, among others. Kaminski *et al.* [43] studied the ability of HTCC to bind to high-molecular-weight (unfractionated) heparin in PBS (phosphate buffer solution) at pH equal to 7.4. They proved that HTCC is able to bind with efficiency comparable to that for the clinically used protein, protamine sulfate. As such, the authors considered that HTCC is a good candidate to be used as intravenously for reversal of high- and low-molecular-weight heparin in blood.

Sun and his coworkers have prepared a new chitosan derivative, *O*-HTCC (*O*-(2-hydroxyl) propyl-3-trimethyl ammonium chitosan chloride), through the reaction of chitosan with GTMAC. This reaction protects the amino groups and the obtained compound is soluble at neutral and basic pH values [25].

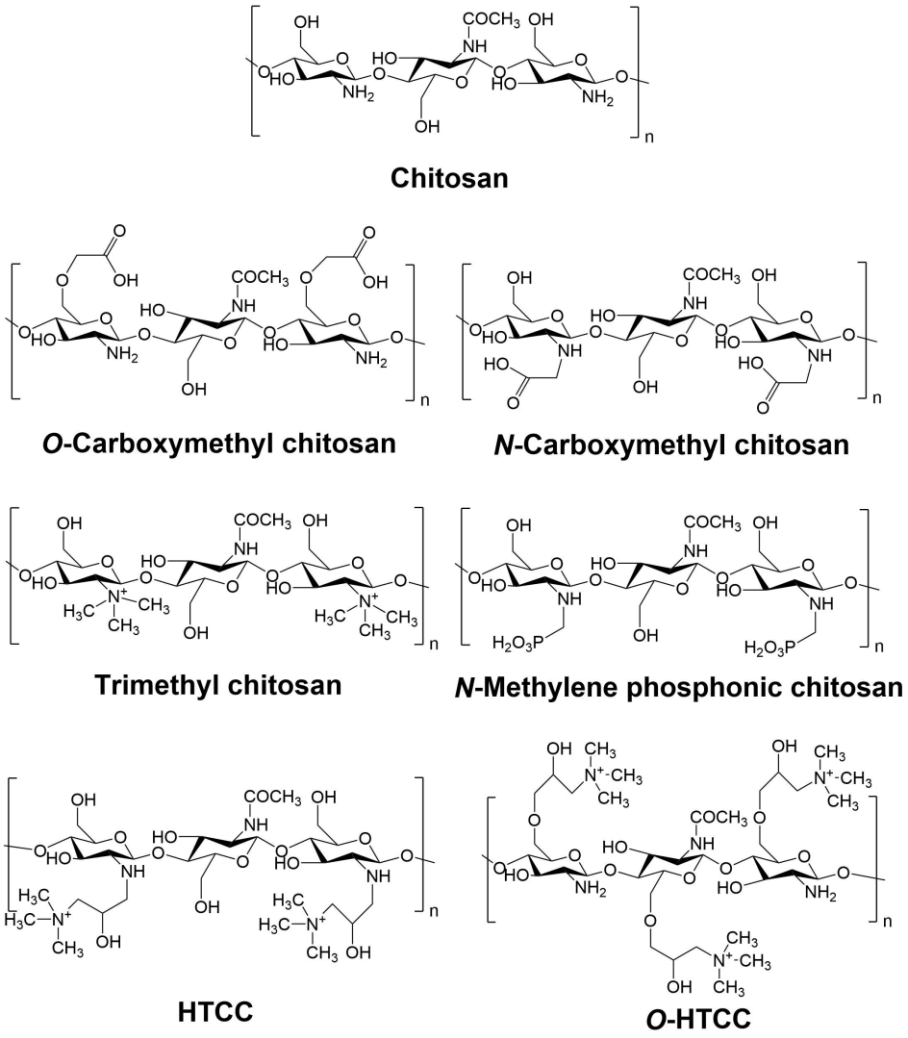

Figure 4.2. Chemical structure of chitosan and some of its derivatives.

4.1.3. Chitosan-based micro/nanoparticles

The solubility in aqueous acidic solutions gives chitosan an inherent advantage for the preparation of micro/nanoparticles since it avoids the use of hazardous organic solvents and allows ionic cross-linking with multivalent ions in the free amine groups. In the form of micro/nanoparticles, chitosan' structure has the inherent ability to control the release of active agents. Moreover, chitosan' inherent mucoadhesive character is maintained once in micro/nanoparticles structure and is the reason to increase residual time at the site of adsorption. Finally, chitosan micro/nanoparticles can be sterilized by different methods such as ionizing radiation, heat, steam, and chemical methods, which is an advantage for clinical applications [44]. Because of all of these advantages, chitosan micro/nanoparticles have been widely used as drug delivery systems [36, 45-48].

There are several reported methods for the production of chitosan micro/nanoparticles. Selection of one of the available methods depends upon factors such as the desired particle size and size distribution, thermal and chemical stability of the active agent when the application is a drug delivery system, stability of the final product, and residual toxicity associated with the final product, among others [44].

4.1.3.1. Emulsion cross-linking

The emulsion cross-linking method is based on the cross-linking between the free amine group of chitosan with the aldehyde group from the cross-linking agent (for example, glutaraldehyde) [44].

In this method, a water-in-oil (w/o) emulsion is prepared whereas chitosan is dissolved in the water phase. The emulsion is stabilized by an adequate surfactant. Further, hardening of the droplets is performed by crosslinking with the crosslinking agent. The size of the particles obtained is generally in the micron range since it is dependent upon the size of the droplets. Moreover, the size of the obtained particles also depends upon the extent of crosslinking agent used and the speed of stirring during the emulsion preparation [3, 44].

Kumbar and his team [49] used this method to prepare chitosan microspheres to encapsulate diclofenac sodium using three crosslinking agents, glutaraldehyde, sulfuric acid and heat treatment. The produced particles were spherical with smooth surfaces and a size within the range of 40 to 230 μm. However, Ohya *et al.* [50] was able to produce chitosan-gel nanospheres using the emulsion crosslinking method. These nanospheres had an average diameter of 250 nm and were able to encapsulate 5-fluorouracil and its derivatives.

An important drawback in this technique is the use of harsh crosslinking agents that have proven to have negative effects on cell viability [3].

4.1.3.2. Coacervation/precipitation

The coacervation/precipitation method uses the cationic profile of chitosan since it is insoluble at alkaline pH medium. As such, chitosan precipitates/coacervates when in contact with alkaline solution. Particles are produced by blowing chitosan solution into an alkaline solution like sodium hydroxide (NaOH), NaOH-methanol or ethanediamine, using a compressed air nozzle to form coacervate droplets [44].

The diameter of the nanoparticles can be controlled by varying the compressed air pressure or spray-nozzle diameter. In addition, the use of a crosslinking agent to harden particles can control

the drug release [44]. The advantage of this technique is the better stability of particles compared to other methods [44].

4.1.3.3. Emulsion droplet coalescence

The emulsion droplet coalescence technique combines both emulsion crosslinking and precipitation described above. Here, the precipitation is induced by allowing coalescence of CS droplets with NaOH droplets [3, 44].

In a first instance, two stable w/o emulsion are prepared: the first one contains chitosan aqueous solution in an oil phase; the second one contains aqueous solution of NaOH. When both emulsions are mixed under high-speed stirring, the droplets of each emulsion collide at a random manner and coalesce, thereby precipitating chitosan droplets to give small size particles [3, 44].

4.1.3.4. Ionic gelation

Ionic gelation method is a very simple and mild process to prepare chitosan micro/nanoparticles, which is the main reason for being a widely used technique [45, 48, 51-54].

This method is based upon a reversible physical crosslinking by electrostatic interaction, avoiding possible toxic effects of the reagents used in chemical crosslinking. Tripolyphosphate (TPP) is a polyanion that is able to interact with chitosan by electrostatic forces and consequently is the most used crosslinking agent. In this technique, chitosan is dissolved in aqueous acidic solution to obtain the cation of CS. This solution is added dropwise under constant stirring to polyanionic TPP solution. Due to the complexation between oppositely charged species, CS undergoes ionic gelation and precipitates to form spherical particles. The disadvantage of this technique is the poor mechanical strength of the obtained particles, limiting their use in drug delivery applications [3, 44, 55].

Bodmeier *et al.* [56] first prepared TPP-CS complex by dropping CS droplets into a TPP solution. The technique was first reported in 1997 by Calvo *et al.* [57] for the preparation of chitosan, chitosan–poly(ethylene oxide) and chitosan–poly(ethylene oxide)–poly(propylene oxide) nanoparticles. Chitosan particles of nanometric size were obtained for chitosan concentrations up to 2.8 $g.l^{-1}$ and TPP concentrations from 0.21 to 0.43 $g.l^{-1}$. Jonassen *et al.* [51] evaluated the stability of CS-TPP nanoparticles and found that upon storage in saline solvents the NPs were stable over a period of one month with respect to changes in particle size and particle compactness.

Other techniques to produce chitosan micro/nanoparticles have been reported: spray drying [58], reverse micellar method [59], microemulsion method [60], polyelectrolyte complex method [61, 62].

4.1.4. Toxicity

As a biocompatible polymer, chitosan is considered to be non-toxic [63]. It is approved for dietary applications in Japan, Italy and Finland [64] and for use in wound dressings by the FDA [65]. However, chitosan modifications can make it more or less toxic and any residual reactants should be carefully removed [1, 66]. Moreover, it is important to consider that chitosan toxicity also depends upon the route of administration, which determines the uptake, concentration, contact time and cell types affected [66].

4.1.4.1. *In vitro* toxicity

In a series of publications, Schipper *et al.* studied chitosan with different molecular weights and degree of deacetylation on CaCo-2 cells, HT29-H and *in situ* rat jejunum. The obtained toxicity results depend upon both DD and molecular weight. At high DD the molecular weight and concentration are responsible for the toxicity, being less toxic and less related to the molecular weight at lower DD. Indeed most of the chitosan tested did not increase dehydrogenase activity significantly in the concentration range tested (1–500 $\mu g.ml^{-1}$) on Caco-2 cells. The *in situ* rat jejunum study showed no increase in lactate dehydrogenase (LDH) activity with any of the CS tested (50 $\mu g.ml^{-1}$) [67, 68].

To investigate the safety of materials the red cell hemolysis assay is widely used. Richardson *et al.* [69] performed this assay using chitosan with different molecular weights. Their results show no hemolysis (< 10%) over 1 h and 5 h with chitosan of molecular weight below 5 kDa, between 5-10 kDa and above 10 kDa at concentrations up to 5 $mg.ml^{-1}$. In another study, no red blood cells lysis was observed with paclitaxel chitosan micelles at 0.025 $mg.ml^{-1}$ [70].

An oligomer of trimethyl chitosan, a chitosan derivative with low cytotoxicity (M_w 3-6 kDa) with degrees of quaternization below 55% have an IC_{50} > 10 $mg.ml^{-1}$. However, the cytotoxicity of this derivative increases with the increase of degree of trimethylation and increase in molecular weight (100 kDa) [71].

The combination of two biocompatible polymers, chitosan and alginate, represents an interesting development for microencapsulation of cells. An interesting study combined these two polymers to provide long-term viability of encapsulated baby-hamster kidney cells. In this case, no toxic

effect was observed using an optimal one-step coating method. Four chitosan were tested: chitosan chloride of 103 and 288 kDa at 87% and 84% DD and chitosan glutamate of 218 and 415 kDa and 85% and 86% DD, respectively. The results were observed over time (40–60 days) concerning the viability. Data were compared to non-encapsulated cells at 12 h *post* seeding; this is a poor comparison, as cell proliferation would increase 'viability'. All capsules were shown to be mechanically stable for 4 months [72].

Interestingly, chitosan and its derivatives seem to be toxic to several bacteria [73], fungi [74] and parasites [75]. This pathogen related toxicity is an effect that could be advantageous in infectious disease control. When emulsions containing chitosan were tested, bacterial inhibition took place in acidic solutions pH 5–5.3, and an 87 kDa 92% DD chitosan was more effective than a 532 kDa 73% DD chitosan against both *Pseudomonas aeruginosa* and *Staphylococcus aureus*. A lipid emulsion of the same chitosan was found to have antimycotic effect against *Candida albicans* and *Aspergillus niger* [73]. However, none of these studies hypothesized a mechanism of action for the inhibitory effect observed.

4.1.4.2. *In vivo* toxicity

In vivo toxicity after administration is of great importance for the design chitosan based structures for biomedical applications. Hirano *et al.* [76] performed a relatively long study (65 days) in which no detrimental effect on body weight was found when chitosan oligosaccharides were injected (7.1 – 8.6 $mg.kg^{-1}$ over 5 days). Only an increase in lysozyme activity was apparent on the first day *post* injections. However, the administration of chitosan intravenously with a higher concentration (50 $mg.kg^{-1}$) caused death. Rao *et al.* [77] have found no significant toxic effects of chitosan in acute toxicity tests in mice, no eye or skin irritation in rabbits and guinea pigs respectively. Moreover, the authors concluded that chitosan was not pyrogenic. Zhang *et al.* [70] found that LD_{50} (lethal dose for 50% of individuals) of paclitaxel chitosan micelles in mice was 72.2 $mg.kg^{-1}$, no anaphylaxis was observed in guinea pigs and no intravenous irritation was observed histopathologically in rabbits at 6 $mg.kg^{-1}$. Furthermore, another research group reported no adverse effects at 3.3-4 $mg.kg^{-1}$ [78].

In a study on fat chelation, 4.5 $g.day^{-1}$ chitosan (molecular weight and DD not specified) in humans was reported not to be toxic, although no significant reduction in fat was found [79]. Arai *et al.* [80] found that chitosan has an LD_{50} comparable to sucrose of >16 $g.kg^{-1}$ in oral administration to mice. No oral toxicity was found in mice treated with 100 $mg.kg^{-1}$ chitosan nanoparticles (80 KDa, 80% DD) [81]. After oral administration of trimethyl chitosan/pDNA nanoparticles a slight toxicity at high dose was observed, causing light diarrhea, which was relieved by stopping

administration [82]. Buccal discs did not cause inflammation of the buccal mucous membrane [83]. Mukhopadhyay *et al.* [84] investigated the chronic oral toxicity of chitosan derivatives in the mice model. No death or other signs of toxicity were observed with a dose of 30 $mg.kg^{-1}$ for one month. Furthermore, the intestinal luminal microbes successfully degraded the administrated polymers (chitosan and its derivatives).

Exposure of rat nasal mucosa to chitosan solutions at 0.5% (w/v) over 1 h caused no significant changes in mucosal cell morphology compared to control [85]. Although most studies reveal low toxicity of chitosan and is approved its adoption as a safe material in drug delivery, among other biomedical applications, it is necessary to consider that any modification of chitosan can change its toxicity profile and so further safety studies are required.

4.1.5. Applications

Chitosan' interesting properties conjugated with its versatility to form different derivatives and different structure (micro/nanoparticles, hydrogels, films, etc.) explains the huge interest in this biopolymer for several applications. Being a polymer obtained from natural sources, chitosan is biocompatible and non-toxic. Furthermore, biodegradation studies have shown that chitosan is degraded into non-toxic residues.

The main areas of applications for chitosan were summarized by Rinaudo *et al.* [7] and include: agriculture, water and waste treatment, food and beverages, cosmetics and toiletries, and finally biopharmaceutics. The latter include a wide range of applications from immunologic to anti-tumoral and wound healing, drug delivery and tissue engineering. In the following, some of the most relevant applications of chitosan in the biomedical field are described.

4.1.5.1. Wound healing

Alemdaroğlu *et al.* [86] prepared a simple chitosan hydrogel system by dissolving chitosan in acid/water mixture. This hydrogel was loaded with epidermal growth factors (EGF) and were able to release EGF within 24 h *in vitro*. *In vivo* studies showed a fastest healing with chitosan gels containing EGF compared to the non-GF-loaded chitosan gel. Another research group has found that chitosan and chitosan-bFGF (basic fibroblast growth factor) scaffolds caused accelerated wound closure in pressure ulcer treatment compared to control. However, only the chitosan-bFGF loaded samples enhanced angiogenesis [87].

Takei et al developed a gluconic acid chitosan derivative that is soluble at neutral pH. [88]. A gel of this derivative was formable by cryogelation (freeze-thawing) being able to maintain pH neutrality, without additives. Moreover, the gel was found to be nontoxic. When applied to full-thickness skin wounds the cryogels were found to promote the accumulation of inflammatory cells, especially polymorphonuclear leukocytes, accelerating wound healing.

4.1.5.2. Tissue engineering

Tissue engineering is a highly interdisciplinary field that combines the principles and methods of life sciences and engineering, which utilizes structural and functional relationships in normal and pathological tissue to develop biological substitutes to restore, maintain, or improve biofunctionality. Chitosan' properties such as biodegradability, nontoxicity and the possibility of being formulated in a variety of forms including powders, gels and films, increases its potential of applications in tissue engineering [1].

Zhang and Zhang [89, 90] have developed chitosan-calcium phosphate composites with a three-dimensional (3D) macroporous bioceramic embedded with porous chitosan sponges to minimize additional local inflammation and to allow osteoconduction. The chitosan sponge enhances the mechanical strength of the ceramic phase through matrix reinforcement and preserves the osteoblast phenotype. Hu *et al*. [10] prepared a chitosan– hydroxyapatite (HA) multilayer nanocomposite with high strength and bending modulus rendering the material suitable for possible application for internal fixation of long bone fractures.

Ang *et al.* [91] designed a robotic desktop rapid prototyping (RP) system to fabricate scaffolds for bone tissue engineering applications. The set-up consisted of a computer-guided desktop robot and a one-component pneumatic dispenser. The dispensing material, chitosan and chitosan–HA dissolved in acetic acid, were forced out through a small Teflon lined nozzle into a dispensing sodium hydroxide–ethanol medium. Layer-by-layer, the chitosan was fabricated with a pre-programmed lay-down pattern. The attachment between layers allowed the chitosan matrix to form interconnected channeled architectures. The *in vitro* osteoblast studies revealed the biocompatibility of the scaffolds with cells exhibiting healthy morphology and avid proliferation throughout the culture period. The rapid prototyping robotic dispensing system is capable of fabricating 3D scaffolds with regular and reproducible macropore architecture.

Chitosan is also used for cartilage [92], liver [93, 94], and nerve tissue [95, 96] engineering.

4.2. Materials and methods

All the chemical reagents used in this research work were of analytical grade and used without further purification.

4.2.1. Chitosan depolymerization

Chitosan (DD 75.5%, *Cognis*) was depolymerized by chemical reaction with sodium nitrite ($NaNO_2$, *Sigma-Aldrich*) based on an adapted method of Huang and coworkers [97]. Briefly, 2.5 g of chitosan was dissolved in 250 ml of acetic acid 1% (V/V) (*Panreac)*, followed by addition of the desired amount of $NaNO_2$, previously dissolved in 10 ml of ultrapure water. The mixture was let to react for 1 hour under mechanical agitation. Low molecular weight chitosan was precipitated with sodium hydroxide (NaOH, *Eka)* 1 M, followed by centrifugation and several washes with ultrapure water. The final obtained product was freeze-dried and stored in a dry place.

4.2.2. Dilute solution viscosity

The molecular weight of depolymerized chitosan was measured by dilute solution viscosity using an Ubbelöhde capillary viscometer (No 0a) at 30 ºC. Chitosan solutions of different concentrations in 0.2 M acetic acid and 0.1 M sodium acetate (*Scharlau*) were prepared. The flow times of chitosan solutions and solvent were recorded in quintuplet and the average value was calculated. The intrinsic viscosity [η] was calculated graphically by extrapolating the curve of reduced viscosity versus concentration to zero concentration. The Mark-Houwink-Sakurada (MHS) equation was used to calculate the molecular weight of depolymerized chitosan ($K = 2.26x10^{-5}$ $dl.g^{-1}$, $\alpha = 0.95$) [98].

4.2.3. *O*-HTCC synthesis

O-HTCC was synthetized using an adapted method of Wang and his coworkers [99]. Chitosan with different molecular weights was used to produce the ammonium quaternary derivative. Briefly, 5 g of chitosan was dissolved in 250 ml of acetic acid 2% and 125 ml of methanol (*Sigma-Aldrich*). After complete dissolution, 32 ml of benzaldehyde (*Fluka*) was added to the reaction vessel. The reaction occurred for 24 h with agitation, forming a white gel. The gel was neutralized with sodium hydroxide 1 M, filtered and washed in turns with acetone (*Fisher chemical*) and methanol. After freeze-drying, the product was mixed with 5 g of glycidil trimethyl ammonium

chloride (GTMAC, *Sigma-Aldrich*) and 50 ml of isopropyl alcohol. The second reaction occurred at 70 ºC for 16 hours. The obtained product was filtered, and washed with acetone and methanol several times. Again, after freeze-drying, the obtained product was added to 100 ml of ethanolic HCl 0.25 M (*Fluka*) and let to react for 24 hours at room temperature. At the end of the reaction, 25 ml of ultrapure water was added, followed by an excess of acetone to precipitate the final product. This product was filtered, and washed several times with acetone and methanol. In order to purify *O*-HTCC, it was re-dissolved in water and precipitated with excess acetone. After filtering and washing, the obtained *O*-HTCC was freeze-dried and stored in a dry place.

4.2.4. Preparation of CS and *O*-HTCC NPs

Chitosan and *O*-HTCC nanoparticles were produced through ionotropic gelation [100] using different concentrations and molecular weight of the polymers and several concentrations of tripolyphosphate (TPP, *Sigma-Aldrich)* (Table 4.1). TPP solution was rapidly added to the polymer solution with magnetic stirring. The nanoparticles suspension was kept on magnetic stirring for a determined incubation time before any characterization.

To produce chitosan and *O*-HTCC coated iron oxide nanoparticles, an appropriate amount of iron oxide NPs suspension (4 $mg.ml^{-1}$) was added to either chitosan or *O*-HTCC solution followed by the addition of TPP. The addition of the polyanion was performed under ultraturrax, and kept under stirring for 5 minutes. For purification, core-shell nanoparticles where separated using a magnet and washed several times with ultrapure water. The final product was freeze-dried and stored in a dry place for further characterization.

4.2.1. Characterization

4.2.1.1. Fourier Transform Infrared (FTIR) spectrometry

To investigate changes in the chemical bounds of the samples Infrared spectrometry was used. FTIR spectra of the samples were obtained using a Nicolet 6700 – Thermo Electron Corporation Attenuated Total Reflectance-Fourier Transform Infrared spectrometer (ATR-FTIR). Measurements were performed in freeze-dried samples in the range of 480 to 4500 cm^{-1}.

Table 4.1. Studied conditions by dynamic light scattering to optimize the production of chitosan and *O*-HTCC nanoparticles.

	CS		***O*-HTCC**		**TPP**		**Incubation time (h)**
	wt.%	**M_v (kDa)**	**wt.%**	**M_v (kDa)**	**wt.%**	**pH**	
Preliminary study	0.2 0.4	469	-	-	0.05-0.4	8.8	0
First step	0.2 0.4	469	0.2 0.4	469	0.05-0.15	8.8	0
Second step	0.2 0.4	469 215 50	0.2 0.4	469 292 50	0.1	8.8	0
Third step	0.2	469 215 50	0.2	469 292 48	0.1	8.8	0 24 48
Forth step	0.2	469 215 170 85 46 39	0.2	469 292 166 97 48	0.1	5 9 13	0

4.2.1.2. ^{1}H NMR and ^{13}C NMR

^{1}H NMR and ^{13}C NMR spectra were recorded on a Bruker Avance III 400, at 400 and 100 MHz respectively, using D_2O as solvent. The solvent signals were used as internal standards for both ^{1}H NMR and ^{13}C NMR recordings.

4.2.1.3. Thermogravimetric analysis (TGA)

Thermogravimetric analysis and differential thermal analysis (DTA) studies were carried out using a Thermal Analyzer NETZSCH STA 449 F3 Jupiter® at a rate of 10 ºC.min^{-1} in a N_2 atmosphere.

4.2.1.4. Dynamic light scattering (DLS)

Hydrodynamic diameter (D_H) of the nanoparticles was measured by means of dynamic light scattering equipment (Avid Nano) using the blade cell at 20 ºC.

Dynamic light scattering and zeta potential measurements were performed using a SZ-100 nanopartica series (Horiba, Lda) with a laser of 532 nm and controlling temperature with a Peltier system (25 ºC). DLS measurements were carried out for diluted NPs suspensions in triplicates using a disposable cell with a scattering angle equal to 90º. Data analysis was performed using cumulants statistics to measure hydrodynamic diameter and polydispersity unless stated otherwise. Zeta potential measurements were performed with a scattering angle equal to 173º, in a graphite electrode cell.

4.2.1.5. X-ray diffraction (XRD)

The crystalline phases of the samples were verified using powder X-ray diffraction. X'Pert PRO PANAlytical X-ray diffractometer was used to obtain X-ray diffraction patterns of the iron oxide nanoparticles previously freeze-dried. The 2θ values were taken from 15º to 80º using a Cu-Kα radiation (k = 1.54060 Å) with a step size of 0.033. The Scherrer's equation was used to measure the average crystallite size.

4.2.1.6. Iron content determination

The iron content of the samples was determined using the 1,10-phenantroline colorimetric method [101], similarly to the description in Chapter 3.

To obtain the nanoparticles concentration the formula [Fe] = 0.7 x [NPs] was used. The ratio was obtained from control experiments.

4.2.1.7. Superconducting quantum interference device (SQUID)

The DC magnetic properties were performed using a 7T SQUID magnetometer (S700X; Cryogenic Ltd.). The zero-field cooled (ZFC) and field-cooled (FC) measurements were performed by cooling the sample to 5 K at zero fields or in the presence of an external field of 100 Oe, respectively. All the magnetic measurements were carried out in increasing temperature range 5–320 K. Isothermal magnetization curves were obtained for fields up to 5 T for temperatures of 10 and 320 K.

4.3. Results and discussion

4.3.1. Chitosan depolymerization

Being a product of chitin deacetylation, chitosan is characterized mainly by two variables, namely, degree of deacetylation and the molecular weight. Degree of deacetylation determines the number of free amino groups present in chitosan chain, which determines it functionality, polarity, and water solubility. On the other hand, molecular weight determines the strength of its fibers/films and viscosity of its solution. Chitosan molecular weight can be manipulated using different depolymerization methods such as acid hydrolysis (HCl, HNO_2, etc.), free radicals (H_2O_2, $K_2S_2O_8$) enzymatic, radiations (UV, γ-rays), ultrasound, microwave, and thermal treatments [102].

Chitosan depolymerization was performed in order to evaluate the influence of the molecular weight in the nanoparticles physicochemical properties. The used technique is very common, simple, and rapid, and allows obtaining chitosan with different molecular weights only by changing the amount of $NaNO_2$ added to the reaction vessel. In acidic solution sodium nitrite produces nitrous acid (HNO_2), which lowers chitosan molecular weight by deamination reaction with subsequent cleavage of β-glycosidic linkages.

FTIR spectrum of the initial chitosan with 469 kDa is shown in Figure 4.3 exhibiting the typical bands for this natural polymer. The band at 3357 cm^{-1} corresponds to the O-H stretching overlapping the N-H stretching, while the band at 2874 cm^{-1} is attributed to the C-H stretching. The amide II bands can be found at 1649 cm^{-1} and 1587 cm^{-1}, corresponding to the C-O stretching of the acetyl group, and to the N-H bending, respectively. The sharp bands at 1415 cm^{-1}, 1374 cm^{-1} and 1316 cm^{-1} are attributed to the $–CH_2$ bending, the asymmetrical C-H bending of the CH_2 group, and the amide III band, respectively. The bands related to the C-O-C bridge are located at 1150 cm^{-1} (anti-symmetric stretching of C-O-C bridge), 1023 cm^{-1} (skeleton vibrations involving the C-O-C stretching bands), and 892 cm^{-1} (C-O-C stretching of the glycosidic linkage). Finally, the band at 1064 cm^{-1} is attributed to the C-N stretching vibration mode [103].

Figure 4.4 shows the FTIR spectra of the four low molecular weight chitosan obtained after depolymerization. Comparison between chitosan and depolymerized chitosan shows almost similar spectra, which indicates that the process of depolymerization caused no chemical change in the structure of the polymer.

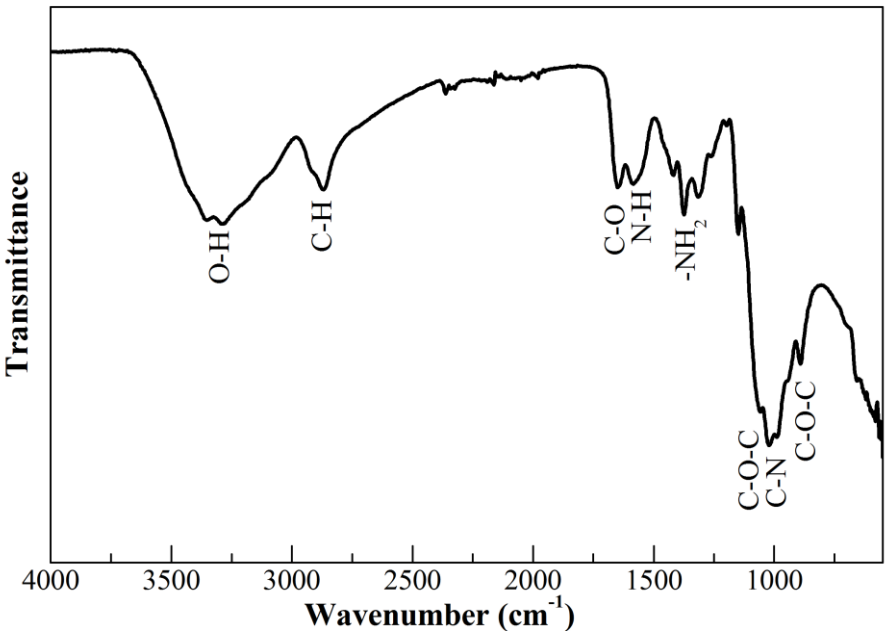

Figure 4.3. FTIR spectrum of initial chitosan before depolymerisation with a molecular weight of 469 kDa.

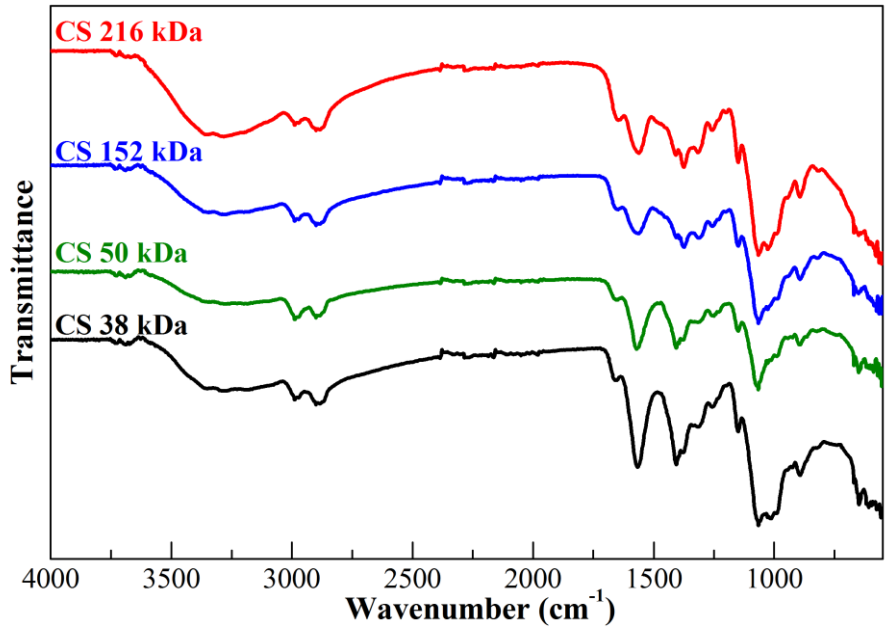

Figure 4.4. FTIR spectra of four low molecular weight chitosan samples obtained from chitosan with 469 kDa using $NaNO_2$ as the depolymerisation agent.

The molecular weight of depolymerized chitosan was measured by dilute solution viscosity. This is a simple and rapid technique to determine a polymer molecular weight. Typically, a polymeric sample is dissolved in an appropriate solvent at a specified concentration in the range of $g.dl^{-1}$.

Polymer solution viscosity is measured relative to the pure solvent viscosity. Relative viscosity (η_r) is given by:

$$\eta_r = \frac{\eta}{\eta_0} \qquad \text{Equation 4.1}$$

Where η is the polymer solution viscosity and η_0 is the viscosity of the pure solvent. The specific viscosity (η_{sp}) is related to the fluid viscosity increase due to all polymer solute molecules and is given by:

$$\eta_{sp} = \frac{(\eta - \eta_0)}{\eta_0} \qquad \text{Equation 4.2}$$

The reduced viscosity (η_{red}) is the fluid viscosity increase per unit of polymer solute concentration (C). The intrinsic viscosity ([η]) can be determined as the limit of the reduced viscosity as the polymer solute concentration approaches zero, or the limit of the inherent viscosity (η_{inh}), $\ln(\eta/\eta_0)$, as the solution polymer concentration approaches zero (Equation 4.3).

$$[\eta] = \lim_{C \to 0} \frac{\eta_{red}}{C} = \lim_{C \to 0} \frac{\ln\left(\frac{\eta}{\eta_0}\right)}{C} \qquad \text{Equation 4.3}$$

Note that the intrinsic viscosity is not viscosity. Intrinsic viscosity is the volume per unit mass that the polymer occupies in a solution, which is the inverse of molecular density. Extrapolation to zero polymer concentration is intended to eliminate polymer intermolecular interactions. The plots used to find the intrinsic viscosity are called the Huggins plot (η_{red} vs. *C*) and the Kraemer plot ($\ln(\eta/\eta_0)$ vs. *C*) as represented in Figure 4.5. The common intercept between both plots is the intrinsic viscosity.

The intrinsic viscosity measured in a specific solvent is related to the average molecular weight (M_v) of the polymer by the Mark-Houwink-Sakurada (MHS) equation:

$$[\eta] = K.{M_v}^{\alpha} \qquad \text{Equation 4.4}$$

Where K and α are Mark-Houwink constants that depend upon the type of polymer, solvent, and the temperature of the viscosity determinations. These constants can be determined experimentally by measuring the intrinsic viscosities of several polymer samples with known molecular weight, measured by an independent method. By plotting the log [η] vs. log M_v the α constant can be determined from the slope of the obtained straight line, while K is obtained from the log

of the intercept. Kasaai [104] proposed two equations as a model to determine α and K for chitosan in any solvent-temperature system, using viscosimetric constants data reported by several research groups. These equations were used in the present work to determine the viscosimetric constants, α (Equation 4.5) and K (Equation 4.6).

$$\alpha = 0.6202 + \frac{0.699x}{0.4806 + x} \qquad \text{Equation 4.5}$$

$$\log K.10^{-5} = -5.7676.\alpha + 5.9232 \qquad \text{Equation 4.6}$$

Where x can be determined by:

$$x = \frac{DA}{pH.\mu} \qquad \text{Equation 4.7}$$

With DA being the degree of acetylation, pH of chitosan solution in any solvent with ionic strength of μ, within a range of temperature of 20 ºC to 30 ºC.

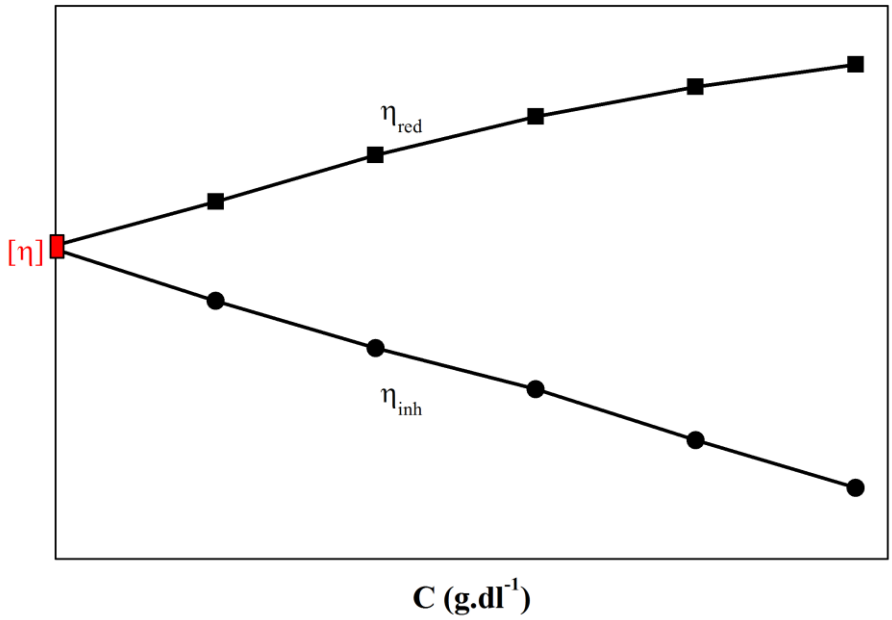

Figure 4.5. Schematic representation of typical Huggins and Kraemer plots showing the common intercept for both curves, which corresponds to the intrinsic viscosity [η] of the polymer.

Five different samples of low molecular weight chitosan were obtained (Table 4.2) using $NaNO_2$ as a depolymerization agent. The depolymerization process used in the present work was not only fast and simple, but also very successful since the M_v of chitosan was lowered by twelvefold, from 469 kDa to 38 kDa. Moreover, the process is reproducible. The obtained low molecular

weight samples were used subsequently for *O*-HTCC synthesis and for chitosan nanoparticles preparation.

Table 4.2. Results from dilute solution viscosity, comparing the amount of $NaNO_2$ used, the intrinsic viscosity ([η]) and the obtained average viscosimetric molecular weight (M_v).

$NaNO_2$ (mg)	**[η] ($dL.g^{-1}$)**	**M_v (kDa)**
0	7.34	469
12.5	3.31 ± 0.05	215 ± 4
25	2.34 ± 0.14	152 ± 9
50	1.34 ± 0.11	87 ± 7
75	0.78 ± 0.03	50 ± 2
100	0.59 ± 0.04	38 ± 3

4.3.2. *O*-HTCC synthesis

O-HTCC synthesis was performed not only to obtain water-soluble chitosan derivative, but also to study the differences between CS and *O*-HTCC NPs.

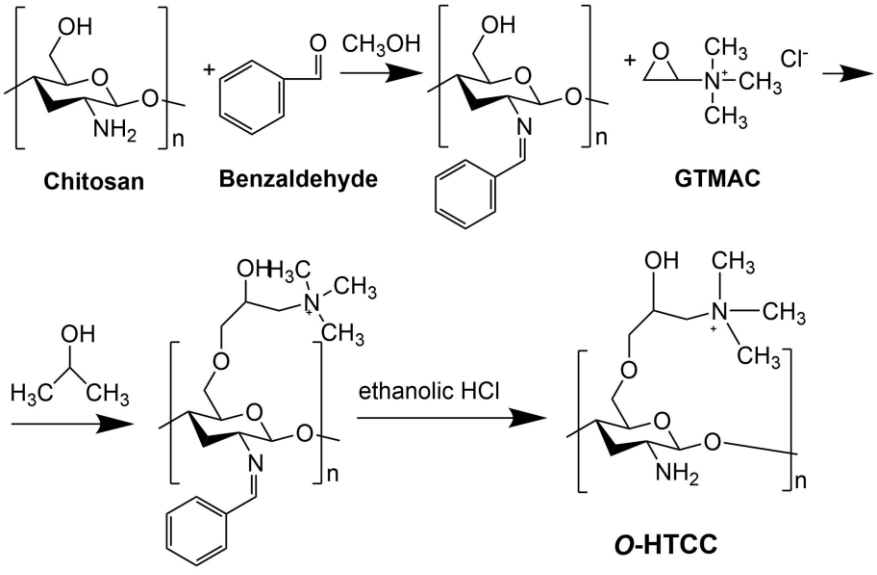

Figure 4.6. Schematic representation of the *O*-HTCC reaction mechanism.

The reaction mechanism is relatively simple and can be divided in three steps as shown in Figure 4.6: the first step is the addition of benzaldehyde to protect the NH_2 groups. This step is crucial to obtain *O*-HTCC, otherwise the GTMAC that couples to chitosan in the second step would have couple to NH_2 group instead of OH. In this scenario, chitosan would lose its positive charge once in acidic solution. The final and third step is the removal of benzaldehyde, reestablishing the NH_2 group.

4.3.2.1. FTIR analysis

FTIR studies were performed to confirm the synthesis of chitosan derivative. Figure 4.7 shows the FTIR spectra of *O*-HTCC and the two intermediate reactions. The first intermediate reaction (CTB) in addition to CS characteristic bands should have the bands correspondent to the aromatic ring of benzaldehyde. The band at 3153 cm^{-1} is attributed to the =CH stretching vibration, while the bands at 2869 cm^{-1} and 1693 cm^{-1} are attributed to the H-C=O and C=O stretching vibrations in the aldehyde group, respectively. The band at 1640 cm^{-1} is caused by the stretching vibration for C=N, obtained from the reaction between $–NH_2$ group of chitosan and benzaldehyde. Further the bands at 1602 cm^{-1}, 1553 cm^{-1} and 1399 cm^{-1} are related to the C-C stretch in the aromatic ring of benzaldehyde [24, 25, 105].

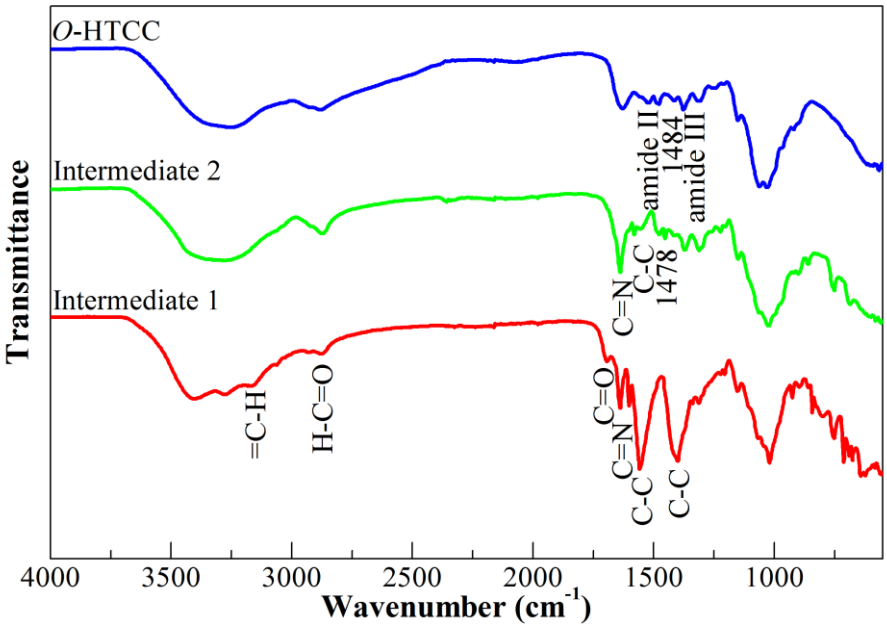

Figure 4.7. FTIR spectra of *O*-HTCC and the two reaction intermediates.

The second intermediate reaction has an extra trimethylammonium group in comparison to CTB that comes from GTMAC. Despite the presence of the remaining bands already described, the

FTIR spectrum of this reaction shows the bands at 1638 cm^{-1} and 1582 cm^{-1} attributed to the C=N stretching vibration and the C-C stretching vibration in the aromatic ring, respectively, showing the presence of benzaldehyde protecting the NH_2 groups. In addition, a band at 1478 cm^{-1} appears which can be attributed to the asymmetric angular bending of methyl groups of quaternary hydrogen [106].

Finally, in *O*-HTCC FTIR spectrum the typical bands of chitosan are present. The band of the primary amino group of *O*-HTCC shifted to 1647 cm^{-1}. The band at 1484 cm^{-1} confirms the presence of the methyl groups of the quaternary hydrogen, which indicates that the substitution reaction occurred successfully The bands at 1522 cm^{-1} and 1309 cm^{-1} are attributed to the stretching vibration of amide II and amide III, respectively, which confirms the successful removal of benzaldehyde [24, 25, 106].

4.3.2.2. ^{1}H NMR and ^{13}C NMR of *O*-HTCC

Figure 4.6 represents ^{1}H NMR and ^{13}C NMR spectra of *O*-HTCC. The peak at 3.36 ppm related with the ^{1}H NMR spectra of CH_2 (O-CH_2) is due to characteristic methylene protons of the reacted chitosan hydroxyl group with quaternary ammonium salts. The peak at 3.13 ppm belongs to three methyl protons of the quaternary ammonium salt. ^{13}C NMR spectra confirm the successful substitution; the peak at 54 ppm is due to the carbon of methyl groups in the ammonium quaternary salt [24, 25].

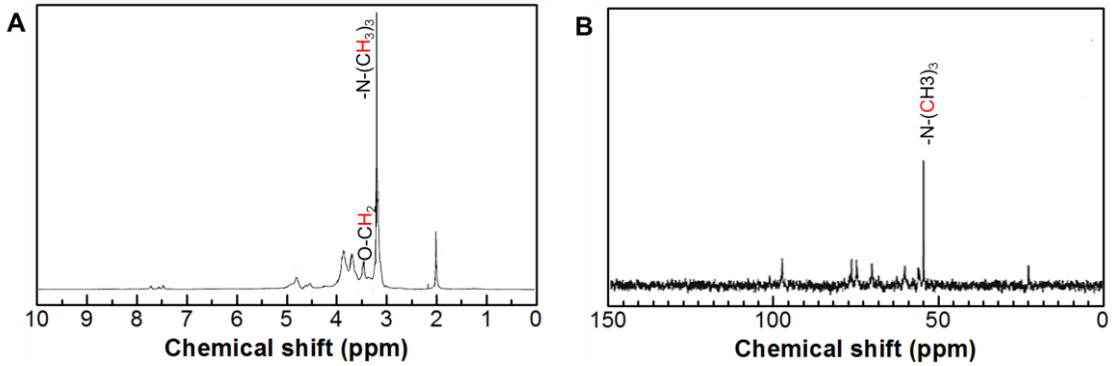

Figure 4.8. A) ^{1}H-RMN of *O*-HTCC; B) ^{13}C-RMN of *O*-HTCC.

4.3.3. Thermal analysis of chitosan and *O*-HTCC

Chitosan and *O*-HTCC were both characterize by thermogravimetric analysis for better understanding of the physical and chemical changes that may have occur in the polymer during synthesis. Thermogravimetric curves (sample weight % as a function of temperature) and its derivative

(DTA) are displayed in Figure 4.9. The chitosan degradation took place in two stages. The first stage occurred between 30 ºC to 130 ºC, which corresponds to a mass loss of 8.5% and is associated to water removal. The second stage started at 260 ºC and reached a maximum at 304 ºC, resulting in a mass loss of 50%. This stage is associated to a complex process including dehydration of saccharide rings, depolymerization, and decomposition of the acetylated units of polymer [105]. The remaining amount of product at 900 ºC was 29.1%.

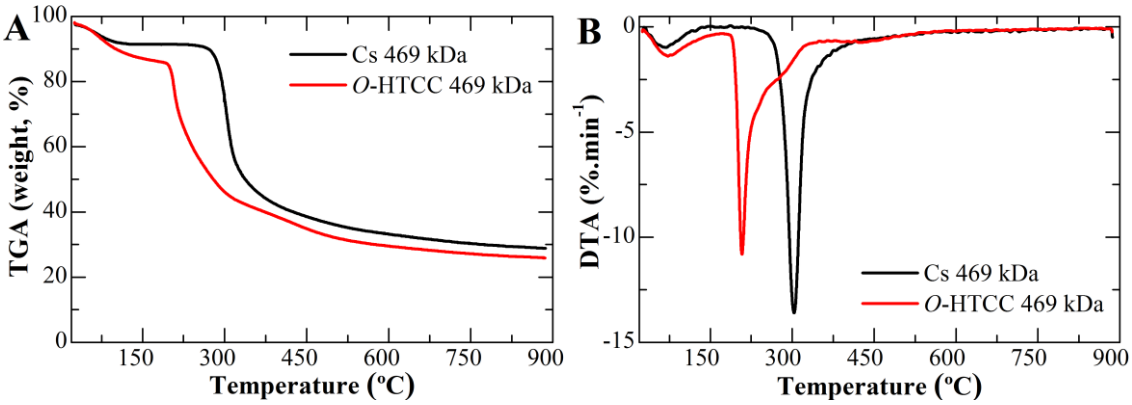

Figure 4.9. TGA and DTA of chitosan (CS 469 kDa) and *O*-HTCC 469 kDa.

Similarly, to chitosan, *O*-HTCC thermal degradation occurred in two steps. The first step that corresponds to the removal of water occurred from 30 ºC to 190 ºC with a weight loss of 14%. The second stage observed among the temperature as 190-300 ºC with a weight loss of 42.3%, corresponds to *O*-HTCC degradation. At 900 ºC the remained amount of product was 26%.

4.3.4. Preparation of CS and *O*-HTCC nanoparticles

There are several available methods to prepare chitosan NPs. In the present work a simple and rapid method was used, the ionotropic gelation technique. In this technique sodium tripolyphosphate (TPP) complexes with chitosan to form ionically cross-linked nanoparticles (Figure 4.10) [47, 57].

4.3.4.1. FTIR analysis

To confirm the ionic bonding between chitosan and TPP, FTIR measurements were performed. Figure 4.11 shows the FTIR spectra of chitosan, tripolyphosphate and chitosan nanoparticles produced by ionotropic gelation. Comparison of the FTIR spectra of chitosan NPs with the one of chitosan shows only small differences. The band at 3357 cm^{-1} becomes wider, indication that hydrogen bounding is enhanced. The band at 1587 cm^{-1} that corresponds to N-H bending vibration

disappears and a new band at 1536 cm^{-1} appears which may be attributed to N-O asymmetric stretching vibration mode [107]. These differences are consistent with the bonding between TPP and CS through the amino groups of chitosan.

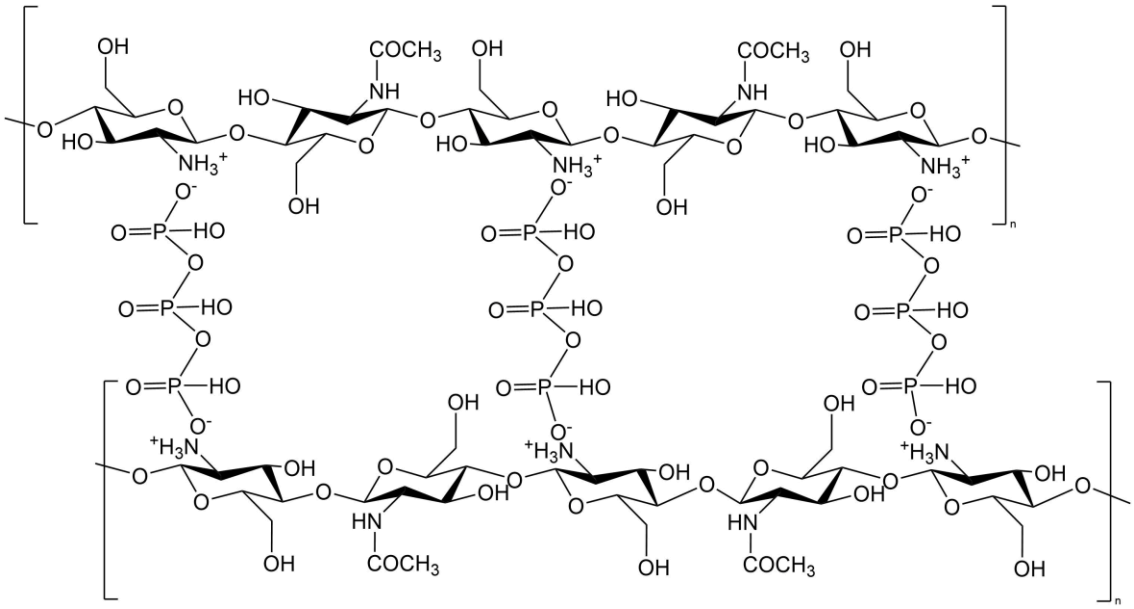

Figure 4.10. Schematic representation of the ionic interaction between chitosan and TPP.

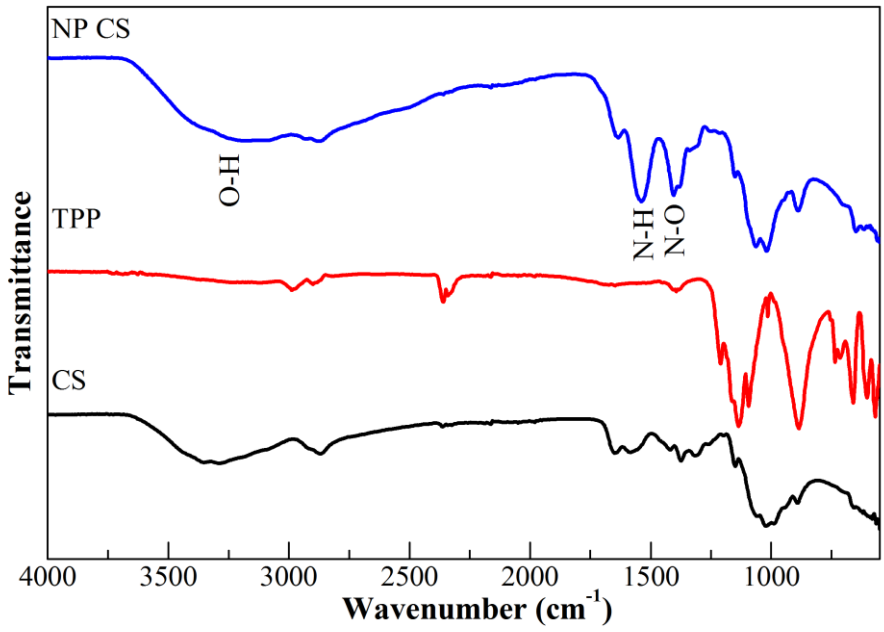

Figure 4.11. FTIR spectra of chitosan (CS), tripolyphosphate (TPP) and chitosan nanoparticles (NP CS).

4.3.4.2. Thermal analysis

Chitosan and *O*-HTCC nanoparticles were both characterized by thermogravimetric analysis for better understanding the physical and chemical changes that may have occurred in the polymer structure upon formation of the nanoparticles. Thermogravimetric curves (sample weight % as a function of temperature) and its derivative (DTA) are displayed in Figure 4.23. Similar to chitosan, chitosan nanoparticles degradation took place in two stages. The first stage occurred between 30 ºC to 160 ºC, corresponds to a mass loss of 20% that is associated with the removal of water. The second stage started at 230 ºC and continued up to 360 ºC, resulting in a mass loss of 32%. This stage is associated to polymer degradation. The remaining amount of product at 900 ºC was 31%. In the case of CS nanoparticles polymer degradation is softer, and starts earlier, around 120 ºC, possibly due to the presence of crosslinking agent, TPP, and their linkage breakage.

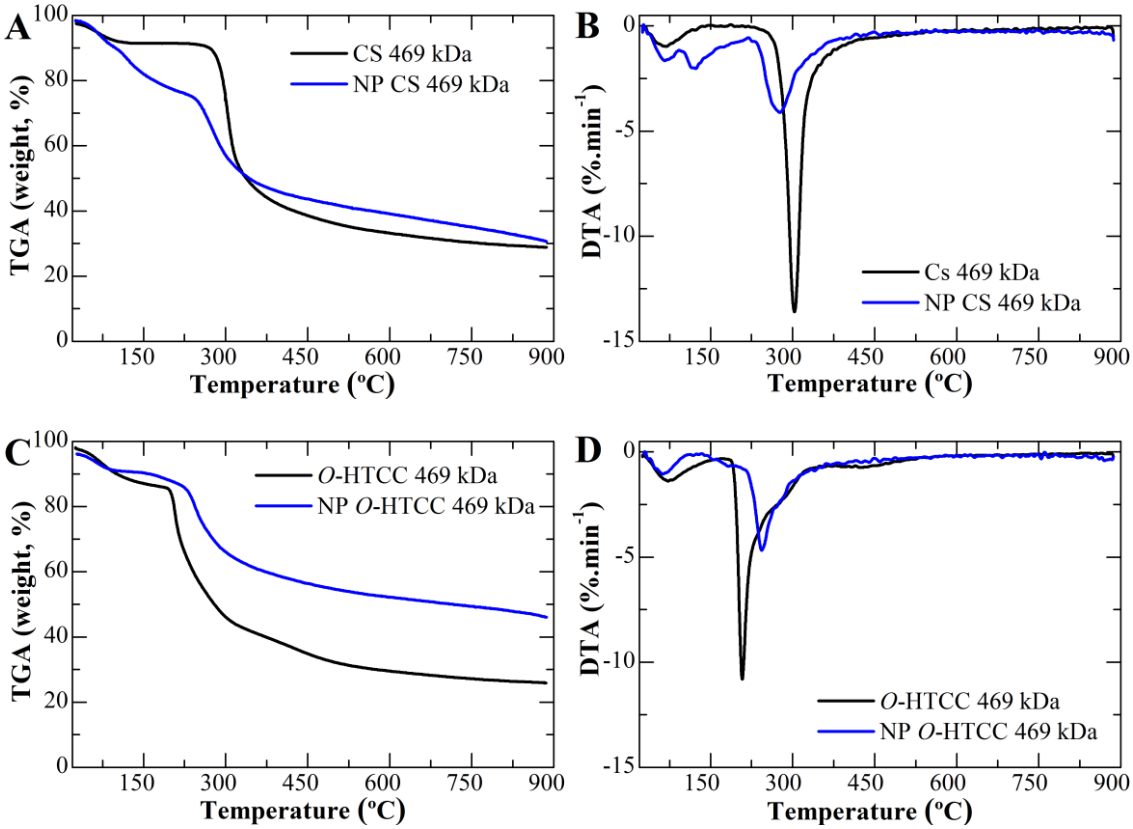

Figure 4.12. TGA (A, C) and DTA (B, D) of chitosan and chitosan nanoparticles, *O*-HTCC and *O*-HTCC nanoparticles, respectively.

Thermal degradation of *O*-HTCC nanoparticles (Figure 4.12 C and D) occurred also in two steps. The first step that corresponds to the removal of water occurred from 30 ºC to 120 ºC with a

weight loss of 9%. The second stage observed among the temperature as 200-330 ºC with a weight loss of 28%, corresponds to *O*-HTCC degradation. At 900 ºC the remained amount of product was 46%.

4.3.4.3. Dynamic light scattering studies

Ionic gelation is a rapid and simple technique to produce chitosan nanoparticles that is highly dependent upon experimental conditions. As a way to optimize the NPs production, an extensive dynamic light scattering study was performed.

Preliminary studies were performed to identify the range of concentrations that produced nanoparticles. Figure 4.13 shows the aspect of chitosan nanoparticles suspension with different TPP and chitosan concentrations. Chitosan solutions with 0.2 wt.% and 0.4 wt.% were prepared by dissolving the desired amount of chitosan in acetic acid 1% (v/v). Further, an equal volume of TPP solutions with different concentrations ranging from 0.05 wt.% to 0.4 wt.% was added to chitosan solution. Different aspects were found from the taken photographs. For smaller concentrations of TPP, a clear solution or an opalescent suspension is visible. Moreover, larger aggregates are formed when the initial concentration of TPP is higher.

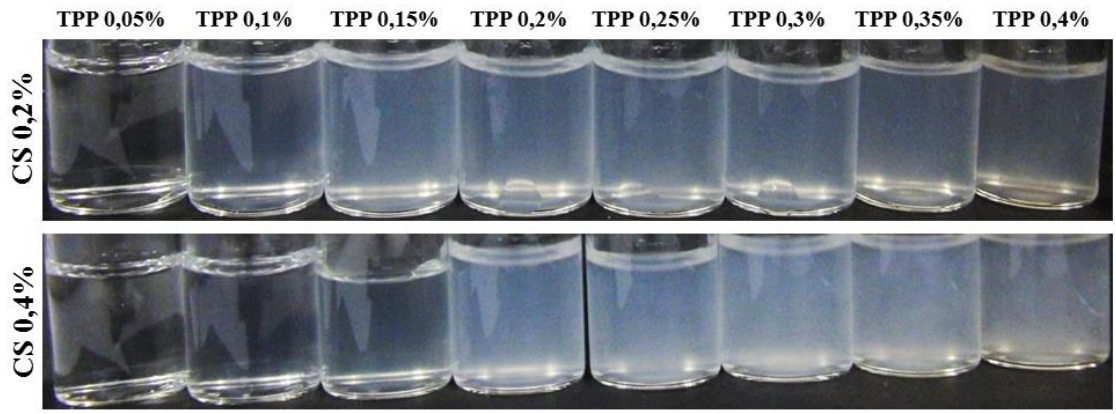

Figure 4.13. Photograph of chitosan nanoparticles prepared by ionotropic gelation using different concentrations of TPP and chitosan.

Based on these preliminary results the initial concentration of TPP selected was within the range of 0.05 wt.% to 0.15 wt.%, since for higher concentrations of TPP larger aggregates are produced. Therefore, in a first step of the dynamic light scattering study CS NPs were produced using chitosan with higher molecular weight, 469 kDa. The variable parameters were chitosan concentration and TPP concentration. At the same time, *O*-HTCC nanoparticles were produced and analyzed using the same conditions as the ones for chitosan.

Figure 4.14 shows the obtained results for the first step of the DLS study for CS and *O*-HTCC NPs. At a first glance, a huge difference in the hydrodynamic diameter can be observed between chitosan and *O*-HTCC NPs. Further, the increase in TPP concentration leads to nanoparticles with higher hydrodynamic diameters for almost all cases. The initial CS concentration of 0.2 wt.% seams to produce nanoparticles with smaller hydrodynamic diameters but for *O*-HTCC the opposite occurs: an initial *O*-HTCC concentration of 0.4 wt.% corresponds to smaller hydrodynamic diameters.

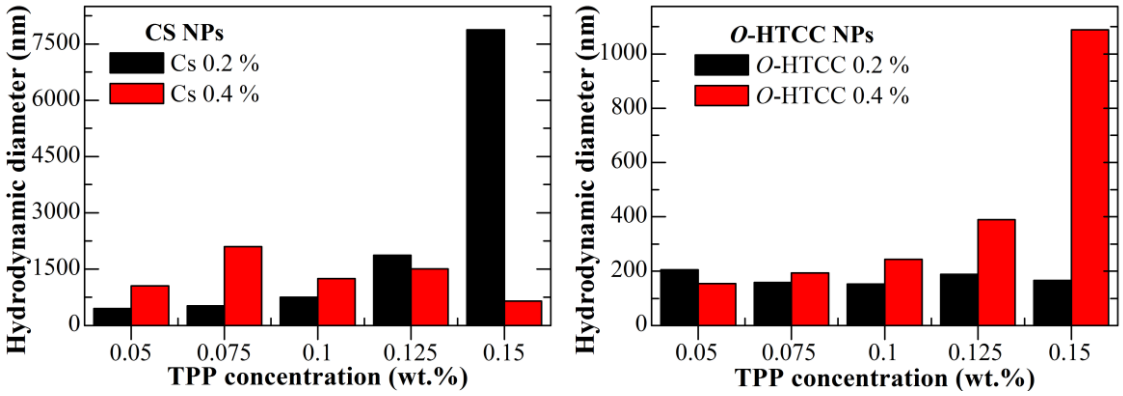

Figure 4.14. Results from the first step of the dynamic light scattering study for CS and *O*-HTCC NPs: hydrodynamic diameter as a function of TPP concentration (wt.%) for two different chitosan and *O*-HTCC concentrations.

Further steps were performed for a TPP concentration of 0.1% for both chitosan and *O*-HTCC nanoparticles production. Next, the ideal concentration of CS and *O*-HTCC for the formation of NPs was confirmed. For that, nanoparticles of either chitosan or *O*-HTCC were produced by changing the polymer concentration and molecular weight (Figure 4.15). Chitosan results show that within the tested range of chitosan molecular weight the obtained hydrodynamic diameter is smaller for nanoparticles produced with CS 0.2 wt.%. Similarly, *O*-HTCC of higher molecular weight produced smaller nanoparticles for an initial concentration of 0.2 wt.%. For the remaining molecular weights, no significant difference can be observed. That said, the remaining DLS study was performed using an initial polymer concentration of 0.2 wt.% for the production of both CS and *O*-HTCC NPs.

The effect of incubation time on the NPs hydrodynamic diameter was evaluated, by producing polymeric nanoparticles using an initial polymer concentration of 0.2 wt.% and TPP 0.1 wt.% (Figure 4.16). DLS measurements were performed immediately after NPs production, 24 h, and 48 h after NPs production. For almost all cases, no significant differences were found between

measurements. Only for nanoparticles produced with chitosan 469 kDa some differences were observed, as the NPs diameter increases with the increase of incubation time.

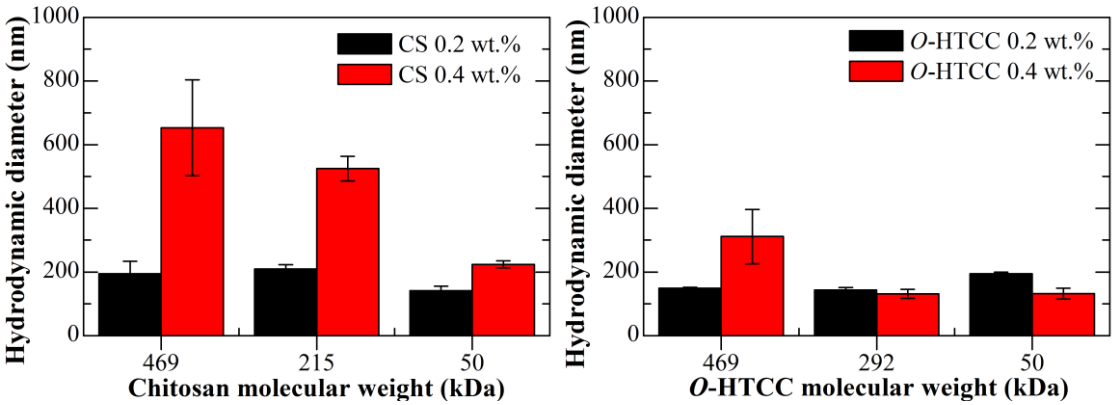

Figure 4.15. Hydrodynamic diameter of chitosan and *O*-HTCC nanoparticles produced with different polymer concentrations (0.2 and 0.4 wt.%) and molecular weight (469 – 50 kDa).

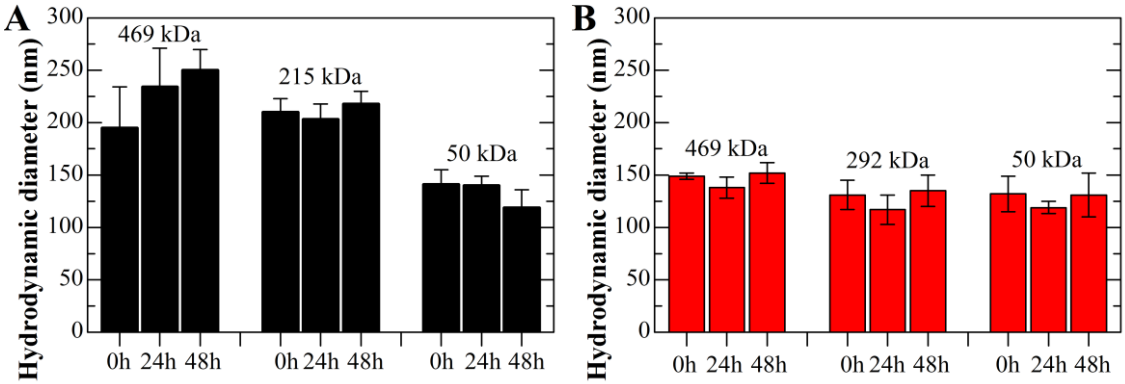

Figure 4.16. Hydrodynamic diameter of polymeric NPs produced using an initial CS (A) or *O*-HTCC (B) concentration of 0.2 wt.% and TPP 0.1 wt.% measured immediately, 24 h and 48 hours after NPs production.

Furthermore, the effect of two variables was accessed: the effect of stirring and the pH of TPP initial solution, by producing polymeric nanoparticles using polymers (CS and *O*-HTCC) with different molecular weights. To a known volume of polymeric solution, the same volume of TPP solution was added, with and without magnetic stirring. TPP solutions were prepared with a concentration of 0.1 wt.% and final pH was adjusted to 5, 9, and 13. Figure 4.17 shows the obtained results. Regarding the influence of the pH of TPP solution, in almost all cases no significant difference is observed between pH 5 and 9, except for the highest molecular weight. Moreover, in some cases pH 13 originates larger nanoparticles. Since no reasoned conclusion was found, TPP 0.1 wt.% was prepared without further adjustments, giving a final pH of about 8.8.

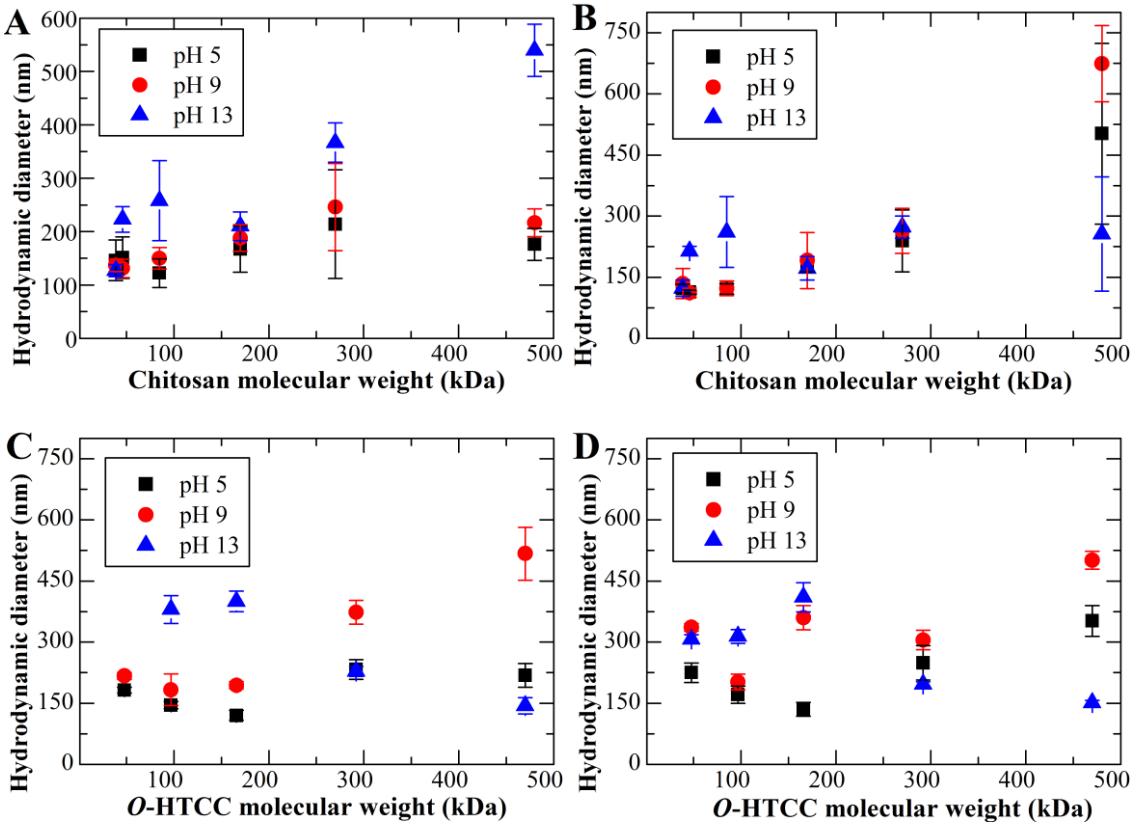

Figure 4.17. Influence of the pH of the initial solution of TPP and of stirring. Hydrodynamic diameter of CS and *O*-HTCC NPs produced (A, C) without and (B, D) with stirring as a function of polymer molecular weight.

Regarding the influence of magnetic stirring (Figure 4.17 B and D) again no significant difference was found. To analyze this issue, *O*-HTCC nanoparticles were subject to sonication for a few seconds and then again measured in DLS. Comparing the *O*-HTCC nanoparticles produced without stirring, with magnetic stirring and with sonication (Figure 4.18) it is clear that within the tested range of molecular weight sonication provides the means to obtain smaller *O*-HTCC nanoparticles. As such, for the next steps polymeric nanoparticles were prepared using sonication for a few seconds, to avoid the degradation of the polymeric chain.

To summarize, optimal conditions to produce both chitosan and *O*-HTCC conditions, under the tested ranges, are:

- Chitosan solution of 0.2 wt.% in acetic acid 1%;
- TPP solution of 0.1 wt.% in water;
- Incubation time has no influence in the hydrodynamic diameter, for almost all cases;
- TPP solution pH as prepared (around 8.8);
- Sonication for a few seconds.

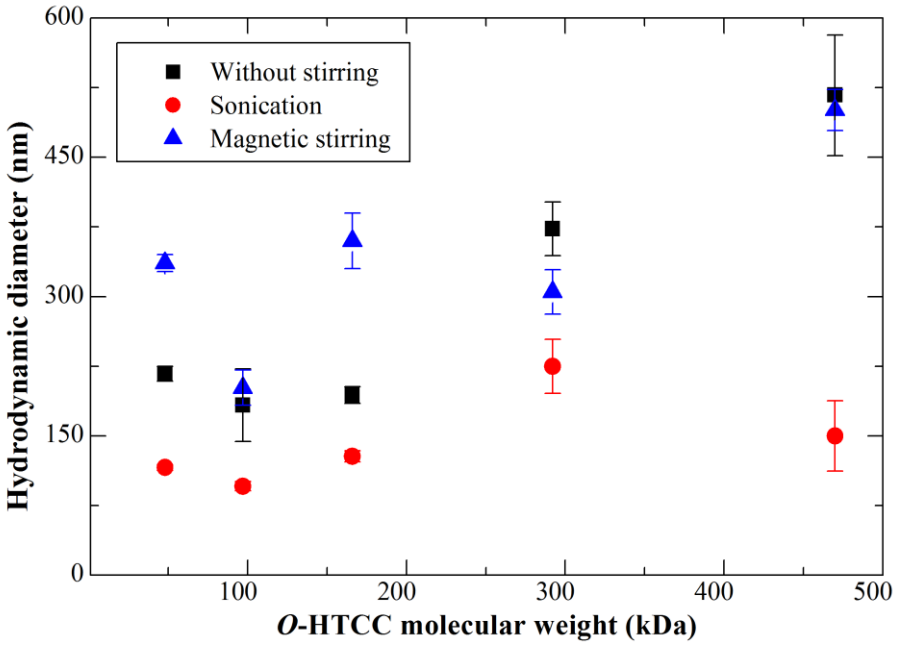

Figure 4.18. Hydrodynamic diameter of *O*-HTCC nanoparticles prepared without stirring, with magnetic stirring and with sonication.

Finally, the hydrodynamic diameter of chitosan and *O*-HTCC within the range of molecular weight tested was measured, and is presented in Figure 4.19. The produced polymeric nanoparticles have an average hydrodynamic diameter below 200 nm, even for the higher molecular weight tested (469 kDa). Comparison between chitosan and *O*-HTCC nanoparticles with similar molecular weight shows no significant differences in almost all cases.

4.3.4.1. Zeta potential measurement

Zeta potential measurements (Figure 4.20) were performed in diluted samples in a volume factor of 1:100, without further adjustment of pH. The final pH of the nanoparticles suspensions is slightly acidic, around 5-6. In both cases, polymeric nanoparticles show a positive zeta potential. Chitosan nanoparticles have a zeta potential above +30 mV that does not significantly change with the molecular weight. This means that the produced chitosan may be considered stable in aqueous suspensions [108].

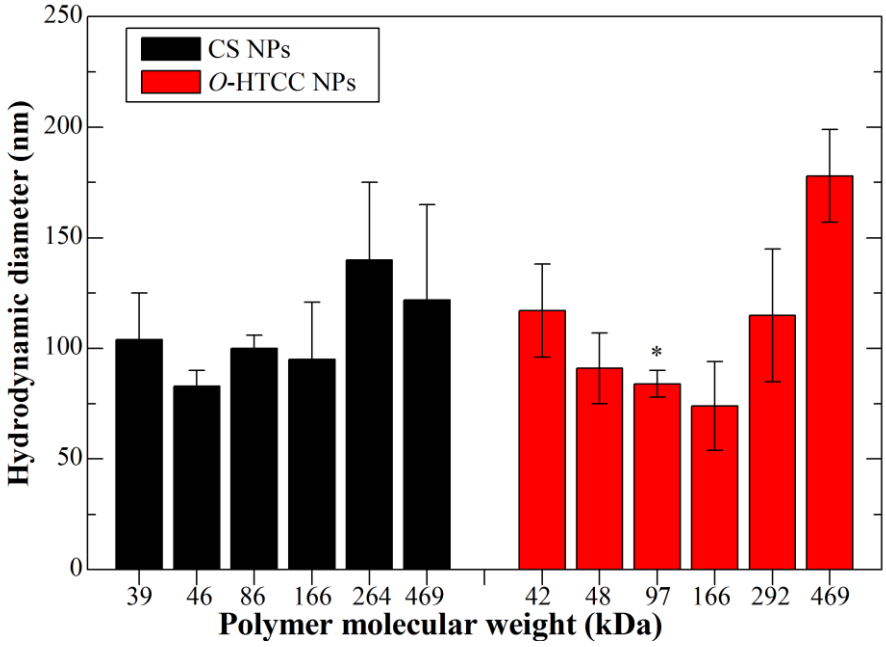

Figure 4.19. Hydrodynamic diameter of CS and *O*-HTCC NPs produced under optimal conditions as a function of the polymer molecular weight. The results are expressed as the average ± standard deviation for 3 independent experiments. *p<0.05 compared with chitosan nanoparticles with similar molecular weight.

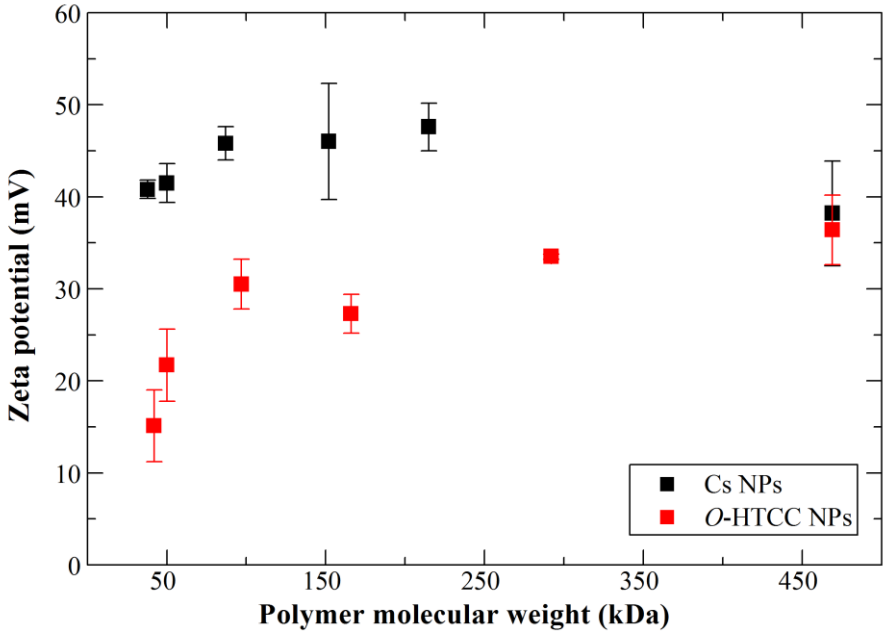

Figure 4.20. Zeta potential of chitosan and *O*-HTCC nanoparticles prepared under optimal conditions as a function of the polymer molecular weight. The results are expressed as the average ± standard deviation for 3 independent experiments.

4.3.5. Preparation of chitosan coated Fe_3O_4 nanoparticles

Chitosan is often used as a coating for Fe_3O_4 NPs for biomedical applications. Since the final purpose of this PhD thesis is to produce multifunctional NPs suitable for cancer theranostics, in this section the optimal conditions for CS-Fe_3O_4 NPs productions are studied.

Preparation of CS-Fe_3O_4 NPs was performed using the optimal conditions obtained for the preparation of Fe_3O_4 NPs and of chitosan NPs. Coating of chitosan was performed for two types of Fe_3O_4 NPs prepared in Chapter 3: pristine Fe_3O_4 and Fe_3O_4 TD. Unless state otherwise, the following studies were performed using chitosan with the highest molecular weight, 469 kDa.

4.3.5.1. Structure and physical characterization

FTIR measurements were performed to confirm the bonding between chitosan and iron oxide nanoparticles. Figure 4.21 shows the FTIR spectrum of chitosan coated Fe_3O_4 NPs in comparison to chitosan spectrum (NP CS) and the respective Fe_3O_4 sample.

FTIR spectrum of chitosan coated Fe_3O_4 NPs produced by chemical precipitation (Figure 4.21 A) is very similar to the one of chitosan coated Fe_3O_4 NPs produced by thermal decomposition (Figure 4.21 B). In both cases, typical bands of chitosan are present in the spectra, with the addition to the band at 560 cm^{-1} attributed to Fe-O stretching vibration mode.

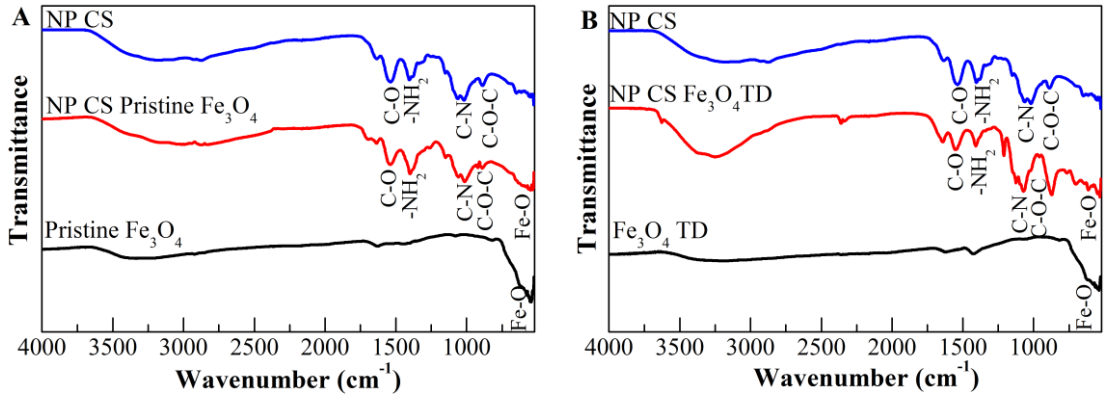

Figure 4.21. FTIR spectra of chitosan coated Fe_3O_4 NPs: A) chitosan conjugated with pristine Fe_3O_4 produced by chemical precipitation (NPs CS Fe_3O_4); B) chitosan conjugated with pristine Fe_3O_4 produced by thermal decomposition (NPs CS Fe_3O_4 TD).

XRD measurements were performed to analyze the structure and crystallinity of the samples. Figure 4.22 shows the XRD patterns obtained for pristine Fe_3O_4 NPs, chitosan and chitosan coated Fe_3O_4 NPs. The six characteristic peaks occurred at 30.1, 35.5, 43.2, 53.5, 57.0, and 62.8 and have been previously identified in Chapter 3 as the diffraction peaks of crystalline cubic magnetite

structure. The same diffraction peaks are present in the spectra of chitosan coated Fe_3O_4 NPs, indicating that the presence of chitosan does not change the crystalline phase of Fe_3O_4.

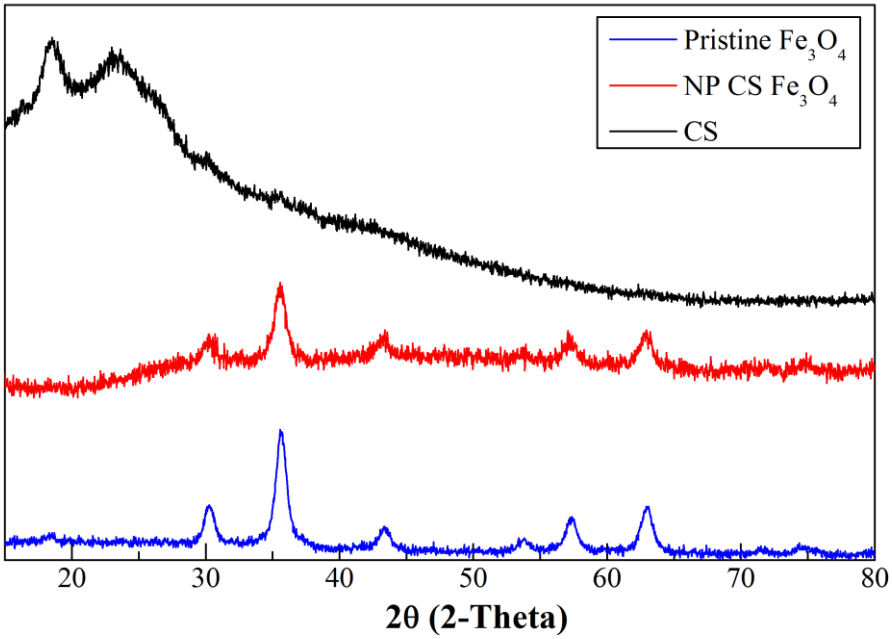

Figure 4.22. X-ray patterns of pristine Fe_3O_4 NPs, chitosan (CS), and chitosan coated Fe_3O_4 NPs (NP CS Fe_3O_4).

4.3.5.2. Thermal analysis

Chitosan-coated pristine Fe_3O_4 nanoparticles were characterized by thermogravimetric analysis for better understanding the physical and chemical changes that may have occurred in the polymer during coating. Thermogravimetric curves (sample weight % as a function of temperature) and its derivative (DTA) are displayed in Figure 4.23.

The degradation took place in two stages. The first stage occurred between 30 ºC to 160 ºC, corresponds to a mass loss of 21% that is associated with the removal of water. The second stage resulted in a mass loss of 24% correspondent to chitosan degradation between 210 ºC and 380 ºC. The remaining amount of product at 900 ºC was 27%. The remaining product of CS Fe_3O_4 NPs is inferior in percentage compared to chitosan nanoparticles. This seams contradictory to what was expected since Fe_3O_4 is not degraded within the tested range of temperature. However, it is important to consider that the total percentage of nanoparticles is not only composed of chitosan. As such, if the remaining amount is normalized taking into consideration the partial amount of chitosan, the remaining amount is composed of 3% of Fe_3O_4 nanoparticles. This means that chitosan was able to encapsulate 3% of Fe_3O_4 nanoparticles.

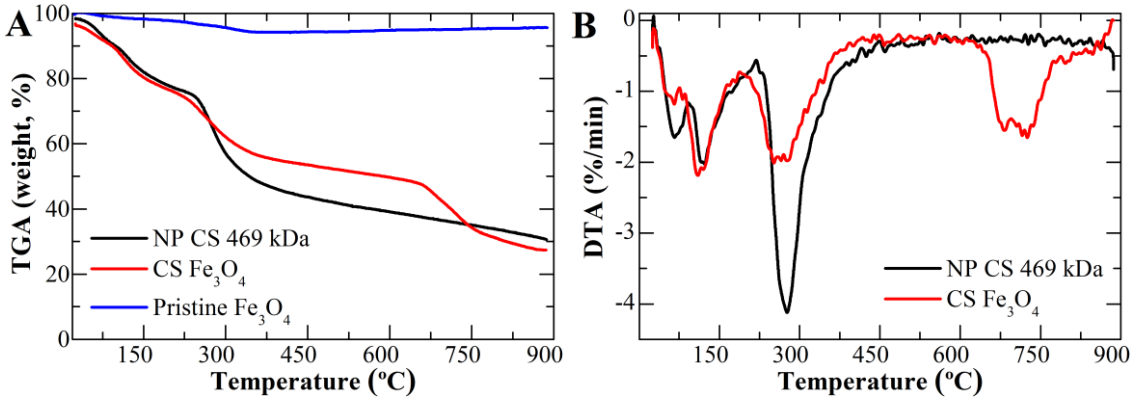

Figure 4.23. TGA and DTA of chitosan nanoparticles (NP CS), chitosan coated Fe_3O_4 NPs (CS Fe_3O_4) and pristine Fe_3O_4 nanoparticles produced by chemical precipitation.

4.3.5.3. Dynamic light scattering studies

Dynamic light scattering studies were performed to compare the differences in the hydrodynamic diameter between chitosan nanoparticles and chitosan coated Fe_3O_4 nanoparticles. Figure 4.24 displays the comparison between the hydrodynamic diameters of chitosan nanoparticles vs. chitosan coated Fe_3O_4 nanoparticles for the tested range of chitosan molecular weight.

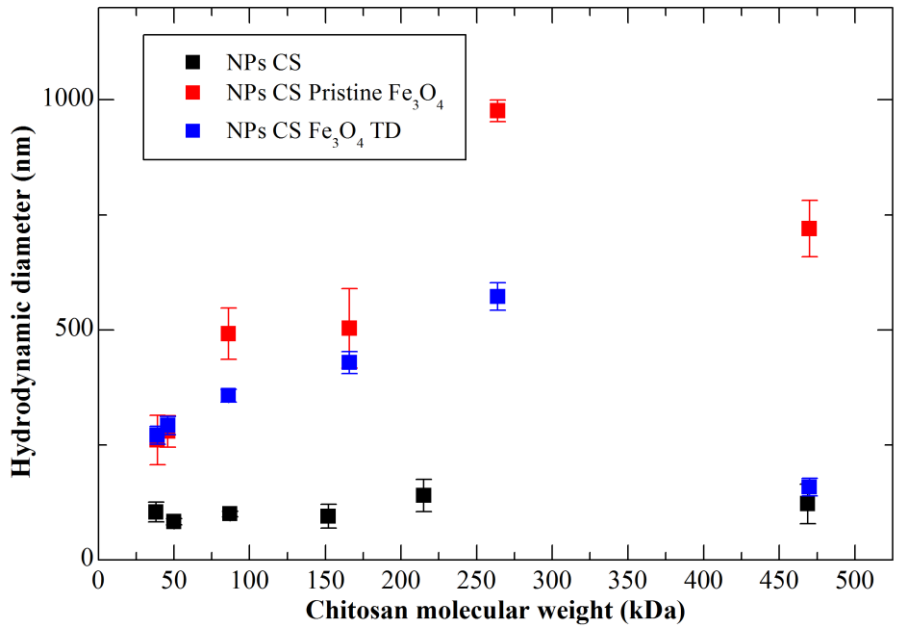

Figure 4.24. Hydrodynamic diameter of chitosan nanoparticles and chitosan coated pristine Fe_3O_4 and Fe_3O_4 TD nanoparticles as a function of chitosan molecular weight.

The results show that in general the hydrodynamic diameter of chitosan coated Fe_3O_4 NPs increases with the increase of chitosan molecular weight. However, for the highest molecular

weight, 469 kDa, the hydrodynamic diameter is significantly smaller in both cases. The difference between single chitosan NPs and chitosan Fe_3O_4 NPs is remarkable: chitosan coated Fe_3O_4 NPs have a much higher hydrodynamic diameter than chitosan nanoparticles but it is significantly reduced for CS Fe_3O_4 TD NPs of higher molecular weights. For the higher molecular weight, the hydrodynamic diameter is similar between chitosan and chitosan Fe_3O_4 TD NPs.

The observed differences between the obtained hydrodynamic diameter were analyzed by auto-correlation functions (ACF) of the two types of chitosan coated Fe_3O_4 NPs (Figure 4.25). Auto-correlation functions of chitosan coated pristine Fe_3O_4 NPs (Figure 4.25 A) show two different behaviors dependent on the molecular weight. For the three lowest molecular weights, the ACF curves show only one relaxation mode as a typical single-exponential relaxation. For higher molecular weight a slow relaxation mode is present, here attributed to very large aggregates of NPs, and contributes largely to the overall measurement. Moreover, the contribution of the slow relaxation mode increases with the increase of the molecular weight.

Autocorrelation functions of chitosan coated Fe_3O_4 TD NPs (Figure 4.25 B) show only one relaxation mode for all cases except for the highest molecular weight. A slow relaxation mode is present, here attributed to very large aggregates of NPs, and contributes largely to the overall measurement. Although the measured hydrodynamic diameter of the NPs is smaller, larger aggregates are present in this sample, which influences the obtained results.

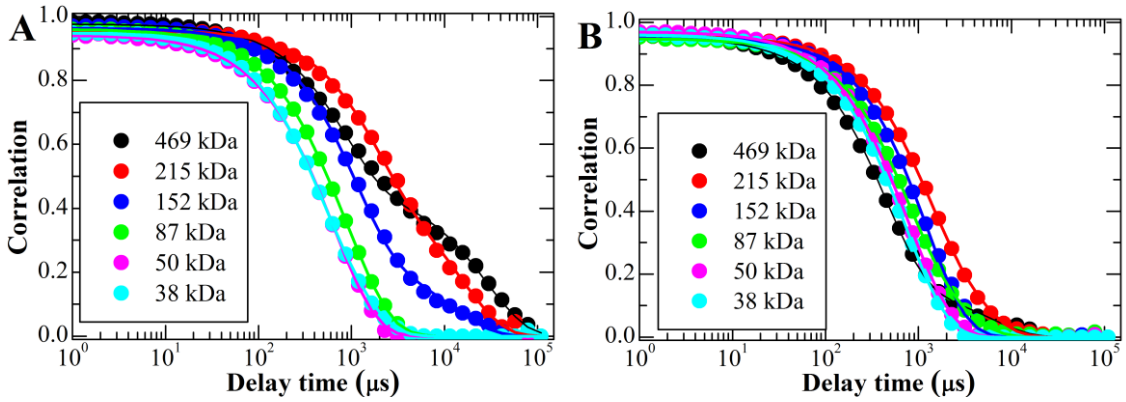

Figure 4.25. Comparison of measured (dots) and adjusted (lines) autocorrelation curves of dynamic light scattering measurements between (A) chitosan coated pristine Fe_3O_4 NPs and (B) chitosan coated Fe_3O_4 TD NPs.

The presence of larger aggregates in some samples may be attributed to chitosan chains that are not cross-linked to form nanoparticles. Consequently, the presence of such polymeric chains in

the solution causes scattering in DLS measurements represented as the slow relaxation modes in ACF curves.

4.3.5.4. SQUID measurements

DC magnetic measurements were performed to access the influence of chitosan in pristine iron oxide NPs magnetic properties. Magnetic saturation values are presented in emu per gram of the whole particle (magnetic and non-magnetic material). Pristine iron oxide NPs exhibit a saturation magnetization (M_S) of around 59 emu.g^{-1} at 320 K (see Chapter 3). When pristine Fe_3O_4 NPs are coated with either high or low molecular weight chitosan, M_S of the nanoparticles is greatly reduced to 18 and 29 emu.g^{-1}, respectively. Based on this difference, the reduction caused by chitosan seems to be dependent upon the polymer molecular weight. Figure 4.26 displays the zero-field cooled (ZFC) and field cooled (FC) and the magnetization versus applied magnetic field at 320 K results for chitosan of high (469 kDa) and low (38 kDa) molecular weights. Inset corresponds to the magnification of the same hysteresis loops.

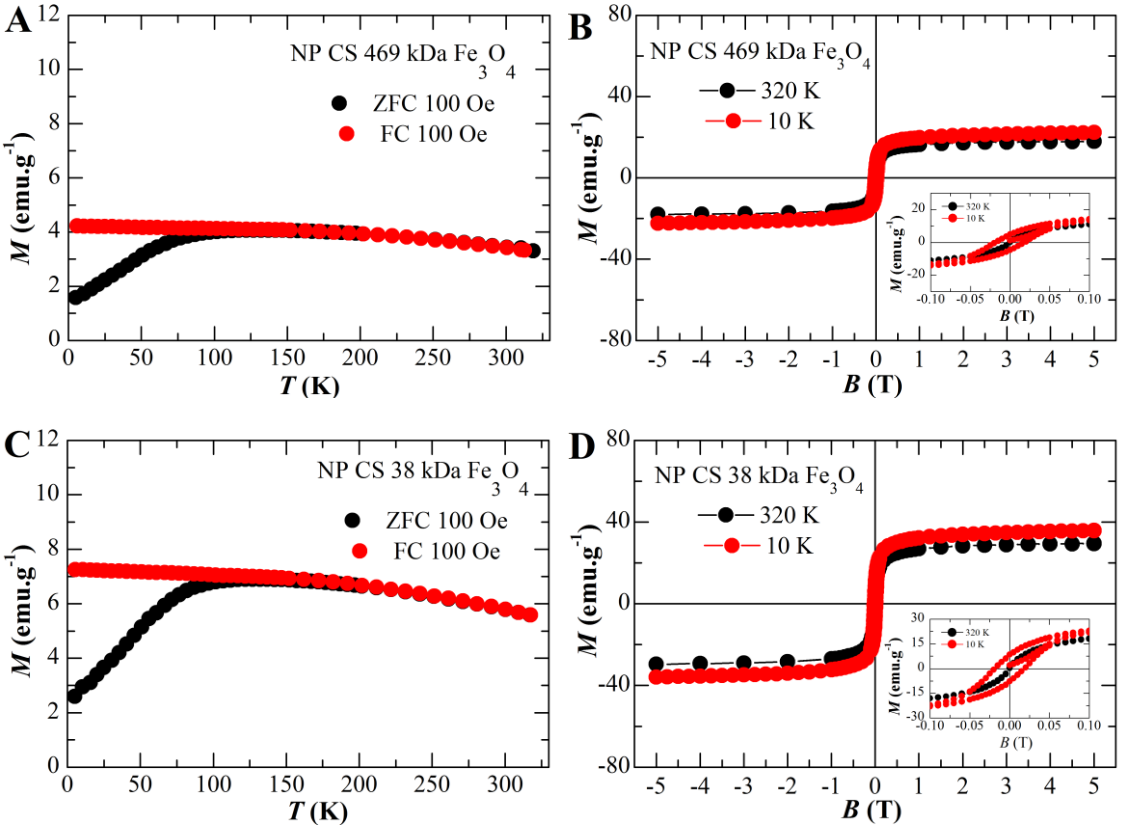

Figure 4.26. Magnetic characterization of chitosan coated pristine Fe_3O_4 nanoparticles (A) Zero-field cooled and field cooled results for chitosan of high molecular weight (469 kDa), (B) Magnetization vs. applied magnetic field at 320 K for chitosan of high molecular weight (469 kDa); (C) ZFC and FC results

for chitosan of low molecular weight (38 kDa); (D) Magnetization vs. applied magnetic field at 320 K for chitosan of low molecular weight (38 kDa).

For all cases it is evident the absence of coercivity and remanence at 320 K, which confirms the superparamagnetic behavior of all samples above the blocking temperature. Accordingly, it is possible to conclude that chitosan coating does not change the superparamagnetic behavior of the NP. However, with the chitosan molecular weight increase, the magnetic saturation of the NPs decreases, which may be attributed to surface effects, caused by the coating.

4.4. Summary

Chitosan is a derivative of chitin, the second most abundant biopolymer in nature, therefore is obtained from natural sources. Moreover, chitosan has profitable properties for biomedical applications, such as biodegradability, nontoxicity, antibacterial, and antifungal activity, and mucoadhesive properties. Due to the great range of beneficial properties, chitosan is used in a widely range of applications, from water treatments to agriculture, not forgetting the biomedical ones. This vast number of applications comes from one of the most interesting characteristic of chitosan that is a huge number of possible conjugations in the amine and hydroxyl free groups.

In this chapter, a detailed study of chitosan and its application in iron oxide NPs was performed. The chitosan was depolymerized starting from the available chitosan in the laboratory, which had a molecular weight of 469 kDa. Five new molecular weights were successfully obtained and applied in the synthesis of a chitosan derivative (*O*-HTCC), an ammonium quaternary derivative of chitosan that is soluble in a wide range of pH, contrary to what happens with chitosan that is soluble only in acidic pH (below pH 6). This derivative was synthetized starting from the high molecular weight chitosan and some of the depolymerized samples. Chitosan and *O*-HTCC were used to produce polymeric nanoparticles by ionic gelation method. The production of these nanoparticles was optimized to achieve an average diameter within the range of 100-200 nm for the overall molecular weights studied. After optimization of the reaction parameter, chitosan-coated Fe_3O_4 nanoparticles were produced by the same method and fully characterized.

Solubility (acidic pH) may limit chitosan's applications in the biomedical field. As such, several modifications performed in chitosan have the purpose to add moieties that provide the polymer solubility in a wide range of pH. Coupling of chitosan with GTMAC provides the desired polymer solubility in a wide range of pH. However, addition of GTMAC to chitosan without previous protection of the free amino groups leads to coupling in both -NH_2 and -OH groups. Since several

properties of chitosan depend upon the free amino groups, the -NH_2 groups were protected with previous treatment with benzaldehyde. Consequently, the final chitosan derivative maintains chitosan free amino groups and adds an ammonium quaternary moiety.

Polymeric nanoparticles were produced by using either chitosan or *O*-HTCC with different molecular weights. The chosen method for the polymeric NPs production was ionic gelation, a simple, rapid, and low cost method. Preliminary hydrodynamic measurements did not show the presence of nanoparticles, but microparticles instead. As such, to optimize the average hydrodynamic diameter and obtain a monodisperse sample, an extensive study was performed using dynamic light scattering. Dynamic light scattering was used as a comparison between samples and experimental conditions were optimizing in such a way to eliminate all possible artefacts. At the end of this extensive study, both chitosan and *O*-HTCC polymers produced nanoparticles with average diameters within the range of 100 to 200 nm and the molecular weight of the polymer has no remarkable influence to it. However, the higher molecular weight used (469 kDa) produced larger particles.

Zeta potential of the polymeric nanoparticles suspensions was measured and found to be positive in all cases. Furthermore, chitosan nanoparticles have a zeta potential above +30 mV that does not significantly change with the molecular weight. Consequently, the produced chitosan may be considered stable in aqueous suspensions.

Chitosan was used to coat Fe_3O_4 NPs produced by either chemical precipitation or thermal decomposition technique (Chapter 3). The samples were fully characterized to confirm the influence of the coating. DLS measurements show an increase of the hydrodynamic diameter when the iron oxide nanoparticles are coated with chitosan. To understand the observed difference in the hydrodynamic diameters, the autocorrelation functions were analyzed. Autocorrelation functions of chitosan coated pristine Fe_3O_4 NPs showed two different behaviors dependent on the molecular weight. For the three lowest molecular weights, the ACF curves show only one relaxation mode as a typical single-exponential relaxation. For higher molecular weight a slow relaxation mode is present, here attributed to very large aggregates of NPs, and contributes largely to the overall measurement. The contribution of the slow relaxation mode increases with the increase of the molecular weight and the presence of larger aggregates in some samples may be attributed to chitosan chains that are not cross-linked to form nanoparticles. Consequently, the presence of such polymeric chains in the solution causes scattering in DLS measurements represented as the slow relaxation modes in ACF curves.

In this chapter was demonstrated the possibility to produce chitosan, *O*-HTCC and polymer-Fe_3O_4 nanoparticles that are stable in aqueous medium. Polymeric nanoparticles are available in different molecular weights and have an average diameter suitable for drug delivery systems. Polymer-Fe_3O_4 NPs were able to maintain the superparamagnetic properties of the iron oxide core. The obtained NPs were fully characterized providing the basis to evaluate their potential in biomedical applications such as magnetic hyperthermia, drug delivery, and MR imaging contrast agents. Moreover, cytotoxicity evaluation and biomedical applications were further studied in Chapter 6 and Chapter 7.

4.5. References

1. M. Dash, F. Chiellini, R. M. Ottenbrite, E. Chiellini, Chitosan—A versatile semi-synthetic polymer in biomedical applications, Progress in Polymer Science, 36 (2011), 981-1014.

2. S. D. Ray, Potential aspects of chitosan as pharmaceutical excipient, Acta poloniae pharmaceutica, 68 (2011), 619-622.

3. C. Liu, Y. Tan, C. Liu, X. Chen, L. Yu, Preparations, characterizations and applications of chitosan-based nanoparticles, Journal of Ocean University of China, 6 (2007), 237-243.

4. K. S. K. S, R. A. K, S. Satyawan, Chitosan : A Platform for Targeted Drug Delivery, International Journal, 2 (2010), 2271-2282.

5. K. Vandevelde, P. Kiekens, Structure analysis and degree of substitution of chitin, chitosan and dibutyrylchitin by FT-IR spectroscopy and solid state C NMR, Carbohydrate Polymers, 58 (2004), 409-416.

6. F. Croisier, C. Jérôme, Chitosan-based biomaterials for tissue engineering, European Polymer Journal, 49 (2013), 780-792.

7. M. Rinaudo, Chitin and chitosan: Properties and applications, Progress in Polymer Science, 31 (2006), 603-632.

8. G.-J. Tsai, W.-H. Su, Antibacterial Activity of Shrimp Chitosan against Escherichia coli, Journal of Food Protection, 62 (1999), 239-243.

9. R. J. Pinto, S. C. Fernandes, C. S. Freire, P. Sadocco, J. Causio, C. P. Neto, T. Trindade, Antibacterial activity of optically transparent nanocomposite films based on chitosan or its derivatives and silver nanoparticles, Carbohydr Res, 348 (2012), 77-83.

10. L. Qi, Z. Xu, X. Jiang, C. Hu, X. Zou, Preparation and antibacterial activity of chitosan nanoparticles, Carbohydr Res, 339 (2004), 2693-2700.

11. Y. Qin, S. Liu, R. Xing, H. Yu, K. Li, X. Meng, R. Li, P. Li, Synthesis and characterization of dithiocarbamate chitosan derivatives with enhanced antifungal activity, Carbohydr Polym, 89 (2012), 388-393.

12. L. Y. Ing, N. M. Zin, A. Sarwar, H. Katas, Antifungal activity of chitosan nanoparticles and correlation with their physical properties, Int J Biomater, 2012 (2012), 632698.

13. Z. Guo, R. Xing, S. Liu, Z. Zhong, X. Ji, L. Wang, P. Li, Antifungal properties of Schiff bases of chitosan, N-substituted chitosan and quaternized chitosan, Carbohydr Res, 342 (2007), 1329-1332.

14. Z. Guo, R. Xing, S. Liu, Z. Zhong, X. Ji, L. Wang, P. Li, Antifungal properties of Schiff bases of chitosan, N-substituted chitosan and quaternized chitosan, Carbohydrate Research, 342 (2007), 1329-1332.

15. S. R. G. Sandri, M. C. Bonferoni, F. Ferrari, M. Mori, C. Caramella, The role of chitosan as a mucoadhesive agent in mucosal drug delivery, Journal of Drug Delivery Science and Technology, 22 (2012), 275-284.

16. K. Leithner, A. Bernkop-Schnürch, Chitosan and Derivatives for Biopharmaceutical Use: Mucoadhesive Properties, in: Chitosan-Based Systems for Biopharmaceuticals, John Wiley & Sons, Ltd, 2012, pp. 159-180.

17. I. A. Sogias, A. C. Williams, V. V. Khutoryanskiy, Chitosan-based mucoadhesive tablets for oral delivery of ibuprofen, Int J Pharm, 436 (2012), 602-610.

18. L. Guo, Z. Y. Zhao, J. Bai, S. Y. Han, X. Zhao, Preparation and Performance Evaluation of the Analgesic and Anti-Inflammatory Effects of Chitosan Composite Materials, Advanced Materials Research, 583 (2012), 171-174.

19. S. Huang, B. Han, K. Shao, M. Yu, W. Liu, Analgesis and wound healing effect of chitosan and carboxymethyl chitosan on scalded rats, Journal of Ocean University of China, 13 (2014), 837-841.

20. X. Huang, Y. Sun, J. Nie, W. Lu, L. Yang, Z. Zhang, H. Yin, Z. Wang, Q. Hu, Using absorbable chitosan hemostatic sponges as a promising surgical dressing, Int J Biol Macromol, 75 (2015), 322-329.

21. H. Xie, L. Lucchesi, J. S. Teach, R. Virmani, Long-term outcomes of a chitosan hemostatic dressing in laparoscopic partial nephrectomy, Journal of biomedical materials research. Part B, Applied biomaterials, 100 (2012), 432-436.

22. P. He, S. S. Davis, L. Illum, In vitro evaluation of the mucoadhesive properties of chitosan microspheres, International journal of pharmaceutics, 166 (1998), 75-88.

23. P.-J. Park, J.-Y. Je, W.-K. Jung, C.-B. Ahn, S.-K. Kim, Anticoagulant activity of heterochitosans and their oligosaccharide sulfates, Eur Food Res Technol, 219 (2004), 529-533.

24. A. Wan, Y. Sun, H. Li, Characterization of Novel Quaternary Chitosan Derivative Nanoparticles Loaded with Protein, Polymer, (2009).

25. Y. Sun, A. Wan, Preparation of Nanoparticles Composed of Chitosan and Its Derivatives as Delivery Systems for Macromolecules, Polymer, 105 (2007), 552-561.

26. M. Kong, X. G. Chen, K. Xing, H. J. Park, Antimicrobial properties of chitosan and mode of action: a state of the art review, Int J Food Microbiol, 144 (2010), 51-63.

27. K. Adibkia, Y. Javadzadeh, S. Dastmalchi, G. Mohammadi, F. K. Niri, M. Alaei-Beirami, Naproxen-eudragit RS100 nanoparticles: preparation and physicochemical characterization, Colloids Surf B Biointerfaces, 83 (2011), 155-159.

28. M. Kucharska, K. Walenko, B. Butruk, T. Brynk, M. Heljak, T. Ciach, Fabrication and characterization of chitosan microspheres agglomerated scaffolds for bone tissue engineering, Materials Letters, 64 (2010), 1059-1062.

29. S. Soenen, G. Velde, A. Ketkar-Atre, U. Himmelreich, M. Cuyper, Magnetoliposomes as magnetic resonance imaging contrast agents, WIREs Nanomedicine and Nanobiotechnology, 3 (2011), 197-211.

30. I. Y. Kim, S. J. Seo, H. S. Moon, M. K. Yoo, I. Y. Park, B. C. Kim, C. S. Cho, Chitosan and its derivatives for tissue engineering applications, Biotechnol Adv, 26 (2008), 1-21.

31. M. N. V. Ravi Kumar, A review of chitin and chitosan applications, Reactive and Functional Polymers, 46 (2000), 1-27.

32. S. C. Chen, Y. C. Wu, F. L. Mi, Y. H. Lin, L. C. Yu, H. W. Sung, A novel pH-sensitive hydrogel composed of N,O-carboxymethyl chitosan and alginate cross-linked by genipin for protein drug delivery, J Control Release, 96 (2004), 285-300.

33. A. Anitha, V. G. Deepagan, V. V. Divya Rani, D. Menon, S. V. Nair, R. Jayakumar, Preparation, characterization, in vitro drug release and biological studies of curcumin loaded dextran sulphate–chitosan nanoparticles, Carbohydrate Polymers, 84 (2011), 1158-1164.

34. X.-G. Chen, H.-J. Park, Chemical characteristics of O-carboxymethyl chitosans related to the preparation conditions, Carbohydrate Polymers, 53 (2003), 355-359.

35. A. Zhu, L. Yuan, T. Liao, Suspension of Fe(3)O(4) nanoparticles stabilized by chitosan and o-carboxymethylchitosan, Int J Pharm, 350 (2008), 361-368.

36. S. K. Sahu, S. K. Mallick, S. Santra, T. K. Maiti, S. K. Ghosh, P. Pramanik, In vitro evaluation of folic acid modified carboxymethyl chitosan nanoparticles loaded with doxorubicin for targeted delivery, J Mater Sci Mater Med, 21 (2010), 1587-1597.

37. P. Datta, S. Dhara, J. Chatterjee, Hydrogels and electrospun nanofibrous scaffolds of N-methylene phosphonic chitosan as bioinspired osteoconductive materials for bone grafting, Carbohydrate Polymers, 87 (2012), 1354-1362.

38. P. Dadhich, B. Das, S. Dhara, Microwave assisted rapid synthesis of N-methylene phosphonic chitosan via Mannich-type reaction, Carbohydrate Polymers, 133 (2015), 345-352.

39. Z.-G. Wang, J.-L. Zhang, D.-H. Sun, J.-Z. Ni, Novel Ti4+-chelated magnetic nanostructured affinity microspheres containing N-methylene phosphonic chitosan for highly selective enrichment and rapid separation of phosphopeptides, J. Mater. Chem. B, 2 (2014), 6886-6892.

40. K. Tian, Q. Du, C. Liao, F. Wei, N-Methylene phosphonic chitosan: a novel self-assembled template for enamel remineralization, Asian Pacific Journal of Microbiology Research, 1 (2013), 10.

41. M. George, T. E. Abraham, Polyionic hydrocolloids for the intestinal delivery of protein drugs: alginate and chitosan--a review, J Control Release, 114 (2006), 1-14.

42. Y. Xu, Y. Du, R. Huang, L. Gao, Preparation and modification of N-(2-hydroxyl) propyl-3-trimethyl ammonium chitosan chloride nanoparticle as a protein carrier, Biomaterials, 24 (2003), 5015-5022.

43. K. Kaminski, K. Szczubialka, K. Zazakowny, R. Lach, M. Nowakowska, Chitosan derivatives as novel potential heparin reversal agents, J Med Chem, 53 (2010), 4141-4147.

44. S. A. Agnihotri, N. N. Mallikarjuna, T. M. Aminabhavi, Recent advances on chitosan-based micro- and nanoparticles in drug delivery, J Control Release, 100 (2004), 5-28.

45. H. Zhang, M. Oh, C. Allen, E. Kumacheva, Monodisperse chitosan nanoparticles for mucosal drug delivery, Biomacromolecules, 5 (2004), 2461-2468.

46. Z. Amoozgar, J. Park, Q. Lin, Y. Yeo, Low molecular-weight chitosan as a pH-sensitive stealth coating for tumor-specific drug delivery, Mol Pharm, 9 (2012), 1262-1270.

47. R. Fernandez-Urrusuno, P. Calvo, C. Remunan-Lopez, J. L. Vila-Jato, M. J. Alonso, Enhancement of nasal absorption of insulin using chitosan nanoparticles, Pharm Res, 16 (1999), 1576-1581.

48. A. Vila, A. Sánchez, K. Janes, I. Behrens, T. Kissel, J. L. V. Jato, M. a. J. Alonso, Low molecular weight chitosan nanoparticles as new carriers for nasal vaccine delivery in mice, European journal of pharmaceutics and biopharmaceutics, 57 (2004), 123-131.

49. S. G. Kumbar, A. R. Kulkarni, M. Aminabhavi, Crosslinked chitosan microspheres for encapsulation of diclofenac sodium: effect of crosslinking agent, J Microencapsul, 19 (2002), 173-180.

50. Y. Ohya, M. Shiratani, H. Kobayashi, T. Ouchi, Release Behavior of 5-Fluorouracil from Chitosan-Gel Nanospheres Immobilizing 5-Fluorouracil Coated with Polysaccharides and Their Cell Specific Cytotoxicity, Journal of Macromolecular Science, Part A, 31 (1994), 629-642.

51. H. Jonassen, A. L. Kjoniksen, M. Hiorth, Stability of chitosan nanoparticles cross-linked with tripolyphosphate, Biomacromolecules, 13 (2012), 3747-3756.

52. J. Guan, P. Cheng, S. J. Huang, J. M. Wu, Z. H. Li, X. D. You, L. M. Hao, Y. Guo, R. X. Li, H. Zhang, Optimized preparation of levofloxacin-loaded chitosan nanoparticles by ionotropic gelation, Physics Procedia, 22 (2011), 163-169.

53. W. Fan, W. Yan, Z. Xu, H. Ni, Formation mechanism of monodisperse, low molecular weight chitosan nanoparticles by ionic gelation technique, Colloids Surf B Biointerfaces, 90 (2012), 21-27.

54. A. Rampino, M. Borgogna, P. Blasi, B. Bellich, A. Cesaro, Chitosan nanoparticles: preparation, size evolution and stability, Int J Pharm, 455 (2013), 219-228.

55. J. J. Wang, Z. W. Zeng, R. Z. Xiao, T. Xie, G. L. Zhou, X. R. Zhan, S. L. Wang, Recent advances of chitosan nanoparticles as drug carriers, Int J Nanomedicine, 6 (2011), 765-774.

56. R. Bodmeier, K.-H. Oh, Y. Pramar, Preparation and Evaluation Of Drug-Containing Chitosan Beads, Drug Development and Industrial Pharmacy, 15 (1989), 1475-1494.

57. P. Calvo, C. Remuñan-López, J. L. Vila-Jato, M. J. Alonso, in: Pharmaceutical research, 1997, pp. 1431-1436.

58. B. N. Estevinho, F. Rocha, L. Santos, A. Alves, Microencapsulation with chitosan by spray drying for industry applications – A review, Trends in Food Science & Technology, 31 (2013), 138-155.

59. T. Banerjee, S. Mitra, A. Kumar Singh, R. Kumar Sharma, A. Maitra, Preparation, characterization and biodistribution of ultrafine chitosan nanoparticles, International journal of pharmaceutics, 243 (2002), 93-105.

60. S. Mitra, U. Gaur, P. C. Ghosh, A. N. Maitra, Tumour targeted delivery of encapsulated dextran-doxorubicin conjugate using chitosan nanoparticles as carrier, J Control Release, 74 (2001), 317-323.

61. Y. Hu, X. Jiang, Y. Ding, H. Ge, Y. Yuan, C. Yang, Synthesis and characterization of chitosan-poly(acrylic acid) nanoparticles, Biomaterials, 23 (2002), 3193-3201.

62. N. Davidenko, M. D. Blanco, C. Peniche, L. Becherán, S. Guerrero, J. M. Teijón, Effects of different parameters on the characteristics of chitosan-poly(acrylic acid) nanoparticles obtained by the method of coacervation, Journal of Applied Polymer Science, 111 (2009), 2362-2371.

63. M. Thanou, J. C. Verhoef, H. E. Junginger, Oral drug absorption enhancement by chitosan and its derivatives, Adv Drug Deliv Rev, 52 (2001), 117-126.

64. L. Ilium, Chitosan and Its Use as a Pharmaceutical Excipient, Pharmaceutical research, 15 (1998), 1326-1331.

65. I. Wedmore, J. G. McManus, A. E. Pusateri, J. B. Holcomb, A special report on the chitosan-based hemostatic dressing: experience in current combat operations, The Journal of trauma, 60 (2006), 655-658.

66. T. Kean, M. Thanou, Biodegradation, biodistribution and toxicity of chitosan, Adv Drug Deliv Rev, 62 (2010), 3-11.

67. N. G. Schipper, K. M. Varum, P. Artursson, Chitosans as absorption enhancers for poorly absorbable drugs. 1: Influence of molecular weight and degree of acetylation on drug transport across human intestinal epithelial (Caco-2) cells, Pharm Res, 13 (1996), 1686-1692.

68. N. G. M. Schipper, K. M. Vårum, P. Stenberg, G. Ocklind, H. Lennernäs, P. Artursson, Chitosans as absorption enhancers of poorly absorbable drugs, European Journal of Pharmaceutical Sciences, 8 (1999), 335-343.

69. S. Richardson, Potential of low molecular mass chitosan as a DNA delivery system: biocompatibility, body distribution and ability to complex and protect DNA, International journal of pharmaceutics, 178 (1999), 231-243.

70. C. Zhang, G. Qu, Y. Sun, X. Wu, Z. Yao, Q. Guo, Q. Ding, S. Yuan, Z. Shen, Q. Ping, H. Zhou, Pharmacokinetics, biodistribution, efficacy and safety of N-octyl-O-sulfate chitosan micelles loaded with paclitaxel, Biomaterials, 29 (2008), 1233-1241.

71. T. Kean, S. Roth, M. Thanou, Trimethylated chitosans as non-viral gene delivery vectors: cytotoxicity and transfection efficiency, J Control Release, 103 (2005), 643-653.

72. L. Baruch, M. Machluf, Alginate-chitosan complex coacervation for cell encapsulation: effect on mechanical properties and on long-term viability, Biopolymers, 82 (2006), 570-579.

73. M. Jumaa, F. H. Furkert, B. W. Müller, A new lipid emulsion formulation with high antimicrobial efficacy using chitosan, European journal of pharmaceutics and biopharmaceutics, 53 (2002), 115-123.

74. Z. Guo, R. Chen, R. Xing, S. Liu, H. Yu, P. Wang, C. Li, P. Li, Novel derivatives of chitosan and their antifungal activities in vitro, Carbohydr Res, 341 (2006), 351-354.

75. G. Pujals, J. M. Sune-Negre, P. Perez, E. Garcia, M. Portus, J. R. Tico, M. Minarro, J. Carrio, In vitro evaluation of the effectiveness and cytotoxicity of meglumine antimoniate microspheres produced by spray drying against Leishmania infantum, Parasitology research, 102 (2008), 1243-1247.

76. S. Hirano, M. Iwata, K. Yamanaka, H. Tanaka, T. Toda, H. Inui, Enhancement of Serum Lysozyme Activity by Injecting a Mixture of Chitosan Oligosaccharides Intravenously in Rabbits, Agricultural and Biological Chemistry, 55 (1991), 2623-2625.

77. S. B. Rao, C. P. Sharma, Use of chitosan as a biomaterial: studies on its safety and hemostatic potential, J Biomed Mater Res, 34 (1997), 21-28.

78. T. Banerjee, S. Mitra, A. Kumar Singh, R. Kumar Sharma, A. Maitra, Preparation, characterization and biodistribution of ultrafine chitosan nanoparticles, Int J Pharm, 243 (2002), 93-105.

79. M. D. Gades, J. S. Stern, Chitosan supplementation and fecal fat excretion in men, Obesity research, 11 (2003), 683-688.

80. K. Arai, T. Kinumaki, T. Fujita, Toxicity of chitosan, Bull. Tokai Reg. Fish. Res. Lab., 56 (1968), 89-94.

81. K. Sonaje, Y. H. Lin, J. H. Juang, S. P. Wey, C. T. Chen, H. W. Sung, In vivo evaluation of safety and efficacy of self-assembled nanoparticles for oral insulin delivery, Biomaterials, 30 (2009), 2329-2339.

82. F. Zheng, X. W. Shi, G. F. Yang, L. L. Gong, H. Y. Yuan, Y. J. Cui, Y. Wang, Y. M. Du, Y. Li, Chitosan nanoparticle as gene therapy vector via gastrointestinal mucosa administration: results of an in vitro and in vivo study, Life Sci, 80 (2007), 388-396.

83. N. Langoth, H. Kahlbacher, G. Schoffmann, I. Schmerold, M. Schuh, S. Franz, P. Kurka, A. Bernkop-Schnurch, Thiolated chitosans: design and in vivo evaluation of a mucoadhesive buccal peptide drug delivery system, Pharm Res, 23 (2006), 573-579.

84. P. Mukhopadhyay, S. Bhattacharya, A. Nandy, A. Bhattacharyya, R. Mishra, P. P. Kundu, Assessment of in vivo chronic toxicity of chitosan and its derivates used as oral insulin carriers, Toxicol. Res., 4 (2015), 281-290.

85. L. Illum, N. F. Farraj, S. S. Davis, Chitosan as a Novel Nasal Delivery System for Peptide Drugs, Pharmaceutical research, 11 (1994), 1186-1189.

86. C. Alemdaroglu, Z. Degim, N. Celebi, F. Zor, S. Ozturk, D. Erdogan, An investigation on burn wound healing in rats with chitosan gel formulation containing epidermal growth factor, Burns, 32 (2006), 319-327.

87. C. J. Park, S. G. Clark, C. A. Lichtensteiger, R. D. Jamison, A. J. Johnson, Accelerated wound closure of pressure ulcers in aged mice by chitosan scaffolds with and without bFGF, Acta Biomater, 5 (2009), 1926-1936.

88. T. Takei, H. Nakahara, H. Ijima, K. Kawakami, Synthesis of a chitosan derivative soluble at neutral pH and gellable by freeze-thawing, and its application in wound care, Acta Biomater, 8 (2012), 686-693.

89. Y. Zhang, M. Ni, M. Zhang, B. Ratner, Calcium phosphate-chitosan composite scaffolds for bone tissue engineering, Tissue engineering, 9 (2003), 337-345.

90. L. Qin, L. Dichen, J. Zhongmin, W. Jue, L. Aimin, W. Zhen, Fabrication and In Vitro Evaluation of Calcium Phosphate Combined with Chitosan Fibers for Scaffold Structures, Journal of Bioactive and Compatible Polymers, 24 (2009), 113-124.

91. T. H. Ang, F. S. A. Sultana, D. W. Hutmacher, Y. S. Wong, J. Y. H. Fuh, X. M. Mo, H. T. Loh, E. Burdet, S. H. Teoh, Fabrication of 3D chitosan–hydroxyapatite scaffolds using a robotic dispensing system, Materials Science and Engineering: C, 20 (2002), 35-42.

92. A. Lahiji, A. Sohrabi, D. S. Hungerford, C. G. Frondoza, Chitosan supports the expression of extracellular matrix proteins in human osteoblasts and chondrocytes, J Biomed Mater Res, 51 (2000), 586-595.

93. J. Li, J. Pan, L. Zhang, X. Guo, Y. Yu, Culture of primary rat hepatocytes within porous chitosan scaffolds, Journal of biomedical materials research. Part A, 67 (2003), 938-943.

94. X. H. Wang, D. P. Li, W. J. Wang, Q. L. Feng, F. Z. Cui, Y. X. Xu, X. H. Song, M. van der Werf, Crosslinked collagen/chitosan matrix for artificial livers, Biomaterials, 24 (2003), 3213-3220.

95. Y. Yuan, P. Zhang, Y. Yang, X. Wang, X. Gu, The interaction of Schwann cells with chitosan membranes and fibers in vitro, Biomaterials, 25 (2004), 4273-4278.

96. A. Matsuda, H. Kobayashi, S. Itoh, K. Kataoka, J. Tanaka, Immobilization of laminin peptide in molecularly aligned chitosan by covalent bonding, Biomaterials, 26 (2005), 2273-2279.

97. M. Huang, E. Khor, L.-Y. Lim, Uptake and cytotoxicity of chitosan molecules and nanoparticles: effects of molecular weight and degree of deacetylation, Pharmaceutical research, 21 (2004), 344-353.

98. M. R. Kassai, Calculation of Mark-Houwink-Sakurada (MHS) equation viscometric constants for chitosan in any solvent-temperature system using experimental reported viscometric constants data, Carbohydrate polymers, 68 (2007), 477-488.

99. F. Wang, J. Yao, M. Russel, H. Chen, K. Chen, Y. Zhou, B. Ceccanti, G. Zaray, M. M. F. Choi, Development and analytical application of a glucose biosensor based on glucose oxidase/O-(2-hydroxyl)propyl-3-trimethylammonium chitosan chloride nanoparticle-immobilized onion inner epidermis, Biosensors & bioelectronics, 25 (2010), 2238-2243.

100. P. Calvo, C. Remuñan-López, J. L. Vila-Jato, M. J. Alonso, in: Pharmaceutical research, 1997, pp. 1431-1436.

101. M. Talelli, C. J. Rijcken, T. Lammers, P. R. Seevinck, G. Storm, C. F. van Nostrum, W. E. Hennink, Superparamagnetic iron oxide nanoparticles encapsulated in biodegradable thermosensitive polymeric micelles: toward a targeted nanomedicine suitable for image-guided drug delivery, Langmuir, 25 (2009), 2060-2067.

102. D. P. Chattopadhyay, M. S. Inamdar, Aqueous Behaviour of Chitosan, International Journal of Polymer Science, 2010 (2010), 1-7.

103. J. Kumirska, M. Czerwicka, Z. Kaczynski, A. Bychowska, K. Brzozowski, J. Thoming, P. Stepnowski, Application of spectroscopic methods for structural analysis of chitin and chitosan, Mar Drugs, 8 (2010), 1567-1636.

104. M. R. Kasaai, Calculation of Mark–Houwink–Sakurada (MHS) equation viscometric constants for chitosan in any solvent–temperature system using experimental reported viscometric constants data, Carbohydrate Polymers, 68 (2007), 477-488.

105. N. Kocak, M. Sahin, G. Arslan, H. I. Ucan, Synthesis of Crosslinked Chitosan Possessing Schiff Base and Its Use in Metal Removal, J Inorg Organomet P, 22 (2011), 166-177.

106. V. A. Spinelli, M. C. M. Laranjeira, V. T. Fávere, Preparation and characterization of quaternary chitosan salt: adsorption equilibrium of chromium(VI) ion, Reactive and Functional Polymers, 61 (2004), 347-352.

107. Y. Wu, W. Yang, C. Wang, J. Hu, S. Fu, Chitosan nanoparticles as a novel delivery system for ammonium glycyrrhizinate, Int J Pharm, 295 (2005), 235-245.

108. V. Tandon, S. K. Bhagavatula, W. C. Nelson, B. J. Kirby, Zeta potential and electroosmotic mobility in microfluidic devices fabricated from hydrophobic polymers: 1. The origins of charge, ELECTROPHORESIS, 29 (2008), 1092-1101.

Chapter 5. Monoclonal antibody production

This chapter is related to the production of the targeted part of the theranostic system developed in this PhD thesis. The chapter starts with a review of some basic concepts related to monoclonal antibodies and their production. A special attention is given to carbonic anhydrase IX, the specific antigen of cancer cells. Following, the methods used for the production of the monoclonal antibody, and the main results obtained are presented and discussed.

5.1. Introduction

According to the National Cancer Institute, biological therapy is "a type of treatment that uses substances made from living organisms to treat disease" [1]. Biological therapy is also called biotherapy, immunotherapy, or biological response modifier therapy. Biological therapies are mechanistically dependent upon tumor–host interaction and use the body's immune system, either directly or indirectly, supressing or stimulating the immune system to fight cancer, infection, and other diseases. The increasing use of molecular biological techniques continues to improve the understanding of the pathophysiology of cancer, with the associated definition of potential therapeutic targets [2].

Biological therapies include immunotherapy, which uses immune-related agents, such as cytokines, cellular or humoral products, some antibodies, and vaccines. Gene therapy and some targeted therapies are also considered biological therapies [3].

5.1.1. Monoclonal antibodies

Paul Ehrlich, the German physician and scientist winner of the Nobel Prize in Physiology or Medicine in 1908 for its contributions in immunology, popularized the concept of a "magic bullet". This concept emerged from the idea of having a compound that selectively target and kill a specific disease-causing organism. Antibodies fit in perfectly into this concept, as they are specific target agents [4].

5.1.1.1. Antibody composition

Antibodies, or immunoglobulins, are proteins produced by the immune system in response to foreign molecules. Each antibody binds to a particular target molecule, an antigen, with remarkable specificity. All antibody molecules share the same basic structural characteristics but display remarkable variability in the regions that bind antigens. An antibody is composed of four polypeptide chains: two identical light chains (220 amino acids) and two identical heavy chains (300-400 amino acids). These chains are bounded through disulfide bonds and non-covalent bonds to compose a Y-shape molecule. Both heavy chains and light chains consist of amino-terminal variable (V) regions that participate in antigen recognition and carboxy-terminal constant (C) regions; the C regions of heavy chains mediate effector functions. In the heavy chains, V region is composed of one Ig domain, and C region is composed of three or four Ig domains. Each light chain is composed of one V region Ig domain and one C region Ig domain. The peptide sequence of the NH_2 extremity of these chains determines the specificity of the antibody to a certain antigen and specific of the antibody (variable domain). This region determines the antibody idiotype, i.e., the site of specific bounding. The remaining domains (constant domains) exist in a specific number of forms: two types for the light chains (α and κ) and five types for the heavy chains (μ, δ, γ, ε and α). The latter determines the classification of the immunoglobulin into one of the five existent classes (or isotypes) in Mammalian: IgM, IgD, IgG, IgE, and IgA [5-7].

The most commonly used immunoglobulin form is IgG. IgG (Figure 5.1) have two binding 'arms', the variable domains of the light chain (V_L) and of the heavy chains (V_H). Antibodies are composed of three functional units: two Fab (fragment antigen binding) units and one Fc (fragment crystallizable) unit. The Fab unit is located in the NH_2 terminal and is composed of by variable region of the light chain and the heavy chain. Antibody-binding specificity is encoded by three complementary determining regions (CDRs), while Fc-region is responsible for binding to some proteins (complement) or cells [8, 9].

An antibody itself does not kill target cells; instead, two possibilities can occur. The antibody can mark the target cell for other components or effector cells of the body. This mechanism in named

antibody dependent complement mediated cytotoxicity (CMC). The alternative occurs when the antibody initiates signaling mechanisms in the targeted cell that leads to self-destruction. The latter mechanism is named antibody dependent cellular toxicity (ADCC). CMC mechanism occurs when IgGs are in close proximity to each other, activating a cascade of complement proteins. The outcome is either cell lysis or attraction of other immune cells to this location for effector cell function. On the other hand, ADCC mechanism requires the recognition of the antibody by immune cells that engage the antibody-marked cells. In this case, cell death is caused by either direct action or through the recruitment of other cell types [9].

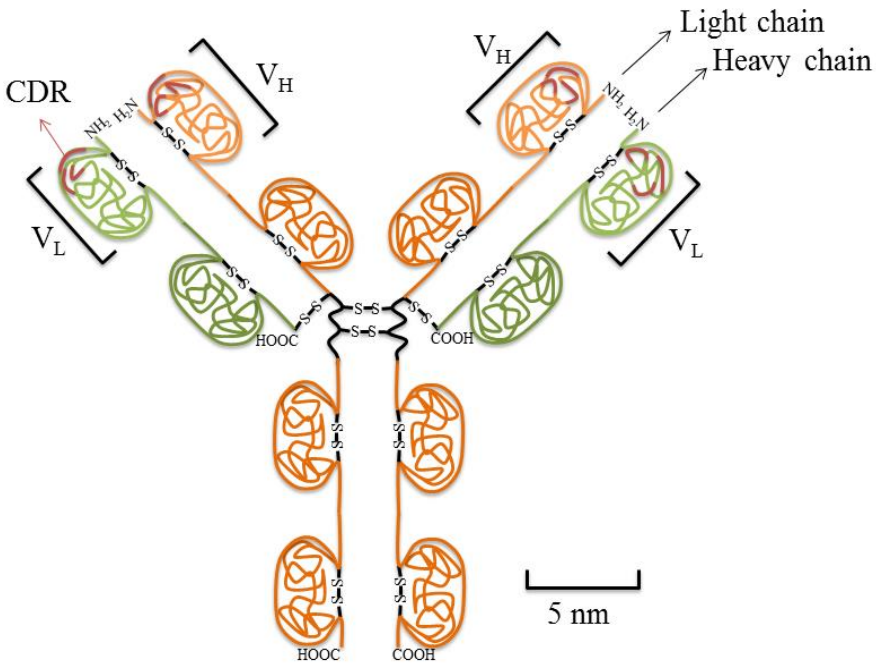

Figure 5.1. Schematic representation of a typical antibody molecule, i.e., an IgG molecule. The molecule is composed of four polypeptide chains, two identical heavy chains and two identical light chains, bounded by disulfide bonds. Each chain is composed of several different domains. The antigen-binding site is formed where a heavy-chain variable domain (V_H) and a light-chain variable domain (V_L) come close together (Adapted from [5, 9]).

Natural occurring antibodies are polyclonal in nature. In other words, an invading organism elicits a response from numerous B-cells, and IgGs of different epitope specificity are produced. On the other hand, monoclonal antibodies (mAb) are monospecific antibodies, i.e., are only specific for binding to one antigen.

Monoclonal antibodies have been considered an important class of pharmaceutical products for cancer treatment, infectious disease, allergy, autoimmune disease and inflammation. Moreover, mAbs belong to a well-established drug class, that has a high success rate from first human studies

to regulatory approval [10]. The high specificity of mAbs is not the only reason for its popularity. mAbs can also be conjugated to another therapeutic entity such as a toxin or radioisotope. The delivery of this entity to a target site can reduce potential side effects [10].

5.1.1.2. Monoclonal antibodies production

Köhler and Milstein [11] produced the first hybridomas (antibody production cells) by fusion of a mouse myeloma and mouse spleen cells from an immunized donor. These researchers won the Nobel Prize in Physiology or Medicine in 1984 for their discovery.

Recombinant mAbs can be produced in transgenic mice that carry human antibody gene loci inserted in their germ line, through bacteriophage display-based technologies yielding high quantities of high-affinity antibodies, and ribosome mRNA display allowing for construction of high-member, high-affinity human immune repertoire antibody libraries. Synthetic antibodies (diabodies, triabodies, tetrabodies) are generated using chemical or molecular biological crosslinking to produce di-, tri-, and tetrameric multivalent conjugates exhibiting enhanced specificity and functional activity [12].

Hybridoma technology has the issue of mouse immunization, i.e., patients treated with mouse antibodies may produce antibodies against the mouse Ig, called human anti-mouse antibodies (HAMA). These anti-Ig antibodies block the function or enhance clearance of the injected mAb and can also cause a disorder called serum sickness [7, 13]. However, hybridoma technology is still the most used technique to produce mAbs for both research and diagnostic applications [12].

5.1.1.2.1.Hybridoma technology

The basis of hybridoma technology is the immortalization of lymphocytes with antibody-producing capacities but limited *in vitro* growth characteristics. The lymphocytes are fused with myeloma cells, a non-antibody-producing and continuously growing tumor cell line. The resultant hybrids, hybridoma cells, continue to secrete antibodies while gaining the immortality of the parent tumor cell. During the fusion process, the number and variety of hybridomas obtained is so large that an intelligent design of assay systems is necessary to select with minimal effort the hybridoma clones which produce the predefined quality of the antibody [14].

The first step to produce mAbs through the hybridoma technology is immunization. This is one of the most significant factors in generating successful hybridomas. The main purpose is to obtain high number and highly proliferating antigen-secreting B-cells. The immunization protocol de-

pends on the investigator's experimental objectives, model, and personal style. However, a specific schedule is followed to avoid neutralization of the injected antigen by circulating antibodies. The harvest of splenocytes and cell fusion occurs generally after 59 days of the first immunization. After successful fusion under optimal conditions, it is expected that approximately 50% of the wells exhibit clonal growth of hybridoma cells. Screening protocols are conducted to identify functional hybridomas. Every primary hybridoma clone requires at least three consecutive rounds of recloning. The purpose of cloning is to have one or less cells per well in order to obtain isolated highly selected hybridoma cell lines [12].

The major problem associated with mAbs obtained from hybridoma technology is the immunogenicity caused by a murine mAb, as above mentioned. These mAb generally have short half-life and decreased effector function. Most of these problems were overcome by replacing all or most of the constant regions of the murine mAb with human ones [15]. Genetic engineering techniques have been used to expand the usefulness of mAbs. The complementary DNA (cDNA) that encodes the polypeptide chains of a mAb can be isolated from a hybridoma, and these genes can be manipulated *in vitro*. Moreover, DNA segments encoding antigen-binding sites from a mouse mAb are inserted into a cDNA encoding a human myeloma protein, creating a hybrid gene. The resultant hybrid protein retains the antigen specificity of the original mouse monoclonal but has the core structure of a human Ig. This hybrid is called a humanized antibody [7]. These humanized mAbs are preferred for chronic administration, since the risk of generation of human anti-mouse antibodies is reduced [10]. Consequently, mAbs are produced in the following main forms: murine (100% mouse protein), chimeric (approximately 65% human and 35% mouse protein), humanized (95% human and 5% mouse protein), fully human (100% human protein) [10]. Fully human mAbs are derived using phage display methods or in mice with B cells expressing human Ig transgenes [7].

5.1.1.3. Commercial mAbs

There are numerous reasons why mAbs have become increasingly popular for commercial development. Monoclonal antibodies are highly specific and bind to a single antigen, causing fewer side effects than conventional drugs. mAbs can also be conjugated with another therapeutic molecule. Advances in molecular biology and protein engineering have enabled the rapid development of highly specific mAbs with high binding affinities for their targets. mAb fragments and mAbs with different isotopes can also be produced to provide control over the pharmacokinetics and effector function of the drug product [10].

In 1986 the US Food and Drug Administration (FDA) approved *Muromab*, a murine IgG1 specific for CD3, for the therapy of transplanted patients undergoing rejection [16]. Since then, dozens of mAbs (murine, chimeric and humanized) have been approved by international regulatory agencies including FDA and EMA (European Medicines Agency) for use in humans against multiple diseases. Of these, at least 14 mAbs are nowadays approved for use in cancer patients (Table 5.1) [8].

mAbs that may have antineoplastic effects can be divided into at least six classes, depending on their function: a) mAbs that target cancer cell-intrinsic pro-survival signal transduction cascades; b) mAbs that interrupt the trophic interaction between malignant cells and their stroma, thus indirectly inhibiting tumor growth; c) mAbs that recognize antigens expressed on the surface of tumor cells and exert antineoplastic effects by initiating immune effector mechanism such as ADCC and CMC; d) trifunctional (bispecific) mAbs that can bind two distinct antigenic targets while retaining the ability of activation immune effector functions; d) immunoconjugates; and e) immunostimulatory mAbs that facilitate the development of an antitumor immune response by influencing the balance between immunogenicity of malignant cells and the immunosuppressive mechanisms that they normally establish [8].

mAbs have also been used to achieve a tumor-specific targeting. For this purpose, an ideal antigen should be expressed in all tumor cells but not on critical host cells. Moreover, the chosen antigen must not suffer any mutation or variation and it should be required for cell survival or for a critical cellular function. Although the mAbs described in Table 5.1 possess a therapeutic effect in their own right, they can also be used as carriers of drug delivery systems for even more effective and less intrusive cancer therapy [17]. This conjugation results in the so-called active targeting. Active targeting is based upon recognition of the ligand by its target substrate. Active targeting can be used to improve cellular internalization of its payload. For example, anti-HER2 targeting moieties on the surface of liposomes strongly increase the uptake of the nanoparticles (NPs) in HER2-expressing cancer cells [18]. Moreover, mAbs can increase the circulation time of its payload. In mice, immunoliposomes (PEGylated liposomes with an active targeting component) with surface-conjugated antibody fragments (Fab') of the mAb 21B2 showed approximately double the circulation time of immunoliposomes with surface-conjugated 21B2 whole mAbs (IgG) over a 24 h period. Immunoliposomes have lower circulation times and consequently are less able to accumulate in the tumor due to the enhanced permeation retention (EPR) effect [19]. In another study immunoliposomes were conjugated with three targeting moieties (whole mAb, Fab', and single chain variable fragment (scFv) targeting CD19, a B-cell antigen. The Fab' immunoliposomes exhibited the most prolonged circulation times [20].

Table 5.1. Monoclonal antibodies currently approved for cancer treatment (adapted from [8, 10]).

mAb (trade name)	Antigen	Approval date	Type	Indications	Company
Alemtuzumab (*Campath*)	CD52	2001	Hz IgG1	CLL	Genzyme
Bevacizumab (*Avastin*)	VEGF	2004	Hz IgG1	Glioblastoma multiform, colorectal, renal and lung cancer	Genentech/ Roche
Brentuximab vedotin (*Adcetris*)	CD30	2011	Ch IgG1	Hodgkin and anaplastic large cell lymphoma (coupled to MMAE)	Seattle Genetics
Catumaxomab (*Removab*)	CD3 Ep-CAM	2009	Murine-Rat hybrid	Malignant ascites in patients with $EpCAM^+$ cancer	Fresenius Biotech/ Trion Pharma
Cetuximab (*Erbitux*)	EGFR	2004	Chimeric IgG1	Head and neck and colorectal cancer	Bristol-Meyers Squibb
Denosumab (*Prolia, Xgeva*)	RANKL	2011	H IgG2	Breast and prostate carcinoma	Amgen
Gemtuzumab (*Mylotarg*)	CD33	2000	Hz IgG4	Acute myeloid leukemia (coupled with calicheamicin)	Wyeth
Ibritumomab tiuxetan (*Zevalin*)	CD20	2002	Murine IgG1	NHL (coupled with ^{90}Y or ^{111}In)	IDEC Pharmaceuticals
Ipilimumab (*Yervoy*)	CTLA-4	2011	Human IgG1	Melanoma	Bristol-Myers Squibb
Panitumumab (*Vectibix*)	EGFR	2006	H IgG2	Colorectal carcinoma	Amgen
Pertuzumab (*Perjeta, Omnitarg*)	HER2	2012	Hz IgG1	Breast cancer	Genentech/Roche
Obinutuzumab (*Gazyva, Gazyvaro*)	CD20	2013	Hz IgG1	CLL	Roche
Ofatumumab (*Arzerra*)	CD20	2009	H IgG1	CLL	GlaxoSmithKline
Rituximab (*Rituxan*)	CD20	1997	Ch IgG1	CLL and NHL	Roche
Tositumomab (*Bexxar*)	CD20	2003	H IgG1	NHL (naked or coupled with 131I)	GlaxoSmithKline
Trastuzumab (*Herceptin*)	HER2	1998	Hz IgG1	Breast carcinoma and gastric or gastroesophageal junction cancer	Genentech

Ch, chimeric; CLL, Chronic lymphocytic leukemia, CTLA-4, cytotoxic T lymphocyte antigen 4; EGFR, epidermal growth factor receptor; EpCAM, epithelial cell adhesion molecule; H, human; Hz, humanized; MMAE, monomethyl auristatin E; NHL, Non-Hodgkin lymphoma; RANKL, receptor activator of NFκB ligand; VEGF, vascular endothelial growth factor.

Some other key factors in the development of antibody-conjugated NPs are the configuration of the antibodies, its origin, and the mode in which these are attached to the nanoparticles. These factors influence the *in vivo* tolerability and efficacy of the system. Antibody fragment containing only the variable region of the antibody are currently more used for targeting-specific therapies. The antibody fragments retain the specificity while lacking the constant Fc effector region which could cause immunogenicity [21].

There are some innate problems associated with the use of antibodies and antibody fragments as targeting agents. The decrease of receptor affinity due to conjugation methods, circulating free antigen, insufficient tumor penetration, binding of antibodies to non-specific Fc receptors and possible changes in the antigen over time, are some of the associated problems [21].

5.1.2. Carbonic Anhydrase

Carbonic anhydrases (CA) are metalloenzymes (zinc) and essential molecules/ions in many important physiologic processes in all life kingdoms (*Bacteria*, *Archaea*, and *Eukarya*). In humans 14 different CA isozymes or Ca-related proteins (CARP) were described so far (Table 5.2), differing in its subcellular localization and tissue distribution. CARPs appear to lack activity because of substitutions in one or more of the histidine residues required to bind to the zinc ion, which is essential for CO_2 hydration activity. Several CA isozymes are located in the cytosol (CA I-III, VII), four are bound to the phospholipidic membrane (IV, IX, XII and XIV), one in located within the mitochondria (CA V) and one is secreted (CA VI) [22-24].

These enzymes play an important role in the red blood cell by catalyzing the hydration of carbon dioxide (Equation 5.1):

$$CO_2 + H_2O \leftrightarrow HCO_3^- + H^+ \qquad \text{Equation 5.1}$$

Consequently, CA enzymes are involved in crucial physiological processes such as:

- Respiration and transport of CO_2/bicarbonate between metabolizing tissues and lungs;
- pH and CO_2 hemostasis;
- Electrolyte secretion in a variety of tissues/organs;
- Biosynthetic reactions (e.g. gluconeogenesis, lipogenesis, ureagenesis);
- Bone resorption;
- Calcification;
- Tumorogenicity [22, 24].

Drugs interfering with the activity of CAs have been clinically used for almost 60 years, and most of them belong to the sulphonamide class. Inhibition of CAs has pharmacological applications in many fields, such as anti-hypertensive, anti-glaucoma, anticonvulsant, some anti-thyroid drugs, anti-obesity, and anticancer/diagnostic tools [22, 23].

Table 5.2. Human CA isozymes known so far, their CO_2 hydrase activity, sub-cellular localization and some examples of their tissue distribution.

Isozyme	**Catalytic activity (CO_2 hydration)**	**Sub-cellular location**	**Tissue distribution (examples)**
CA I	Low (10%[1])	Cytosol	Red blood, cell, intestine
CA II	High	Cytosol	Ubiquitous
CA III	Very low (0.3%[1])	Cytosol	Red muscle, adipose tissue
CA IV	High	Membrane-bound (extra-cellular)	Kidney, lung, gut, brain, eye
CA V	Moderate-high[2]	Mitochondria	Liver
CA VI	Moderate	Secreted into saliva	Saliva
CA VII	High	Cytosol	Brain, salivary gland, lung
CARP VIII	-	NA	Brain, especially Purkinje cells of the cerebellum
CA IX	High	Transmembrane (extra-cellular domain)	Various tumors, gastric mu-cosa
CARP X	-	Unknown	Brain, pineal gland, placenta
CARP XI	-	Secreted	Brain
CA XII	Active[3]	Transmembrane (extra-cellular domain)	Colon, kidney, prostate
CA XIII	NA[4]	Unknown	NA
CA XIV	Low	Transmembrane (extra-cellular domain)	Kidney, heart

[1]Compared to CA II catalytic activity; [2]Depending upon pH: moderate at 7.4; high at pH 8.2 or higher; [3]No quantitative data available; [4]NA – data not available.

5.1.2.1. CA IX

As mentioned above, some CA isozymes are predominantly found in cancer cells and are lacking from their counterparts. It is the case of CA IX, a membrane bound CA isozyme that is controlled via the hypoxia-inducible factor (HIF). CA IX has been identified in human HeLa call line derived from carcinoma of the cervix [25], in the tumorigenic phenotype of somatic cell hybrids between HeLa and normal human fibroblasts *in vitro* [26], among others.

Although this CA isoform expression is related to several physiological processes including lipo- and ureagenesis, gluconeogenesis and bone resorption, its most relevant function is the intracellular pH (pH_i) regulation in cancer cells exposed to acidic environment caused by metabolic products of glycolysis [27].

During solid tumor growth, subpopulations of cancer and stromal cells are exposed to variable conditions depending upon local and temporal supply of oxygen, nutrients, growth factors and signaling molecules. Highly proliferative cancer cells generate excessive amounts of lactate, carbon dioxide, and protons. These metabolites are extruded to the extracellular environment where they accumulate due to poor vasculature. The combination of these factors leads to a continuously decrease of the extracellular pH (pH_e). To neutralize their pH_i, bicarbonate anions generated by CA IX-catalyzed hydration of CO_2 are transported into the cells by anion transporters to interact with protons liberated by the glycolytic metabolism. This process leads to an extracellular acidification, generating acidosis partially caused by tumor hypoxia [27].

Hypoxia is a biologically and clinically important phenomenon with pronounced effects on tumor phenotype and cancer progression. The connection between hypoxia and poor prognosis and resistance to conventional treatments modalities is clearly proved and has led to implementation of modified treatment regimens [28].

Reduced oxygen availability leads to the activation of a core cellular response to hypoxia initiated by its master regulators, the transcription factor HIF. HIF is composed of two subunits, α and β, being α sensitive to oxygen [29, 30]. In normoxia HIF-α is dependent upon von Hippel-Lindau tumor suppressor protein (pVHL)-mediated poly-ubiquitylation and subsequent proteasome degradation. In hypoxia, HIF-α is stabilized and following entry to the nucleus and dimerization with the constitutive HIF-β subunit, it can either turn on or elevate the transcription of numerous genes containing HIF-responsive elements in regulatory regions. The proteins encoded by these genes execute the adaptive responses to hypoxia and are therefore active players in tumor progression [29].

Being a hypoxia-induced enzyme, CA IX plays important roles in tumor progression such as increased adaptation of tumor cells to microenvironmental stress, resistance to therapy, increased tumor cell migration and invasiveness, increases focal adhesion during cell spreading, destabilization of intracellular contacts, maintenance of stem cell phenotype, tumor-stroma crosstalk, signal transduction, among others [30]. The consequence of pharmacological inhibition of CA IX, either by mAb or small molecule CA IX inhibitors, is explained in Figure 5.2. Hypoxia induces a HIF-1-mediated signaling cascade that results nuclear translocation of HIF-1α and activation of hypoxia-regulated genes, including GLUT1, MCT1/4 and CA IX. Cells undergo the glycolytic pathway, which results in increased production and export of lactate, leading to a decline in pH_e. One consequence of extracellular acidification is the disruption of the intracellular pH, which affects basic cellular functions. The overexpression of CA IX in hypoxia catalyzes the hydrolysis of CO_2 to HCO_3^- and H^+ in the extracellular microenvironment. The HCO_3^- is actively transported into the cancer cell, thereby regulating pH_i and maintaining cell survival. The H^+ contributes to the increasingly acidic extracellular space, promoting tumor cell invasiveness. Inhibition of CA IX catalytic activity prevents the production of these enzymatic metabolites, leading to decreased survival and reduced invasive capacity [31].

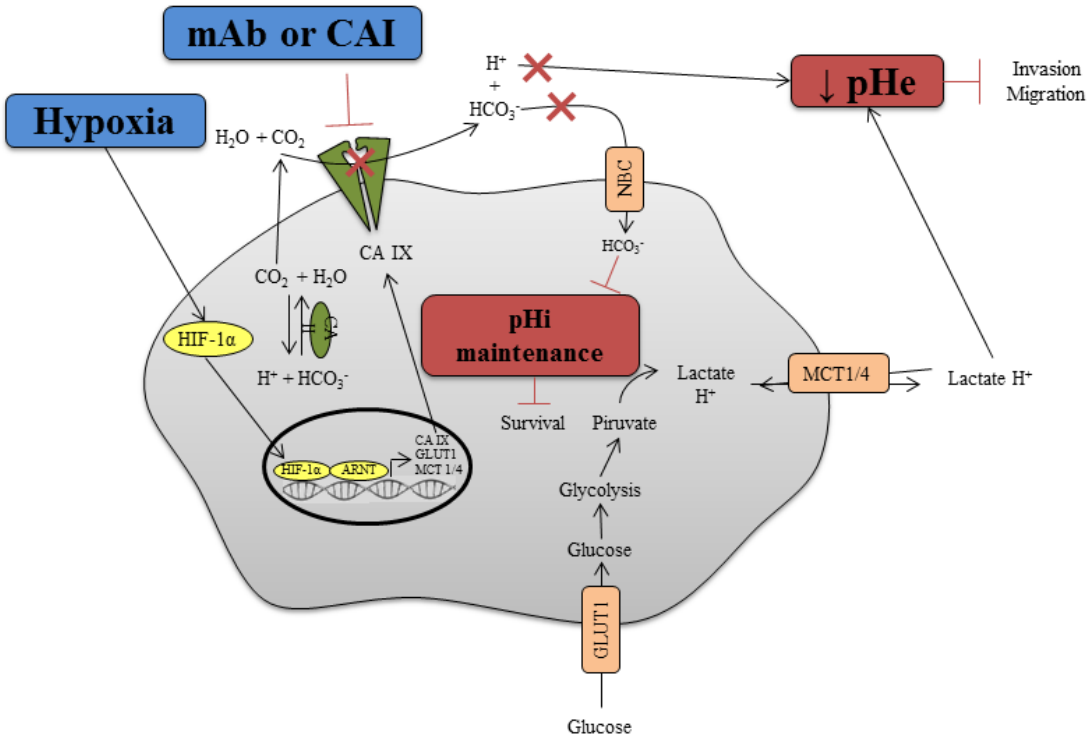

Figure 5.2. Inhibition of cancer cell survival and invasion by pharmacologic inhibition of CA IX (adapted from [31]).

Consequently, CA IX appears to have an important role as a predictive outcome of cancer treatments. Theoretically, the association with hypoxia and acidosis, factors that are linked with poor prognosis, predisposes CA IX to indicate bad outcome and serve as the stratification marker. Furthermore, the correlation between decrease CA IX levels and progression of kidney cancer indicates that reduced CA IX expression in this tumor type may be linked with better treatment outcome [30]. Several evidences confirmed these theories. CA IX was shown to be predictive of outcome of doxorubicin resistance in early-stage breast cancer independent of HER2 and TOP2A amplification [32]. In addition, it may also predict chemosensitivity to neoadjuvant taxane and anthracycline therapy in breast cancer patients [33]. CA IX is also helpful to indicate preoperative chemotherapy response in renal adenocarcinoma [34] and to predict survival benefit from lower dose of bevacizumab in metastatic colorectal cancer [35].

5.1.2.2. CA IX as a therapy target

CA IX is an attractive target for anticancer therapy since it is selectively expressed by tumor cells being absent in its counterparts. Moreover, it provides functions critical for tumor growth and metastasis, including pH regulation, survival, and adhesion/migration. It is located on the extracellular surface of cell membranes, which allows efficient targeting by antibodies or small molecule inhibitors. Direct binding of CA IX-specific mAbs to CA IX can trigger an anti-tumor response by activating the ADCC mechanism, delivering of therapeutic payloads (e.g. cytotoxins and radionuclides) or selective blocking of CA IX function [31].

Rencarex® is an anti-CA IX antibody currently under phase III clinical trials as an adjuvant therapy aimed to reduce recurrence in surgically treated renal cell carcinoma patients. This chimeric mAb could elicit ADCC mechanism [36]. So far, it has demonstrated to be safe, well tolerated, and able to positively influence disease burden, alone and together with interferon (IFN)-α treatment [37, 38].

Other antibodies have been developed with the aim of targeting CA IX catalytic domain by phage display. These ones are expected to selective blocking of CA IX function. Some studies have shown that these antibodies are able to selectively bind to tumors *in vivo*. However, evaluation of anti-tumor efficacy was not performed [39]. Furthermore, a similar mAb was developed and tested *in vivo* using hybridoma technology. The results showed efficient binding, internalization and persistence in cultured cells [40].

5.2. Materials and methods

5.2.1. Cell culture

SaOs-2 osteosarcoma cell line was grown in McCoy 5A medium (*Sigma-Aldrich*), supplemented with 10% fetal bovine serum (*Sigma-Aldrich*) and 1% Penicillin-Streptomycin (10,000 U/mL; *Gibco/Invitrogen*), while MDA-MB-231 cells were grown in Dulbecco's modified Eagle's medium (DMEM) supplemented with 10% fetal bovine serum, Penicillin-Streptomycin (100 U/ml penicillin and 100 μg/ml Streptomycin, *Gibco/Invitrogen*), and 2 mM L-glutamine (*Gibco/Invitrogen*). Cells were maintained in CO_2 incubator (37°C; 5% CO_2).

5.2.2. Mice immunization

Female Balb/c mice (4-5 weeks) were immunized with intraperitoneal injection of the CA IX antigens: total protein (*R&D Systems* 2188-CA), N-terminal and central peptide (*Eurogentec* EP112430 and EP112431) emulsified in complete Freund's adjuvant (*Sigma*). In addition, SaOs-2 extract was intraperitoneal injected, emulsified in incomplete Freund's adjuvant under similar conditions to the proteins. Antigens were inoculated separated by 1-2 weeks intervals, 6-times for total protein and N-terminal peptide, and 9-times for central peptide. After each inoculation, the presence of mAbs was verified by collecting serum and evaluating it by flow cytometry. Three days after the last injection mice were sacrificed and the spleen was removed and used for cell fusion. Collected sera were stored at -20 ºC until used.

5.2.3. Cell fusion

Splenocytes (7.7×10^7) and Sp2/0 Ag14 myeloma cells (5.3×10^7) previously grown Dulbeco's Minimal Essential Medium (DMEM) (*Sigma*) containing 20% (v/v) fetal calf serum (FCS) and gentamicin were pooled and fused in the presence of 50% PEG 4000/DMSO. 0.8 ml of PEG/DMSO was added slowly over a one min period with gently stirring and kept without any stirring for one further minute. The fusion suspension was then diluted adding 1 ml of DMEM medium over a period of 1 min, followed by 20 ml at a rate of 4 ml per min. Total fusion time was therefore 8 min. After centrifugation (290x*g*, 5 minutes) the fusion product, resuspended in DMEM containing 20% (v/v) fetal calf serum and HAT medium (1×10^{-4} M Hypoxanthine, 4×10^{-7} M Aminopterin,1.6×10^{-5} M Thymidine) (*Sigma*), was placed on 96-well plates and incubated overnight at 37ºC, 5% CO_2, 95% humidity, for hybrid selection. The supernatants of each

well were replaced with fresh HAT medium when necessary judged by pH medium color and microscopy visualization.

Circa the day 15, the wells were screened for the desired antibody by flow cytometry. Positive wells were transferred to 24-well plates (*Costar*) previously filled with 1 ml of HAT. Afterwards, the supernatants were screened by Flow Cytometry and the positive antibody-producing cells were expanded for analysis and frozen in FCS containing 4% DMSO. Tubes were first frizzed at -20 ºC and after transferred to liquid nitrogen container (-180 ºC) for long storage.

5.2.4. Flow cytometry

The presence of anti-CA IX mAbs in both the serum and the hybridomas supernatant was tested by flow cytometry. Flow cytometry acquisition was performed, using the Attune® Acoustic Focusing Cytometer (*Applied Biosystems*). File data was analyzed using the Attune Cytometric Software v1.2.5 and FLOWING (*Turku, Finland*) software to discriminate specific populations, and to determine the mean fluorescence intensity (MFI) of the cells.

The used protocol was as follows: The presence of anti-CA IX mAbs was tested using SaOs-2 and MDA-MB-231 cell lines. Cells were washed with PBS 1x, centrifuged at 1500xg for 2 minutes and resuspended in PBS 1x. Cell suspensions were previously treated with BD Cytofix/Cytoperm™ fixation/permeabilization kit. Then, cell suspensions ($0.4x10^6$ cell/microtube) were incubated with 1 ml of the respective supernatant, and with the positive control using anti-CA IX mAb (clone H-11, *Santa Cruz Biotechnology, Inc.*). After 30 minutes of incubation at 4ºC, cell suspensions were washed with PermWash buffer®, centrifuged at 1500 xg, 2min and resuspended in PermWash buffer. Next, cell suspensions were incubated with the secondary antibody, anti-mouse polyvalent immunoglobulins (G, A, M)-FITC (*Dako*), for 15 minutes, 25 ºC. As a negative staining control, cells were incubated with only the secondary antibody. Finally, cells were washed, resuspended in PermWash buffer, and analyzed by flow cytometry.

5.2.5. Western blot

Protein samples were prepared by resuspend SaOs-2 and MDA-MD-231 cell lines pellets with lysis buffer [150 mM NaCl, 50 mM Tris-HCl (pH 7.5), 20 $\mu g.ml^{-1}$ PMSF, 2% NP-40 and protease inhibitor cocktail (*Roche*)] and vortexed at 4ºC, overnight. The protein amount was determined by Pierce™ BCA Protein Assay Kit. Cell pellets were resuspended in 1x loading buffer (*nzytech*) and heated for 5 min at 100 ºC. A 8% polyacrylamide gel was used as the resolving gel and 4% as the stacking gel. Both gels were placed in the Multiple Gel Caster (*Amersham Biosciences*).

After gel solidification, both were placed in the SDS-Page electrophoretic system (*Amersham Biosciences*) with the running buffer. Protein samples and molecular weight standards were placed into the wells and separated at 150 V. Samples were blotted onto PVDF membrane (*Bio-RAD*) previously activated with methanol (*VWR*) for 5 min, for 90 min at 0.4 A. The membranes were blocked for 1h with 10% dry milk in TBS-T (Tris-buffered saline with 0,1% Tween-20) and probed either with anti-CA IX mAb (1:100) or the hybridoma supernatant overnight at 4 ºC, followed by incubation with anti-mouse Ig secondary antibody (1:1000; *BD biosciences*) for 1 h. Finally, the membranes were covered with Lumi-Light Western Blotting substrate (*Roche*) and revealed in Amersham hyperfilm ECL (*GE Healthcare*).

5.2.6. Dot blot

Dot blot was performed to confirm the specific bounding between CA IX and the mAbs produced by the selected hybridomas. 1 ng of CA IX protein was placed in each spot. Membranes were blocked with 10% milk in PBS-T for 1h, and probed either with anti-CA IX mAb (1:100) or the hybridoma supernatant for 1 h at 4º C, followed by incubation with anti-mouse Ig secondary antibody (1:1000; *BD biosciences*) again for 1 h. Finally, the membranes were covered with Lumi-Light Western Blotting substrate (*Roche*), and reveled in Amersham hyperfilm ECL (*GE Healthcare*).

5.2.7. Confocal laser scanning microscopy

Cells were cultured in cover glasses overnight to adhere. Then cells were treated with BD Cytofix/Cytoperm™ fixation/permeabilization kit. After blocking with 1% bovine serum albumin (BSA), cells were stained using anti-CA IX mAb (clone H-11) or hybridoma supernatants, followed by fluorescent polyclonal anti-mouse Ig antibody. The cell nuclei were stained with 1 mM TO-PRO-3 dye (*Molecular Probes, Leiden, Netherlands*). Images were acquired with a Leica TCS SP2 AOBS confocal microscope (*Leica Microsystem, Mannheim, GmbH*).

5.3. Results and discussion

Carbonic anhydrase IX are one of the most induced proteins in response to hypoxia. Several studies showed an abnormal expression of CA IX in a broad range of human tumor, including carcinomas of the uterine cervix, kidney, brain, head and neck, esophagus, lung, colon, ovaries, endometrium, vulva and breast [41].

The main purpose of the present work was to produce monoclonal antibodies anti-CA IX through hybridoma technology. To achieve this goal, three antigens were used: the whole CA IX protein, a central peptide and an N-terminal peptide of CA IX. Further, the produced mAbs were tested for effectiveness in two tumor cell lines: a breast cancer (MDA-MB-231) and an osteosarcoma (SaOs-2) cell line. The purpose of using these two cell lines is to test the versatility of the final multifunctional nanoparticle. Nevertheless, before mice immunization, both cell lines were tested for the presence of CA IX expression using a commercial mAb anti-CA IX.

5.3.1. Identification of Ca IX presence in cell lines

Flow cytometry was used to identify the presence of CA IX in both breast cancer and osteosarcoma cell lines. Figure 5.3 displays the flow cytometry results for MDA-MB-231 cells stained for CA IX using the anti-human CA IX. Two protocols were tested: cells without permeabilization (Figure 5.3 A), and cells treated with the fixation/permeabilization kit (Figure 5.3 B).

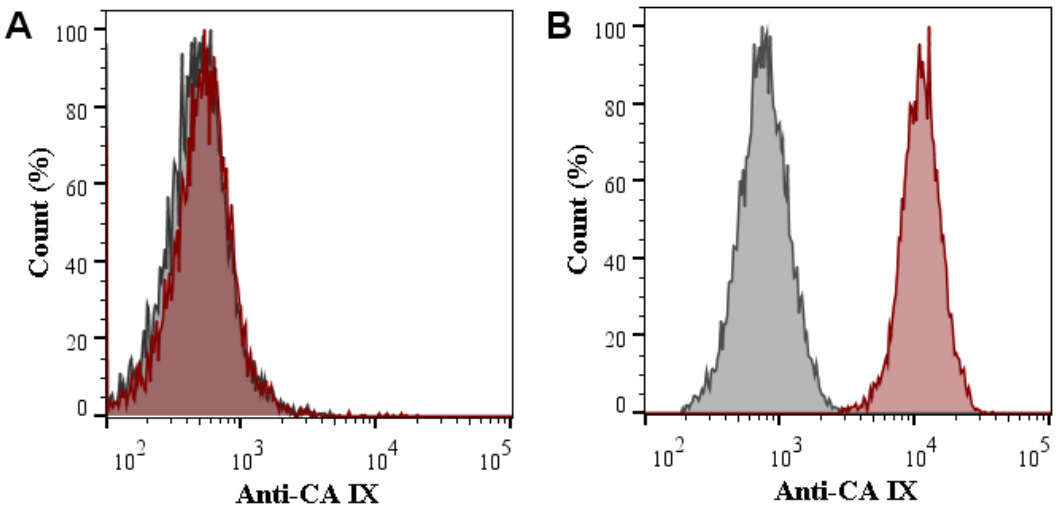

Figure 5.3. Flow cytometry analysis of MDA-MB-231 cell line expression of CA IX extra- (A) and intracellular (B). Gray histogram corresponds to the negative staining control, i.e., cells stained with only the secondary antibody.

The results show that cells without previous permeabilization treatment do not show the presence of CA IX. However, when cells are previously treated with the fixation/permeabilization kit, the presence of CA IX is positive, meaning that CA IX is present intracellularly but not in the membrane of these cells. In the case of SaOs-2, the results are similar (data not shown).

Both breast cancer and osteosarcoma cell lines were maintained in normoxia. Being CA IX over-expressed in response to hypoxia, its expression should be lower and maintained in a stationary state in these cell conditions. Moreover, we hypothesize that CA IX location must not be restricted to the membrane, but may also be located intracellularly, e.g., in high-density (ER/Golgi) fractions [42].

To confirm the flow cytometry results, confocal microscopy was performed. Figure 5.4 shows the confocal microscopy results for MDA-MB-231 and SaOs-2 cell lines. Both cell lines were stained with anti-CA IX mAb followed by fluorescent polyclonal anti-mouse Ig antibody. The cell nuclei were stained with 1 mM TO-PRO-3 dye. Negative control was obtained by staining with only the secondary antibody. In both cell lines, the expression of CA IX is confirmed. However, the obtained images do not allow confirming the location of CA IX within the cell, which may be or not in the membrane.

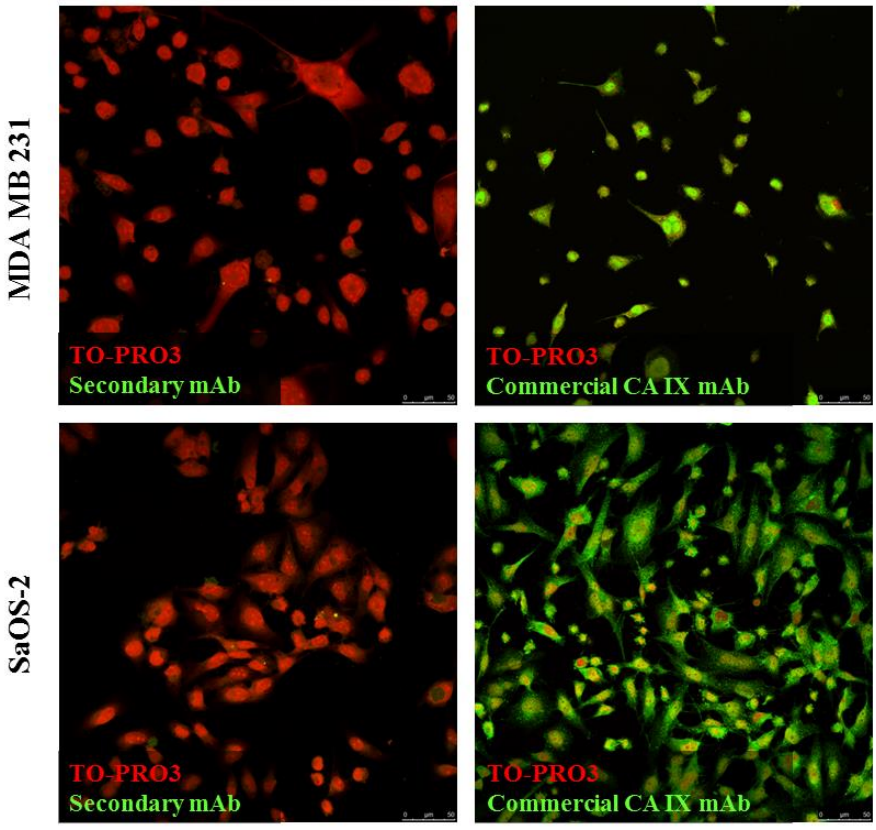

Figure 5.4. Confocal microscopy of MDA-MB-231 and SaOs-2 cell lines stained with commercial anti-CA IX mAb (Green) and TO-PRO3 (Red) for the nucleus.

Ultimately, western blot analysis provides crucial information about a protein, including molecular weight, abundance, and post-translational modifications. Figure 5.5 shows the western blot

results of CA IX expression in SaOs-2 and MDA-MB-231. CA IX protein was detected in both breast cancer and osteosarcoma cell lines. Typically, CA IX migrates as a doublet of 54 KDa and 58 KDa [42], which corresponds to the obtained data.

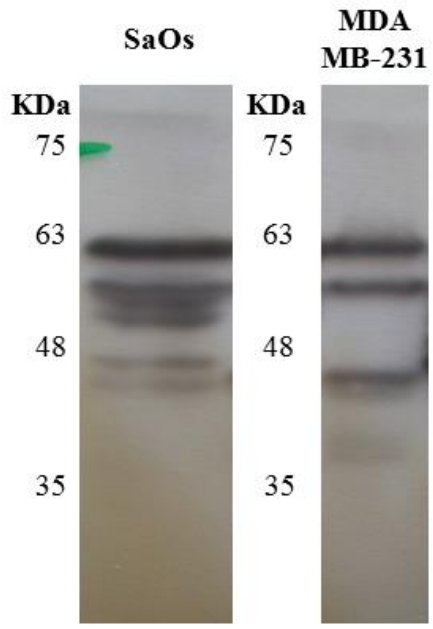

Figure 5.5. Western blot analysis of total lysates from SaOs-2 and MDA-MB-231 cell lines treated with commercial mAb anti-CA IX

5.3.2. Murine immunization

Different murine were immunized with CA IX N-terminal peptide and CA IX central peptide. To evaluate the immunization effectiveness, murine serum was removed at fixed times and checked for the presence of antibodies anti-CA IX. Further, the same evaluation was performed before fusion of the splenocytes from the murine with the myeloma cells. Figure 5.6 shows the flow cytometry analysis on murine serum immunized with CA IX N-terminal peptide using SaOs-2 cell line. The results show the presence of antibodies anti-CA IX in the murine serum.

After confirmation that the immunized mice was producing antibodies anti-CA IX, the mice was sacrificed, the spleen removed and used for cell fusion. Cell fusion was carried out between splenocytes from both mice immunized with CA IX N-terminal peptide and CA IX central peptide, and Sp2/0 myeloma cells to produce hybridomas.

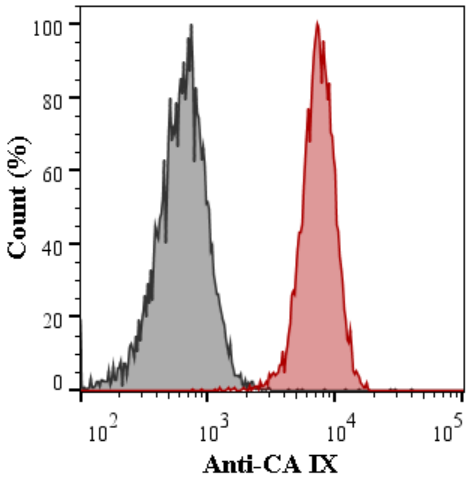

Figure 5.6. Flow cytometry analysis of murine serum immunized with CA IX N-terminal peptide using SaOs-2 cell line stained intracellularly. Gray histogram corresponds to the negative staining control, i.e., cells stained with only the secondary antibody.

5.3.3. Hybridomas selection

Hybridomas selection was performed using the following techniques: flow cytometry, fluorescence microscopy, and dot blot.

5.3.3.1. mAb anti-CA IX N-terminal

After fusion, cells were seeded in 96-well plates. The supernatants were screened after a fixed time to identify the positives one. A good technique to perform this screening is flow cytometry. Figure 5.7 corresponds to two positive hybridoma supernatants resultant from fusion of splenocytes from mice immunized with CA IX N-terminal peptide with myeloma cells. Moreover, the same technique was also used to evaluate the stability of the hybridoma. As such, the analysis was performed 7 weeks and 4 months after fusion (Figure 5.7 A and B, respectively). 3G9 hybridoma cells appear to maintain its antibody producing ability over time. However, 3B5 hybridoma cells decrease their antibody production ability over time. These results suggest that 3G9 cells are more likely to be selected for future developments.

Furthermore, flow cytometry analysis was performed 8 months after fusion using two cell lines: MDA-MB-231 and SaOs-2 (Figure 5.8). In SaOs-2, it is possible to verify that supernatant 3G9 remains stable after 8 months, while supernatant 3B5 continues to decrease its intensity. In MDA-MB-231 cell line, the expression of CA IX is lower and consequently, the signal intensity is lower.

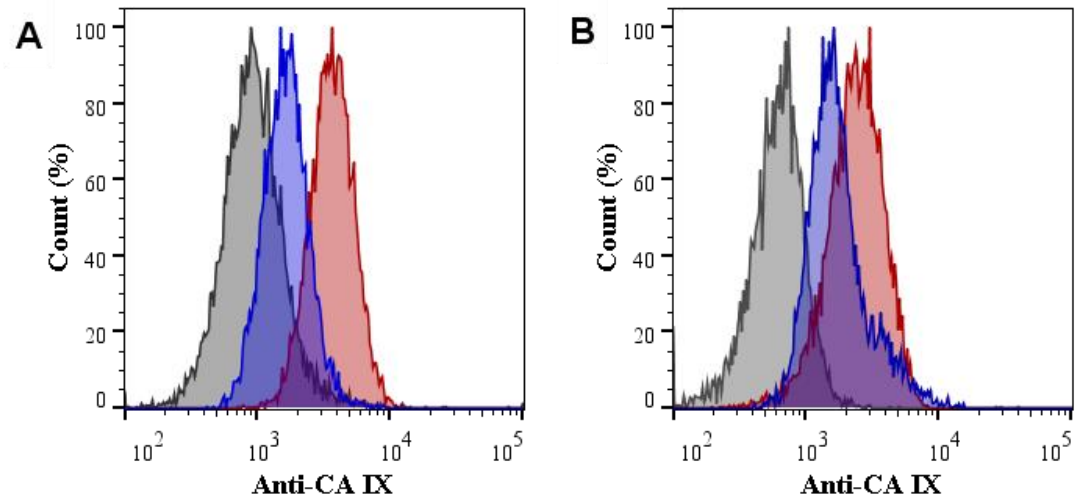

Figure 5.7. Flow cytometry analysis of hybridoma supernatant producing N-terminal antigen using SaOs-2 cell line 7 weeks (A) and 4 months (B) after fusion. Gray histogram corresponds to the negative control, i.e., cells stained treated with only the secondary antibody. Red histogram corresponds to the supernatant from 3B5 hybridoma cells and the blue one to 3G9.

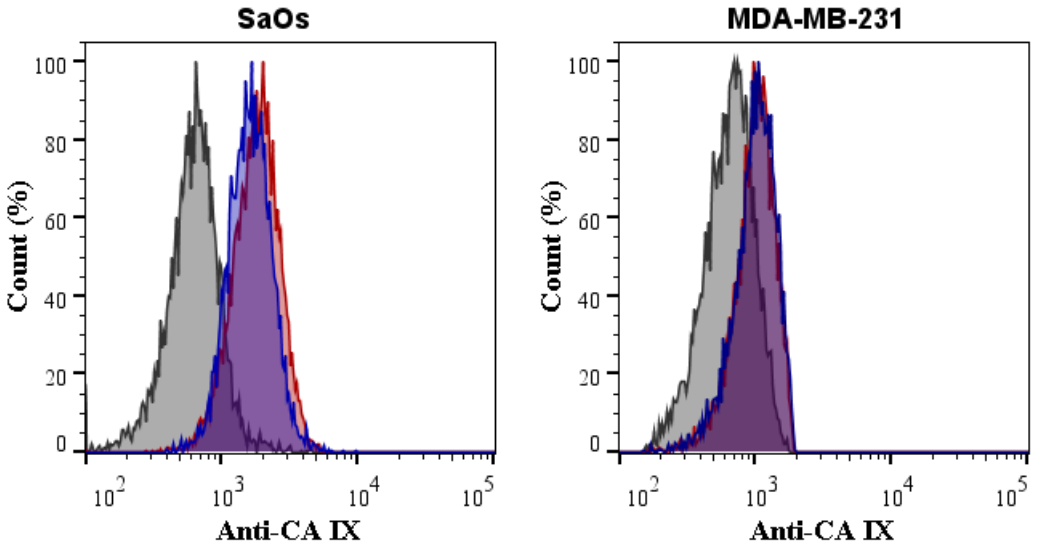

Figure 5.8. Flow cytometry analysis of hybridoma supernatant producing N-terminal antigen using Samos cell line (A) and MDA-MB-231 cell line (B) 8 months after fusion. Gray histogram corresponds to the negative control, i.e., cells stained with only the secondary antibody. Red histogram corresponds to the supernatant from 3B5 hybridoma cells and the blue one to 3G9.

Fluorescence microcopy was performed using both SaOs-2 and MDA-MB-231 cell lines (Figure 5.9). Cells were incubated with supernatant from 3G9 hybridoma cells (green), the apparently most stable one, followed by fluorescent polyclonal anti-Ig antibody. The cell nuclei were stained

with TO-PRO-3 dye (red). Negative control was obtained by staining with only the secondary antibody. In both cell lines, the presence of CA IX is barely noted. This may be a consequence of two factors: since the used cell lines are grown in normoxia, CA IX expression is low; the amount of anti-CA IX antibody produced by the hybridoma is low, and consequently, the amount of antibody available to bind to CA IX in the cells is not enough to produce a fluorescence good signal.

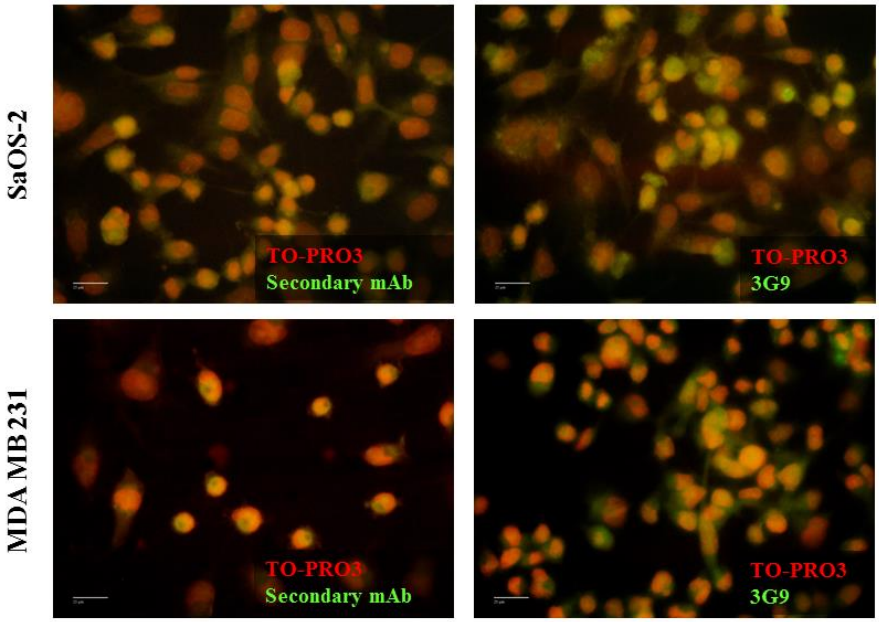

Figure 5.9. Fluorescence microscopy of MDA-MB-231 and SaOs-2 cell lines treated with hybridoma supernatant 3G9 producing N-terminal anti-CA IX mAb (Green) and TO-PRO3 (Red) for the nucleus.

To confirm whether the supernatant from 3B5 hybridoma cells, which was losing signal capacity by flow cytometry as time was passing, contained anti-CA IX antibodies, dot blot analysis was performed using CA IX protein as target. In this technique, a known amount of CA IX protein is placed in a spot in a membrane and the membrane is incubated with the respective antibody. In this case, the positive control was incubated with commercial mAb anti-CA IX (H-11), while the sample was incubated with the 3B5 hybridoma supernatant. As can be seen in Figure 5.10, there are anti-CA IX antibodies IX in the 3B5 hybridoma supernatant, although its titer appears to be low judging by the low intensity of the signal.

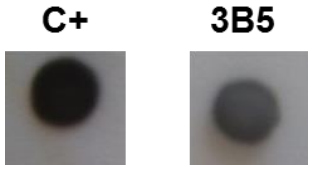

Figure 5.10. Dot blot analysis of 3B5 hybridoma supernatant producing N-terminal anti-CA IX mAb using CA IX protein as target.

5.3.3.2. Anti-CA IX central peptide mAb

Figure 5.11 corresponds to the staining of SaOs-2 and MDA-MB-231 cells with three positive hybridoma supernatants resultant from fusion of splenocytes from mice immunized with CA IX central peptide with myeloma cells. Supernatant 3D2 (red histogram) corresponds to the hybridoma with higher specificity and/or titer.

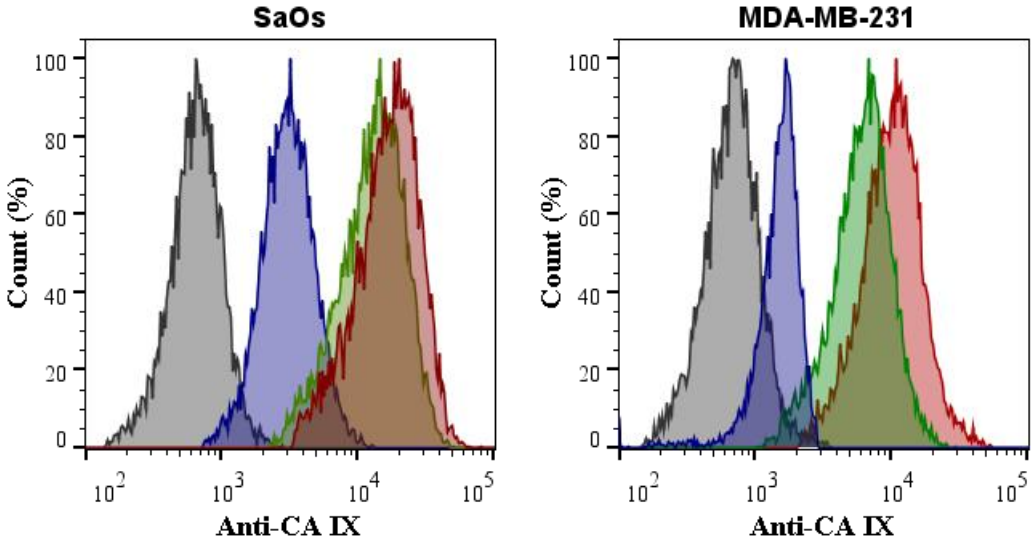

Figure 5.11. Flow cytometry analysis of hybridoma supernatant containing central peptide antibodies using SaOs-2 (A) and MDA-MB-231 (B) cell lines, 3 months after fusion. Gray histogram corresponds to the negative control, i.e., cells stained with only the secondary antibody. Red histogram corresponds to the supernatant from 3D2 hybridoma cells, green histogram corresponds to supernatant 4C5 and the blue histogram corresponds to supernatant 1D3.

Fluorescence microscopy images of SaOs-2 and MDA-MB-231 cells incubated with the supernatants of each of the selected hybridomas are showed in Figure 5.12. In the three cases the presence of antibodies against CA IX are confirmed in both cell lines. However, similarly to what occurred in the previous cases, it is not possible to distinguish the location of the CA IX within the cell. Furthermore, expression of CA IX in MDA-MB-231 cells appears to be smaller than the one observed in SaOs-2 cells.

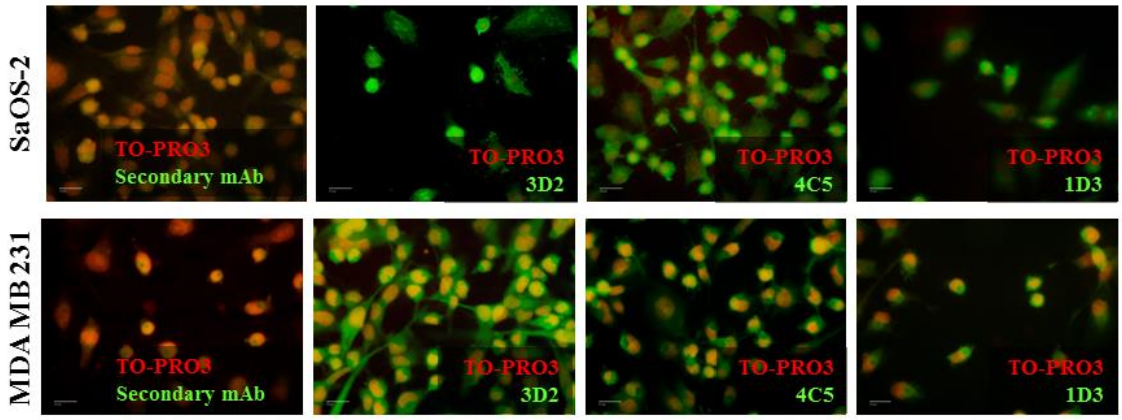

Figure 5.12. Fluorescence microscopy of MDA-MB-231 and SaOs-2 cell lines treated with hybridoma supernatant containing central peptide anti-CA IX mAb (Green) and TO-PRO3 (Red) for the nucleus staining.

Dot blot analysis was performed to confirm the specificity of the antibodies produced by the selected hybridomas to CA IX. This analysis was performed for the two supernatants with best performance in both flow cytometry and fluorescent microscopy. Figure 5.13 shows the obtained results where it is visible that 3D2 hybridoma supernatant has antibodies against CA IX although in a small amount. Furthermore, 4C5 supernatant has a very low signal, which may indicate that the hybridoma is producing antibodies that are not only specific for CA IX protein, since it shows a significant staining of both cell lines by flow cytometry and fluorescence microscopy.

Figure 5.13. Dot blot analysis of hybridoma supernatant containing central peptide anti-CA IX mAb using CA IX protein as target.

Since 3D2 supernatant is the one with best performance in flow cytometry, fluorescence microscopy and dot blot, western blot analysis was performed to confirm the specificity of the produced antibody. Both SaOs-2 and MDA-MB-231 cell lysates were used. Figure 5.14 displays the obtained results for both cell lines, compared to positive staining control for CA IX. In the case of SaOs-2 cells, the antibodies produced by the selected hybridoma clearly bound to CA IX, producing a similar pattern as the positive control. This is not the case of MDA-MB-231 in which the obtained pattern has more bands comparing to control. However, CA IX specific bands are present in the obtained pattern. This means that the selected hybridoma is producing antibodies against CA IX but not exclusively.

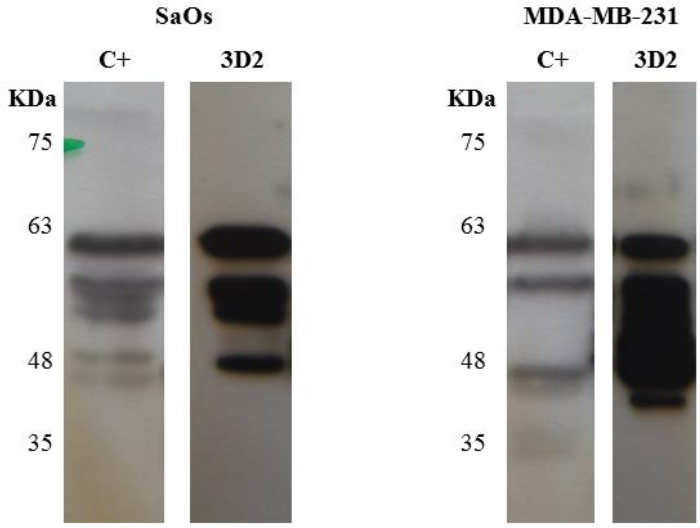

Figure 5.14. Western blot analysis of total lysates from SaOs-2 and MDA-MB-231 cell lines stained with 3D2 hybridoma supernatant containing antibodies against the central peptide of CA-IX.

5.4. Summary

Monoclonal antibodies, the "magic bullet" imagined by Ehrlich, are nowadays and important class of pharmaceutical products for treatment of cancer, infectious disease, allergy, autoimmune disease and inflammation. Typically, monoclonal antibodies are produced using the hybridoma technology. However, for clinical application, humanization of these mAbs is required to decrease their immunogenicity.

In the present work, the main purpose was the production of monoclonal antibodies anti-CA IX, a carbonic anhydrase protein present mostly in tumor tissues and recognized as a predictive outcome of cancer treatments. The desired antibody was produced using the hybridoma technology and tested against to tumor cell lines: a breast cancer cell line (MDA-MB-231) and an osteosarcoma cell line (SaOs-2).

In a first stage of this work, the used cell lines were tested for the presence of CA IX. It is important to consider that both cell lines were maintained in normoxia conditions. As such, CA IX should not be overexpressed. However, the presence of CA IX was still identified by flow cytometry, confocal microscopy, and western blot analysis. For a more complete analysis, both cell lines should be cultured in hypoxia conditions and CA IX catalytic activity measured. Moreover, subcellular location of CA IX should be determined, to confirm if whether the protein was kept in the membrane.

Murine were immunized with three different antigens: the whole CA IX protein, an N-terminal peptide, and a central peptide. Only the N-terminal and central peptide were selected for further cell fusion. After fusion, viable hybridomas were selected using flow cytometry, fluorescence microscopy and dot blot analysis. The hybridomas' supernatants were tested against both MDA-MB-231 and SaOs-2 cell lines. The obtained results showed that at least one hybridoma from each immunization were viable for production of antibodies anti-CA IX.

Some lack of specificity was observed when the supernatant of the hybridoma producing a central peptide anti-CA IX was observed. This may be resolved by the following step, which was not performed during this work. Further recloning would provide the means to obtain isolated highly selected hybridoma cell lines. Although this step was not performed, the obtained results provide the basis to predict a successful outcome. Moreover, the produced antibodies using hybridoma technology demonstrated to bind to both osteosarcoma and breast cancer cell lines. This versatility is crucial when developing a mAb to be used for active targeting therapies. Nevertheless, a large amount of work still need to be done in order to obtained a mAb suitable for use as an active targeting agent.

5.5. References

1. Dictionary of cancer terms, http://www.cancer.gov/Common/PopUps/popDefinition.aspx?id=45617&version=Patient&language=English, accessed on July, 28th, 2015

2. R. L. Souhami, Oxford Textbook of Oncology, 2nd ed., Oxford University Press, Oxford, 2002.

3. J. Cassidy, D. Bissett, R. A. Spence, Oxford Handbook of Oncology, Oxford University Press Inc., New York, 2002.

4. M. R. Kaser, G. C. Howard, Antibodies, in: Gary C. Howard, Matthew R. Kaser (Eds.) Making and using Antibodies - A pratical handbook, CRC Press Taylor & Francis Group, New York, 2007.

5. B. Alberts, D. Bray, K. Hopkin, A. Johnson, J. Lewis, M. Raff, K. Roberts, P. Walter, Essential cell biology, Third edition ed., Garland Science, Taylor & Francis Group, New York, 2010.

6. J. H. Weil, M. C. Lechner, Bioquimica Geral, Fundação Calouste Gulbenkian, Lisboa, 2000.

7. A. K. Abbas, A. H. Lichtman, S. Pillai, Cellular and Molecular Immunology, Elsevier, Canada, 2014.

8. E. Vacchelli, A. Eggermont, J. Galon, C. Sautes-Fridman, L. Zitvogel, G. Kroemer, L. Galluzzi, Trial watch: Monoclonal antibodies in cancer therapy, Oncoimmunology, 2 (2013), e22789.

9. R. M. Sharkey, D. M. Goldenberg, Targeted therapy of cancer: new prospects for antibodies and immunoconjugates, CA Cancer J Clin, 56 (2006), 226-243.

10. S. J. Shire, W. Gombotz, K. Bechtold-Peters, J. Andya, Volume XI: Current Trends in Monoclonal Antibody Development and Manufacturing, Springer, New York, 2010.

11. G. Kohler, C. Milstein, Continuous cultures of fused cells secreting antibody of predefined specificity, Nature, 256 (1975), 495-497.

12. M. Albitar, Monoclonal Antibodies: Methods and Protocols, Humana Press, 2007.

13. B. J. Scallon, L. A. Snyder, G. M. Anderson, Q. Chen, L. Yan, L. M. Weiner, M. T. Nakada, A review of antibody therapeutics and antibody-related technologies for oncology, Journal of immunotherapy (Hagerstown, Md. : 1997), 29 (2006), 351-364.

14. O. T. Schonherr, E. H. Houwink, Antibody engineering, a strategy for the development of monoclonal antibodies, Antonie van Leeuwenhoek, 50 (1984), 597-623.

15. A. Iannello, A. Ahmad, Role of antibody-dependent cell-mediated cytotoxicity in the efficacy of therapeutic anti-cancer monoclonal antibodies, Cancer Metastasis Rev, 24 (2005), 487-499.

16. O. M. T. S. Group, A randomized clinical trial of OKT3 monoclonal antibody for acute rejection of cadaveric renal transplants. Ortho Multicenter Transplant Study Group, N Engl J Med, 313 (1985), 337-342.

17. L. Brannon-Peppas, J. O. Blanchette, Nanoparticle and targeted systems for cancer therapy, Adv Drug Deliv Rev, 56 (2004), 1649-1659.

18. D. B. Kirpotin, D. C. Drummond, Y. Shao, M. R. Shalaby, K. Hong, U. B. Nielsen, J. D. Marks, C. C. Benz, J. W. Park, Antibody targeting of long-circulating lipidic nanoparticles does not increase tumor localization but does increase internalization in animal models, Cancer Res, 66 (2006), 6732-6740.

19. K. Maruyama, N. Takahashi, T. Tagawa, K. Nagaike, M. Iwatsuru, Immunoliposomes bearing polyethyleneglycol-coupled Fab' fragment show prolonged circulation time and high extravasation into targeted solid tumors in vivo, FEBS letters, 413 (1997), 177-180.

20. W. W. Cheng, T. M. Allen, Targeted delivery of anti-CD19 liposomal doxorubicin in B-cell lymphoma: a comparison of whole monoclonal antibody, Fab' fragments and single chain Fv, J Control Release, 126 (2008), 50-58.

21. J. D. Byrne, T. Betancourt, L. Brannon-Peppas, Active targeting schemes for nanoparticle systems in cancer therapeutics, Adv Drug Deliv Rev, 60 (2008), 1615-1626.

22. C. T. Supuran, A. Scozzafava, A. Casini, Carbonic anhydrase inhibitors, Med Res Rev, 23 (2003), 146-189.

23. C. T. Supuran, Carbonic anhydrases: from biomedical applications of the inhibitors and activators to biotechnological use for CO(2) capture, Journal of enzyme inhibition and medicinal chemistry, 28 (2013), 229-230.

24. W. Chegwidden, N. D. Carter, Y. H. Edward, The Carbonic Anhydrases: New Horizons Springer Basel AG, Berlin, 2000.

25. S. Pastorekova, Z. Zavadova, M. Kostal, O. Babusikova, J. Zavada, A novel quasi-viral agent, MaTu, is a two-component system, Virology, 187 (1992), 620-626.

26. J. Zavada, Z. Zavadova, S. Pastorekova, F. Ciampor, J. Pastorek, V. Zelnik, Expression of MaTu-MN protein in human tumor cultures and in clinical specimens, Int J Cancer, 54 (1993), 268-274.

27. M. Benej, S. Pastorekova, J. Pastorek, Carbonic anhydrase IX: regulation and role in cancer, Sub-cellular biochemistry, 75 (2014), 199-219.

28. A. Lin, S. M. Hahn, Hypoxia imaging markers and applications for radiation treatment planning, Seminars in nuclear medicine, 42 (2012), 343-352.

29. O. Sedlakova, E. Svastova, M. Takacova, J. Kopacek, J. Pastorek, S. Pastorekova, Carbonic anhydrase IX, a hypoxia-induced catalytic component of the pH regulating machinery in tumors, Front Physiol, 4 (2014), 400.

30. J. Pastorek, S. Pastorekova, Hypoxia-induced carbonic anhydrase IX as a target for cancer therapy: from biology to clinical use, Seminars in cancer biology, 31 (2015), 52-64.

31. P. C. McDonald, J. Y. Winum, C. T. Supuran, S. Dedhar, Recent developments in targeting carbonic anhydrase IX for cancer therapeutics, Oncotarget, 3 (2012), 84-97.

32. A. S. Betof, Z. N. Rabbani, M. E. Hardee, S. J. Kim, G. Broadwater, R. C. Bentley, S. A. Snyder, Z. Vujaskovic, E. Oosterwijk, L. N. Harris, J. K. Horton, M. W. Dewhirst, K. L. Blackwell, Carbonic

anhydrase IX is a predictive marker of doxorubicin resistance in early-stage breast cancer independent of HER2 and TOP2A amplification, Br J Cancer, 106 (2012), 916-922.

33. N. Aomatsu, M. Yashiro, S. Kashiwagi, H. Kawajiri, T. Takashima, M. Ohsawa, K. Wakasa, K. Hirakawa, Carbonic anhydrase 9 is associated with chemosensitivity and prognosis in breast cancer patients treated with taxane and anthracycline, BMC cancer, 14 (2014), 400.

34. N. Guedj, F. Bretagnol, P. E. Rautou, L. Deschamps, D. Cazals-Hatem, P. Bedossa, Y. Panis, A. Couvelard, Predictors of tumor response after preoperative chemoradiotherapy for rectal adenocarcinomas, Hum Pathol, 42 (2011), 1702-1709.

35. Y. S. Hong, H. J. Cho, S. Y. Kim, K. H. Jung, J. W. Park, H. S. Choi, J. H. Oh, B. C. Kim, D. K. Sohn, D. Y. Kim, H. J. Chang, Carbonic anhydrase 9 is a predictive marker of survival benefit from lower dose of bevacizumab in patients with previously treated metastatic colorectal cancer, BMC cancer, 9 (2009), 246.

36. J. E. Surfus, J. A. Hank, E. Oosterwijk, S. Welt, M. J. Lindstrom, M. R. Albertini, J. H. Schiller, P. M. Sondel, Anti-renal-cell carcinoma chimeric antibody G250 facilitates antibody-dependent cellular cytotoxicity with in vitro and in vivo interleukin-2-activated effectors, Journal of immunotherapy with emphasis on tumor immunology : official journal of the Society for Biological Therapy, 19 (1996), 184-191.

37. M. Siebels, K. Rohrmann, R. Oberneder, M. Stahler, N. Haseke, J. Beck, R. Hofmann, M. Kindler, P. Kloepfer, C. Stief, A clinical phase I/II trial with the monoclonal antibody cG250 (RENCAREX(R)) and interferon-alpha-2a in metastatic renal cell carcinoma patients, World journal of urology, 29 (2011), 121-126.

38. I. D. Davis, G. A. Wiseman, F. T. Lee, D. N. Gansen, W. Hopkins, A. T. Papenfuss, Z. Liu, T. J. Moynihan, G. A. Croghan, A. A. Adjei, E. W. Hoffman, J. N. Ingle, L. J. Old, A. M. Scott, A phase I multiple dose, dose escalation study of cG250 monoclonal antibody in patients with advanced renal cell carcinoma, Cancer immunity, 7 (2007), 13.

39. J. K. Ahlskog, C. Schliemann, J. Marlind, U. Qureshi, A. Ammar, R. B. Pedley, D. Neri, Human monoclonal antibodies targeting carbonic anhydrase IX for the molecular imaging of hypoxic regions in solid tumours, Br J Cancer, 101 (2009), 645-657.

40. M. Zatovicova, L. Jelenska, A. Hulikova, L. Csaderova, Z. Ditte, P. Ditte, T. Goliasova, J. Pastorek, S. Pastorekova, Carbonic anhydrase IX as an anticancer therapy target: preclinical evaluation of internalizing monoclonal antibody directed to catalytic domain, Current pharmaceutical design, 16 (2010), 3255-3263.

41. S. Pastorekova, M. Zatovicova, J. Pastorek, Cancer-associated carbonic anhydrases and their inhibition, Current pharmaceutical design, 14 (2008), 685-698.

42. Y. Li, H. Wang, E. Oosterwijk, C. Tu, K. T. Shiverick, D. N. Silverman, S. C. Frost, Expression and activity of carbonic anhydrase IX is associated with metabolic dysfunction in MDA-MB-231 breast cancer cells, Cancer Invest, 27 (2009), 613-623.

– This page is intentionally blank –

Chapter 6. Theranostic part I: Magnetic hyperthermia, MRI and cytotoxicity

In the previous chapters, the individual parts of the theranostic system were developed and fully characterized. In this chapter, their suitability as theranostic agents is accessed, starting with a brief introduction to two possible applications: magnetic hyperthermia agents and contrast agents for magnetic resonance imaging. The obtained results are presented and discussed. At the end of this chapter, results of *in vitro* cytotoxicity assays of the produced components of the theranostic system are presented and discussed.

6.1. Introduction

In the last decade several nanoparticle-based products for diagnostic and therapeutic have been approved for clinical applications, and even more are currently under clinical trials [1-5]. An important aspect of nano-medicine research is the development of multifunctional nanoparticles, i.e., nanoparticles (NPs) with the ability to accomplish multiple purposes such as imaging and therapy [1]. Among the different type of nanoparticles, magnetic NPs have been extensively investigated for biomedical applications such as magnetic resonance image (MRI) contrast agents for diagnosis [6-9] and magnetic hyperthermia agents for cancer treatment [10-14].

6.1.1. Magnetic Hyperthermia

Hyperthermia is an old technique recognized as a possible treatment option for cancer. Hippocrates, the father of medicine, treated surface tumors by cauterizing them with a hot iron. More recently further advanced hyperthermia methods have been employed in cancer treatment such as

hot bath water, pyrogen (for example, a mixture of bacterial toxins), perfusion heating, high frequency radiation and magnetic fluid hyperthermia [15]. The theory behind hyperthermia is to kill cancer cells without the use of drugs (chemotherapy) or radiation (radiotherapy) just by increasing temperature in the tumor site. This idea is based on the higher sensitivity of cancer cells to temperature oscillations when compared to normal cells, therefore decreasing the side effects [16, 17]. Tumor cells usually survive in a microenvironment with reduced blow flow, thus favoring hypoxia, acidosis and energy deprivation. Many researchers have demonstrated that hyperthermia reduces blow flow, and as a consequence there is a reduction of oxygen and nutrients supply, leading to intracellular acidosis [18-20].

6.1.1.1. Hyperthermic perfusion

Hyperthermic perfusion was one of the first used techniques, probably because it tends to mimic the natural occurrence phenomena in a mammalian body, i.e., fever. Fever is a mechanism by which the body fights disease because it has more adverse effect on the pathogen or diseased tissue than on the rest of the body, thus allowing the body to overcome the disease condition [21]. As so, hyperthermic perfusion may be used for cancer treatment locally or systemically, as well as for other diseases such as viral infections like hepatitis C [22] or herpes viruses [23]. The whole-body hyperthermic perfusion has the inherent difficulty of body temperature control, thus causing side effects such as elevation of serum transaminases and bilirubin, neurological damage associated with serum hypophosphatemia or even death presumably from massive liver tumor necrosis. Another technique for hyperthermic perfusion is by heating only a cavity of the body like peritoneal or chest cavity with treated fluids. This method is simpler, since it can be accomplished using a hemodialysis equipment, but it may be more aggressive for the patient than the disease itself [24]. Despite of these difficulties, intraperitoneal and intrapleural hyperthermia perfusion is still being performed. Li *et al.* [25] used a swine model of experimental distal gastrostomy with Billroth II reconstruction to investigate the safety of intraoperative and early postoperative continuous hyperthermia intraperitoneal perfusion. The results showed that at perfusate temperature above 43.5 ºC promotes harmful, hampering anastomotic healing and abdominal adhesion. However, at a perfusate temperature of 42.5 ºC, the pigs were not significantly harmed in terms of their vital signs, liver function, renal function, and anastomotic healing. Ba *et al.* [26] went further on the studies of hyperthermic perfusion and studied the efficacy of B-ultrasound guided and laparoscopic-assisted continuous hyperthermic intraperitoneal perfusion chemotherapy to treat malignant ascites. The results showed similar clinical efficacy between both methods being the main difference the duration of surgery and hospitalization costs, but B-ultrasound guided continuous hyperthermic intraperitoneal perfusion chemotherapy was more advantageous.

These authors used the same method for malignant pleural effusion [27]. They were able to heat uniformly the entire pleural cavity with distilled water at 46ºC, while the temperature in the thoracic esophagus did not exceed 40 ºC during one hour of treatment. In addition, chemotherapy was avoided during this procedure. Other authors studied the effect of intrapleural hyperthermic perfusion chemotherapy for metastatic pleural malignancies [28], or for thymoma or thymic carcinoma with pleural dissemination [29], both with improved results. Further, hyperthermic perfusion may be useful for some patients, for example, as adjuvant of chemotherapy, thus sensitizing the tumor cells for the drug. However, it still misses on the specificity and on the ability to maintain a severe temperature control to avoid damaging the surrounding tissues.

6.1.1.2. Hyperthermia by an external electromagnetic field

The application of an external electromagnetic field for hyperthermic treatment is common to several techniques. However, the use of plain wave electromagnetic radiation, such as microwave heating and radiofrequency waves and ultrasound have some disadvantages, for example: low tissue penetration, rapid decrease of energy with depth increase; perturbations induced by tissue interfaces with air or bone; variation in heat effect or focusing on heating deeper organs; all cells are heated [30]. Researchers have employed ways to circumvent these problems and to improve the effectiveness of the treatment, for example using frequency enhancers, catheters, or magnetic particles. The use of small magnetic particles that generate heat by application of an alternate magnetic field of high frequency is currently one of the most interesting and more researched techniques. These particles may be delivered to the target by many ways such as direct injection, antibody targeting or intravascular infusion [30].

6.1.1.3. Magnetic hyperthermia

Magnetic hyperthermia is based on locating magnetic nanoparticles into the desired site and to apply an external alternating magnetic field in such a way to cause heat generation by the magnetic nanoparticles. The magnetic field has the advantage of not being absorbed by the living tissues and enabling deep penetration into those tissues. The important properties of magnetic particles for inducing hyperthermia are non-toxicity, biocompatibility, injectability, high-level accumulation in the target tumor and effective absorption of the energy of the alternating magnetic field [16, 31]. The best candidates for effective treatment are magnetic materials with Curie temperatures between 42 ºC and 60 ºC, since they act as *in vivo* temperature control switches avoiding overheating [16]. An important requirement for hyperthermia treatment is the thermal

dose applied which is related to the volume of the tumor and with the procedure used. For example, for a tumor with a diameter of 3 mm and a concentration of magnetic NPs of 0.01 $g.cm^{-3}$ it is required a power of more than 1 $kW.g^{-1}$. The correlation between the thermal dose applied and the clinical outcome parameters can be estimated by the "cumulative equivalent minutes at 43 ºC". This parameter is related with the heat exposure time at the given temperature and in clinical trials it is attained at 90% of tumor related measure points [17, 31, 32].

Gilchrist and his coworkers [33] were the first to study the use of magnetic iron oxide nanoparticles to induce heat in lymph nodes missed at operation. Later in 1979, Gordon *et al.* [34] first proposed the concept of inducing intracellular hyperthermia using dextran magnetic NPs. Magnetite nanoparticles were administered intravenously to Sprague-Dawley rats bearing mammary carcinomas and showed that AMF-induced heating occurred in their *in vivo* experiments. Jordan *et al*. [35] have proposed magnetic fluid hyperthermia (MFH) in several other comprehensive *in vitro* studies. They have demonstrated that magnetic fluid hyperthermia is able to inactivate tumor cells *in vitro* and that there is a sensitizer effect of ferrofluids at 43 ºC, probably caused by the oxidative stress induced by free ferric ions. With these findings, Jordan and his team proposed MFH as a new method of cancer treatment. Chan *et al.* [36] reported on modified dextran magnetite and its hyperthermic effect by using several human carcinoma cell lines *in vitro*. The specific absorption rate (SAR) of conventional dextran magnetite, which indicates the heat evolution rate in hyperthermia, is low. Magnetite NPs behave as superparamagnetic rather than ferromagnetic due to its small size; hence, its hysteresis loss is very low. These authors controlled the oxygen concentration in the preparation of dextran magnetite and selected particles of approximately 15 nm. Other authors reported that particle size is a critical factor in obtaining a high SAR value [15]. In addition, some theoretical considerations have been made to study the size dependence of the SAR and to predict the optimum parameters of the nanoparticles employed in the magnetic hyperthermia [37-39].

6.1.1.4. Clinical application of hyperthermia

Clinical application of hyperthermia is not established as a single treatment modality but as a way to improve chemotherapy and radiotherapy results, when applied in repetitively short intervals. Local and regional radiofrequency hyperthermia can be regarded as a well-established, non-toxic treatment, which is used according standardized protocols worldwide. In fact, according to the US National Institutes of Health, there are currently 158 clinical studies related with hyperthermia and cancer, from which only three studies evaluate hyperthermia as a single treatment option. The

majority of the clinical trials correlate hyperthermia with chemotherapy or radiation therapy. Although, these studies are distributed among the world (Figure 6.1), there are more studies ongoing in the developed countries [40].

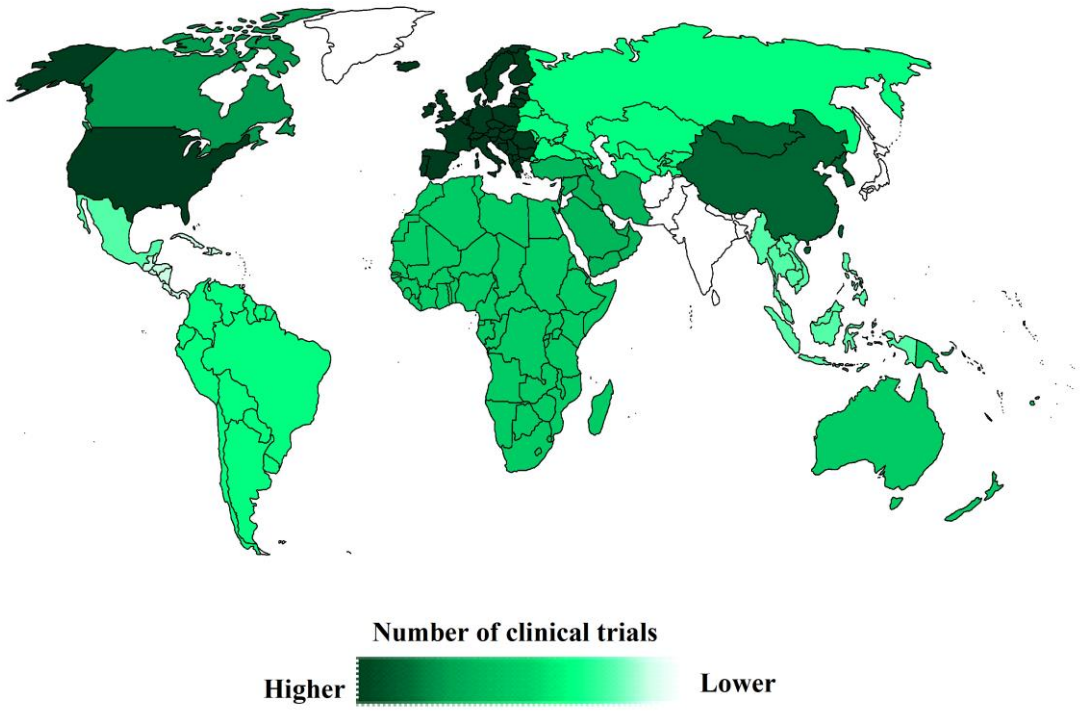

Figure 6.1. World map representing the distribution per region of clinical trials related with hyperthermia and cancer (Source: www.clinicaltrials.gov. Search terms: 'hyperthermia' and 'cancer'. Date of search: August 2015).

NanoTherm™ is a ferrofluid composed of iron oxide nanoparticles with an average diameter of 15 nm, coated with an aminosilane. NanoTherm™ is still in clinical trials for three types of tumors: glioblastoma multiform, prostate carcinoma [41-43] and pancreatic carcinoma. The research group that formed the company MagForce Nanotechnologies AG has tested their iron oxide formulations for glioblastoma multiform in a feasibility study and found that all the patients tolerated the administration of the nanoparticles without further complications. Thermotherapy was applied at magnetic field strengths of 3.8 to 13.5 $kA.m^{-1}$, leading to a T90 median (temperature exceeded by 90% of the tumor) of 40.5 ºC [44]. The autopsy findings of two glioblastoma patients treated with MFH demonstrated that most of the nanoparticles were aggregated and preferentially located in geographic necrosis within the tumor, restricted to the sites of instillation. In

addition, at the borders of the aggregates the nanoparticles were phagocytosed mainly by macrophages [45]. Phase II clinical trials showed an extension of the median OS-2 (overall survival following the first diagnosis of tumor recurrence or progression) to 13.4 months, comparing to 6.2 months of a reference study. In this study, thermotherapy was applied in combination with a lower radiotherapy dosage of 30 Gy [46]. Preclinical studies are also being developed in different types of tumors, such as lung cancer [47], bladder cancer [48], pancreatic cancer [49], or for general cancer treatment [50, 51].

Currently, hyperthermia is approved to treat advanced cancer, such as recurrent rectal cancer, prostate cancer, uterine cancer, head and neck cancer, lung cancer, and breast cancer, in conjugation with chemotherapy and radiotherapy [32, 52].

6.1.2. Magnetic Resonance Imaging

Another application of magnetic NPs is MRI, which is a powerful imaging tool due to its non-invasive nature, high spatial resolution, and tomographic capabilities [16]. MRI is based on the principles of nuclear magnetic resonance (NMR), a spectroscopy technique used to obtain microscopic and physical information about molecules [53].

6.1.2.1. Brief history of MRI

In 1946, Bloch and Purcell first discovered the magnetic resonance phenomenon, both of whom were awarded the Nobel Prize in 1952. In the following two decades, NMR was developed for chemical and physical molecular analysis. Only later, in 1971, Damadian demonstrated that nuclear magnetic relaxation times of healthy tissues and tumoral tissues differed [54].

Meanwhile, Lauterbur developed the first NMR imaging technique, obtaining a “zeugmatogram”, a cross-sectional image of NMR test tubes containing pure water [55]. A few years later, Ernst proposed MRI using phase and frequency encoding, and the Fourier Transform, which are the basis of current MRI techniques [56].

Later on, in 1980, Edelstein demonstrated imaging of the body using Ernst’s technique, taking 5 minutes to obtain a single image [57]. Six years later, this time was reduced to 5 seconds, without highly compromise image resolution [53].

6.1.2.2. MRI fundamentals

MRI fundamentals relay on computer-assisted imaging of relaxation signals of proton spins within a body excited by radiofrequency waves in a strong magnetic field. Most commonly, water

protons (^{1}H) are imaged due to its abundance in living organisms. Water protons that exist in the same magnetic environment resonate at the same frequency. Consequently, NMR signal is proportional to the volume of water. Moreover, MRI may impose special variations on the magnetic field to distinguish spins by their locations. As such, the magnetic gradient causes oscillations at different frequencies in water protons at different locations, originating a map of the spatial distribution of nuclear spins [6, 58, 59].

The relaxation of proton spins to their equilibrium state occurs by two independent processes: longitudinal relaxation, characterized by relaxation time T1, and transverse relaxation, characterized by relaxation time T2. In soft tissues, T1 is around one second while T2 is much faster, within the milliseconds range. However, these values depend upon the tissue type in addition to their dependence on external magnetic fields, providing MRI a large soft tissue contrast [6, 58, 59].

6.1.2.3. MRI contrast agents

Various types of contrast agents have been developed to enhance MRI contrast between healthy and diseased tissues. The main purpose of these agents is to reduce the T1 or T2 relaxation times of protons located nearby. Reduction of T1 relaxation time originates a positive contrast by hypersignaling. On the other hand, reduction of T2 relaxation time originates negative contrast by reducing both T2 and T2* (describing the decay of transverse magnetization taking into account the inhomogeneity of local static magnetic fields). Agents with unpaired electron spins such as gadolinium, manganese, and iron, can effectively reduce the T1 relaxation time. Consequently, these metals have been incorporated into several types of small molecular weight metal-organic complexes to be used as positive contrast agents. One of the most used positive contrast agents is gadolinium (Ga)-based small molecular complexes, such as Ga-DTPA (DTPA, diethylenetriaminepentaacetic acid) [58, 60].

Iron oxide nanoparticles provide contrast enhancement by producing predominantly spin-spin relaxation effects due to the induced local field inhomogeneities, resulting in shorter T1 and T2 relaxation times. However, T1 shortening process requires a close interaction between protons and T1-agents that can be hindered by the thickness of the coating on the NP. On the other hand, T2 shortening is caused by the large susceptibility difference between the particles and surrounding medium, originating microscopic magnetic field gradients. Diffusion of protons through these field gradients leads to dephasing of the proton magnetic moments, thus decreasing T2 relaxation times. As a result, iron oxide NPs are typically used as negative contrast agents.

6.1.2.4. Iron oxide NPs as MRI contrast agents

The use of superparamagnetic iron oxide nanoparticles provides a better differentiation between healthy and pathological tissues and specifically allows for cancer cell targeting [61]. For example, some authors have used magnetic NPs to detect apoptosis, an active process of cellular self-destruction present in many disorders, such as neurodegenerative diseases (e.g. Alzheimer, Parkinson), by MRI [62-64]. The specific targeting may be achieved using numerous biomarkers, specifically overexpressed by the target cells [16]. Monoclonal antibodies were the first targeting agents to exploit molecular recognition to deliver magnetic NPs [65]. Huh *et al*. [66] used magnetic nanocrystals conjugated with Herceptin, a cancer-targeting monoclonal antibody used for breast cancer treatment, and successfully monitored *in vivo* selective targeting events of human cancer cells implanted in live mice. In addition, radioconjugated nanoparticles have been developed using recombinant antibody fragments. DeNardo and his team [67] conjugated a bioprobe (^{111}In- DOTA-ChL6) to polyethylene glycol-iron oxide-impregnated dextran 20 nm particles (^{111}In-probes) and tested its effectiveness in human breast cancer xenografts in mice. The results showed tumor response with heat dose dependence without toxicity. In fact, a member of the same work group invented the magnetic nanoparticles coated with dextran and embedded with a specific ligand to its use in targeted thermotherapy [68]. Other authors tested the recombinant antibody fragments di-scFv-c (^{111}In-DOTA-di-scFv-NP) for imaging and therapy of anti-MUC-1 10 expressing cancers [69]. Further conjugation with fluorescent dye-labeled antibodies enables both *in vitro* and *ex vivo* optical detection of cancer, as well as *in vivo* MRI, which are potentially applicable for an advanced multimodal detection system.

6.2. Materials and methods

All the chemical reagents used in this research work were of analytical grade and used without further purification.

6.2.1. Samples preparation

Iron oxide nanoparticles were prepared according to the protocol described in Chapter 3. For this study were used the following NPs: iron oxide NPs produced by chemical precipitation technique without further treatment (**Pristine Fe_3O_4 NPs**); stabilized with either tri-sodium citrate (**Fe_3O_4 TC**), or oleic acid (**Fe_3O_4 OA 64 mM**); and finally, iron oxide NPs prepared by thermal decomposition technique (**Fe_3O_4 TD**).

Polymeric coating of both chitosan (CS) and *O*-HTCC (the chitosan derivative) was produced according to the procedure described in Chapter 4.

6.2.2. Magnetic hyperthermia

Magnetic hyperthermia measurements were obtained using a DM100 series from *Nb Nanoscale Biomagnetics* apparatus. This apparatus allows measurements at different magnetic field intensities up to 24 $kA.m^{-1}$ with a fixed frequency of 418.5 kHz. The heating ability of 1 ml sample of freshly prepared NPs solution was measured in different sets.

To evaluate the concentration effect on thermal behavior of pristine Fe_3O_4 colloids, measurements were performed during 40 minutes by keeping magnetic field intensity and frequency constant, and varying iron concentration.

To study the influence of both oleic acid and tri-sodium citrate in the heating ability of the NPs samples with different NPs concentrations were subjected to magnetic field intensities from 8 to 24 $kA.m^{-1}$, varying the surfactant concentration.

Samples for *in vitro* heat generation were prepared as following: NPs colloids were dispersed in a hot agar solution (1 wt.% of agar) in a glass vial. Samples were sonicated for 1 min. to disperse the NPs, and then solidified at room temperature. Iron content of all samples was kept constant at 94 mM. Agar phantoms were subjected to an alternating current (AC) magnetic field of 24 $kA.m^{-1}$, with a frequency of 418.5 kHz for 10 minutes. The overall study is summarized in Table 6.1.

Further studies were performed using the following fixed conditions, unless stated otherwise: AC magnetic field of 24 $kA.m^{-1}$, with a frequency of 418.5 kHz for 10 minutes, using 1 ml of sample.

6.2.1. Nuclear magnetic resonance

Measurement of the NPs efficiency as contrast agents for MRI was performed using samples prepared with iron concentrations ranging from 0.2 to 2.6 mM in aqueous agar solution of 0.5 wt.%. The longitudinal and transverse relaxation times of these samples were measured in a Bruker Avance III NMR spectrometer in a 7 T magnetic field at 25 ºC using an inversion-recovery and a Carr Purcell Meiboom Gill impulse sequences, respectively.

Table 6.1. Tested conditions to evaluate the influence of the stabilizers (oleic acid and sodium tri-citrate) in the heating ability of the iron oxide colloids.

	Substrate	**Magnetic field strength ($kA.m^{-1}$)**	**Time of field application (minutes)**	**Iron concentration (mM)**	**Stabilizer concentration (mM)**
Pristine Fe_3O_4	Water	24	40	[0.4 – 376]	--
			10	[5.4 – 107]	
		8, 12, 18, 24	10	[32.6 – 376]	
	Agar	24	10	94	
Fe_3O_4 OA	Water	24	10	[5.4 – 107]	64
		8, 12, 18, 24	10	[32.6 – 376]	[0 – 64]
	Agar	24	10	94	64
Fe_3O_4 TC	Water	24	10	[5.4 – 107]	10
		8, 12, 18, 24	10	[32.6 – 376]	[0 – 30]
	Agar	24	10	94	10

6.2.2. Cytotoxicity assays

Cell viability studies were performed on Vero (fibroblast-like kidney cell) and SaOs-2 (primary osteogenic sarcoma) cell lines using the resazurin assay. The cells were seeded at density of $5x10^4$ $cells.ml^{-1}$ in 96-well plates. SaOs-2 cell line was grown in McCoy 5A medium, supplemented with 10% fetal bovine serum and 1% Penicillin-Streptomycin (10,000 $U.ml^{-1}$), while Vero cell line was grown in Dulbecco's modified Eagle's medium (DMEM) supplemented with 10% fetal bovine serum, 1% Penicillin-Streptomycin (10,000 $U.ml^{-1}$), sodium pyruvate (100 mM), and GlutaMAX™ Supplement followed by incubation at 37 ºC in 5% CO_2 overnight. Next day, cells were treated with fresh medium containing a known concentration of nanoparticles ranging from 12.5 mM to 0.78 mM Fe in each well in triplicates and the plates were incubated for 24 h. After this time, the medium was removed and rezasurin was added to each well. After 2 h incubation, time the absorbance was measured at 570 and 600 nm. Control cells were treated similarly, and were incubated with the respective medium at the same dilution as the one used for incubation with nanoparticles. Cell viability was expressed as a percentage of the control, given by [% cell viability = NP treated cells/control cells x 100].

6.2.3. Magnetic hyperthermia *in vitro*

Cell viability studies were performed by resazurin assay on Vero and SaOs-2 cell lines. The cells were seeded at density of $40x10^4$ cells.ml^{-1} in hyperthermia tubes. SaOs-2 cell line was grown in McCoy 5A medium, supplemented with 10% fetal bovine serum and 1% Penicillin-Streptomycin (10,000 U.ml^{-1}), while Vero cell line was grown in Dulbecco's modified Eagle's medium (DMEM) supplemented with 10% fetal bovine serum, 1% Penicillin-Streptomycin (10,000 U.ml^{-1}), Sodium Pyruvate (100 mM), and GlutaMAX™ Supplement followed by incubation at 37 ºC in 5% CO_2 overnight. Next day, cells were treated with fresh medium containing a known concentration of either 1 mg.ml^{-1} or 5 mg.ml^{-1} in each tube, in triplicates. Hyperthermia control cells and tested tubes were subjected to an AC magnetic field of 24 kA.m^{-1} and frequency of 418.5 kHz for 10 minutes, unless stated otherwise. Then plates were incubated for 24 h. After this time, the medium was removed and rezasurin was added to each well. After 2 h incubation, time the absorbance was measured at 570 and 600 nm. Control cells were treated similarly, and were incubated with the respective medium at the same dilution as the one used for incubation with nanoparticles. Cell viability was expressed as a percentage of the control, given by [% cell viability = NP treated cells/control cells x 100].

6.2.4. Iron content determination

The iron content of the samples was determined using the 1,10-phenantroline colorimetric method [70], similarly to the description in Chapter 3.

To obtain the nanoparticles concentration the formula [Fe] = 0.7 x [NPs] was used. The ratio was obtained from control experiments.

6.3. Results and discussion

6.3.1. Magnetic hyperthermia

Magnetic hyperthermia assays were performed to evaluate the heating ability of the iron oxide nanoparticles produced in Chapter 3. Further, the influence of both surfactants and polymeric coating on the heating ability of the same colloids was also accessed. For a better understanding, the obtained results are divided into bare iron oxide nanoparticles, and polymer-coated iron oxide nanoparticles. It should be noted that bare iron oxide includes Fe_3O_4 NPs stabilized with surfactants.

6.3.1.1. Bare iron oxide NPs

Bare iron oxide NPs includes four types: Fe_3O_4 produced by chemical precipitation method without further treatment (**Pristine Fe_3O_4**), Fe_3O_4 produced by chemical precipitation method stabilized with either tri-sodium citrate (**Fe_3O_4 TC**) or with oleic acid (**Fe_3O_4 OA**), and Fe_3O_4 NPs produced by thermal decomposition method (**Fe_3O_4 TD**).

In a first step the hyperthermia capability of several concentrations of pristine Fe_3O_4 NPs were tested for a frequency of 418.5 kHz, AC magnetic field intensity of 24 kA.m^{-1}, 1 ml of the colloid and 40 minutes of field application. All the heating curves where adjusted to a mathematical model (Equation 6.1) of the ZAR v1.0 software from *Nb nanoscale Biomagnetics*.

$$T(t) = \left(T_0 - T_{eq}\right)e^{-\frac{1}{\tau}t} + T_{eq} \qquad \text{Equation 6.1}$$

In the equation T_0 is the initial temperature of the colloid, T_{eq} is the equilibrium temperature of the colloid; T the maximum temperature reached by the colloid and τ is characteristic time of heating.

Figure 6.2 represents the temperature variation of pristine Fe_3O_4 NPs as a function of iron concentration obtained using the above stated experimental conditions. The red line is an exponential adjustment to the obtained data. This exponential adjustment demonstrates that the heating ability of the NPs tends to decrease for high NPs concentration according to the empirical equation:

$$\Delta T(ºC) = -33.2e^{-\frac{[Fe](mM)}{11.1}} + 60.0 \qquad \text{Equation 6.2}$$

with a correlation factor (R^2) of 0.995. Exponential adjustment to experimental data suggests an increase of generated heat as the NPs concentration increases with a tendency to saturate at a very high iron concentration. This is correlated to the appearance of agglomerates. Superparamagnetic nanoparticles show weak dipole-dipole interaction, whereas the exchange interactions dominate. On the other hand, agglomerates behave like a particle, with an effective volume larger than a single core, behaving like a ferromagnetic particle.

Figure 6.3 represents the temperature variation as a function of iron concentration for the optimal surfactant concentrations. These experiments were performed for 10 minutes, with an AC magnetic field intensity of 24 kA.m^{-1} and a frequency of 418.5 kHz.

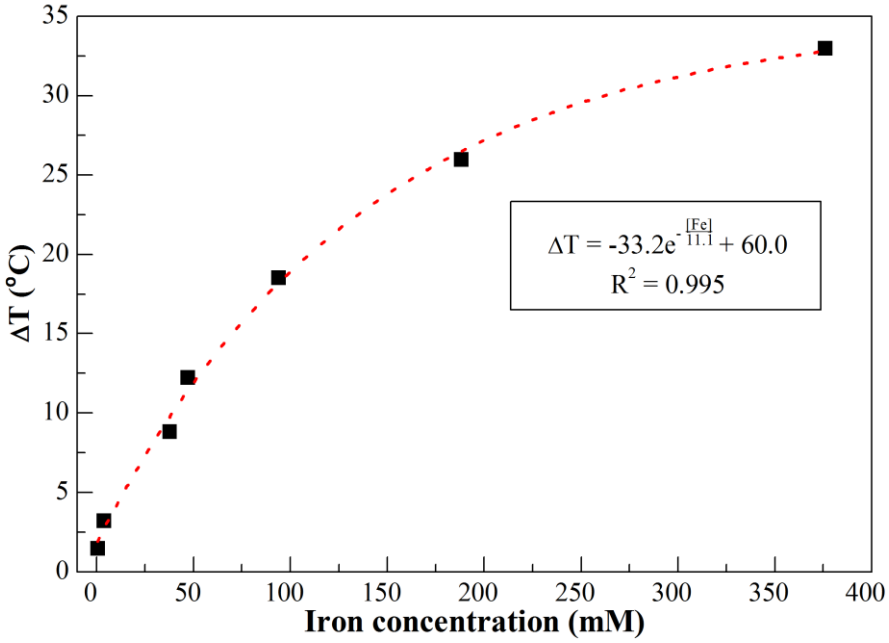

Figure 6.2. Temperature variation generated by pristine Fe_3O_4 during 40 minutes of an AC magnetic field application with intensity of 24 $kA.m^{-1}$ and 418.5 kHz as a function of iron concentration.

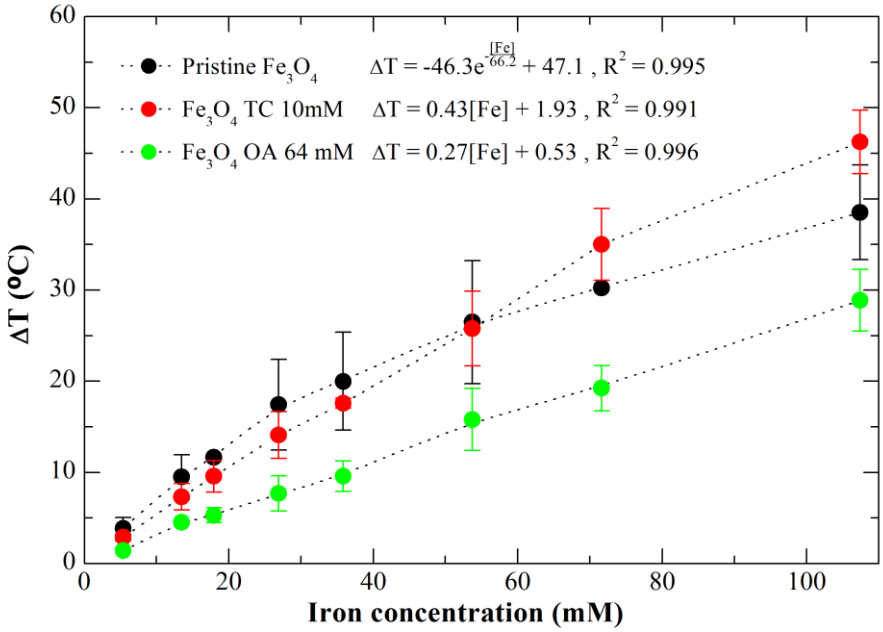

Figure 6.3. Generated temperature by pristine Fe_3O_4 (black dots), tri-sodium citrate 10 mM (red dots) and oleic acid 64 mM (green dots) stabilized NPs during 10 minutes of an AC magnetic field application with intensity of 24 $kA.m^{-1}$ and 418.5 kHz of frequency as a function of iron concentration.

Similarly to the observed in Figure 6.2, it is possible to verify that the pristine Fe_3O_4 heating ability tends to stabilize for high iron concentrations as expressed by the empirical equation: $\Delta T =$

$-46.3e^{-\frac{[Fe]}{66.2}} + 47.1$. However, when the surfactant is present this effect is no longer observed and the best fitting equation is $\Delta T = 0.27[Fe] + 0.53$ and for OA $\Delta T = 0.43[Fe] + 1.93$ for TC. The surfactant reduces the aggregation and so the heating ability is still efficient even for higher concentration of iron NPs. However, if normal body temperature is considered, a temperature variation of five degrees is enough to achieve the hyperthermia range of temperature (around 42ºC). Within the tested conditions, an iron concentration above 10 mM for pristine and tri-sodium citrate Fe_3O_4 and 20 mM for oleic acid Fe_3O_4 is enough to generate the required temperature.

The influence of the surfactants in the heating ability of the NPs was tested with four iron concentrations: 32.6, 60.2, 125 and 376 mM, and four different applied AC magnetic field intensities: 8, 12, 18, and 24 kA.m^{-1}. Both frequency and time of experiment were fixed to 418.5 kHz and 10 minutes, respectively.

SAR is use to characterize the heating efficiency of a magnetic material through energy absorption during its exposure to an AC magnetic field. The value is defined as the quantity of power absorbed by the sample per mass unit (W.g^{-1}) and was calculated using the following equation:

$$SAR\ (W/g) = \frac{C_{NP} m_{Fe} + C_l m_l}{m_{Fe}} \left(\frac{dT}{dt}\right)_{max} \qquad \text{Equation 6.3}$$

where $(dT/dt)_{max}$ is the maximum gradient of the temperature curve of the colloid submitted to an hyperthermia test, C_{NP} is the specific heat of the nanoparticles, C_l is the specific heat of the liquid, m_l is the fluid mass, and m_{Fe} is the iron mass in the colloid.

An accurate estimation of SAR values of magnetic colloids must be taken under adiabatic conditions. As such, to calculate SAR values we used the maximum of the derivative dT/dt. Since maximum increase always occurs in the initial few seconds of the experiments the adiabatic conditions are secured [71].

SAR values as a function of the surfactant concentration are shown in Figure 6.4 for the four different magnetic field intensities and different iron concentrations. The results clearly show that the addition of surfactants, even in concentrations as low as 5 mM for tri-sodium citrate or 8 mM for oleic acid, strongly reduces the SAR values to values below 60 W.g^{-1} and 20 W.g^{-1} respectively. Moreover, this behavior is observed independently of the iron concentration or magnetic field applied. However, a small increase in SAR value is obtained for concentrations bellow 2 mM of tri-sodium citrate. This increase depends on the iron concentration and on the magnetic field applied.

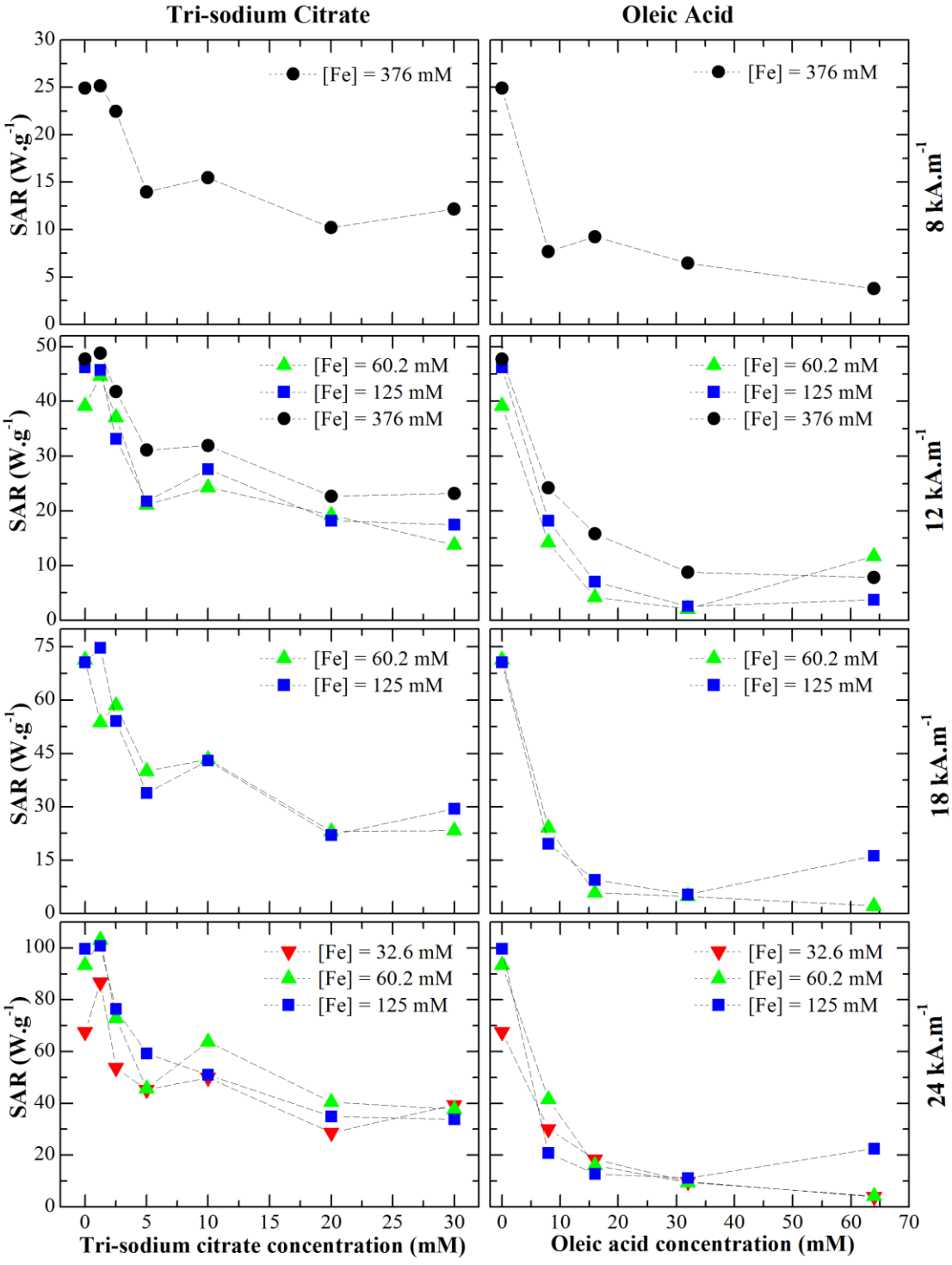

Figure 6.4. SAR values as a function of surfactant concentration for different iron concentrations at 8, 12, 18 and 24 $kA.m^{-1}$of the AC magnetic field strength, with a fixed frequency of 418.5 kHz.

Figure 6.5 represents the temperature variation obtained from magnetic hyperthermia test as a function of iron concentration for pristine NPs and 4 different concentrations of oleic acid. These

experiments were performed for 10 minutes with an AC magnetic field intensity of 24 kA.m^{-1} and a frequency of 418.5 kHz. The heating ability of oleic acid coated NPs seem to have the same relation with the iron concentration, as observed for pristine Fe_3O_4 NPs. Moreover, with an amount of 8% of oleic acid the heating ability of Fe_3O_4 NPs is not greatly reduced, probably due to the small amount of surfactant. As the oleic acid concentration increases to values above the critical concentration of the formation of a bilayer, the heating ability of Fe_3O_4 greatly reduces. However, if the concentration increases and the bilayer stabilizes, the heating ability of the NPs is recovered, although not to values as high as for pristine Fe_3O_4.

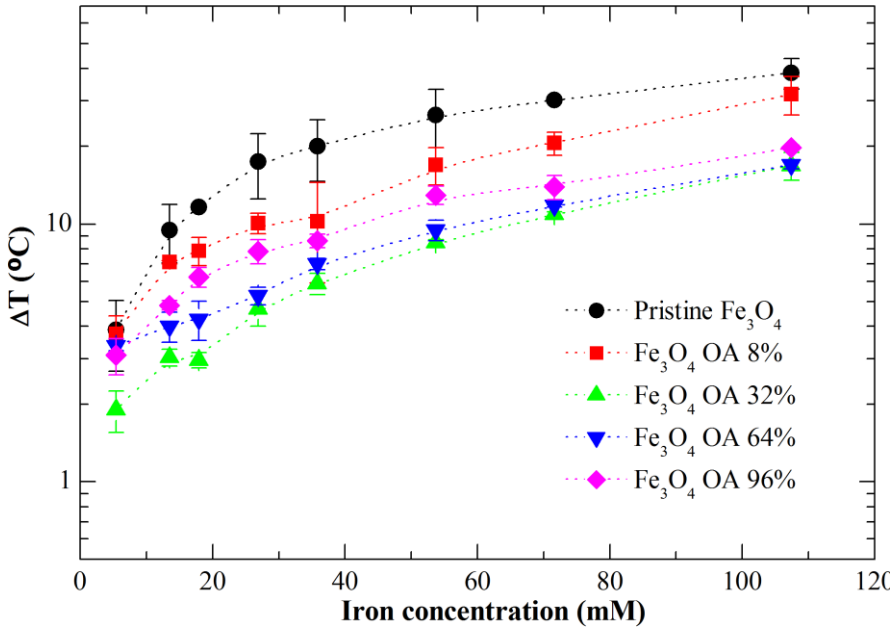

Figure 6.5. Temperature variation as a function of iron concentration generated by pristine Fe_3O_4 NPs (black dots) and Fe_3O_4 OA NPs with different surfactant concentrations: 8% (red dots) 64 mM (green dots) and 96% (pink dots) generated by the application of an AC magnetic field, for 10 minutes, with intensity of 24 kA.m^{-1} and with 418.5 kHz of frequency.

In 2002, Rosensweig [37] developed relationships based on rotational relaxation of single domain magnetic particles dispersed in a liquid matrix. The magnetic material when submitted to an AC magnetic field exhibits both Brownian and Néel relaxations. Nevertheless, Néel relaxation must not be allowed to dominate. The expressions of Brownian (Equation 6.4) and Néel (Equation 6.5) relaxations times are the following:

$$\tau_B = \tau_0 . \frac{3\eta . V_h}{k . T_B} \qquad \text{Equation 6.4}$$

$$\tau_N = \tau_0 . e^{\frac{K_{eff}.V_m}{k.T}}$$ Equation 6.5

Where η is the viscosity of the carrier liquid, V_h is the effective hydrodynamic volume and V_m is the particle volume, k is the Boltzmann constant, T_B is temperature, K_{eff} is the magnetic anisotropy and τ_0 is the characteristic flipping time [72]. These relaxation times are related to the vanishing of the remnant magnetization once the applied AC magnetic field is removed.

When the nanoparticles are in suspension both relaxation paths are present. Furthermore, Brownian relaxation occurs due to the ability of the particles to freely rotate. This relaxation mechanism is mainly due to the NPs hydrodynamic volume and the viscosity of the carrier fluid as seen in Equation 6.4. However, when the NPs are injected into the body or directly into the tissue the NPs are taken up by tumor cells and stay fixed. In this situation, no Brownian relaxation may occur when an AC magnetic field is applied [73, 74].

Considering this magnetic hyperthermia tests in agar phantoms containing a known concentration of NPs have been performed. Figure 6.6 shows that SAR values decrease for lower iron concentration of pristine iron oxide NPs, which is related to the aggregation of pristine iron oxide NPs, affecting their heating generation ability as previously discussed.

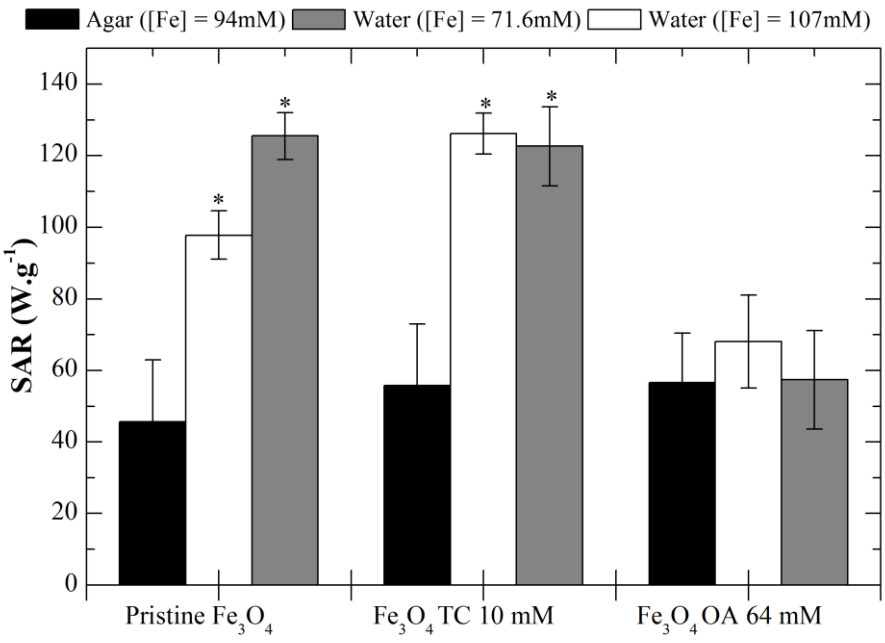

Figure 6.6. Comparison of SAR values of pristine and coated NPs in agar phantoms and water. The results are expressed as the average ± standard deviation for 3 independent experiments. * $p<0.05$ compared with the respective agar sample.

For pristine and tri-sodium citrate-stabilized Fe_3O_4 NPs, SAR values decrease about 50% when comparing to the ones obtained for water. Agar phantoms cause the entrapment of the NPs, eliminating their Brownian movements. Therefore, heat generation can only be attributed to Néel relaxation. However, for oleic acid stabilized NPs the SAR value is almost the same as the one of water dispersed NPs. This is related to the bilayer formed around the iron oxide cores where oleic acid has a similar effect than agar phantoms, entrapping the NPs and eliminating their Brownian movements, which can also explain the low M_S observed in these samples (Chapter 3).

Goya *et al.* [75] have proposed a versatile diagram to identify the dominant heating mechanism of magnetic single domains in magnetic fluid hyperthermia. This diagram considers the magnetic mechanism of relaxation (Néel relaxation) and the viscous mechanism of relaxation (Brownian relaxation). The probabilities of viscous and magnetic relaxation are proportional to $1/\tau_B$ and $1/\tau_N$, respectively. In this diagram, they have identified three regions: 1) $\tau_B < 0.1\tau_N$ where the viscous mechanism is dominant (viscous region), 2) $\tau_N < 0.1\tau_B$ where magnetic mechanism is dominant and 3) $\tau_N \sim \tau_B$ where both mechanisms contribute for heat generation. Analyzing the results in Table 6.2 is clear that when the NPs are dispersed in water the Brownian mechanism is dominant. In this case, the NPs are able to rotate freely and so the viscous mechanism is dominant over the magnetic mechanism. However, when the NPs are dispersed in the agar gel, they are entrapped into the gel and so their rotation is limited. In this case, the Néel mechanism is clearly dominant.

Table 6.2. Estimated Brownian (τ_B) or viscous and Néel (τ_N) or magnetic relaxation times for pristine and tri-sodium citrate (TC) 10mM and oleic acid (OA) 64 mM iron oxide nanoparticles both in water and agar 1% wt.

Sample	Substrate	τ_N (s)	τ_B (s)
Pristine Fe_3O_4	Agar	1.43×10^{-8}	1.01×10^{-5}
	Water		2.36×10^{-11}
Fe_3O_4 TC 10 mM	Agar	7.57×10^{-8}	6.26×10^{-6}
	Water		1.46×10^{-11}
Fe_3O_4 OA 64 mM	Agar	6.78×10^{-8}	2.55×10^{-5}
	Water		5.96×10^{-11}

For pristine and tri-sodium citrate iron oxide NPs the reduction in the SAR value is probably due to this change in the dominant relaxation mechanism. However, for oleic acid this difference is

not observed. In this case, although the viscosity of the fluid is not clearly affected, the coating acts as an entrapment for the iron oxide cores, eliminating their mobility, and consequently decreasing the Brownian relaxation mechanism influence for the effective relaxation time of the nanoparticles.

6.3.1.1.1.Iron oxide NPs produced by thermal decomposition

As previously described in Chapter 3, thermal decomposition technique was used to produce highly monodispersed NPs. This technique is based on the thermal decomposition of an iron precursor, $Fe(acac)_3$, in triethyleneglycol (TREG) at high temperature, without the use of further stabilizers. This method is composed of two heating stages: the first related with solution dehydration, and the second one causing decomposition of the iron precursor at the solvent boiling point. With the purpose of optimizing the synthesis protocol, different times on the first and second stages were tested. Table 6.3 displays the permanence times in each stage from each tested condition to optimize synthesis of iron oxide NPs by thermal decomposition technique.

Table 6.3. Tested conditions to optimize the synthesis of iron oxide NPs by thermal decomposition technique.

Sample	First stage (120 ºC)	Second stage (300 ºC)
Fe_3O_4 TD 1	-	30 min
Fe_3O_4 TD 2	30 min	30 min
Fe_3O_4 TD 3	1h	30 min
Fe_3O_4 TD 4	1h	1h
Fe_3O_4 TD 5	1h	2h

Ideally, each of these conditions would be characterized by different techniques in order to correctly access the obtained differences. However, only magnetic hyperthermia was used to perform this evaluation. Figure 6.7 shows SAR values obtained by subjecting each Fe_3O_4 TD sample to an AC magnetic field intensity of 24 $kA.m^{-1}$ and a frequency of 418.5 kHz for 10 minutes, at an iron concentration of 71.6 mM. The obtained results clearly show that sample 3 is able to generate more heat than the others are. These results correlate with visual analysis of each sample, i.e., except for sample 3, the other ones suffer a high degree of sedimentation after a few hours, while Fe_3O_4 TD 3 remained stable, without any sedimentation, for a large period of time (at least three months).

Further analysis of Fe_3O_4 TD 3 sample was performed to access if the synthesis method influenced the heating ability of the iron oxide NPs. For that, the heating ability of Fe_3O_4 TD 3 NPs was evaluated at different iron concentrations, keeping the remaining parameters constant: AC magnetic field intensity of 24 $kA.m^{-1}$, frequency of 418.5 kHz, 1 ml of sample and 10 minutes of application (Figure 6.8). The obtained results show that although the relation between the obtained temperature variation and iron concentration is linear, the temperature variation is much smaller than the one obtained for either pristine Fe_3O_4 NPs, or stabilized Fe_3O_4 NPs, for the same iron concentration. Consequently, although the obtained iron oxide nanoparticles by thermal decomposition technique are expected to be highly stable and are monodisperse in size, its application in magnetic hyperthermia is compromised by the low heating ability of the obtained NPs. Nevertheless, further characterization of Fe_3O_4 TD NPs is required, and possibly a more detailed optimization of the synthesis protocol.

6.3.1.1. Polymer-coated iron oxide NPs

After complete evaluation of the heating ability of bare iron oxide nanoparticles, the influence of polymeric coating has accessed. Primarily, low molecular weight chitosan (38 kDa) was used as a polymeric coating for three types of iron oxide nanoparticles: pristine Fe_3O_4, Fe_3O_4 TC 10 mM, and Fe_3O_4 OA 64 mM. In the three cases, the amount of CS and tripolyphosphate was kept constant, while the amount of iron oxide NPs was varied. Moreover, magnetic hyperthermia measurements were performed for not freeze-dried and freeze-dried samples. This later variation intended to verify is freeze-drying process, which is used as a way to prevent polymer degradation upon storage, influences the heating ability of the NPs. Figure 6.9 show the variation of the generated temperature by each sample as a function of iron concentration. As a reference, bare iron oxide NPs results in the same tested conditions were added to each case.

In the case of pristine Fe_3O_4 NPs (Figure 6.9 A) the presence of chitosan coating does not influence the generated temperature by the iron oxide cores. However, when chitosan-coated NPs are freeze-dried, the generated temperature by the iron oxide cores is lower. On the other hand, chitosan-coated Fe_3O_4 TC 10 mM NPs (Figure 6.9 B) present a reduction in the generated temperature compared to the reference. As such, in this case chitosan has a negative influence for the application of Fe_3O_4 TC 10 mM NPs in magnetic hyperthermia. Similar to pristine Fe_3O_4 NPs, freeze-drying process also reduces the generated temperature by the iron oxide cores. The same was observed for chitosan-coated Fe_3O_4 OA 64 mM NPs (Figure 6.9 C). In this case, no differences are found between freeze-dried and not freeze-dried NPs, probably due to the very small

ΔT values obtained. The reduction of the generated temperature after freeze-drying process may be related to the formation of some aggregates of Fe_3O_4 NPs during the process.

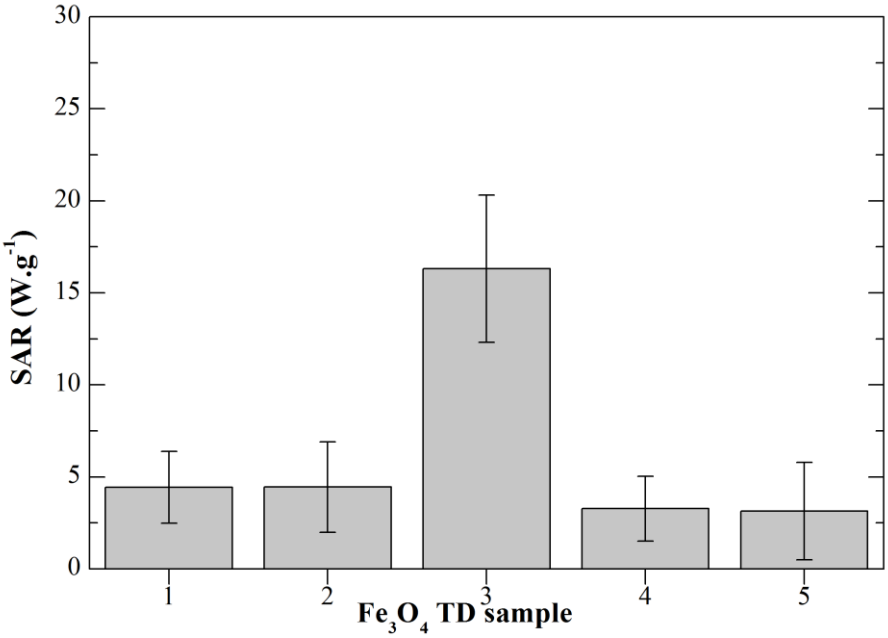

Figure 6.7. Comparison of SAR values of Fe_3O_4 TD NPs samples in water solution at an iron concentration of 71.6 mM. The results are expressed as the average ± standard deviation for 3 independent experiments.

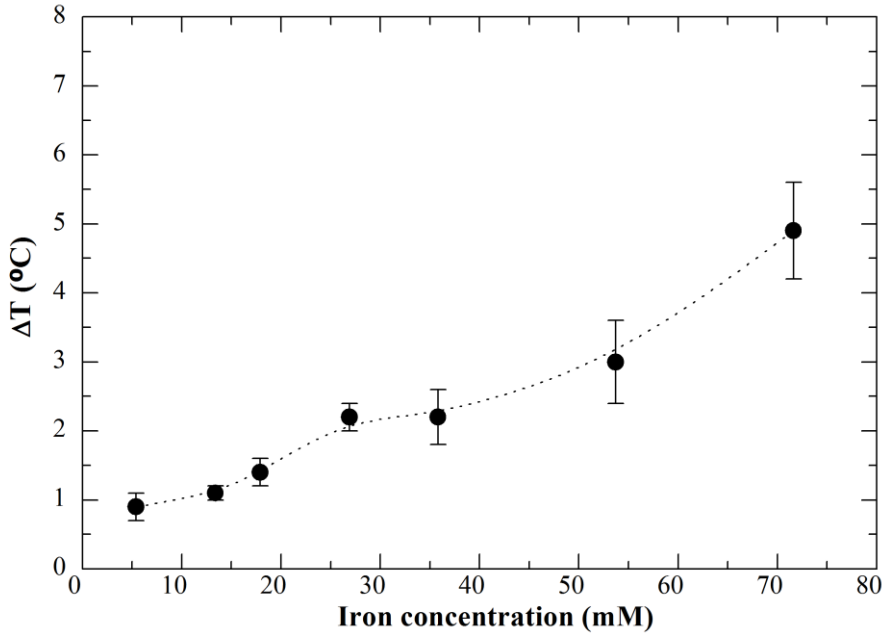

Figure 6.8. Generated temperature by Fe_3O_4 TD 3 NPs during 10 minutes of an AC magnetic field application with intensity of 24 $kA.m^{-1}$ and 418.5 kHz of frequency as a function of iron concentration.

The influence of polymeric coating, CS or *O*-HTCC (the chitosan derivative synthesized in Chapter 4), was accessed for the Fe_3O_4 NPs studied. Each of the polymers was used with two molecular weights. Figure 6.10 shows the obtained SAR values at a constant iron concentration of 6.3 mM and the samples were freeze-dried prior to magnetic hyperthermia measurements. Figure 6.10 shows that SAR values decrease with the increase of polymer molecular weight and that SAR values are higher for *O*-HTCC Fe_3O_4 NPs than CS Fe_3O_4 NPs. This behavior is even more evident for Fe_3O_4 TD NPs, were the difference is around 7-fold. However, in the case of Fe_3O_4 OA 64 mM NPs, the result is contradictory and may be related to the presence of an extra positive charge in *O*-HTCC, compared to chitosan, causing the later superficial charges of NPs unbalanced.

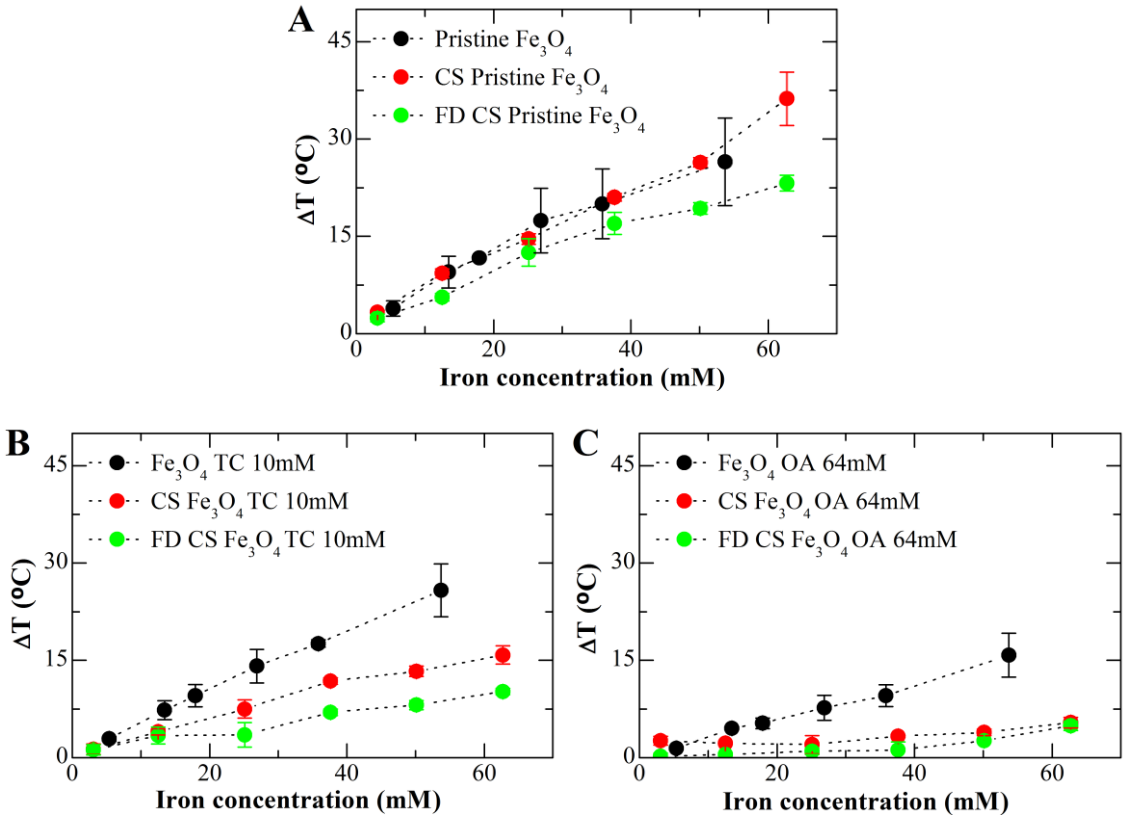

Figure 6.9. Generated temperature by pristine Fe_3O_4 (A), Fe_3O_4 TC 10 mM, (B) and Fe_3O_4 OA 64 mM (C) during 10 minutes of an AC magnetic field application with intensity of 24 $kA.m^{-1}$ and 418.5 kHz of frequency as a function of iron concentration. Comparison between bare Fe_3O_4 NPs, not freeze-dried and freeze-dried (FD) chitosan-coated Fe_3O_4 NPs is displayed for each case.

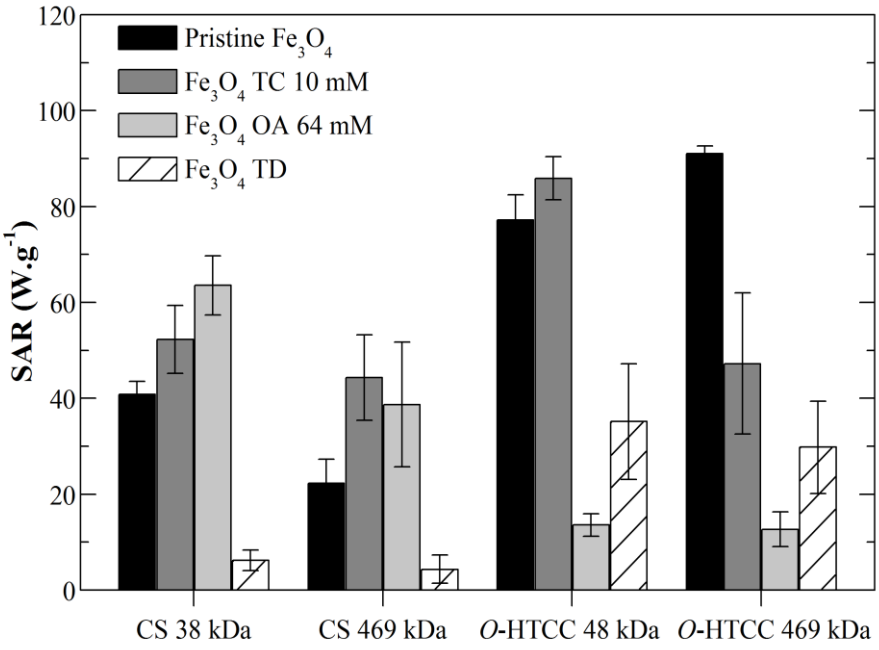

Figure 6.10. Comparison of SAR values of freeze-dried polymer-coated Fe_3O_4 NPs. Fe_3O_4 NPs were coated with either CS or *O*-HTCC of low and high molecular weight. The results are expressed as the average ± standard deviation for 3 independent experiments.

6.3.2. NMR relaxometry

NMR relaxometry experiments were performed for a restrict number of samples due to equipment limitations. T1 and T2 relaxation times were measured for Fe_3O_4 OA 96% NPs, as a continuation of the study of oleic acid bilayer, since this was the most stable sample (see Chapter 3).

Figure 6.11 show the transverse relaxation rate for Fe_3O_4 OA 96% NPs in different pH environment. The aim was to evaluate the existence of a difference in these parameters between OA NPs with and without the formation of a bilayer that make them efficient as contrast agents for MRI. As such, this was investigated at pH 5, 7, and 9.

The following equation was fitted to the experimental transverse relaxation data [76]:

$$\frac{1}{T2} = \frac{1}{T2_0} + r_2[Fe] \qquad \text{Equation 6.6}$$

Where r_2 stands for the NPs transverse relaxivity, a measurement of the efficiency of the nanosystem as a contrast agent for MRI, [Fe] is the iron concentration, and $1/T2_0$ is the transverse relaxation rate of the medium without Fe_3O_4 NPs. The same equation can be fitted for the longitudinal relaxation rate experimental data and the longitudinal relaxivity obtained at pH 5, 7 and 9 was 0.05, 0.05, 0.07 $(mMs)^{-1}$, respectively.

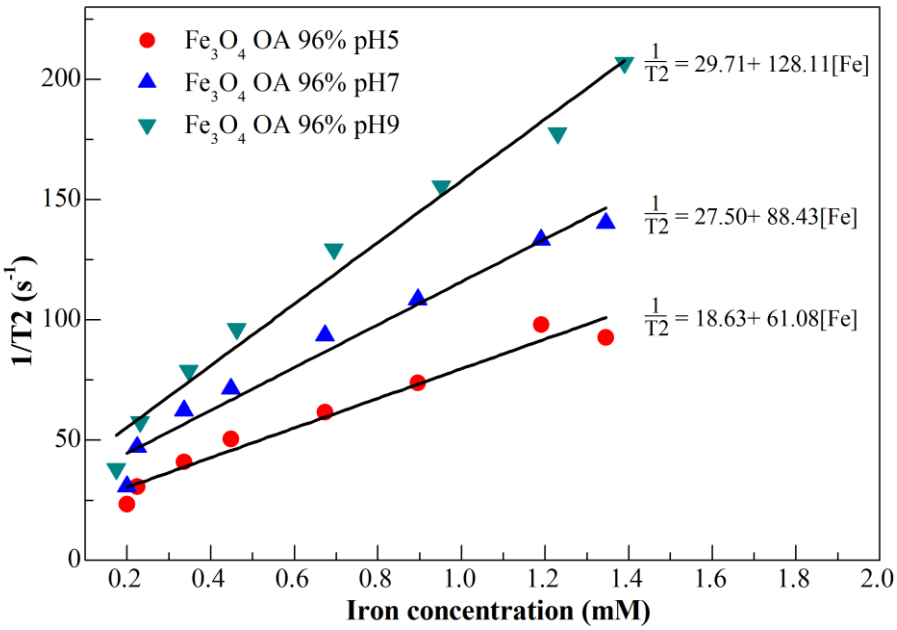

Figure 6.11. Transverse relaxation rate (1/T2) for Fe_3O_4 OA 96% NPs at different pH: 5, 7, and 9, as a function of iron concentration.

It is clear that the medium longitudinal relaxation time is slightly altered. However, for the transverse relaxivity the obtained values for the three pH 5, 7 and 9 were 68.6, 88.4 and 128.1 $(mMs)^{-1}$, respectively. Thus, the transverse relaxation time remarkably increases with pH as expected by the enhancement of the proton exchange rate.

6.3.3. Cytotoxicity assays

When developing a biomaterial one of the most important characteristics, if not the most important one, is its toxicity. In the present research work, two cell lines were used to evaluate NPs cytotoxicity *in vitro*: Vero, a fibroblast-like kidney cell, and SaOs-2, an osteosarcoma cell line. The purpose was to evaluate differences between a "normal" cell line and a tumoral cell line.

Cytotoxicity of the iron oxide cores was evaluated for pristine Fe_3O_4, Fe_3O_4 TC 10 mM, Fe_3O_4 OA 64 mM, and Fe_3O_4 TD. The results are expressed as % of cell viability calculated by [% cell viability = NP treated cells/control cells x 100]. Control cells were maintained with the same condition as the tested ones, without the addition of nanoparticles. Figure 6.12 and Figure 6.13 show the obtained results of Vero and SaOs-2, respectively, cell line viability after 24 hours of exposition to the four types of iron oxide nanoparticles.

The results show that both Vero and SaOs-2 cell lines do not show significant toxicity to pristine and tri-sodium citrate Fe_3O_4 NPs in the range of 62.5 – 1000 μg.ml^{-1}. However, oleic acid Fe_3O_4 the cytotoxicity profile is different. For Vero cell line an iron concentration above 500 μg.ml^{-1} reduces cell viability up to 20%, thus causing severe cytotoxic effects. For SaOs-2 cell line, cell viability is reduced for the tested range of NP concentration, although the cytotoxic effect is mild for a NP concentration up to 250 μg.ml^{-1}. Finally, Fe_3O_4 TD NPs do not cause significant cytotoxic effects on Vero cell lines at a concentration below 500 μg.ml^{-1}. However, SaOs-2 cell lines are more sensitive to this type of iron oxide nanoparticles, thus showing severe cytotoxic effects with a NP concentration above 500 μg.ml^{-1}.

Chitosan is known to be a non-toxic and biocompatible biopolymer. However, the presence of cross-linking agents may cause some toxic effects. Chemical modifications such as the ones to produce chitosan' derivatives can also cause some toxic effects. Considering these facts, cytotoxicity assays were also performed for both chitosan and *O*-HTCC NPs, at the highest and lowest molecular weight.

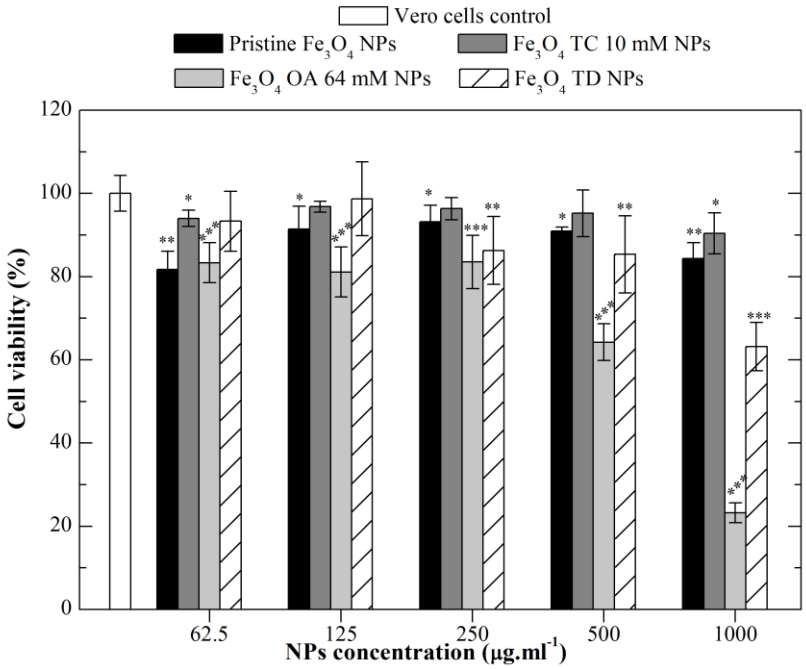

Figure 6.12. Vero cell line viability after 24 h exposition to four types of iron oxide nanoparticles: pristine Fe_3O_4, Fe_3O_4 TC 10 mM, Fe_3O_4 OA 64 mM, and Fe_3O_4 TD. Data is expressed as average ± standard deviation for at least three independent experiments. *p<0.05, **p<0.005, ***p<0.001 compared to untreated control cells.

Figure 6.14 and Figure 6.15 show the obtained results of Vero and SaOs-2, respectively, cell line viability after 24 h ours of exposition to either chitosan or *O*-HTCC NPs. Analyzing the obtained results for Vero cell line, neither chitosan nor *O*-HTCC show severe toxic effects in the range of concentration tested. Low molecular weight chitosan (38 kDa) causes a small reduction in cell viability, which is more evident at the higher concentration tested (500 μg.ml^{-1}). Since low molecular weight CS was obtained by depolymerisation of high molecular weight CS, it is possible that some of the used reagents have remained in the sample, thus causing cytotoxic effects.

SaOs-2 cell lines show a different cytotoxic profile when exposed to polymeric NPs. Chitosan nanoparticles of 469 kDa cause some severe cytotoxic effects for the intermediate concentrations. Since it is not a concentration-dependent effect, the best explanation for these results is the presence of reagents from the preparation of the NPs in this sample, which may be cytotoxic for SaOs-2 cell lines. As for *O*-HTCC NPs, NP concentrations above 125 μg.ml^{-1} cause cell viability reduction. Moreover, *O*-HTCC NPs of 469 kDa at a concentration of 500 μg.ml^{-1} cause severe cytotoxic effects, reducing cell viability to 5%.

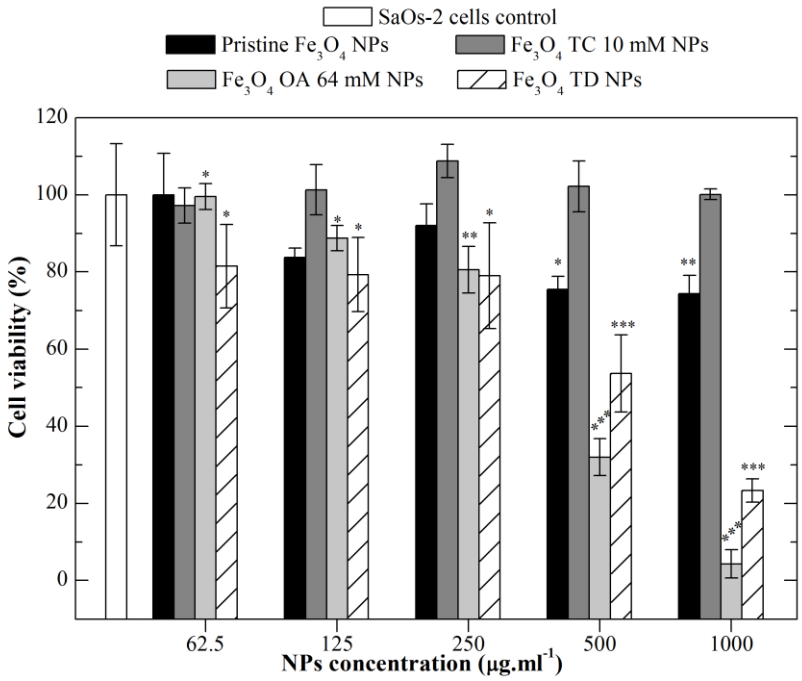

Figure 6.13. SaOs-2 cell line viability after 24 h exposition to four types of iron oxide nanoparticles: pristine Fe_3O_4, Fe_3O_4 TC 10 mM, Fe_3O_4 OA 64 mM, and Fe_3O_4 TD. Data is expressed as average ± standard deviation for at least three independent experiments. *p<0.05, **p<0.005, ***p<0.001 compared to untreated control cells.

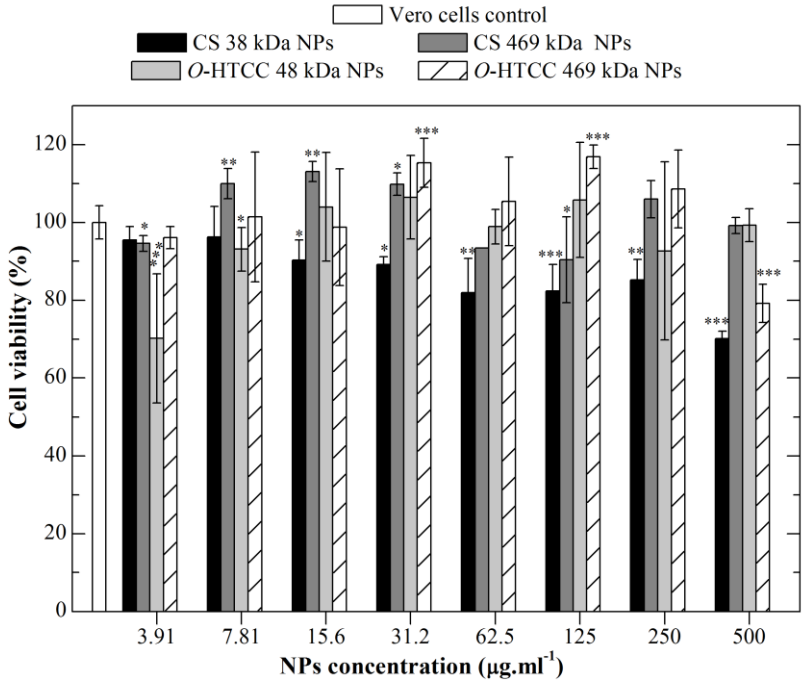

Figure 6.14. Vero cell line viability after 24 h exposition to chitosan NPs at 38 and 469 kDa, and to *O*-HTCC NPs at 48 and 469 kDa. Data is expressed as average ± standard deviation for at least three independent experiments. *p<0.05, **p<0.005, ***p<0.001 compared to untreated control cells.

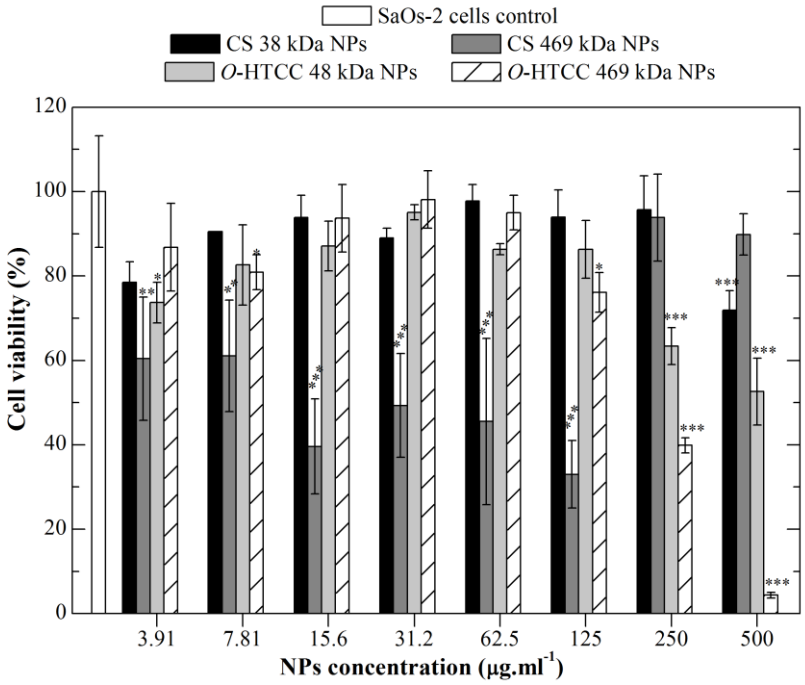

Figure 6.15. SaOs-2 cell line viability after 24 h exposition to chitosan NPs at 38 and 469 kDa, and to *O*-HTCC NPs at 48 and 469 kDa. Data is expressed as average ± standard deviation for at least three independent experiments. *p<0.05, **p<0.005, ***p<0.001 compared to untreated control cells.

6.3.4. Magnetic hyperthermia *in vitro*

A preliminary study of the cytotoxic effects caused by magnetic hyperthermia in the presence of pristine Fe_3O_4 NPs was performed. Four samples were used to perform this study: Vero and SaOs-2 cell control (cells without any further treatment); hyperthermia control (control cells exposed to an AC magnetic field with intensity of 24 $kA.m^{-1}$ and 418.5 kHz of frequency for 10 minutes); NPs control (cells exposed to NPs at either 1 $mg.ml^{-1}$ or 5 $mg.ml^{-1}$ during 24h, without the application of the AC magnetic field); and NPs + hyperthermia (cells exposed to NPs and an AC magnetic field with intensity of 24 $kA.m^{-1}$ and 418.5 kHz of frequency for 10 minutes in the case of 1 $mg.ml^{-1}$ NPs, or 200 seconds in the case of 5 $mg.ml^{-1}$). The later application of the AC magnetic field was performed for a shorter period of time since after 200 seconds the sample reaches a temperature of 43ºC, which was considered the limit temperature before massive cell death.

Figure 6.16 shows the obtained results of both Vero and SaOs-2 cell line viability before and after application of magnetic hyperthermia at 1 $mg.ml^{-1}$ pristine Fe_3O_4 NPs. In both cases, no cytotoxic effect was observed neither by the presence of NPs, nor by the application of the AC magnetic field. The main reason is that the NP concentration used was not enough to cause a reduction is cell viability. Moreover, although the application of the AC magnetic field was performed during 10 minutes, it was not enough to achieve a hyperthermic temperature (all samples achieve a maximum of 37 ºC, considering that the starting temperature was room temperature).

However, an important conclusion can be retained by the obtained results: the application of an AC magnetic field does not have any harm effect of both Vero and SaOs-2 cell lines.

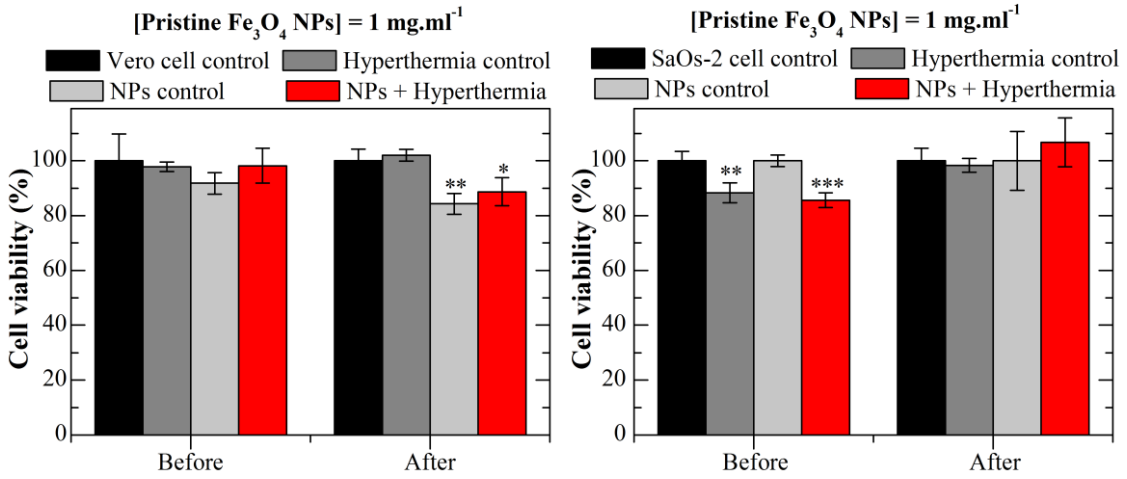

Figure 6.16. Vero and SaOs-2 cell line viability before and after 24 h exposition to hyperthermia with and without the presence of pristine Fe_3O_4 NPs at 1 $mg.ml^{-1}$. Data is expressed as average ± standard deviation for at least three independent experiments. *p<0.05, **p<0.005, ***p<0.001 compared to control cells.

Figure 6.17 shows the obtained results of both Vero and SaOs-2 cell line viability before and after application of magnetic hyperthermia at 5 mg.ml^{-1} pristine Fe_3O_4 NPs. In this case, samples with NPs were subjected to the AC magnetic field during 200 seconds, since at this time a temperature around 43 ºC was achieved. If the test were maintained for 10 minutes, the temperature would most probably continue to rise up to temperatures where massive cell death would have occurred.

The conclusion obtained in the later results can be obtained in this case: the application of an AC magnetic field do not cause harm to both cell lines tested. However, now hyperthermic temperatures were achieved. Consequently, cytotoxic effects were observed in both cases. In Vero cell lines a significant difference was observed between cytotoxicity caused by the presence of pristine Fe_3O_4 NPs alone, and by the application of an AC magnetic field in the presence of pristine Fe_3O_4 NPs. As such, the application of the magnetic field increases cell death, increasing the effectiveness of pristine Fe_3O_4 NPs. However, in SaOs-2 cell lines, both the presence of pristine Fe_3O_4 NPs as the application of the AC magnetic field in the presence of pristine Fe_3O_4 NPs, cause severe cell death. As such, no significant differences were found between both cases. As previously observed, SaOs-2 cell lines are more sensitive to pristine Fe_3O_4 NPs-induced cell death, which may justify the obtained results.

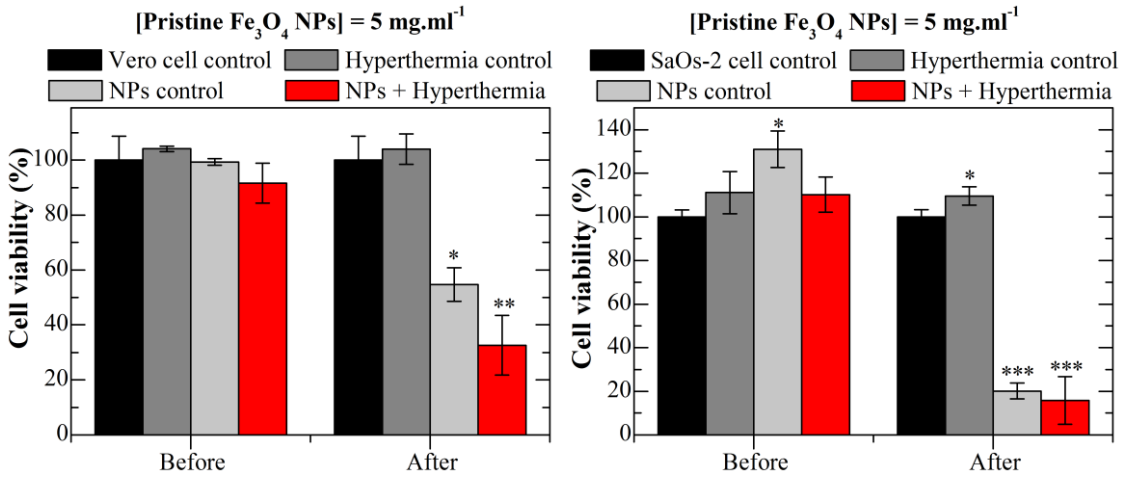

Figure 6.17. Vero and SaOs-2 cell line viability before and after 24 h exposition to magnetic hyperthermia with and without the presence of pristine Fe_3O_4 NPs at 5 mg.ml^{-1}. Data is expressed as average ± standard deviation for at least three independent experiments. *p<0.05, **p<0.005, ***p<0.001 compared to control cells.

Comparison of the later results with *in vitro* cytotoxicity assays seems contradictory. However, it is important to consider that *in vitro* cytotoxicity assays were performed using 5x10^4 cells per well, while magnetic hyperthermia was performed using 40x10^4 cells per vial. This is the main

reason why a concentration of 1mg.ml^{-1} of pristine Fe_3O_4 NPs was not enough to reduce cell viability. The ratio between the number of cells and the NPs concentration is 5 cells per μg of NPs in the cytotoxicity assays. In magnetic hyperthermia tests, the ratio is higher: 40 cells per μg of NPs for 1 mg.ml^{-1}, and 8 cells per μg of NPs for 5 mg.ml^{-1}.

These preliminary data were preliminary results and some factors were not controlled such as cells were seeded in glass vials designed for hyperthermia tests, instead of containers designed for cell culture, and cell culture laboratory and the magnetic hyperthermia device are located in different buildings, requiring transport of cell cultures. This is also the reason why hyperthermia tests started at room temperature instead of 37 ºC. Further studies such as NPs uptake by cells should be performed to corroborate the obtained results. Moreover, NPs concentration should be optimized to allow the application of the AC magnetic field for a period of 10 minutes, similar to control cells. Also, different cell lines should be used to verify if tumoral cells are indeed more sensitive to both Fe_3O_4 NPs-induced cell death in the presence of an AC magnetic field or not.

6.4. Summary

Current interest in nanotechnology has expanded the range of applications, especially in the biomedical field. In the last decade, several nanoparticle-based products for diagnostics and therapeutics have been approved for clinical applications. Among the different type of NPs, magnetic NPs are of great interest due to their unique physical properties and ability to function at cellular and molecular level. These types of NPs have several biomedical applications such as contrast agents for magnetic resonance imaging and magnetic hyperthermia.

In the present chapter, the iron oxide nanoparticles synthesized and characterized in Chapter 3 were tested for its applicability in both MRI and magnetic hyperthermia. The influence of polymeric coating developed in Chapter 4 was also accessed in magnetic hyperthermia tests and cytotoxicity assays were performed for both iron oxide nanoparticles and polymeric nanoparticles.

Magnetic hyperthermia measurements were performed in different set of samples to fully characterize the synthesized iron oxide NPs. The main conclusion was the generated temperature during the application of an AC magnetic field is proportional to the iron concentration. This conclusion is true for pristine Fe_3O_4 NPs, surfactant-stabilized Fe_3O_4 NPs, and polymeric-coated Fe_3O_4 NPs. The surfactants (tri-sodium citrate and oleic acid) reduce SAR values of Fe_3O_4 NPs, which is more evident for higher surfactant concentrations. For concentrations of oleic acid below the formation of the bilayer, SAR value is reduced in a directly proportional manner to surfactant

concentration. However, when the bilayer stabilizes, the heating ability of the NPs is partially recovered.

Magnetic hyperthermia assays were performed in agar phantoms to simulate the *in vivo* situation, where NPs are taken up by tumor cells and stay fixed. In this situation, no Brownian relaxation occurs when an AC magnetic field is applied. Therefore, heat generation can only be attributed to Néel relaxation. The elimination of Brownian movements highly affect pristine and TC 10 mM Fe_3O_4 NPs, but in in Fe_3O_4 NPs stabilized with an oleic acid bilayer no significant differences were observed between Fe_3O_4 NPs dispersed in water or agar phantoms. The conclusion is that oleic acid has a similar effect than agar phantoms, entrapping the NPs and eliminating their Brownian movements, which can also explain the low M_S observed in these samples.

The heating ability of coated Fe_3O_4 NPs shows that chitosan coating does not influence the temperature generated by the iron oxide cores. However, freeze-drying process reduces the generated temperature, probably due to some aggregation that occurs during the process. In the case of surfactant-stabilized Fe_3O_4 NPs, the presence of chitosan reduced the heating ability of the iron oxide cores. Furthermore, SAR value decreases with the increase of polymer molecular weight; and *O*-HTCC Fe_3O_4 NPs have a higher SAR value than CS Fe_3O_4 NPs. The later difference is even more evident for Fe_3O_4 TD NPs, were the difference is around 7-fold.

NMR relaxometry experiments were performed for a restrict number of samples, T1 and T2 relaxation times were measured for Fe_3O_4 OA 96% NPs for three pH: 5, 7, and 9. The medium longitudinal relaxation time is slightly altered while the transverse relaxation time remarkably increases with pH, which was expected due to the enhancement of the proton exchange rate.

Cytotoxicity assays were performed in two cell lines: Vero, a fibroblast-like kidney cell, and SaOs-2, an osteosarcoma cell line. The results show that both Vero and SaOs-2 cell lines viability is not significantly affected by pristine and tri-sodium citrate Fe_3O_4 NPs in the range of tested concentrations. However, oleic acid Fe_3O_4 causes a significant reduction in cell viability in both Vero and SaOs-2 cell lines. Finally, Fe_3O_4 TD NPs do not cause significant cytotoxic effects on both Vero and SaOs-2 cell lines at a NP concentration below 500 $\mu g.ml^{-1}$.

Cytotoxicity assays in polymeric NPs (chitosan and *O*-HTCC) do not show a significant reduction in cell viability in both SaOs-2 and Vero cell lines. In some cases, a reduction of cell viability was attributed to the presence of remnant reagents from NPs synthesis or chitosan depolymerisation.

Magnetic hyperthermia assays were performed in both Vero and SaOs-2 cell lines and it was observed that the magnetic field does not harm both cell lines tested. Consequently, the presence

of pristine Fe_3O_4 NPs is the major contribution for cell viability reduction. Furthermore, if hyperthermic temperature is achieved during the application of the AC magnetic field, pristine Fe_3O_4 NPs-induced cytotoxicity is enhanced, at least in Vero cell lines.

The present work demonstrated the potential of the developed iron oxide NPs as magnetic hyperthermia agents. Several details were studied such as NPs concentration, Brownian and Néel relaxations, the influence of surfactants and polymeric coating, among others. Moreover, cytotoxicity assays were performed. However, further studies should be performed before the developed iron oxide NPs are perfectly suitable for *in vivo* magnetic hyperthermia tests.

6.5. References

1. G. Bao, S. Mitragotri, S. Tong, Multifunctional nanoparticles for drug delivery and molecular imaging, Annu Rev Biomed Eng, 15 (2013), 253-282.

2. D. ME, C. ZG, S. DM, Nanoparticle therapeutics: an emerging treatment modality for cancer, Nat. Rev. Drug Discov., 7 (2008), 771.

3. P. D, K. JM, H. S, F. OC, M. R, L. R, Nanocarriers as an emerging platform for cancer therapy, Nat. Nanotechnol., 2 (2007), 751.

4. K. BY, R. JT, C. WC, Nanomedicine, N. Engl. J. Med., 363 (2010), 2434.

5. J. Hrkach, D. V. Hoff, A. M. Mukkaram, E. Andrianova, J. Auer, Preclinical development and clinical translation of a PSMA-targeted docetaxel nanoparticle with a differentiated pharmacological profile, Sci. Transl. Med., 4 (2012), 128ra139.

6. C. Sun, J. S. Lee, M. Zhang, Magnetic nanoparticles in MR imaging and drug delivery, Adv Drug Deliv Rev, 60 (2008), 1252-1265.

7. A. Jafari, S. Farjami Shayesteh, M. Salouti, K. Boustani, Dependence of structural phase transition and lattice strain of Fe3O4 nanoparticles on calcination temperature, Indian Journal of Physics, 89 (2014), 551-560.

8. J. Atefeh, S. Mojtaba, S. Saber Farjami, H. Zahra, R. Ahmad Bitarafan, B. Komail, N. Ali, Synthesis and characterization of Bombesin-superparamagnetic iron oxide nanoparticles as a targeted contrast agent for imaging of breast cancer using MRI, Nanotechnology, 26 (2015), 075101.

9. W. Ming, Z. Da, Z. Yongyi, W. Lingjie, L. Xiaolong, L. Jingfeng, Nanocluster of superparamagnetic iron oxide nanoparticles coated with poly (dopamine) for magnetic field-targeting, highly sensitive MRI and photothermal cancer therapy, Nanotechnology, 26 (2015), 115102.

10. T. Kobayashi, Cancer hyperthermia using magnetic nanoparticles, Biotechnol J, 6 (2011), 1342-1347.

11. I. Obaidat, B. Issa, Y. Haik, Magnetic Properties of Magnetic Nanoparticles for Efficient Hyperthermia, Nanomaterials, 5 (2015), 63-89.

12. G. Eneko, S. Olivier, C. Juan-Mari, G. Jose Angel, M. Stéphane, P. Fernando, Specific absorption rate dependence on temperature in magnetic field hyperthermia measured by dynamic hysteresis losses (ac magnetometry), Nanotechnology, 26 (2015), 015704.

13. P. Guardia, R. Di Corato, L. Lartigue, C. Wilhelm, A. Espinosa, M. Garcia-Hernandez, F. Gazeau, L. Manna, T. Pellegrino, Water-soluble iron oxide nanocubes with high values of specific absorption rate for cancer cell hyperthermia treatment, ACS Nano, 6 (2012), 3080-3091.

14. J. Kolosnjaj-Tabi, R. Di Corato, L. Lartigue, I. Marangon, P. Guardia, A. K. Silva, N. Luciani, O. Clement, P. Flaud, J. V. Singh, P. Decuzzi, T. Pellegrino, C. Wilhelm, F. Gazeau, Heat-generating iron oxide nanocubes: subtle "destructurators" of the tumoral microenvironment, ACS Nano, 8 (2014), 4268-4283.

15. A. K. Gupta, M. Gupta, Synthesis and surface engineering of iron oxide nanoparticles for biomedical applications, Biomaterials, 26 (2005), 3995-4021.

16. C. C. Berry, Progress in functionalization of magnetic nanoparticles for applications in biomedicine, Journal of Physics D: Applied Physics, 42 (2009), 224003.

17. E. Kita, T. Oda, T. Kayano, S. Sato, M. Minagawa, H. Yanagihara, M. Kishimoto, C. Mitsumata, S. Hashimoto, K. Yamada, N. Ohkohchi, Ferromagnetic nanoparticles for magnetic hyperthermia and thermoablation therapy, Journal of Physics D: Applied Physics, 43 (2010), 474011.

18. P. Vaupel, F. Kallinowski, P. Okunieff, Blood flow, oxygen and nutrient supply, and metabolic microenvironment of human tumors: a review, Cancer Res, 49 (1989), 6449-6465.

19. B. Hildebrandt, P. Wust, O. Ahlers, A. Dieing, G. Sreenivasa, T. Kerner, R. Felix, H. Riess, The cellular and molecular basis of hyperthermia, Crit Rev Oncol Hematol, 43 (2002), 33-56.

20. C. Streffer, Aspects of metabolic change after hyperthermia, Recent results in cancer research. Fortschritte der Krebsforschung. Progres dans les recherches sur le cancer, 107 (1988), 7-16.

21. J. P. Sites, P. R. Glassel, M. D. Miller, C. B. Norgaard, T. A. Roman, D. J. Ziebarth, in, BioThermics, Inc., US, 2002.

22. K. E. Groth, T. C. Kelly, T. L. Westerbeck, G. Blick, in, First Cicle Medical, Inc., US, 2002.

23. K. E. Groth, T. C. Kelly, T. L. Westerbeck, G. Blick, in, First Circle Medical, Inc., US, 2002.

24. J. Landy, M. Gildersleeve, Y. W. P. Tseng, in, Belmont Instrument Corporation, US, 2010.

25. S. Li, Y. L. Zhang, J. Y. Sun, Y. W. Hua, P. H. Wu, Safe temperature range for intraoperative and early postoperative continuous hyperthermic intraperitoneal perfusion in a swine model of experimental distal gastrectomy with Billroth II reconstruction, J Transl Med, 11 (2013), 181.

26. M. C. Ba, H. Long, S. Z. Cui, Y. Q. Tang, Y. B. Wu, X. L. Zhang, H. S. Tang, S. X. Bai, Multivariate comparison of B-ultrasound guided and laparoscopic continuous circulatory hyperthermic intraperitoneal perfusion chemotherapy for malignant ascites, Surg Endosc, 27 (2013), 2735-2743.

27. M.-C. Ba, H. Long, Y. Wang, Y.-Q. Tang, Y.-B. Wu, X.-L. Zhang, S.-Z. Cui, Intrapleural hyperthermic perfusion using distilled water at 48°C for malignant pleural effusion, J Cancer Res Clin Oncol, 139 (2013), 2005-2012.

28. A. F. Isik, M. Sanli, M. Yilmaz, F. Meteroglu, O. Dikensoy, A. Sevinc, C. Camci, B. Tuncozgur, L. Elbeyli, Intrapleural hyperthermic perfusion chemotherapy in subjects with metastatic pleural malignancies, Respir Med, 107 (2013), 762-767.

29. L. Yu, Y. Jing, S. Ma, F. Li, Y. F. Zhang, Cytoreductive surgery combined with hyperthermic intrapleural chemotherapy to treat thymoma or thymic carcinoma with pleural dissemination, Onco Targets Ther, 6 (2013), 517-521.

30. S. K. Jones, K. F. Rutherford, A. J. Ruys, B. N. Gray, in, US, 2006.

31. S. Wada, L. Yue, K. Tazawa, I. Furuta, H. Nagae, S. Takemori, T. Minamimura, New local hyperthermia using dextran magnetite complex (DM) for oral cavity: experimental study in normal hamster tongue, Oral diseases, 7 (2001), 192-195.

32. B. Minev, Cancer Management in Man: Chemotherapy, Biological Therapy, Hyperthermia and Supporting Measures, Media, (2010).

33. R. K. Gilchrist, R. Medal, W. D. Shorey, R. C. Hanselman, J. C. Parrott, C. B. Taylor, Selective inductive heating of lymph nodes, Ann Surg, 146 (1957), 596-606.

34. R. T. Gordon, J. R. Hines, D. Gordon, Intracellular hyperthermia. A biophysical approach to cancer treatment via intracellular temperature and biophysical alterations, Med Hypotheses, 5 (1979), 83-102.

35. A. Jordan, P. Wust, R. Scholz, B. Tesche, H. Fähling, T. Mitrovics, T. Vogl, J. Cervós-navarro, R. Felix, Cellular uptake of magnetic fluid particles and their effects on human adenocarcinoma cells exposed to AC magnetic fieldsin vitro, Int J Hyperther, 12 (1996), 705-722.

36. D. C. F. Chan, D. B. Kirpotin, P. A. Bunn, Synthesis and Evaluation of Colloidal Magnetic Iron-Oxides for the Site-Specific Radiofrequency-Induced Hyperthermia of Cancer, Journal of Magnetism and Magnetic Materials, 122 (1993), 374-378.

37. R. E. Rosensweig, Heating magnetic fluid with alternating magnetic field, Journal of Magnetism and Magnetic Materials, 252 (2002), 370-374.

38. J. Carrey, B. Mehdaoui, M. Respaud, Simple models for dynamics hysteresis loop calculations of magnetic single-domain nanoparticles: Application to magnetic hyperthermia optimization, Journal of Applied Physics, 109 (2011), 083921.

39. K. M. Krishnan, Biomedical Nanomagnetics: A Spin Through Possibilities in Imaging, Diagnostics, and Therapy, IEEE Trans Magn, 46 (2010), 2523-2558.

40. Home - Clinicaltrials.gov, accessed on August 21, 2015,

41. M. Johannsen, U. Gneveckow, B. Thiesen, K. Taymoorian, C. H. Cho, N. Waldofner, R. Scholz, A. Jordan, S. A. Loening, P. Wust, Thermotherapy of prostate cancer using magnetic nanoparticles: feasibility, imaging, and three-dimensional temperature distribution, Eur Urol, 52 (2007), 1653-1661.

42. M. Johannsen, U. Gneveckow, K. Taymoorian, B. Thiesen, N. Waldofner, R. Scholz, K. Jung, A. Jordan, P. Wust, S. A. Loening, Morbidity and quality of life during thermotherapy using magnetic nanoparticles in locally recurrent prostate cancer: results of a prospective phase I trial, Int J Hyperthermia, 23 (2007), 315-323.

43. M. Johannsen, U. Gneveckow, L. Eckelt, A. Feussner, N. WaldÖFner, R. Scholz, S. Deger, P. Wust, S. A. Loening, A. Jordan, Clinical hyperthermia of prostate cancer using magnetic nanoparticles: Presentation of a new interstitial technique, Int J Hyperther, 21 (2005), 637-647.

44. K. Maier-Hauff, R. Rothe, R. Scholz, U. Gneveckow, P. Wust, B. Thiesen, A. Feussner, A. von Deimling, N. Waldoefner, R. Felix, A. Jordan, Intracranial thermotherapy using magnetic nanoparticles combined with external beam radiotherapy: results of a feasibility study on patients with glioblastoma multiforme, J Neurooncol, 81 (2007), 53-60.

45. F. K. H. van Landeghem, K. Maier-Hauff, A. Jordan, K.-T. Hoffmann, U. Gneveckowc, R. Scholz, B. Thiesen, W. Brück, A. von Deimling, Post-mortem studies in glioblastoma patients treated with thermotherapy using magnetic nanoparticles, Biomaterials, 30 (2009), 52-57.

46. K. Maier-Hauff, F. Ulrich, D. Nestler, H. Niehoff, P. Wust, B. Thiesen, H. Orawa, V. Budach, A. Jordan, Efficacy and safety of intratumoral thermotherapy using magnetic iron-oxide nanoparticles combined with external beam radiotherapy on patients with recurrent glioblastoma multiforme, J Neurooncol, 103 (2011), 317-324.

47. T. Sadhukha, T. S. Wiedmann, J. Panyam, Inhalable magnetic nanoparticles for targeted hyperthermia in lung cancer therapy, Biomaterials, 34 (2013), 5163-5171.

48. T. R. Oliveira, P. R. Stauffer, C. T. Lee, C. D. Landon, W. Etienne, K. A. Ashcraft, K. L. McNerny, A. Mashal, J. Nouls, P. F. Maccarini, W. F. Beyer, Jr., B. Inman, M. W. Dewhirst, Magnetic fluid hyperthermia for bladder cancer: a preclinical dosimetry study, Int J Hyperthermia, 29 (2013), 835-844.

49. L. Wang, J. Dong, W. Ouyang, X. Wang, J. Tang, Anticancer effect and feasibility study of hyperthermia treatment of pancreatic cancer using magnetic nanoparticles, Oncol Rep, 27 (2012), 719-726.

50. T. Sadhukha, L. Niu, T. S. Wiedmann, J. Panyam, Effective elimination of cancer stem cells by magnetic hyperthermia, Mol Pharm, 10 (2013), 1432-1441.

51. D. Zhao, W. Huang, M. N. Rahaman, D. E. Day, D. Wang, Y. Gu, Preparation and characterization of composite microspheres for brachytherapy and hyperthermia treatment of cancer, Materials Science and Engineering: C, 32 (2012), 276-281.

52. A. Matsumine, K. Kusuzaki, T. Matsubara, K. Shintani, H. Satonaka, T. Wakabayashi, S. Miyazaki, K. Morita, K. Takegami, A. Uchida, Novel hyperthermia for metastatic bone tumors with magnetic materials by generating an alternating electromagnetic field, Clin Exp Metastasis, 24 (2007), 191-200.

53. J. P. Hornak, The Basics of MRI, in, Interactive Learning Software, Henietta, NY, https://www.cis.rit.edu/htbooks/mri/inside.htm, 1996-2014.

54. R. Damadian, Tumor detection by nuclear magnetic resonance, Science, 171 (1971), 1151-1153.

55. P. C. Lauterbur, Image Formation by Induced Local Interactions: Examples Employing Nuclear Magnetic Resonance, Nature, 242 (1973), 190-191.

56. A. Kumar, D. Welti, R. R. Ernst, NMR Fourier zeugmatography, Journal of Magnetic Resonance (1969), 18 (1975), 69-83.

57. W. A. Edelstein, J. M. Hutchison, G. Johnson, T. Redpath, Spin warp NMR imaging and applications to human whole-body imaging, Physics in medicine and biology, 25 (1980), 751-756.

58. R. Qiao, C. Yang, M. Gao, Superparamagnetic iron oxide nanoparticles: from preparations to in vivo MRI applications, Journal of Materials Chemistry, 19 (2009), 6274.

59. M. Mahmoudi, S. Sant, B. Wang, S. Laurent, T. Sen, Superparamagnetic iron oxide nanoparticles (SPIONs): development, surface modification and applications in chemotherapy, Adv Drug Deliv Rev, 63 (2011), 24-46.

60. Q. A. Pankhurst, J. Connolly, S. K. Jones, J. Dobson, Applications of magnetic nanoparticles in biomedicine, Journal of Physics D: Applied Physics, 36 (2003), R167-R181.

61. M. A. Oghabian, N. M. Farahbakhsh, Potential Use of Nanoparticle Based Contrast Agents in MRI: A Molecular Imaging Perspective, Journal of Biomedical Nanotechnology, 6 (2010), 203-213.

62. M. Zhao, D. A. Beauregard, L. Loizou, B. Davletov, K. M. Brindle, Non-invasive detection of apoptosis using magnetic resonance imaging and a targeted contrast agent, Nat Med, 7 (2001), 1241-1244.

63. H. Poptani, A. Puumalainen, O. Grohn, S. Loimas, R. Kainulainen, S. Yla-Herttuala, R. Kauppinen, Monitoring thymidine kinase and gancyclovir induced changes in rat malignant glioma in vivo by nuclear magnetic resonance imaging, Cancer Gene Ther, 5 (1998), 101-109.

64. F. G. Blankenberg, P. D. Katsikis, R. W. Storrs, C. Beaulieu, D. Spielman, J. Y. Chen, L. Naumovski, J. F. Tait, Quantitative analysis of apoptotic cell death using proton nuclear magnetic resonance spectroscopy, Blood, 89 (1997), 3778-3786.

65. Cerdan S, Lotscher H R, Kunnecke B, S. J., Monoclonal antibody-coated magnetite particles as contrast agents in magnetic resonance imaging of tumors Mag Reson Med, 12 (1989), 151-163.

66. Y. M. Huh, Y. W. Jun, H. T. Song, S. Kim, J. S. Choi, J. H. Lee, S. Yoon, K. S. Kim, J. S. Shin, J. S. Suh, J. Cheon, In vivo magnetic resonance detection of cancer by using multifunctional magnetic nanocrystals, J Am Chem Soc, 127 (2005), 12387-12391.

67. S. J. DeNardo, G. L. DeNardo, A. Natarajan, L. A. Miers, A. R. Foreman, C. Gruettner, G. N. Adamson, R. Ivkov, Thermal Dosimetry Predictive of Efficacy of ^{111}In-ChL6 Nanoparticle AMF–Induced Thermoablative Therapy for Human Breast Cancer in Mice, Journal of Nuclear Medicine, 48 (2007), 437-444.

68. R. Ivkov, in, US, 2006.

69. A. Natarajan, S. J. Denardo, G. L. Denardo, C. Gruettnre, in, The regents of the University of California, Oakland CA, USA, 2010.

70. M. Talelli, C. J. Rijcken, T. Lammers, P. R. Seevinck, G. Storm, C. F. van Nostrum, W. E. Hennink, Superparamagnetic iron oxide nanoparticles encapsulated in biodegradable thermosensitive polymeric micelles: toward a targeted nanomedicine suitable for image-guided drug delivery, Langmuir, 25 (2009), 2060-2067.

71. a. S. Lübbe, C. Alexiou, C. Bergemann, Clinical applications of magnetic drug targeting, The Journal of surgical research, 95 (2001), 200-206.

72. X. Liu, M. D. Kaminski, Y. Guan, H. Chen, H. Liu, A. J. Rosengart, Preparation and characterization of hydrophobic superparamagnetic magnetite gel, Journal of Magnetism and Magnetic Materials, 306 (2006), 248-253.

73. X. Liu, M. D. Kaminski, Y. Guan, H. Chen, H. Liu, A. J. Rosengart, Preparation and characterization of hydrophobic superparamagnetic magnetite gel, Journal of Magnetism and Magnetic Materials, 306 (2006), 248-253.

74. S. Dutz, R. Hergt, Magnetic nanoparticle heating and heat transfer on a microscale: Basic principles, realities and physical limitations of hyperthermia for tumour therapy, Int J Hyperthermia, 29 (2013), 790-800.

75. E. Lima, E. De Biasi, R. D. Zysler, M. Vasquez Mansilla, M. L. Mojica-Pisciotti, T. E. Torres, M. P. Calatayud, C. Marquina, M. Ricardo Ibarra, G. F. Goya, Relaxation time diagram for identifying heat generation mechanisms in magnetic fluid hyperthermia, Journal of Nanoparticle Research, 16 (2014), 1-11.

76. E. Merbach, E. Tóth, The Chemistry of Contrast Agents in Medical Magnetic Resonance Imaging, Wiley, 2001.

Chapter 7. Theranostic part II: Drug release studies

This chapter is a continuation of the later one. In this chapter, the application as a drug delivery system is evaluated. In the first part of this chapter a brief introduction is given, related to the used drug, doxorubicin, and the need to encapsulate this drug is explored. Following, the mechanisms of drug release from chitosan are explored and some mathematical models are presented as an aid to better understand these mechanisms. Drug release results are presented and discussed, as well as the results from the mathematical models fitting.

7.1. Introduction

Drug delivery systems consists in a controlled release system, where the active substance is loaded into a carrier or device and then released at a predictable rate *in vivo* when administered by an injected or non-injected route. This is an important field of research, which has caught the attention of pharmaceutical researchers, medical doctors, and industry. The main reason for this interest is that a safe and targeted drug delivery could improve the performance of some classic drugs already in the market.

To develop appropriate drug carriers, it is important to have knowledge on drug incorporation and release, formulation stability and shell life, biocompatibility, biodistribution and targeting, and functionality. In addition, it is important to consider the fate of the carrier after the drug is completely released; in this respect, biodegradable nanoparticles (NPs) with a limited half-life in blood would be optimal [1-3].

Doxorubicin (DOX) is a member of the anthracyclines family, a chemotherapeutic agent's family. It is a chemotherapeutic drug widely used clinically in the treatment of various solid tumors such as lung and breast cancer, as well as leukemia, and lymphomas. However, its use is limited by the

severe side effects, which include specific cytotoxicity and dose-dependent congestive heart failure [4]. Consequently, DOX is a perfect candidate drug for a drug delivery system.

7.1.1. Anthracyclines family

Anthracyclines belong to the group of the most effective anticancer drugs ever developed [5]. The first members of this family were originally isolated from the pigment-producing *Streptomyces peucetius* in the 1960s and were named doxorubicin (DOX) and daunorubicin (DNR) [6].

DOX (Figure 7.1) is active against breast cancer, childhood solid tumors (like osteosarcoma), soft tissue sarcomas, and aggressive lymphomas while DNR is more active against acute lymphoblastic or myeloblastic leukemia [5].

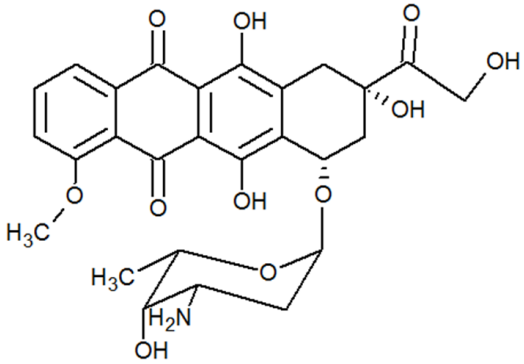

Figure 7.1. Chemical structure of doxorubicin.

The major drawbacks of these compounds are their cardiotoxicity leading to congestive heart failure and the development of spontaneous and acquired resistance. Intensive researches to find analogues that circumvent these problems lead to the development of more than 300 new compounds, whereas more than 2000 analogues were issued from structural modifications of natural compounds or from synthesis [7]. However, from those only few members of the anthracyclines family have reached the stage of clinical development and approval, including: DOX, DNR, epirubicin (EPI, 4'-*epi*-doxorubicin or Farmorubicin®), idarubicin (IDA, 4-demethoxy-daunorubicin or Zavedos®), pirarubicin (4'-tetrahydropyranyl-doxorubicin), aclacinomycin A (aclarubicin) and mitoxantrone [5, 8].

7.1.1.1. Mechanism of action

The mechanism by which anthracyclines inhibit cancer growth is still not completely clear and multiple pathways are thought to be involved in the cytotoxicity of this class of anticancer drugs.

According to Gewirtz [9] anthracyclines act by eight different mechanisms: 1) intercalation into DNA, leading to inhibited synthesis of macromolecules; 2) generation of free radicals, leading to DNA damage or lipid peroxidation; 3) DNA binding and alkylation; 4) DNA cross-linking; 5) interface with DNA unwinding or DNA strand separation and helicase activity; 6) direct membrane effects; 7) initiation of DNA damage via inhibition of topoisomerase II; and 8) induction of apoptosis in response to topoisomerase II inhibition. However, these mechanisms did not occur all at the same dosage; more so, some of them were observed at concentrations considered too high to be administrated to patients.

7.1.1.2. Cardiotoxicity

One of the major problems of anthracyclines usage is related to cumulative dose-dependent cardiotoxicity, responsible for developing late-onset heart failure. Anthracycline-induced secondary cardiotoxicity is seen in 5-23% of patients [10, 11].

The mechanism behind the anthracyclines cardiac toxicity and their specificity to myocyte cells remains controversial and not completely understood. Sawyer *et al*. [10] propose several mechanisms to explain the cardiotoxicity of anthracyclines, including (Figure 7.2): 1) generation of oxidative stress through formation of hydroxyl radical, leading to myocyte cell dead; 2) inducing apoptosis via a mitochondrial pathway involving Bax, cytochrome c and caspase-3 activation; 3) inducing apoptosis through intercalation between base pairs in DNA, originating DNA damage; 4) DNA damage by suppression of expression and/or activity of transcription factors that modulate sarcomere synthesis, as well as cell survival; 5) suppression of sarcomere protein synthesis. These mechanisms may not occur all at once, they are probably induced by different doses of the chemotherapeutic agent.

Since anthracyclines are interesting therapeutic agents being its cardiotoxicity a major limitation, efforts to circumvent this problem include: limiting dose exposure; encapsulated anthracyclines in liposomes to reduce myocardial uptake; administering concurrently with the iron chelator dextrazone to reduce free iron-catalyzed reactive oxygen species formation; and modify anthracyclines structure in an effort to reduce myocardial toxicity [11].

7.1.1. Alternative formulations of DOX

Doxorubicin plays an important role in cancer chemotherapeutic treatment, so its clinical unresponsiveness is a major concern. Liposomal doxorubicin (Caelyx® in Europe, Doxil® in USA) is currently approved for cancer treatment and its formulation has the advantage of enhancing the

antitumor effect, reducing toxicity, and improving pharmacokinetics, when compared to free DOX. These improvements are due to several factors: the polyethylene glycol (pegylated) coating reduces the uptake of liposomes by cells of the reticuloendothelial system (RES), thus prolonging the time of circulation; because normal blood vessels are not as fenestrated as tumor vessels, liposomes are confined to the intravascular space, reducing toxicity in normal tissues [12].

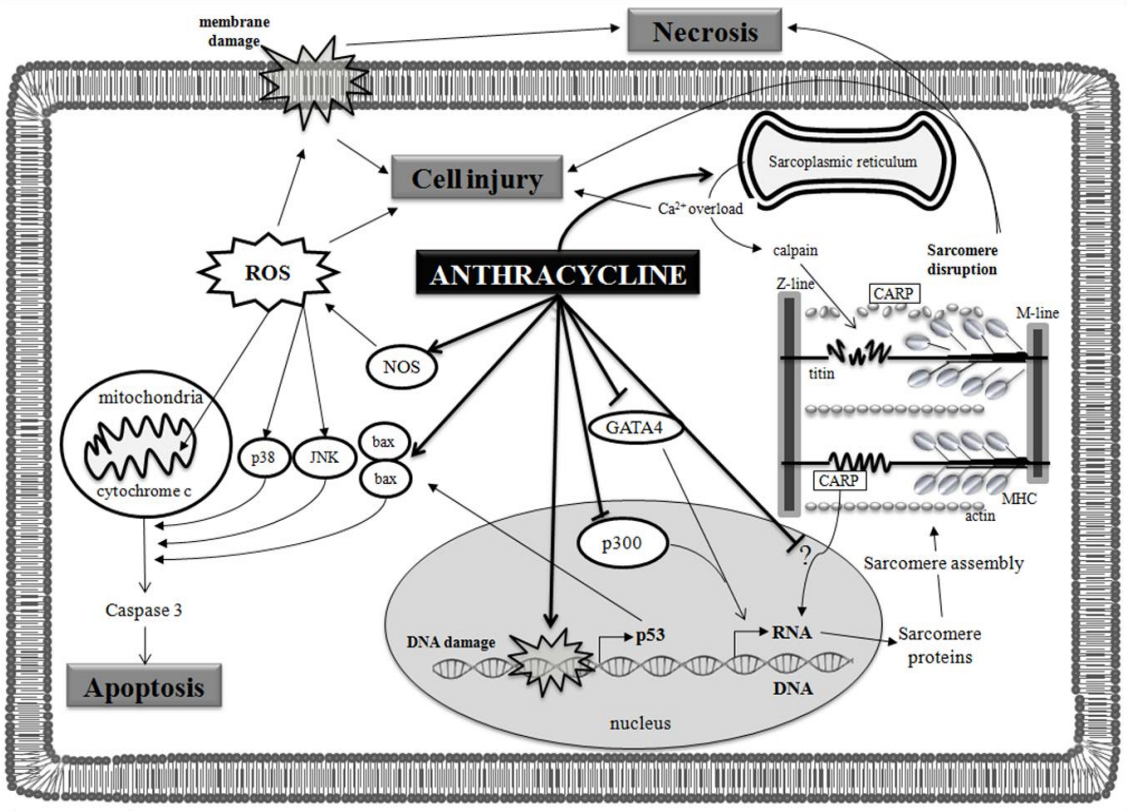

Figure 7.2. Possible mechanisms by which anthracyclines causes cardiac toxicity. The formation of reactive species is induced by the quinone moiety of anthracyclines and by induction of nitric oxide synthase, leading to nitric oxide and peroxynitrite formation. Another method of anthracyclines cardiotoxicity is to intercalate into nucleic acids, causing suppression of DNA, RNA, and protein syntheses, as well as damaging some transcriptional regulatory proteins that seem important for regulation of cardiac-specific genes. Anthracyclines also accelerate myofilament degradation, leading to a net negative balance of sarcomeric proteins ("cardiac sarcopenia") and induce changes in adrenergic function and adenylate cyclase as well as abnormalities in Ca^{2+} handling, functions that are critical for cardiac function. By last, anthracyclines also induce necrosis and apoptosis of myocyte cells. ROS – reactive oxygen species; JNK – c-Jun N-terminal kinases; bax – Bcl-2-associated X protein; NOS – nitric oxide synthase; GATA4 – gene name, member of GATA family of zinc-finger transcription factors; MHC – myosin heavy chain; CARP – cardiac ankyrin repeat protein and cardiac adriamycin-responsive protein [10].

Besides Caelyx®, another two liposomal formulations of anthracyclines have showed promising results: an uncoated formulation in which citrate is included for increasing DOX encapsulation above the levels predicted by the maintenance of a transmembranar pH gradient; and a liposomal DNR (DaunoXome) [5]. The first formulation is not as advantageous as the pegylated liposomal DOX, but still is better than free DOX and its main indication is treatment of metastatic breast cancer [13].

Tan *et al.* [14] produced an alternative drug delivery system composed by chitosan-dextran sulfate using a combinational coacervation method. DOX was successfully encapsulated into these microparticles and the *in vitro* studies demonstrated a reduction in SaOS-2 cell viability through various cell death mechanisms such as necrosis, and apoptosis. Treatment of mice bearing orthotropic osteosarcoma with DOX microparticles decreased tumor volume, bone lysis, and reduced secondary metastasis to the lungs. In addition, the treated mice maintained their weight and did not appear to suffer from any visible side effects such as heart failure or dry skin.

Another approach to decrease anthracyclines cardiotoxicity is by its encapsulation into nanoparticles. Betancour *et al.* [15] reported acid-copped poly(lactic-coglycolic acid) nanoparticles as a carrier for DOX that deliver the drug into MDA-MB-21 breast cancer cells quickly and in higher quantity than free DOX. Janes *et al.* [16] showed similar results using chitosan nanoparticles in human melanoma A375 cells. Bisht *et al.* [17] reviewed the usage of dextran-DOX conjugates encapsulated in chitosan nanoparticles in solid tumors therapy and showed that nanoparticles in the range of 10-100 nm diameter are able to deliver chemotherapeutic drugs to solid tumor. Susa *et al.* [18] incorporated DOX into a lipid-modified dextran based polymeric nano-system and demonstrated improved anti-proliferative effects against osteosarcoma cell lines compared to free DOX.

Wang *et al.* [19] demonstrated a way to overcome multidrug resistance in MCF-7/ADR cancer cells using a drug delivery system that tethers DOX onto the surface of gold nanoparticles with a poly(ethylene glycol) spacer via an acid-labile linkage (DOX-Hyd@AuNPs). These nanoparticles release DOX in response to pH of acidic organelles after endocytosis, inducing elevated apoptosis in cancer cells. This process may be monitored by the fluorescence of DOX from quenching due to the nanosurface energy transfer between the doxorubicinyl groups and the gold nanoparticles.

However, cardiotoxicity is still observed in patients treated with Caelyx® [23] and its safety has constantly been under scrutiny due to the adverse side effects still experienced by patients. For instance, incidences of dermatological toxic reaction, palmar-plantar erythrodysesthesia, have been reported in up to 50% of all patients [20], while another 50% of patients suffered from various hematologic adverse reactions such as anemia, leucopenia, and neutropenia. Alternative

formulations have been studied such as polymeric nanoparticles-based delivery systems that offer a significant advantage over other nanocarrier platforms. Since there is a tremendous versatility in choice of polymeric matrices that can be used it allows for the tailoring of nanoparticles properties to meet the specific needs they are intended to meet. Other advantages of these formulations are easy surface modification; greater encapsulation efficiency of the payload; payload protection; large surface area-to-volume ratio; and slow or fast polymer erosion for temporal control over the release of drugs.

Furthermore, the development of nanostructured delivery systems that combine carriers with cancer-targeting molecules can potentially overcome the drawbacks presented by conventional approaches [21]. Salerno *et al*. [22] developed biodegradable, biocompatible nanoparticles made of a conjugate between poly (D, L lactide-co-glycolic) acid and alendronate, suitable for systemic administration and directly targeting the site of tumor induced osteolysis. These nanoparticles were loaded with doxorubicin and the *in vitro* and *in vivo* activity of the drug encapsulated in the carrier system was analyzed in a panel of human cell lines, representative for primary or metastatic bone tumors, and in an orthotropic mouse model for breast cancer bone metastasis. Their results showed a significant dose-dependent growth inhibition of all cell lines. The use of polymeric nanocarriers allows the combination of various anti-cancer strategies. For example, some studies use magnetic nanoparticles loaded with chemotherapeutic agents [16, 23-26]. This combination is suitable to use intracellular hyperthermia, a technique in which the particles are concentrated at the tumor site and are remotely heated using an applied magnetic field to the required hyperthermic temperatures (42-45 ºC), thus killing the cancer cells with the heat generated [27, 28].

7.1.2. Chitosan as a drug delivery system

Chitosan (CS) is a polysaccharide obtained from deacetylation of chitin widely used as a drug delivery system for gene delivery, implants and nasal, oral, parental and transdermal administration [29]. Drug release from chitosan is dependent upon its swelling behavior and drug-chitosan interactions, which are influenced by pH of the medium [30]. Chitosan's dependence upon pH of the medium may be used to achieve a controlled drug delivery for cancer treatment. It is known that the tumor microenvironment is characterized by an acidic pH (around 6.5) due to the increase production of lactate by the glycolytic pathway. The export of lactate for the poorly vascularized extracellular medium leads to a decrease in the pH of the tumor microenvironment [31]. Furthermore, intracellular organelles such as liposomes and endosomes have a more acidic pH, between 3 and 5.5 [32].

7.1.2.1. pH-sensitive swelling of CS

Drug release from ionically cross-linked CS exhibits increased pH-sensitive swelling compared to covalently cross-linked CS. Swelling behavior of ionically cross-linked CS are influenced by ionic interactions between CS chains, which depend on the cross-linking density set during the formation of the network. An increased cross-linking density leads to a decreased swelling and decreased pH sensitivity, and consequently, decreased drug release from the polymeric chains. Since ionic cross-linking is reversible, it can be modified by the pH of the application medium. Therefore swelling occurs in both acidic and basic conditions, extending the range of application [33].

When the pH decreases, the charge density of the cross-linker also decreases, leading to a decreased cross-linking density and CS swelling. Thus, swelling is favored by protonation and repulsion of CS from amino groups. If the pH decrease is too large it may lead to dissociation of ionic linkages and dissolution of the network. If the pH increases, the protonation of CS amino groups decrease, leading to a decrease in the cross-linking density and thus allowing swelling. However, if the pH increase is too large, amino groups of CS are neutralized and ionic cross-linking is inhibited. Consequently, interactions are not strong enough to avoid dissolution and the ionic cross-linker is released [33].

CS swelling depends not only upon pH, but is also influenced by other parameters. The presence of ions weakens ionic interactions through shielding effect, which increases swelling and drug delivery. Moreover, decrease of CS molecular weight (M_w) has proven to decrease CS swelling and thus favoring dissolution. Furthermore, drug release depends upon the solubility and M_w of the drug, and is influenced by its concentration inside the network [33].

7.1.2.2. Mechanisms of drug release from CS NPs

Drug release from CS NPs can occur through three different mechanisms: release from the surface of NPs, diffusion through the swollen rubbery matrix, and release due to polymer erosion [34]. In most of the cases, release occurs through more than one mechanism.

Drug release from the surface of the NPs occurs when the drug immediately dissolves when it is exposed to the release medium. This kind of mechanism leads to a burst effect in the early stages of dissolution [35].

Drug diffusion through the swollen rubbery matrix is composed of three steps. The first step is the swelling of the polymer matrix due to water penetration into the system. In the second step,

the conversion of glassy polymer into rubbery matrix occurs. Finally, drug diffuses from the swollen rubbery matrix of CS. Drug release through this mechanism is slow initially and later becomes faster. This type of release is more relevant in CS hydrogels [34].

When considering drug diffusion from polymer swelling, two aspects must be taken into consideration. In a swollen polymer, the length of the diffusion pathways increases, resulting in decreasing drug concentration gradients (the driving forces from diffusion), potentially decreasing drug release rates. The second aspect is that the mobility of the polymer significantly increases, leading to increased drug release rates [36]. Consequently, in a swollen drug delivery system, there are two moving fronts: the *swelling front* and the *diffusion front*. The swelling front occurs when the polymer contacts with the release medium and water diffuses into the system. With increasing water content, the mobility of the polymer chains increases. Hence, the conversion of glassy polymer into rubbery matrix occurs. This is a moving boundary that separates the swollen from non-swollen matrix. In this stage, dissolved and non-dissolved drug may co-exist in the polymer matrix. At this stage, dissolved drug diffuse out of the swollen matrix into the release medium. The *diffusion front* separates the swollen matrix containing only dissolved drug from the swollen matrix that contains both dissolved and non-dissolved drug. In some cases a third front can also be present, the *erosion front*, which separates the polymer matrix from the release medium [34, 36].

7.1.2.3. DOX release profile from CS NPs

Several investigators have studied DOX release profile from CS NPs. In most of the cases, the drug delivery system is placed into a dialysis bag, and drug release to the release medium is measured over time. The release medium may differ depending on the study purpose.

Janes *et al*. [16] studied DOX release profile from CS-TPP NPs in acetate buffer (pH 4). The results showed a burst release of 4.5% during the first 2 h, which was maintained stable through the next 5 days. This result was explained by the interactions between DOX and CS, resulting in very stable bonding. DOX and CS show overwhelming charge repulsion between them. However, even then small quantities of DOX are able to complex with CS. This may be explained by the amphoteric property of this drug and due to the hydrophobic/hydrophilic interactions and resonance effects. The authors concluded that drug release is caused by CS degradation or by release of DOX bonded to CS surface. Moreover, *in vitro* studies showed that CS NPs enter cells through endocytosis and are degraded intracellularly, thus causing DOX release.

Yuan and co-workers [30] have studied chitosan-clay and chitosan-aluminosilicate clay nanocomposite as DOX delivery systems. DOX release was studied at 37 ºC and at pH 1.2 (gastric fluid), 5.3, and 7.4. Control experiments were performed by submitting free DOX to the same

release conditions. In control experiments, DOX was completely release after 1 h, 5 h, and 12 h, at pH 1.2, 5.3 and 7.4, respectively. DOX release from the nanocarrier was slower, without achieving total drug release.

DOX release from CS NPs incorporated with iron oxide NPs (Fe_3O_4) was studied by Javid *el al.* [37]. The authors tested different release mediums with pH from 1.5 to 7.0 during a period of 48 h. The results showed that pH increase lead to smaller amount of drug released. Maximization of DOX release was achieved at pH between 4.5 and 6.4, corresponding to internalization and endocytosis of DOX-loaded NPs in tumor cells. In a more recent research, Unsoy and co-workers [32] studied DOX release from CS Fe_3O_4 NPs with different sizes. Release profiles were studied at pH 4.2 and 5 at 37ºC, during a maximum period of 30 h, with the purpose to simulate endosomal environment. A burst release in the first half hour was observed, followed by a slower release rate after 7 h of experiment. Reduction of particle size only cause an increase of drug release of about 10%. Moreover, increased DOX release was observed at pH 4.2. Furthermore, DOX-loaded CS Fe_3O_4 NPs have a higher cross-linking density, thus leading to decreased swelling.

7.1.3. Mathematical modelling for drug delivery systems

Mathematical modelling can be very helpful to better understand drug release profiles from different systems such as nanoparticles. Moreover, these models can predict the system performance. The use of mathematical models applied to drug delivery systems can help to improve the system's effectiveness and easiness of application. It also has the advantage of reducing time and costs, since the number of experiments made are reduced, and the procedures are optimized.

In 1961, Higuchi was the first to publish a mathematical model of drug delivery. His famous equation provides a simple description of drug release from an ointment base exhibiting a considerable initial excess of non-dissolved drug within and inert matrix with film geometry [38]. Since then, numerous mathematical models have been developed for different kinds of systems. These models can be divided into empirical/semi-empirical and mechanistic realistic ones. In the first case, the predictable power is usually low since the mathematical treatment (at least partially) is purely descriptive and not based on real physical, chemical, and/or biological phenomena. Consequently, great caution must be paid when making quantitative predictions or mechanistic conclusions. This type of models is very useful when comparing different release profiles [36]. On the other hand, mechanistic realistic models are based on real phenomena, such as diffusion, dissolution, swelling, erosion, precipitation, and/or degradation [39, 40]. As such, these models allow prediction of different processes that are involved in the studied system, offering a deeper insight into the underlying drug release mechanisms [36]. However, some divergences have been

found between theories and experimental data, mainly because several driving forces can be present in a single transport process [41]. In these cases, the initial and boundary conditions must be known, such as drug distribution through the system before it contacts with the release medium. The solutions of these equations may be analytical or numerical, according to the complexity of the resulting set of mathematical equations that represent the system. Usually some approximations and simplifications are needed to achieve a relatively simple mathematical system [36]. In some cases, simplifications of the mechanistic models derived into empiric or semi-empirical models.

Controlled release systems can be divided by their mechanisms of drug release into: diffusion-controlled, chemically controlled, and swelling-controlled. Ordinary diffusion occurs in each of these mechanisms to a certain degree. Furthermore, most of the models used are based on diffusion equations [42].

7.1.3.1. Fundamentals of ordinary diffusion

Diffusion in defined by the release of an active agent from a polymeric carrier by the movement of the drug through the bulk of the polymer. This phenomenon is mainly controlled by the mass transfer limitations at the boundary between the polymeric carries and its surroundings. Fick's law of diffusion describes the diffusion of drug molecules through a polymeric carrier on a macroscopic level. For transport in one dimension, Fick's law is given by:

$$j_i = -D_{ip}\frac{dc_i}{dx} \qquad \text{Equation 7.1}$$

$$\frac{dc_i}{dt} = D_{ip}\frac{\partial^2 c_i}{\partial x^2} \qquad \text{Equation 7.2}$$

Where the concentration and mass flux of the species, i, are designated as c_i and j_i, respectively; D_{ip} is the diffusion coefficient of species, i, in the polymer matrix, and x and t stand for the independent variables of position and time, respectively [42].

These equations describe the release of a drug from a carrier of a thin planar geometry. Moreover, in the above written form of Fick's law, the diffusion coefficient is assumed independent of concentration. As such, initial and boundary conditions, which are necessary for solving Equation 7.1 and Equation 7.2, allow for the appropriate description of the experimental conditions imposed upon the drug release device. Several solutions of the above-mentioned equation have been obtained to be applied to various *in vitro* and *ex vivo* experiments [42].

7.1.3.2. Zero-order kinetics

Zero-order kinetics model are present when the drug is released from carriers that do not disaggregate. Drug release is slow and no equilibrium conditions are reached.

This kinetic can be used to describe drug release from several types of carriers, such as transdermal systems, matrix tablets with low soluble drugs, coated forms, osmotic systems, among others [43, 44].

7.1.3.3. First-order kinetics

First-order kinetics modulates dissolutions profiles where the quantity of drug released is proportional to the amount that is still in the dosage form that decreases by unit of time.

It is usually used for porous dosage forms containing water-soluble drugs, in which drug release is proportional to the amount of drug remaining in the interior, in such a way that the amount of drug released per unit of time diminishes.

In some cases, this model has also been used to describe absorption and/or elimination of some drugs, although it is difficult to conceptualize this mechanism in a theoretical basis [43, 44].

7.1.3.4. Higuchi model

As above mentioned, Higuchi [38] was the first author to develop a mathematical model describing water soluble and low soluble drug release from semi-solid and/or solid matrix systems. Higuchi model describes the release based on Fick's law for diffusion, and dependent of the square root of time. Initially was applied for planar systems, but after several modifications it was extended to different geometries and porous systems [43, 44].

Higuchi model is based on the following assumptions: a) initial drug concentration in the matrix is much higher than drug solubility; b) drug diffusion takes places only in one dimension; c) drug particles are much smaller than system thickness; d) swelling and dissolution of the matrix are negligible; e) drug diffusion is constant; and f) perfect sink conditions are always attained in the release environment [43].

Higuchi model is more precise in systems of unidimensional matrixes with low solubility, in which drug diffuses in only one direction and without swelling behavior. It is usually used for matrix tablets with soluble drugs or transdermal systems [44].

7.1.3.5. Hixson-Crowell model

Hixson and Crowell (1931) described a model where the cubic root of the unreleased drug fraction versus time is linear if the equilibrium conditions are not reached and if the geometrical shape of the dosage form diminishes proportional over time. For the application of this model, it must be assumed a release rate limited by the drug particles dissolution rate and not by the diffusion that might occur through the polymeric matrix [43, 44].

Hixson-Crowell model is used to pharmaceutical dosage forms such as tablets, where the dissolution occurs in planes that are parallel to the drug surface if the table dimensions diminish proportionally [44].

7.1.3.6. Korsmeyer-Peppas model

Korsmeyer and Peppas [45] developed a simple, semi-empirical model based on the power law, which relates exponentially the drug released to the elapsed time. The most used and simple equation is derived from a mechanistic model that describes drug diffusion from a controlled release polymeric system with the form of a plane sheet. Application of some assumptions and boundaries lead to the simplification of the initially proposed equation, which facilitates its application to experimental data.

Korsmeyer-Peppas mathematical model is also applicable to polymeric systems with swelling ability and its constants assume different values depending on the release mechanism, with different boundary values according to the geometry of the device.

Considering chitosan nanoparticles, there is only interest in the release from spheres [46]. This model is applicable to experimental data by doing the approximation to the first 60% of release, which means that $M_t/M_\infty < 0.6$, where M_t is the amount of drug released at time t and M_∞ is the cumulative quantity of drug released when time approaches infinite (equilibrium state of release) [44, 46, 47]. Depending on the value of the diffusional exponent n, different types of release profile can be identified. For spherical particles, $n \leq 0.43$ correspond to Case I or Fickian diffusion where the diffusion contributes more than the relaxation mechanism. When $n = 0.85$, it is Case II transport or also called relaxation-controlled transport where the relaxation contribution is higher than diffusion. When n is between these values it is called anomalous or non-Fickian diffusion, where there is a similarity between diffusion and relaxation contribution [48]. Another category of release profile, when $n > 0.85$, is called Super Case II transport [44]. In this model K is related to the shape and structure of the polymer [36]. These two constants allow the comparison of

experimental data of systems with different characteristics and the understanding of release mechanism.

7.1.3.7. Hopfenberg model

Hopfenberg studied the release of drugs from surface-eroding devices with several geometries and have proposed a general mathematical equation describing drug release from slabs, spheres, and infinite cylinders displaying heterogeneous erosion [49].

This model assumes erosion of the matrix as rate-limiting step for drug release. Moreover, time dependent diffusional resistances internal or external to the eroding matrix do not influence drug release [44].

7.1.3.8. Peppas-Sahlin model

In 1989, Peppas and Sahlin [50] described a modification of the previously published Korsmeyer-Peppas semi-empirical equation by decoupling diffusion and Case-II transport. The resultant equation has two parcels; the first one represents Fickian diffusional contribution and the second one is related to dissolution and relaxation of polymeric chains contribution to release. The exponent, *m*, of the equation is related with *n* exponent of Korsmeyer-Peppas model, and its values closely related [51].

7.1.3.9. Weibull model

In 1951, Weibull described a general empirical equation which was later adapted to the dissolution/release process. This equation fits most of the drug release profiles, and similarly to Korsmeyer-Peppas model, describes the initial 60% of drug release. However, it lacks kinetic basis and none of its parameters are related with the intrinsic dissolution rate of the drug [44, 52].

This equation has two constants: *a*, a time scale parameter, and constant *b*, a shape parameter. The shape parameter, *b*, characterizes the curve as either exponential ($b = 1$), sigmoid ($b > 1$) or parabolic ($b < 1$) [44].

In 2006, Papadopoulou *et al.* [52] have correlate parameter *b* of Weibull model with exponent *n* of Korsmeyer-Peppas model. In this way, *b* can be used as an indicator for the mechanism of drug release as for $b \leq 0.75$ it is a Fickian diffusion, while for $0.75 < b < 1$ is a mixed mechanism, between Fickian diffusion and Case II transport, and when $b > 1$ drug is released through a complex release mechanism.

Table 7.1 summarizes the overall mathematical models above described.

Table 7.1. Summary of the most used mathematical models for drug delivery systems

Model	Equation	Application	Ref.
Zero-order[1]	$Q_t = Q_0 + K_0 t$	Systems where release rate is independent of the concentration of dissolved substance.	[43, 44]
First-order[2]	$\log Q_t = \log Q_0 + K_1 t$	Systems where release rate is dependent on the concentration.	[43, 44]
Higuchi[3]	$Q_t = Q_0 + K_H t^{1/2}$	Fickian diffusion.	[38, 43, 44]
Hixson-Crowell[4]	$\sqrt[3]{Q_t} - \sqrt[3]{Q_0} = K_{HC} t$	Release by dissolution where the surface area and diameter particles change; related to erosion release mechanism.	[43, 44]
Korsmeyer-Peppas[5]	$Q_t = k t^n$	Fickian ($n \leq 0.43$); Case II transport ($n = 0.85$); Non-Fickian ($0.43 < n < 0.85$); Super Case II: $n > 0.85$.	[44, 45, 48]
Hopfenberg[6]	$Q_t = 1 - \left(1 - \frac{k_0 t}{c_0 a}\right)^n$	Surface eroding polymer matrices.	[44, 49]
Peppas-Sahlin	$Q_t = k_1 t^m + k_2 t^{2m}$	k_1 – Fickian contribution; k_2 – relaxation contribution; m - correspondent to exponent n of Korsmeyer-Peppas model.	[50, 51]
Weibull	$Q_t = 100\left(1 - e^{-\frac{tb}{a}}\right)$	Fickian diffusion ($b \leq 0.75$); Combined mechanism of Fickian and Case II ($0.75 < b < 1$); Complex mechanism ($b > 1$).	[44, 52]

[1] Q_0, Initial amount of drug in solution; Q_t, amount of drug released at time t; K_0, zero-order release constant. [2] K_1, first-order release constant. [3] K_H, Higuchi dissolution constant. [4] K_{HC}, Hixson-Crowell constant. [5] n, empirical release exponent; k, related to polymer structure and geometry. [6] c_0 - uniform initial drug concentration in the system; a, radius of a sphere; k_0, rate constant; n- shape factor.

7.2. Materials and methods

All the chemical reagents used in this research work were of analytical grade and used without further purification.

7.2.1. Preparation of buffer solutions

Phosphate buffer solution with pH 7.4 (PBS 7.4) was prepared as followed: to 800 ml of distilled water were added 4 g of sodium chloride (NaCl, *Sigma-Aldrich)*, 0.1 g of potassium chloride (KCl, *Sigma-Aldrich)*, 0.72 g of disodium hydrogen phosphate (Na_2HPO_4, *Sigma-Aldrich*) and 0.12 g of potassium dihydrogen phosphate (KH_2PO_4, *Sigma-Aldrich).* After complete dissolution of the salts, pH was adjusted to 7.4 using HCl. Finally, the volume was adjusted to 1000 ml.

Phosphate buffer solution with pH 6.5 (PBS 6.5) was prepared as followed: to 800 ml of distilled water were added 8 g of NaCl, 0.2 g of KCl, 0.61 g of Na_2HPO_4 and 0.19 g of KH_2PO_4. After complete dissolution of the salts, pH was adjusted to 6.5 using HCl. Finally, the volume was adjusted to 1000 ml.

0.2 M acetic acid (*Panreac*) and 0.1 M sodium acetate (*Scharlau*) was used as a pH 4.5 buffer.

7.2.2. DOX calibration curves

To determine DOX concentration through the further assays, DOX calibration curves were constructed by measuring the absorbance by ultraviolet visible spectrophotometer (UV-Vis, *T90+ PG Instruments*) in a range of concentrations between 5 and 50 $\mu g.ml^{-1}$ of doxorubicin hydrochloride (*Fluka*). The maximum absorbance at 480 nm, DOX maximum absorbance peak [32, 53], was determined at different DOX concentrations, as represented in Figure 7.3.

DOX calibration curves were performed for all solvents used in the experiments: water, PBS 7.4, PBS 6.5 and HAc/NaAc (pH 4.5). These measures to obtain the calibration curves were made in quadruplicates.

7.2.1. Selection of DOX carriers

Different types of DOX loaded NPs were prepared: DOX-loaded Fe_3O_4 NPs, DOX-loaded polymeric NPs, and DOX loaded polymeric-Fe_3O_4 NPs.

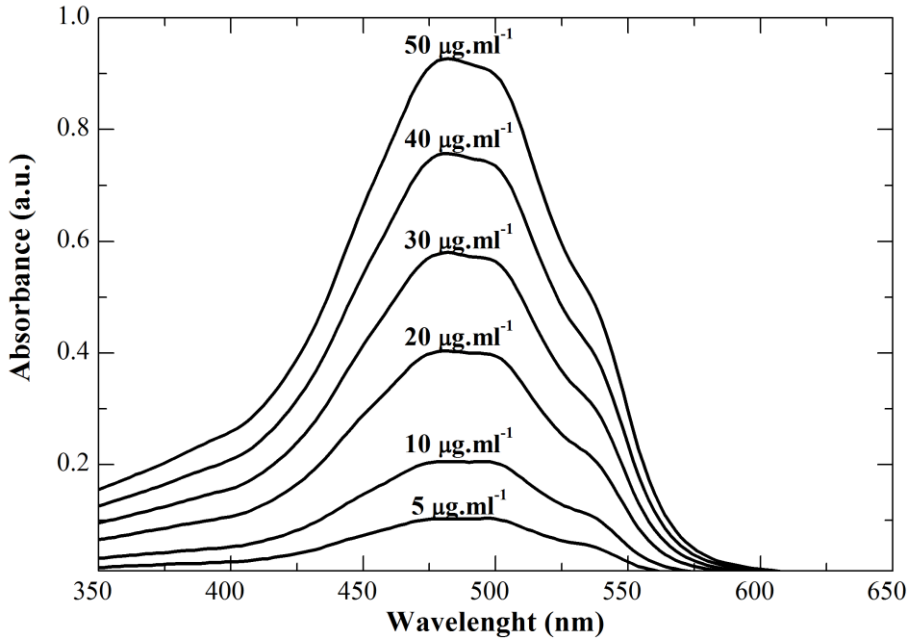

Figure 7.3. Example of the evolution of the maximum absorbance peak (480 nm) of DOX at different concentrations.

Iron oxide NPs (Fe_3O_4) were prepared according to the procedure described in Chapter 3. The NPs used were: iron oxide NPs prepared by chemical precipitation technique without further treatment (Pristine Fe_3O_4 NPs), and stabilized with either a concentration of 10 mM of tri-sodium citrate (Fe_3O_4 TC 10 mM) or a concentration of 64 mM of oleic acid (Fe_3O_4 OA 64 mM); and finally, iron oxide NPs prepared by thermal decomposition technique (Fe_3O_4 TD).

Regarding DOX-loaded polymeric NPs, was used chitosan (CS) and *O*-HTCC, a chitosan derivative synthetized in Chapter 4. Four molecular weights of each polymer were tested for drug delivery studies. Polymeric nanoparticles were produced through ionotropic gelation using tripolyphosphate (TPP) and a similar procedure was employed to produce polymeric NPs incorporated with Fe_3O_4 NPs. Detailed procedures for the preparation of these NPs are described in Chapter 4.

7.2.2. DOX encapsulation efficiency studies

DOX-loaded Fe_3O_4 NPs were prepared as followed: 2 ml of DOX solution with different concentrations (2 $mg.ml^{-1}$, 1 $mg.ml^{-1}$ and 0.5 $mg.ml^{-1}$) was added to 1 ml of an aqueous suspension of 10 $mg.ml^{-1}$ Fe_3O_4 NPs. A magnet was used to separate DOX-loaded NPs from free DOX and the supernatant was removed. The absorbance of the supernatant at 480 nm was measured by UV-VIS spectroscopy.

DOX-loaded CS and *O*-HTCC NPs, were prepared with different DOX concentrations added to polymer acidic solution (1.2% w/v in acetic acid at 1% v/v) being magnetic stirred for 10 min. After adding TPP (0.25% w/v) to 0.5 ml of DOX+polymer solution, the solution was centrifuged (*Sigma 1-13 centrifuge*) for 5 min at 10000 rpm. Supernatant was removed and added 1 ml of distilled water to the pellet and was centrifuged again under the same conditions. The absorbance of the obtained supernatants was measured by UV-VIS spectroscopy at wavelength of 480 nm. This procedure was repeated for the following tests.

Different weight ratios CS:DOX were tested: 1 ml of CS solution and 2 ml of DOX with four different concentrations (2 $mg.ml^{-1}$, 1 $mg.ml^{-1}$, 0.5 $mg.ml^{-1}$, and 0.25 $mg.ml^{-1}$); 0.5 ml of these samples with 1.5 ml of TPP added.

Different ratios of CS:TPP and *O*-HTCC:TPP were also tested: 1 ml of polymer solution with 1 ml of DOX solution at 2 $mg.ml^{-1}$; 0.5 ml of this solution and different amounts of TPP solution (0.5 ml, 1 ml, and 1.5 ml).

DOX-loaded CS and *O*-HTCC NPs incorporated with Fe_3O_4 NPs were produced by adding a known amount of Fe_3O_4 NPs added to the polymer solution before addition of DOX.

7.2.3. DOX release studies

DOX release profiles were determined using three different buffers: PBS 7.4, PBS 6.5 and HAc/NaAc buffer at pH 4.5, which represent the pH of the blood flow, pH of the tumor microenvironment, and the pH of lysosomes and endosomes, respectively [54, 55]. All release studies started with 1 mg of DOX and a total volume of 1 ml.

Release studies from not freeze-dried CS NPs were prepared as following: 1 ml of CS+DOX was added to 4.5 ml of TPP (0.25% w/v), stirred in ULTRA-TURRAX for 5 min. This solution was then centrifuged (*Heraeus Multifuge X1R centrifuge – Thermo Scientific*) for 10 min at 12000 rpm. The resultant supernatant was stored and 3 ml of water were added to the pellet; the solution was centrifuged again in the same conditions and this resultant supernatant was stored. The resultant pellet was resuspended in 1 ml of PBS 7.4 and dialyzed (*Spectrum Laborato*ries, cut off M_w = 10-12 KDa) in 10 ml of release buffer at 37 ºC for 72 h. Periodically, 3 ml of release medium was removed and the same volume of new buffer was added. The absorbance of all samples was measured at 480 nm, including the two supernatants resultant from the two initials centrifugations. These values of absorbance and with the help of DOX calibration curves, allowed the determination of DOX concentration and the calculation of the percentage of released drug during a period of time.

Controls were made by dialyzing 1 ml of free DOX and varying the pH of the release medium (4.5, 6.5 and 7.4).

Release studies from DOX-loaded Fe_3O_4 NPs were performed as following: 5 mg of Fe_3O_4 NPs and 1 mg of DOX in PBS 7.4 were placed in a dialysis bag. The following procedure was the same as the described above.

For the preparation of freeze-dried samples, 1 ml of polymer (CS and *O*-HTCC)+DOX or Polymer+Fe_3O_4+DOX was added to 4.5 ml of TPP (0.25% w/v), stirred in *ULTRA-TURRAX* for 5 min, and then freeze-dried for 24 h (VaCo2 ZIRBUS technology; -45 ºC and 0.07 mbar). The resultant powder of DOX-loaded polymer nanoparticles was then resuspended in 1 ml of PBS 7.4, and dialyzed. The remaining procedure was the same as the above described.

All drug release experiments were performed in triplets.

7.2.4. Characterization

7.2.4.1. Fourier Transform Infrared (FTIR) spectrometry

FTIR spectra of the samples were obtained to investigate changes in the chemical bound of the samples in a Nicolet 6700 – Thermo Electron Corporation Attenuated Total Reflectance-Fourier Transform Infrared spectrometer (ATR-FTIR). Measurements were performed in freeze-dried samples in the range of 480 to 4500 cm^{-1}.

7.2.4.2. Thermogravimetric analysis (TGA)

Thermogravimetric analysis and differential thermal analysis (DTA) studies were carried out using a Thermal Analyzer NETZSCH STA 449 F3 Jupiter® at a rate of 10 ºC.min^{-1} in a N_2 atmosphere.

7.2.4.3. Iron content determination

The iron content of the samples was determined using the 1,10-phenantroline colorimetric method [56], similarly to the description in Chapter 3 by the formula [Fe] = 0.7 x [NPs].

7.3. Results and discussion

7.3.1. Characterization of DOX loaded polymeric NPs

Figure 7.4 displays the FTIR spectra of doxorubicin-loaded CS and *O*-HTCC nanoparticles. Doxorubicin spectrum shows multiple bands typical of this compound: two single vibration modes of O-H stretching at 3525 cm^{-1} and 3314 cm^{-1}; a multiple band at 2890 cm^{-1} of C-H stretching vibration mode; at 1729 cm^{-1} the C=O stretching vibration band; the multiple bands at 1620 cm^{-1} and 1578 cm^{-1} are attributed to the N-H bending vibration mode of a primary amine; the aromatic rings of DOX are identified by a multiple band at 1414 cm^{-1} of stretching vibration in-ring; at 1276 cm^{-1}, 1114 cm^{-1} and 1068 cm^{-1} are the C-O stretching vibration mode; and at 867 cm^{-1} is C-H out-of-plane vibration mode in the aromatic ring [32].

The chitosan nanoparticles and DOX-loaded chitosan nanoparticles spectra are different in the bands at 1414 cm^{-1} and 877 cm^{-1} that identify the presence of the aromatic rings of doxorubicin, only present in the DOX-loaded chitosan NPs. The band at 1068 cm^{-1} of C-O stretching vibration is more pronounced. Similar behavior is observed in DOX-loaded *O*-HTCC NPs. The presence of these bands confirms the DOX encapsulation in the polymeric nanoparticles. The molecular weight does not influence the chemical bonds between chitosan and doxorubicin or *O*-HTCC, since the spectra are similar.

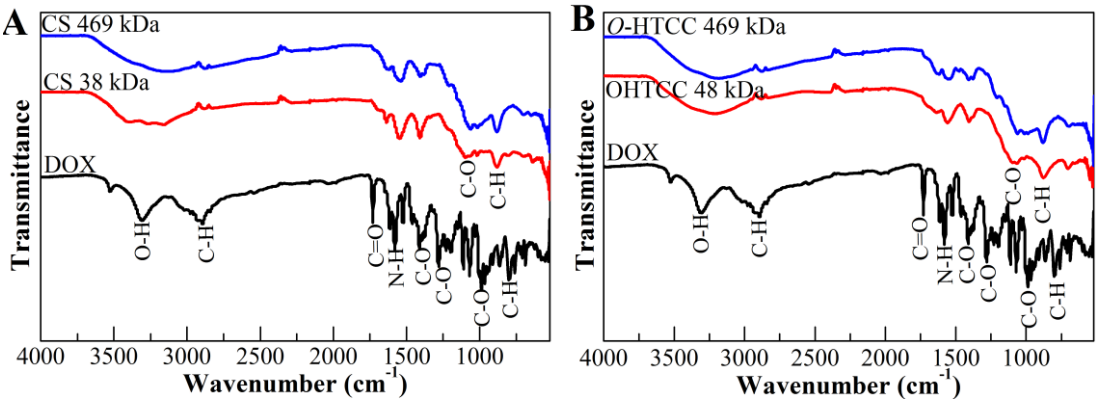

Figure 7.4. FTIR spectra of doxorubicin loaded chitosan nanoparticles (A) and doxorubicin loaded *O*-HTCC nanoparticles (B). Comparison was performed with DOX alone (DOX), and two molecular weights of CS, 38 and 469 kDa, and *O*-HTCC, 48 and 469 kDa.

Thermogravimetric curves (sample weight % as a function of temperature) and its derivative (DTA) are displayed in Figure 7.5.

Comparison was performed using polymeric NPs and DOX-loaded polymeric NPs. The results confirm that DOX does not enhance the degradation of polymer; in both cases, the remaining amount of product at 900 ºC is superior when polymeric NPs are loaded with DOX. According to Manocha *et al.* [57] most of the DOX do not decompose to vapor state. A slight weight loss is observed around DOX melting peak at 195ºC. As such, most of the mass loss observed is attributed to polymer degradation, as explained in Chapter 4.

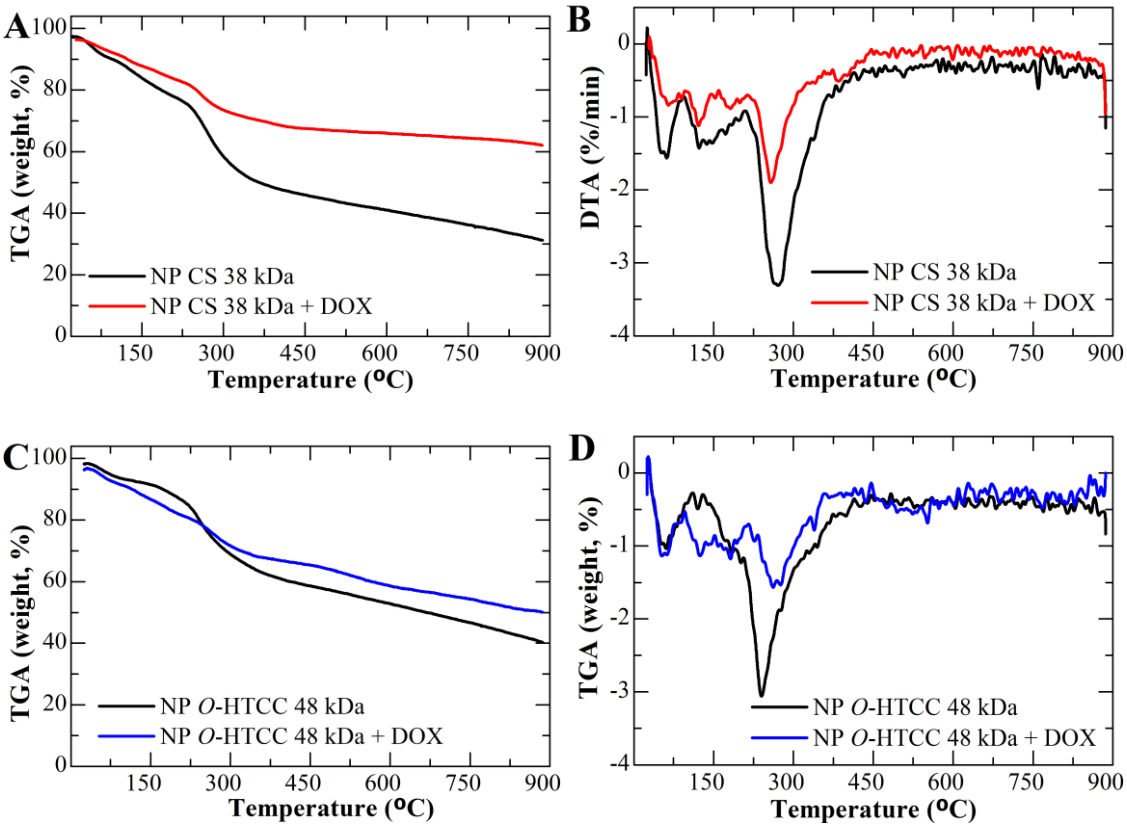

Figure 7.5. TGA (A, C) and DTA (B, D) of DOX-loaded chitosan and *O*-HTCC nanoparticles, respectively.

7.3.2. Encapsulation efficiency

To evaluate the encapsulation efficiency of DOX, the initial concentration of DOX was varied, keeping the remaining parameters fixed. The results are shown in Figure 7.6 A, expressed by the percentage of drug encapsulated as a function of chitosan molecular weight, for different CS:DOX ratios. Encapsulation efficiency (EE) was determined indirectly by measuring DOX concentration in the supernatant after centrifugation of DOX-loaded CS NPs [16, 55, 58]:

$$EE(\%) = \frac{(Total\ DOX - DOX\ in\ the\ supernatant)}{Total\ DOX} \times 100 \qquad \text{Equation 7.3}$$

In general, the encapsulation efficiency increases with the increase of DOX initial concentration. No significant differences were found between the four molecular weights tested. Considering these results, the mass ratio of CS:DOX 1:3 was chosen for the following tests, which correspond to an initial DOX amount of 1 mg.

Using this amount of DOX as a reference, the ratio of CS:TPP or *O*-HTCC:TPP was changed to achieve the maximum encapsulation. Figure 7.6 displays the results for chitosan (B) and *O*-HTCC (C) nanoparticles loaded with DOX. In both cases, the ratio 1:0.625 was not suitable to encapsulate DOX, probably due to an amount of TPP not enough to produce polymeric nanoparticles. It is known that a critical number of cross-links (TPP) per chain is required to allow the formation of a network, in this case, a nanoparticle [33].

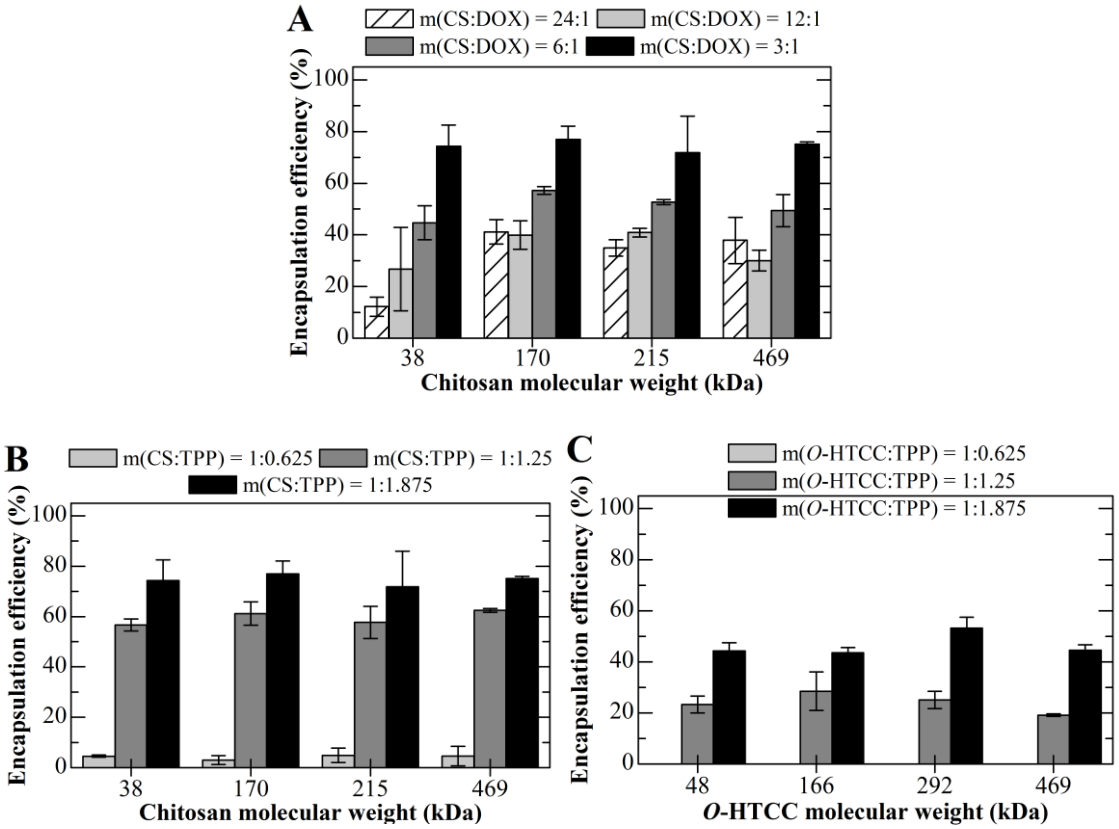

Figure 7.6. A) Effect of doxorubicin amount in its encapsulation efficiency in chitosan nanoparticles, as a function of chitosan molecular weight; B) Encapsulation efficiency of chitosan nanoparticles as a function of molecular weight, for different CS:TPP ratios; C) Encapsulation efficiency of *O*-HTCC nanoparticles as a function of molecular weight, for different *O*-HTCC:TPP ratio. The results are expressed as average ± standard deviation for three independent experiments.

Recalling that CS:TPP ratio of 1:0.5 produced polymeric nanoparticles with smaller hydrodynamic diameters (Chapter 4). However, in this case it is important to consider the presence of DOX, a positively charged molecule that can ionically interact with TPP negatively charged phosphate groups, therefore preventing chitosan interaction with TPP, and consequently the formation of nanoparticles. As such, the amount of TPP was increased, confirming an effective encapsulation of DOX into the polymeric nanoparticles. The higher amount of TPP contributed to enhance the encapsulation efficiency of both chitosan and *O*-HTCC nanoparticles.

The encapsulation efficiency was also evaluated for three types of Fe_3O_4 NPs (pristine Fe_3O_4, Fe_3O_4 TC 10 mM, and Fe_3O_4 OA 64 mM) by using a fixed amount of NPs and varying the initial concentration of DOX. The results in Figure 7.7 A show that DOX initial concentration does not have a high influence in encapsulation efficiency by pristine Fe_3O_4 NPs. However, surfactant coated Fe_3O_4 NPs show a different behavior. For both Fe_3O_4 TC 10 mM and OA 64 mM the encapsulation efficiency increases with the decrease of DOX initial concentration. In general, the encapsulation efficiency is lower for oleic acid coated Fe_3O_4 NPs.

The three types of Fe_3O_4 NPs were coated with low molecular weight chitosan, 38 kDa. Similarly to the previous analysis, the initial concentration of DOX was varied, changing the CS:DOX ratio. The obtained results are similar to previous ones: with the decrease in DOX initial concentration, the efficiency encapsulation decreases. For polymeric nanoparticles alone, the better ratio CS:DOX was 3:1. The same was found in CS-coated Fe_3O_4 NPs. As such, chitosan determines the encapsulation efficiency of DOX.

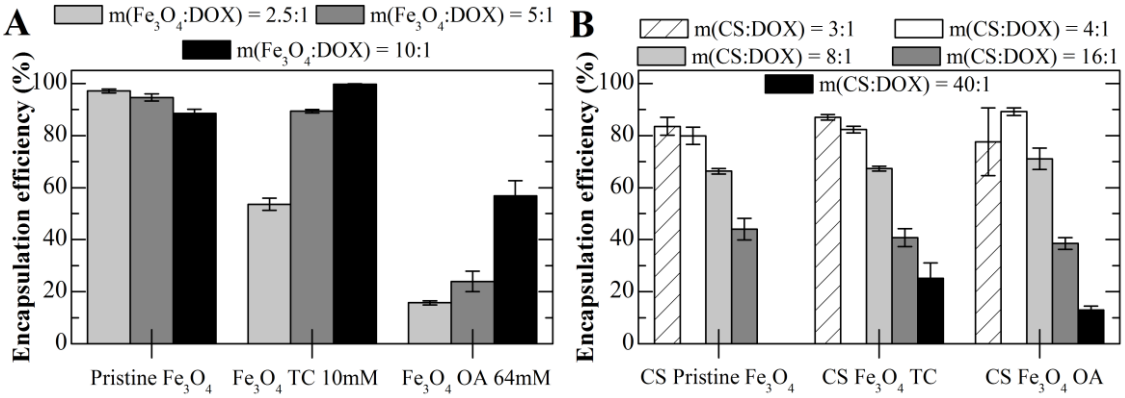

Figure 7.7. Effect of DOX concentration in its encapsulation efficiency in 10 mg of pristine Fe_3O_4, Fe_3O_4 TC 10 mM and OA 64 mM uncoated (A) and coated with chitosan (B) of low molecular weight (38 kDa). The results are expressed as average ± standard deviation for three independent experiments.

The encapsulation efficiency of DOX into polymer-coated Fe_3O_4 TD NPs was studied using the best parameters found in the previous encapsulation tests. The polymer (CS or *O*-HTCC):TPP ratio was 1:1.875 and the polymer:DOX ratio 6:1, the encapsulation efficiency is around 50-60% (Figure 7.8) and is similar to both CS and *O*-HTCC alone. Therefore, the presence of Fe_3O_4 TD does not influence the encapsulation efficiency of DOX into polymeric nanoparticles.

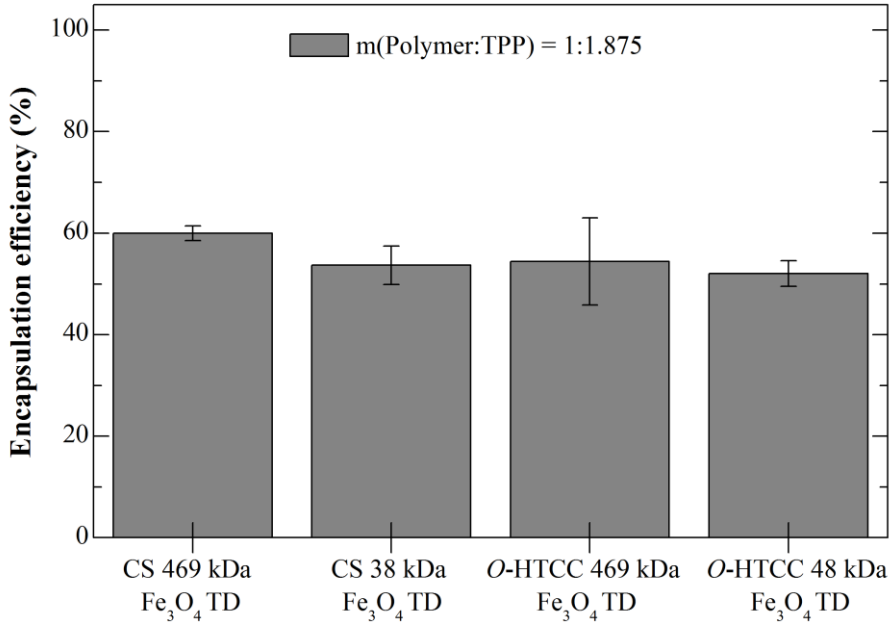

Figure 7.8. Encapsulation efficiency of doxorubicin in Fe_3O_4 TD NPs coated with either chitosan or *O*-HTCC. The results are expressed as average ± standard deviation for three independent experiments.

The overall obtained results for DOX encapsulation efficiency in either single polymeric NPs or polymer-Fe_3O_4 NPs are within the obtained range described in literature, in some cases even better. For CS NPs, Janes *et al*. [16] obtained a DOX encapsulation efficiency around 9%. Higher entrapment efficiency, of about 60%, was obtained by Mitra *el al*. [58] as they conjugated dextran with doxorubicin when producing DOX loaded CS NPs. For CS coated magnetic NPs Unsoy *et al*. [32] achieved 99% of DOX loading efficiency to 150 $\mu g.ml^{-1}$ and 81% to 600 $\mu g.ml^{-1}$, difference justified by DOX saturation.

The influence of pH on DOX release studies was performed at pH 4.5, 6.5, and 7.4. The procedure was similar for all the experiments: 1 ml of a suspension of DOX-loaded nanoparticles in PBS 7.4 was placed inside a dialysis membrane with a cut-off of 10-12 kDa. The membrane was emerged in 10 ml of the buffer with the desired pH. Samples of the release medium (3 ml) were collected at specific times and replaced with fresh medium.

The optimal conditions determined in the encapsulation efficiency studies were used for the preparation of DOX-loaded nanoparticles. However, the polymer:DOX weight ratio used was not the optimal one; instead, the weight ratio was 6:1 (polymer:DOX). Although the encapsulation efficiency is lower using this ratio, this was the one used due to DOX amount limitation. The used conditions for each type of DOX-loaded nanoparticles are summarized in Table 7.2.

Table 7.2. Amount of polymer, iron oxide nanoparticles (Fe_3O_4 NPs), doxorubicin (DOX) and sodium tripolyphosphate (TPP) used for the preparation of DOX-loaded NPs.

DOX-loaded NP type	**Weight amount (mg)**			
	Polymer	**Fe_3O_4 NPs**	**DOX**	**TPP**
CS	6	-	1	11.25
***O*-HTCC**	6	-	1	11.25
Fe_3O_4	-	10	1	-
CS + Fe_3O_4	6	0.5	1	11.25
		1.5		
***O*-HTCC + Fe_3O_4**		6		

7.3.3. DOX release studies from CS and *O*-HTCC nanoparticles

DOX release from chitosan nanoparticles at pH 4.5 and 7.4 at 25 ºC and 37 ºC (Figure 7.9). The results of this preliminary experiment show that DOX release saturates at 60-70% for all the tests between 10 h and 20 h. The initial release is however dependent of medium pH and temperature. The DOX release from CS NPs is faster at physiological temperature, 37 ºC. Although a slow drug release is desired, the studied drug delivery system is to be applied in physiological condition. Therefore, the experiments were performed at 37 ºC.

Due to chitosan hydrophilicity, at pH 4.5 a huge initial boost is observed, similar to control experiments. Consequently, at 37ºC even in pH 7.4 chitosan reaches easily its complete swollen state, therefore having a release profile similar to pH 4.5. Another control experiment was performed at 37ºC using 1 mg of free DOX placed inside a dialysis bag and emerged in three different mediums: pH 4.5, 6.5 and 7.4 (Figure 7.10). The results show that after 8 h of experiment a plateau is achieved for the pH mediums tested. At pH 4.5 total DOX amount is released from the dialysis

bag, while around 90% is released at pH 6.5 and at pH 7.4 only 60% of DOX is released. Consequently, these thresholds were considered as the maximum DOX release in the following experiments.

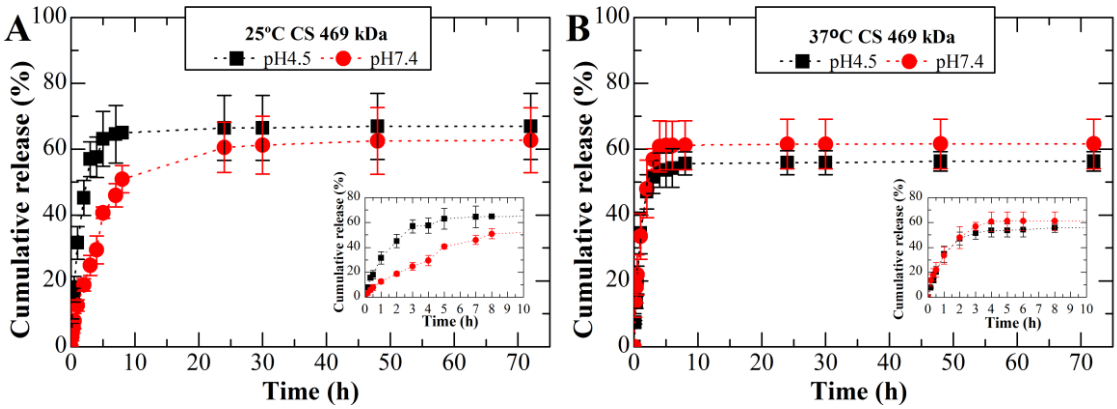

Figure 7.9. DOX release profile from chitosan nanoparticles with a molecular weight of 469 kDa, at pH 4.5 and pH 7.4 at 25 ºC (A) and 37 ºC (B). Insets correspond to a magnification of the burst release in the first 8 h of the experiment. The results are expressed as average ± standard deviation for three independent experiments.

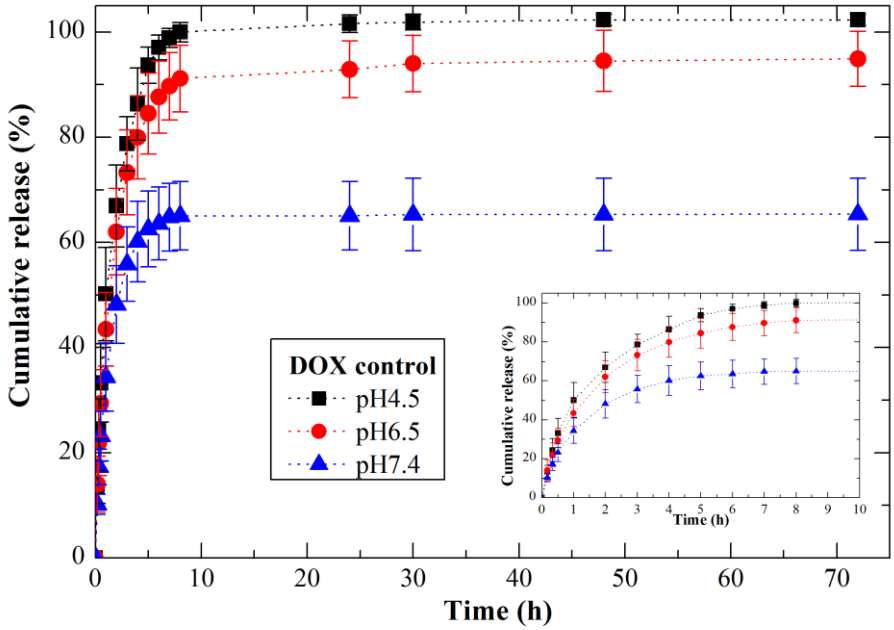

Figure 7.10. Free DOX release profile from a dialysis bag at 37 ºC at three mediums with different pH: 4.5, 6.5, and 7.4. Inset corresponds to a magnification of the burst release in the first 8 h of the experiment. The results are expressed as average ± standard deviation for three independent experiments.

DOX-loaded chitosan NPs were freeze-dried previously to drug release experiments with the purpose to investigate whether DOX release profile was affected by this step. It is important to consider that freeze-drying is an employed technique to prevent polymer degradation and drug leakage and desorption. Moreover, nanoparticles are more easily redispersible when freeze-dried [59].

Freeze dried sample was resuspended in 1 ml of PBS 7.4 and placed inside the dialysis bag. Figure 7.11 shows the DOX release from chitosan nanoparticles after freeze-drying. Comparing Figure 7.9 B and Figure 7.11, i.e., not freeze-dried and freeze-dried samples, respectively, is observed a slower release in the first hours of experiment for freeze-dried samples. Chitosan is already in its swollen state in not freeze-dried samples; therefore, the initial boost observed, which is similar to control experiments, is caused by the absence of the CS initial swelling stage. At pH 7.4 freeze-dried samples lead to a more controlled drug release (around 20% of DOX released), while not freeze-dried samples released around 60% of DOX.

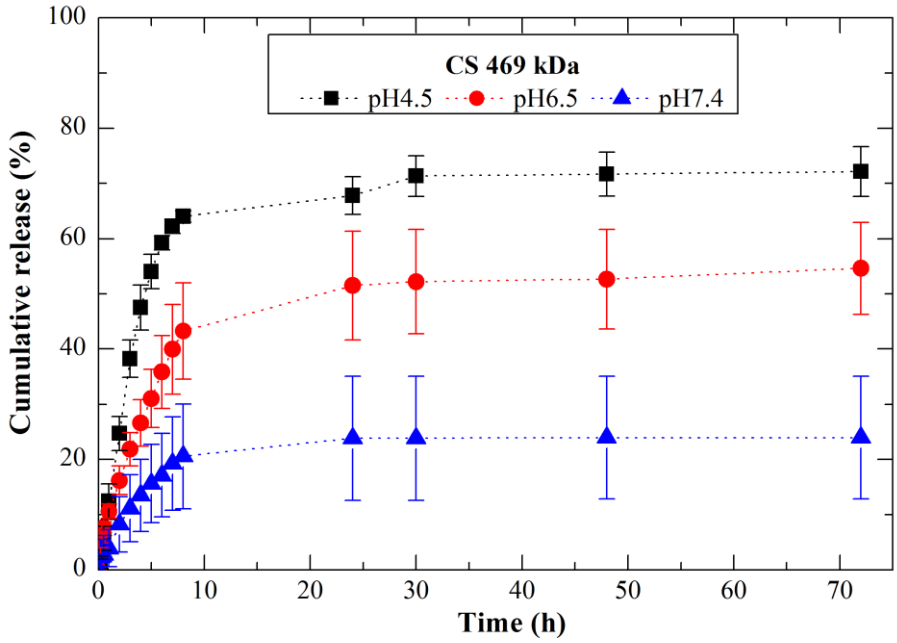

Figure 7.11. DOX release profile from freeze-dried chitosan nanoparticles with a molecular weight of 469 kDa, at pH 4.5, 6.5, and 7.4 at 37 ºC. The results are expressed as average ± standard deviation for three independent experiments.

The influence of the polymer molecular weight and the differences between chitosan and *O*-HTCC were analyzed. The DOX release profile from CS and *O*-HTCC NPs with low and high molecular weight is shown in Figure 7.12 at pH 4.5 (A), 6.5 (B) and 7.4 (C). At pH 4.5 the four samples show a similar drug release profile. The lowest and highest molecular weight samples of CS NPs show a similar drug release profile, but the higher molecular weight enhances the total

DOX release by about 5%. In *O*-HTCC NPs, the same difference can be observed and even though the final amount of drug released is different, the drug release profile is similar in all cases. At pH 6.5, the transition pH of CS solubility (pKa around 6-6.5), the DOX-loaded CS NPs show identical drug release profile, but the influence of molecular weight is the opposite. In this case, CS NPs with 469 kDa at pH 6.5 caused a reduction of the total amount of DOX released in about 20%, comparing to pH 4.5. In DOX-loaded *O*-HTCC NPs for the lowest molecular weights, there is a reduction in the total amount of DOX released at pH 6.5. The exception is for *O*-HTCC NPs with the highest molecular weight, were no significant differences are found between pH 4.5 and 6.5. Overall, the release profiles are similar at pH 4.5 and 6.5.

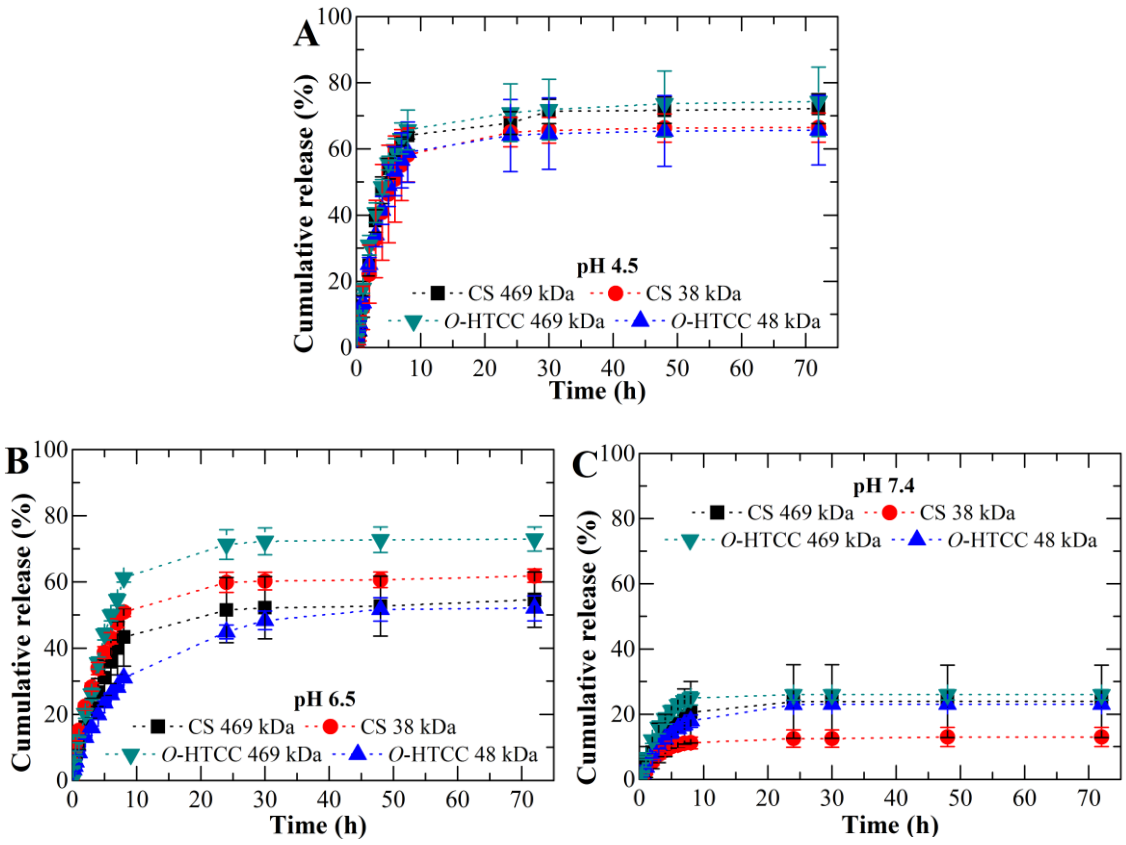

Figure 7.12. DOX release profile from freeze-dried chitosan and *O*-HTCC nanoparticles with a molecular weight of 39 KDa and 469 KDa or 48 KDa and 469 KDa, respectively, at pH 4.5 (A), pH 6.5 (B) and pH 7.4 (C) at 37 ºC. The results are expressed as average ± standard deviation for three independent experiments.

At pH 7.4 the amount of DOX released from both types of polymeric NPs is much smaller, being the maximum obtained of about 25% for both polymers. In this case, since the total amount of DOX released is so small, no significant differences were found by changing the molecular weight of the polymers.

7.3.4. DOX release studies from iron oxide nanoparticles

Figure 7.13 displays the DOX release of pristine Fe_3O_4 NPs (A), and coated with TC 10 mM (B) and OA 64 mM (C). A strong influence of pH on the DOX release is observed for the iron oxide NPs. At pH 4.5, DOX is nearly all (about 98%) released within 10 h. The value of DOX release decreases to 50% reached also in 10 h when pH is 6.5. If pH is 7.4 DOX is released within 8 hours of experiment being the maximum value 20%. The Fe_3O_4 TC 10 mM NPs and Fe_3O_4 OA 64 mM NPs have similar drug release profiles and DOX retention at pH 4.5. Interestingly Fe_3O_4 NPs stabilized with oleic acid (Figure 7.13 (C)) at pH 6.5 retains more 20% to 30% of DOX than the other iron oxide NPs tested. The formation of the oleic acid bilayer, described in Chapter 3, is maybe the main cause for this difference.

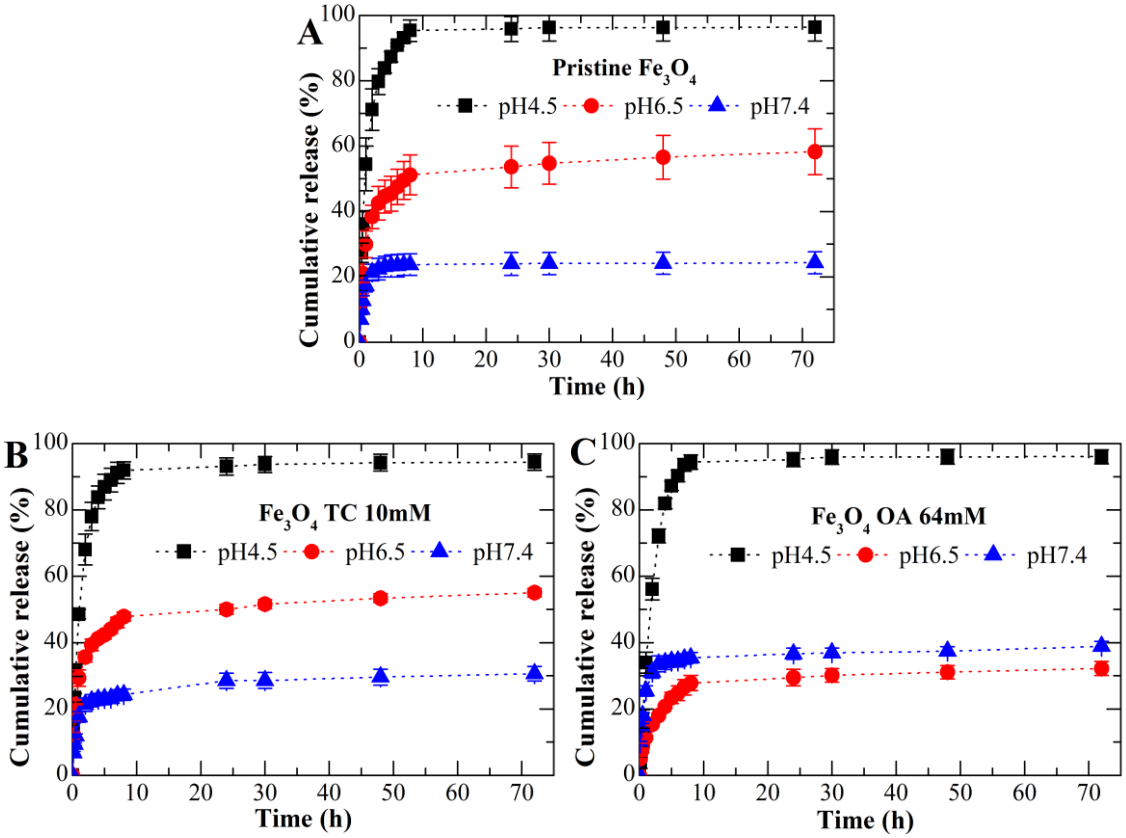

Figure 7.13. DOX release profile from pristine Fe_3O_4 NPs (A), and Fe_3O_4 NPs stabilized with tri-sodium citrate 10 mM (B) and oleic acid 64 mM (C) at pH 4.5, pH 6.5, and pH 7.4 at 37 ºC. The results are expressed as average ± standard deviation for three independent experiments.

7.3.5. DOX release studies from polymer-coated Fe_3O_4 NPs

Concerning DOX release studies from chitosan coated pristine Fe_3O_4 and Fe_3O_4 TC 10 mM and OA 64 mM the obtained results are shown in Figure 7.14.

The amount of DOX release from DOX-loaded CS NPs with and without Fe_3O_4 NPs is higher in the presence of Fe_3O_4 NPs, although the influence of pH is quite similar to all particles. At pH 4.5 and 6.5 the maximum release is 60-70% obtained within 10 h, while at pH 7.4 the total released is lower than 20% in CS and around 30% for coated Fe_3O_4 NPs. CS Fe_3O_4 OA 64 mM has a different behavior at pH 6.5, leading to a decrease in the maximum release.

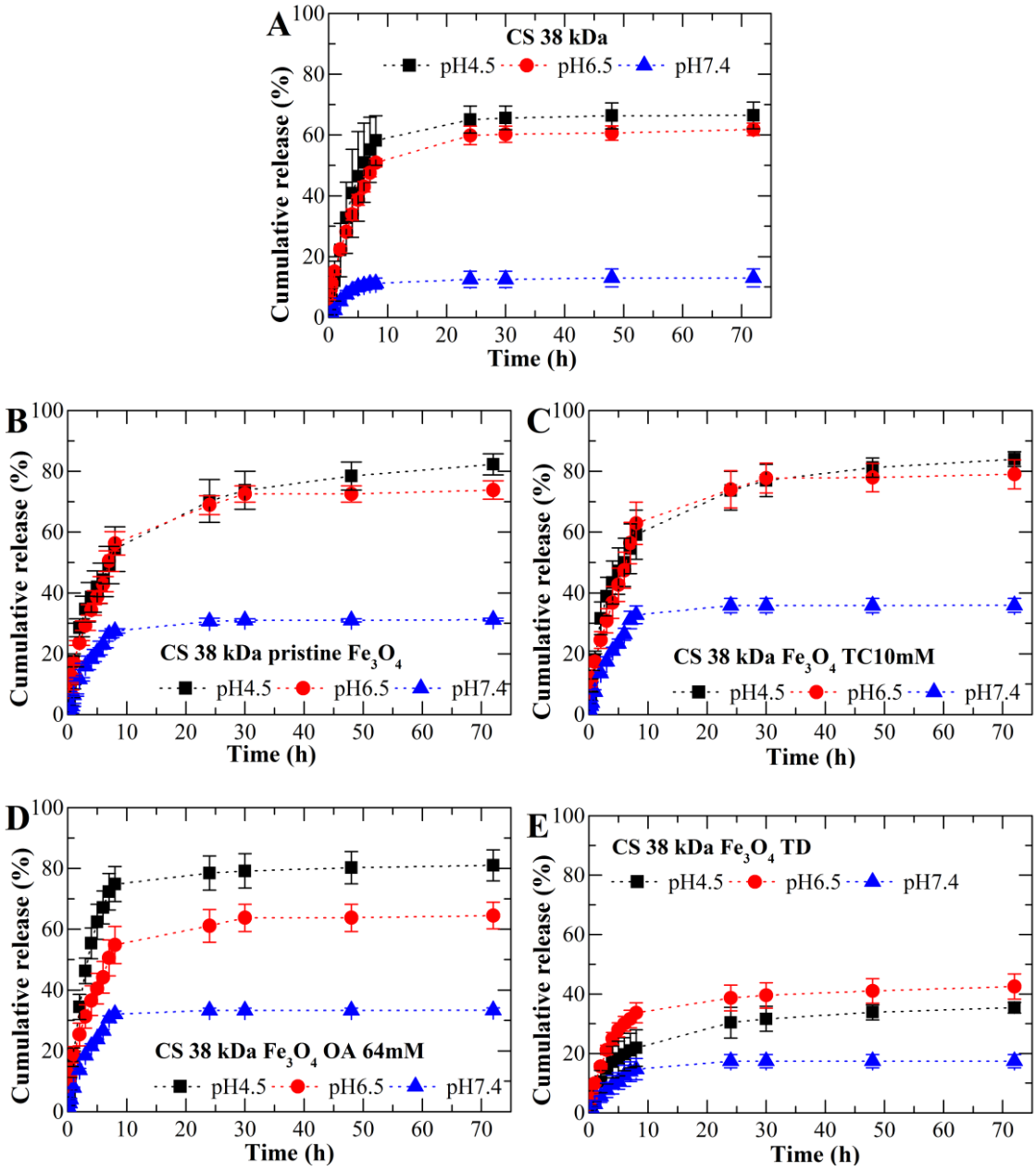

Figure 7.14. DOX release profile from CS NPs (A), CS-coated pristine Fe_3O_4 NPs (B), CS Fe_3O_4 NPs stabilized with tri-sodium citrate 10 mM (C) and oleic acid 64 mM (D), and CS Fe_3O_4 TD NPs (E) at pH 4.5, pH 6.5, and pH 7.4 at 37 ºC. The results are expressed as average ± standard deviation for three independent experiments.

Finally, DOX release from chitosan-coated Fe_3O_4 TD NPs is displayed in Figure 7.14 E. These Fe_3O_4 NPs are obtained from thermal decomposition technique and therefore are more stable in aqueous solution than pristine Fe_3O_4 NPs. The incorporation of this type of iron oxide nanoparticles in chitosan strongly decreases for all the pH studied, even though the increase of pH reduces the overall release as observed for the other NPs.

Comparison of DOX release from CS pristine Fe_3O_4 and CS Fe_3O_4 TD shows a decrease of around 40% and 30% of total DOX release at pH 4.5 and pH 6.5, respectively. At physiological pH the decrease is not so marked, about 10 %.

The amount of Fe_3O_4 incorporated in CS NPs was also varied from 0.5 mg to 1.5 mg and 6 mg. Figure 7.15 shows the obtained DOX release profiles for CS-coated pristine Fe_3O_4 NPs varying the amount of Fe_3O_4 NPs added to chitosan. DOX release studies performed at pH 4.5 are not influenced by the increase of Fe_3O_4 amount from 0.5 to 1.5 mg.

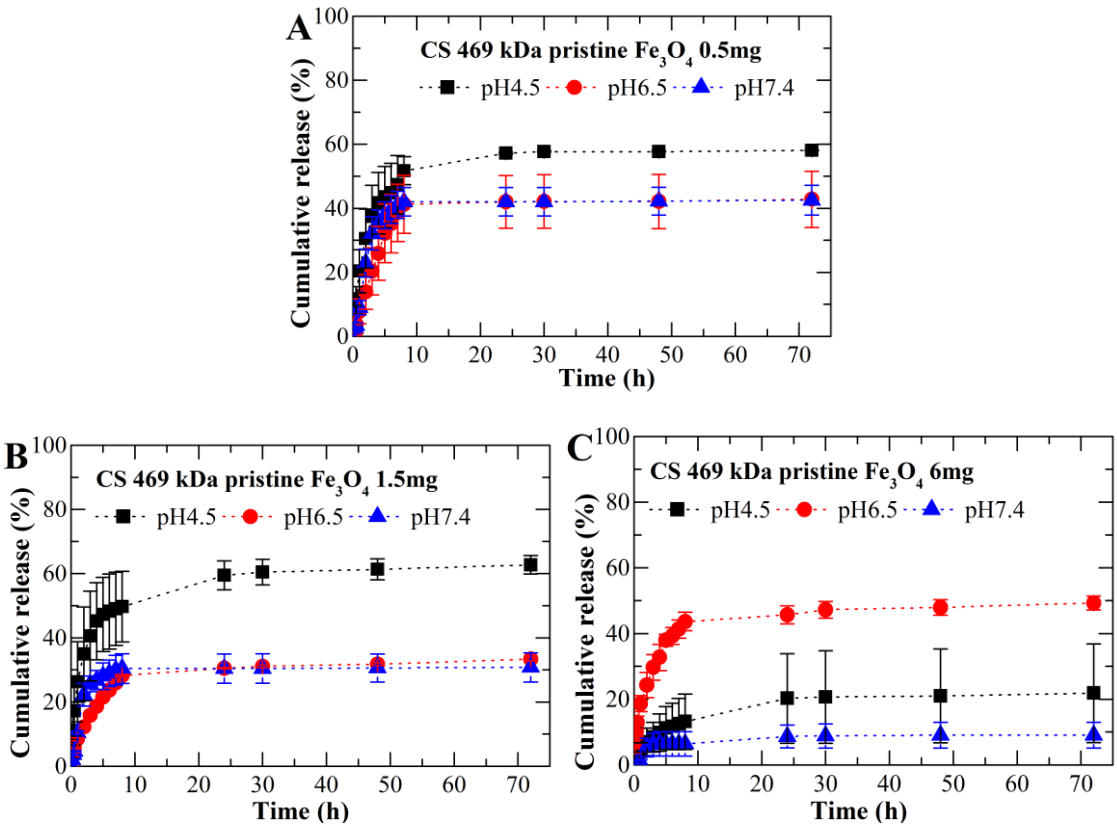

Figure 7.15. DOX release profile from CS NPs with 0.5 mg (A), 1.5 mg (B) and 6 mg (C) of pristine Fe_3O_4 NPs at pH 4.5, pH 6.5, and pH 7.4 at 37 ºC. The results are expressed as average ± standard deviation for three independent experiments.

When the Fe_3O_4 amount is increased up to 6 mg, DOX release decreases from about 60% to 20%. At physiological pH (7.4) the total DOX release is almost linear with the increase in Fe_3O_4 amount, decreasing from around 40% to 30 % and 10 % for 0.5 mg, 1.5 mg, and 6 mg, respectively. Again, at pH 6.5 DOX has an abnormal release profile, apparently not related to Fe_3O_4 weight. Since this is a transition pH of CS solubility, the drug release mechanism is always complex at this pH. However, for most cases, the increase in Fe_3O_4 amount leads to a decrease in total DOX release.

DOX release studies were also performed from Fe_3O_4 NPs incorporated in *O*-HTCC NPs. Figure 7.16 shows the DOX release profile of *O*-HTCC NPs with and without Fe_3O_4 at pH 4.5, 6.5, and 7.4. Some differences can be observed at the most acidic pH (4.5). Although in all cases the total DOX released achieves the same value (around 60%), the release is slower and more controlled for *O*-HTCC with pristine Fe_3O_4, TC 10 mM and Fe_3O_4 TD. The presence of Fe_3O_4 OA 64 mM does not seem to influence DOX release from *O*-HTCC NPs. At physiological pH (7.4) although some differences in the total DOX released, no significant differences in DOX release profile can be observed between the analyzed samples. Finally, at pH 6.5 an increase in total DOX released in some cases and no shift in another. However, in all the analyzed cases the incorporation of Fe_3O_4 in *O*-HTCC appears to fasten the DOX release, compared to *O*-HTCC alone.

Similar to what was performed with chitosan, different amounts of pristine Fe_3O_4 NPs were incorporated into *O*-HTCC NPs to access its influence in DOX release profile. DOX release profile from *O*-HTCC with 0.5 mg, 1.5 mg, and 6 mg of pristine Fe_3O_4 NPs at pH 4.5, 6.5, and 7.4 is represented in Figure 7.17.

The increase of Fe_3O_4 weight from 0.5 to 1.5 and 6 slightly decreases the total DOX released from *O*-HTCC NPs. At pH 4.5, the difference observed is of about 15% when the Fe_3O_4 weight increases from 0.5 to 1.5 mg. However, when the amount of Fe_3O_4 is 6 mg, no significant differences are observed, compared to 1.5 mg. Moreover, at this acidic pH, DOX release is slower with the increase of Fe_3O_4 amount. A similar behavior is found at pH 6.5.

When the Fe_3O_4 weight increases from 0.5 mg to 1.5 mg, a decrease in about 15% is observed in total DOX released. However, when Fe_3O_4 weight increases up to 6 mg, no significant differences are observed. Finally, at pH 7.4 a slight decrease in total DOX release is observed for a higher weight of Fe_3O_4 (6 mg) incorporated, although DOX release profile from *O*-HTCC NPs is not altered.

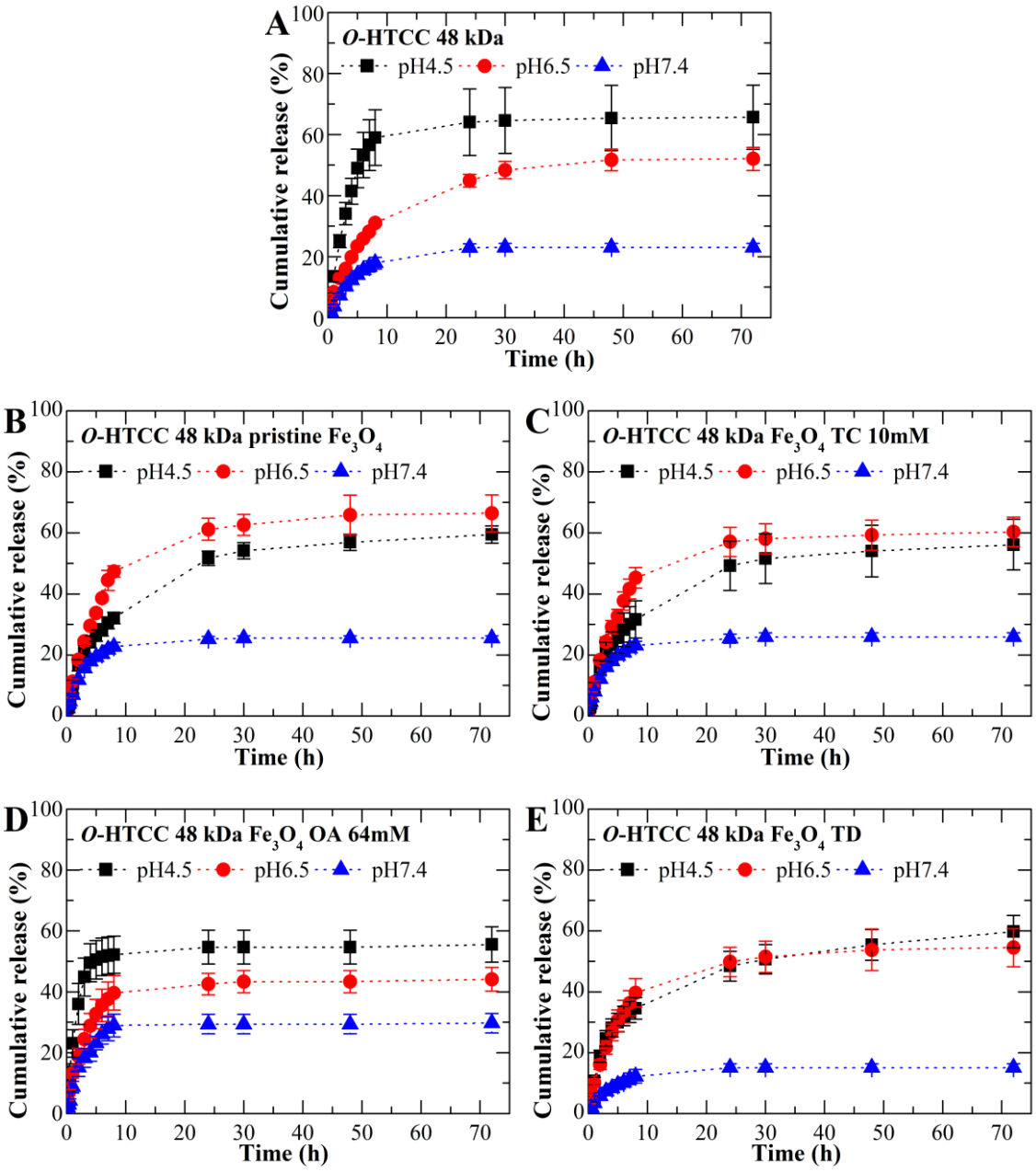

Figure 7.16. DOX release profile from *O*-HTCC NPs (A), *O*-HTCC-coated pristine Fe_3O_4 NPs (B), *O*-HTCC Fe_3O_4 NPs stabilized with tri-sodium citrate 10 mM (C) and oleic acid 64 mM (D), and *O*-HTCC Fe_3O_4 TD NPs (E) at pH 4.5, pH 6.5, and pH 7.4 at 37 ºC. The results are expressed as average ± standard deviation for three independent experiments.

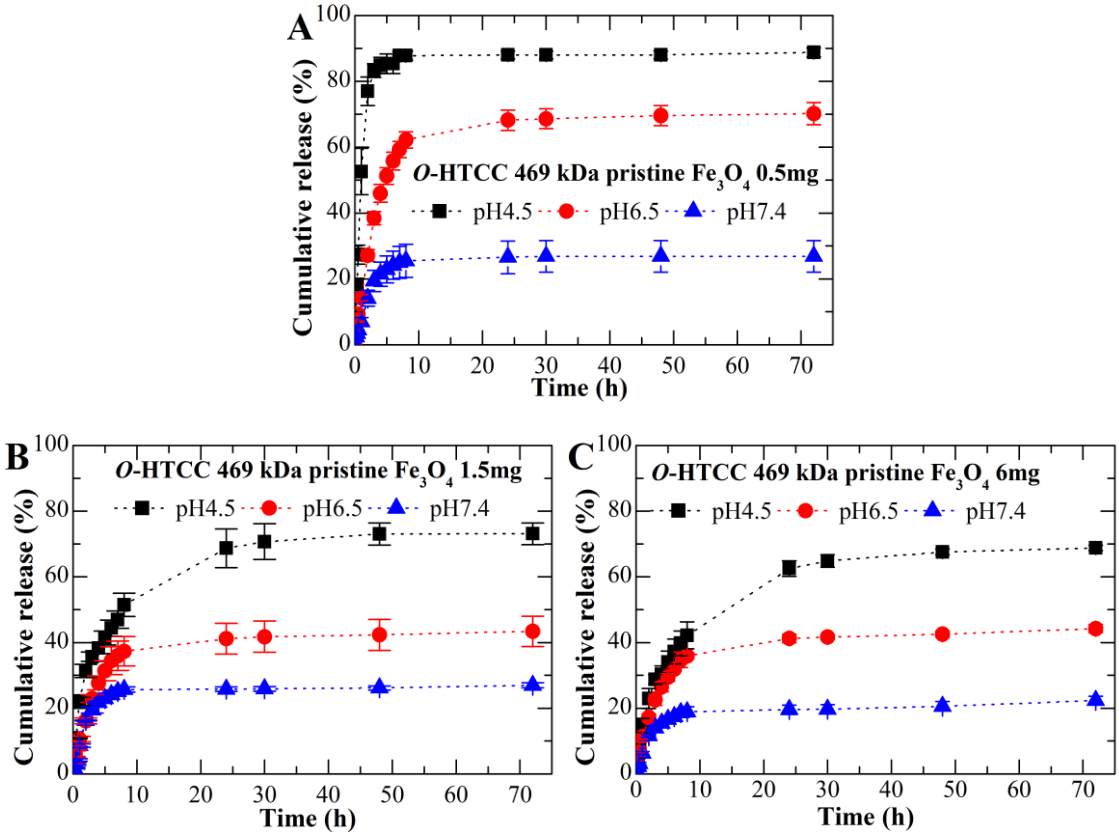

Figure 7.17. DOX release profile from *O*-HTCC NPs with 0.5 mg (A), 1.5 mg (B) and 6 mg (C) of pristine Fe_3O_4 NPs at pH 4.5, pH 6.5, and pH 7.4 at 37 ºC. The results are expressed as average ± standard deviation for three independent experiments.

7.3.6. Mathematical modeling of DOX release profiles

A wide variety of mathematical models is available to fit drug release data, most of which are presented as nonlinear equations. However fitting these nonlinear equations to drug release data is not easy to be done by hand. Zhang and coworkers developed a freely available add-in program called DDSolver. This program can be used to facilitate modeling of dissolution data using non-linear optimization methods based in a build-in model library containing several dissolution models. Furthermore, this program speeds up the calculation and reduces errors of calculation [60].

The fitting of the drug release data was performed using DDSolver, in which the desired model is selected, experimental data is chosen (time intervals and drug percentage), and the software provides the results from the specific modelling. An example of the obtained results can be seen in Figure 7.18. The software not only provides the adjusted data but also the "goodness of fit" where several parameters are calculated to determine in the selected model fits to experimental data.

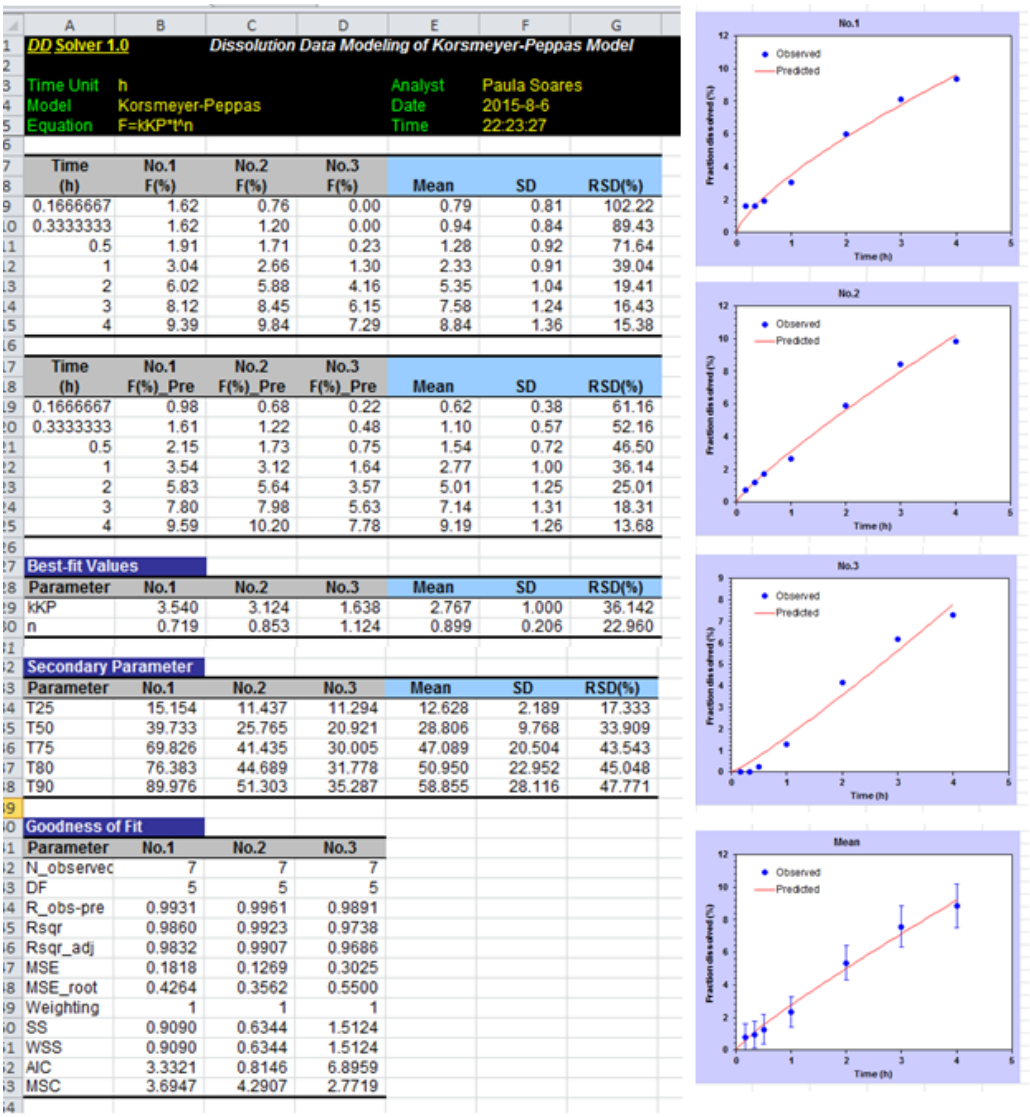

DD Solver 1.0				Dissolution Data Modeling of Korsmeyer-Peppas Model		
Time Unit	h			Analyst	Paula Soares	
Model	Korsmeyer-Peppas			Date	2015-8-6	
Equation	F=kKP*t^n			Time	22:23:27	

Time (h)	No.1 F(%)	No.2 F(%)	No.3 F(%)	Mean	SD	RSD(%)
0.1666667	1.62	0.76	0.00	0.79	0.81	102.22
0.3333333	1.62	1.20	0.00	0.94	0.84	89.43
0.5	1.91	1.71	0.23	1.28	0.92	71.64
1	3.04	2.66	1.30	2.33	0.91	39.04
2	6.02	5.88	4.16	5.35	1.04	19.41
3	8.12	8.45	6.15	7.58	1.24	16.43
4	9.39	9.84	7.29	8.84	1.36	15.38

Time (h)	No.1 F(%)_Pre	No.2 F(%)_Pre	No.3 F(%)_Pre	Mean	SD	RSD(%)
0.1666667	0.98	0.68	0.22	0.62	0.38	61.16
0.3333333	1.61	1.22	0.48	1.10	0.57	52.16
0.5	2.15	1.73	0.75	1.54	0.72	46.50
1	3.54	3.12	1.64	2.77	1.00	36.14
2	5.83	5.64	3.57	5.01	1.25	25.01
3	7.80	7.98	5.63	7.14	1.31	18.31
4	9.59	10.20	7.78	9.19	1.26	13.68

Best-fit Values

Parameter	No.1	No.2	No.3	Mean	SD	RSD(%)
kKP	3.540	3.124	1.638	2.767	1.000	36.142
n	0.719	0.853	1.124	0.899	0.206	22.960

Secondary Parameter

Parameter	No.1	No.2	No.3	Mean	SD	RSD(%)
T25	15.154	11.437	11.294	12.628	2.189	17.333
T50	39.733	25.765	20.921	28.806	9.768	33.909
T75	69.826	41.435	30.005	47.089	20.504	43.543
T80	76.383	44.689	31.778	50.950	22.952	45.048
T90	89.976	51.303	35.287	58.855	28.116	47.771

Goodness of Fit

Parameter	No.1	No.2	No.3
N_observec	7	7	7
DF	5	5	5
R_obs-pre	0.9931	0.9961	0.9891
Rsqr	0.9860	0.9923	0.9738
Rsqr_adj	0.9832	0.9907	0.9686
MSE	0.1818	0.1269	0.3025
MSE_root	0.4264	0.3562	0.5500
Weighting	1	1	1
SS	0.9090	0.6344	1.5124
WSS	0.9090	0.6344	1.5124
AIC	3.3321	0.8146	6.8959
MSC	3.6947	4.2907	2.7719

Figure 7.18. Example of the data sheet obtained using DDSolver program in fitting the Korsmeyer-Peppas model to DOX release from CS 38 kDa NPs at pH 7.4.

When fitting a mathematical model to drug release experimental data it is important to correctly select the mathematical models suitable for the drug release data in study. Taking into consideration the studied drug "containers", chitosan and *O*-HTCC are both hydrophilic polymers. Moreover, DOX is a cationic amphiphilic drug. Thus, mathematical models such as zero-order, first-order, Higuchi, Hixson-Crowell, and Hopfenberg are not applicable in these cases. Zero-order kinetics is used for drugs with low solubility in matrix tables, while first-order kinetics describes drug absorption and is used for water-soluble drugs in porous materials. Chitosan is considered to be a swelling matrix, which means that Higuchi model cannot be applied since it describes drug diffusion from a non-swelling matrix, typically used for matrix tablets [61]. Moreover, Hixson-

Crowell model is applicable for systems where the surface are and diameter of the "carrier" is maintained constant, which is not the case. Finally, Hopfenberg model describes drug release from eroding polymers, which do not fit chitosan profile, within the studied conditions.

Consequently, the mathematical models that best fit experimental data of DOX release from both chitosan and *O*-HTCC NPs are Korsmeyer-Peppas, Weibull, and Peppas-Sahlin. The three mathematical models were applied to all experimental data of DOX release from CS and *O*-HTCC NPs with and without Fe_3O_4 NPs incorporated. To determine the most appropriate model, the adjusted coefficient of determination (R^2_{adj}) was used, which is calculated by:

$$R^2_{adj} = 1 - \frac{n-1}{n-p}(1 - R^2) \qquad \text{Equation 7.4}$$

where *n* is the number of data points and *p* is the number of parameters in the model. Therefore, the best model to fit the experimental data is the one with highest R^2_{adj} [60].

Although an extensive description of the mathematical models in available in the introduction section of this chapter, a brief summary will be presented here.

Peppas and Sahlin model is described by an equation with two parcels; each parcel has a constant *k*. Using the constant values, the percentage of Fickian and relaxational drug release can be determined [50]. The exponent *m* can be related to the exponent *n* of Korsmeyer-Peppas model, since the value should be the same. Exponent *n* of Korsmeyer-Peppas model gives information about the release mechanism. If $n \leq 0.43$ it is a Fickian diffusion, if $n = 0.85$ it is a case II transport, which is related to polymer matrix relaxation and swelling. If *n* is between 0.43 and 0.85 it corresponds to an anomalous transport, resultant from the combination of Fickian diffusion and case II transport. Exceptionally, if $n > 0.85$ it is super case II transport [43]. Weibull model also has two constants, *a* and *b*. *a* is a time factor, and *b* is related to the shape of release curve and can be correlated to exponent *n* of Korsmeyer-Peppas model. If $b \leq 0.75$ it is a Fickian diffusion, for *b* between 0.75 and 1 is a combined mechanism, and for $b > 1$ drug is released through a complex mechanism [52].

7.3.6.1. Chitosan and *O*-HTCC NPs

For the application of the chosen mathematical model it was taken into account that chitosan has a swelling behavior. As such, fitting was performed for freeze-dried samples. However, an exception was made for not freeze-dried chitosan nanoparticles with the purpose to better understand the differences between freeze-dried and not freeze-dried samples. Korsmeyer-Peppas, Weibull, and Peppas-Sahlin models were applied to experimental data of DOX release from not

freeze-dried chitosan nanoparticles with four different molecular weights: 38 kDa, 170 kDa, 215 kDa, and 469 kDa. The obtained results from DDSolver program are represented in Table 7.3. Parameters values of each mathematical model as well as R^2_{adj} are described. Moreover, the higher R^2_{adj} of each sample is highlighted at bold and green.

Almost all experimental data is well fitted by Weibull model, although small deviations are found from Korsmeyer-Peppas adjusted coefficient of determination. Parameter *b* of Weibull model is not equal to all samples. For higher molecular weights, *b* is between 0.75 and 1, indicating a mixed mechanism between Fickian and Case II. For the remaining molecular weights, *b* is below 0.75, indicating Fickian diffusion. To understand these differences, parameters from the other two models were also analyzed. Exponent *n* from Korsmeyer-Peppas model presents a value below 0.85 for most cases, indicating an anomalous or non-Fickian diffusion. However, for most cases the value approaches 0.5, which is close to the established limit between Fickian and non-Fickian diffusion. On the other hand, exponent *m* from Peppas-Sahlin model has an average value of 0.35 for all cases, which indicates a Fickian diffusion mechanism of release. In Peppas-Sahlin model, constant k_1 is much higher than k_2, meaning that Fickian diffusion is the predominant mechanism. At higher molecular weight, since the polymer network is much denser, the relaxation rate has some contribution to DOX release. However, as the molecular weight decreases, the polymer' network becomes thinner, facilitating drug release. DOX release is predominated by Fickian' diffusion mechanism since chitosan is already in its swollen state.

In the case of freeze-dried chitosan NPs (Table 7.4), experimental data from all samples at pH 4.5 and 7.4 are well fitted by Weibull model, while experimental data from samples at pH 6.5 are fitted by Korsmeyer-Peppas model. However, the adjusted coefficient of determination is very similar between both models. It should be noticed that these two models are only applicable for the first 60% of drug release, where it has a straight profile. First, considering the Weibull model' parameters, constant *b* is higher than 1 at pH 4.5 and 7.4, which indicates a complex release mechanism. At pH 6.5, *b* value is below 0.85, corresponding to a Fickian release mechanism. Exponent *n* from Korsmeyer-Peppas model is higher than 0.85 at pH 4.5 and 7.4, and below 0.85 at pH 6.5 in the four molecular weights, indicating an anomalous mechanism and a complex drug release or super case II transport, respectively. Regarding Peppas-Sahlin parameters, exponent *m* is between 0.5 and 0.6 for all samples which indicates an anomalous transport, while k_1 although is higher that k_2, is much smaller than the one obtained for not freeze-dried samples. Moreover, k_1 values decreases with the increase of pH, indicating that the Fickian contribution also decreases.

Table 7.3. DOX release profile from not freeze-dried chitosan nanoparticles at different molecular weights (M_v): parameters values and R^2_{adj} obtained from fitting the mathematical models to experimental data.

M_v (kDa)	pH	Korsmeyer-Peppas			Weibull			Peppas-Sahlin			
		n	K	R^2_{adj}	a	b	R^2_{adj}	k_1	k_2	m	R^2_{adj}
469	**4.5**	0.83 ± 0.048	34 ± 6.5	0.988	2.4 ± 0.63	0.95 ± 0.079	**0.990**	38 ± 4.9	-5.8 ± 1.1	0.36 ± 0.013	0.832
	7.4	0.55 ± 0.087	33 ± 6.9	**0.984**	2.6 ± 0.65	0.62 ± 0.077	0.978	43 ± 5.7	-7.2 ± 2.2	0.35 ± 0.050	0.842
215	**4.5**	1.0 ± 0.27	40 ± 4.6	0.984	1.9 ± 0.31	1.2 ± 0.330	**0.985**	43 ± 0.53	-6.6 ± 0.22	0.37 ± 0.004	0.775
	7.4	0.56 ± 0.036	37 ± 7.6	0.964	2.2 ± 0.54	0.66 ± 0.038	**0.968**	46 ± 6.3	-7.6 ± 1.6	0.34 ± 0.018	0.858
170	**4.5**	0.56 ± 0.15	40 ± 6.6	0.915	1.9 ± 0.38	0.67 ± 0.19	**0.928**	46 ± 5.2	-8.5 ± 0.91	0.31 ± 0.019	0.825
	7.4	0.59 ± 0.029	29 ± 2.5	**0.983**	2.9 ± 0.29	0.66 ± 0.024	**0.983**	39 ± 4.4	-5.9 ± 0.82	0.36 ± 0.013	0.850
38	**4.5**	0.59 ± 0.16	31 ± 1.7	0.874	2.7 ± 0.17	0.67 ± 0.18	**0.882**	38 ± 3.2	-6.3 ± 0.52	0.34 ± 0.043	0.842
	7.4	0.47 ± 0.13	35 ± 7.6	0.961	2.4 ± 0.62	0.58 ± 0.13	**0.963**	46 ± 10	-7.1 ± 2.8	0.36 ± 0.051	0.888

Consequently, in freeze-dried samples the contribution of Fickian diffusion for DOX release is much smaller. In this case, both Fickian diffusion and relaxation-controlled transport contribute to DOX release from CS NPs. Furthermore, at pH 4.5 and 7.4 the release mechanisms are clearer. Again at pH 6.5, which is the transitory pH of chitosan due to its own pKa (6.0 – 6-5), DOX release occurs through a mixed mechanism between Fickian diffusion and Super-Case II transport, where both diffusion rate and relaxation rate play an important role.

Table 7.4. DOX release profile from freeze-dried chitosan nanoparticles at different molecular weights (M_v): parameters values and R^2_{adj} obtained from fitting the mathematical models to experimental data.

M_v (kDa)	pH	Korsmeyer-Peppas			Weibull			Peppas-Sahlin			
		n	K	R^2_{adj}	a	b	R^2_{adj}	k_1	k_2	m	R^2_{adj}
469	**4.5**	0.99 ± 0.11	12 ± 2.8	0.996	7.9 ± 1.8	1.2 ± 0.12	**0.998**	25 ± 2.2	-1.9 ± 0.29	0.52 ± 0.017	0.891
	6.5	0.64 ± 0.04	11 ± 1.3	**0.994**	8.6 ± 0.96	0.71 ± 0.06	0.990	15 ± 2.3	-1.04 ± 0.13	0.53 ± 0.015	0.962
	7.4	0.83 ± 0.26	4.9 ± 4.2	0.981	31 ± 22	0.87 ± 0.26	**0.981**	7.5 ± 4.4	-0.55 ± 0.40	0.54 ± 0.040	0.932
215	**4.5**	1.1 ± 0.16	9.7 ± 3.9	0.996	11 ± 3.8	1.2 ± 0.15	**0.997**	19 ± 4.8	-1.6 ± 0.28	0.50 ± 0.009	0.873
	6.5	0.68 ± 0.11	12 ± 3.9	**0.987**	8.9 ± 3.9	0.76 ± 0.099	0.983	16 ± 4.9	-1.1 ± 0.58	0.55 ± 0.064	0.958
	7.4	1.08 ± 0.0061	2.4 ± 0.52	0.987	44 ± 11	1.1 ± 0.007	**0.989**	5.3 ± 1.3	-0.28 ± 0.093	0.61 ± 0.028	0.930
170	**4.5**	1.05 ± 0.17	9.9 ± 4.4	0.996	11 ± 4.6	1.1 ± 0.16	**0.998**	19 ± 5.4	-1.6 ± 0.39	0.50 ± 0.014	0.876
	6.5	0.61 ± 0.054	12 ± 1.2	**0.996**	7.6 ± 0.82	0.68 ± 0.06	0.992	16 ± 1.2	-1.1 ± 0.25	0.53 ± 0.035	0.968
	7.4	1.05 ± 0.037	2.2 ± 0.39	0.983	46 ± 7.6	1.1 ± 0.037	**0.985**	4.8 ± 0.92	-0.25 ± 0.082	0.62 ± 0.038	0.932
38	**4.5**	0.91 ± 0.11	10 ± 4.5	0.996	10 ± 3.7	1.02 ± 0.11	**0.998**	19 ± 7.2	-1.5 ± 0.83	0.53 ± 0.055	0.908
	6.5	0.55 ± 0.02	15 ± 0.81	**0.997**	5.8 ± 0.32	0.62 ± 0.027	0.994	20 ± 1.3	-1.6 ± 0.25	0.50 ± 0.021	0.968
	7.4	0.89 ± 0.21	2.8 ± 1.0	0.981	407 ± 18	0.92 ± 0.21	**0.981**	4.8 ± 1.03	-0.41 ± 0.15	0.50 ± 0.032	0.890

Table 7.5. DOX release profile from freeze-dried *O*-HTCC nanoparticles at different molecular weights (M_v): parameters values and $R^2_{adjusted}$ obtained from fitting the mathematical models to experimental data.

M_v (kDa)	pH	Korsmeyer-Peppas			Weibull			Peppas-Sahlin			
		n	K	R^2_{adj}	a	b	R^2_{adj}	k_1	k_2	m	R^2_{adj}
469	**4.5**	0.75 ± 0.021	17 ± 1.4	0.996	5.1 ± 0.45	0.89 ± 0.018	**0.999**	27 ± 1.6	-2.4 ± 0.52	0.49 ± 0.030	0.914
	6.5	0.79 ± 0.024	12 ± 1.01	**0.991**	7.8 ± 0.69	0.89 ± 0.022	0.983	19 ± 1.7	-1.2 ± 0.27	0.56 ± 0.029	0.945
	7.4	0.97 ± 0.024	5.7 ± 0.53	0.975	17 ± 1.7	1.0 ± 0.03	**0.978**	10 ± 0.99	-0.91 ± 0.13	0.49 ± 0.012	0.882
292	**4.5**	0.85 ± 0.054	14 ± 3.2	**0.999**	6.8 ± 1.6	1.0 ± 0.032	0.998	-4.5 ± 5.9	19 ± 9.3	0.39 ± 0.065	**0.999**
	6.5	0.76 ± 0.043	9.0 ± 1.5	**0.997**	11 ± 1.9	0.88 ± 0.083	0.995	0.32 ± 1.7	9.6 ± 2.0	0.39 ± 0.043	**0.997**
	7.4	0.79 ± 0.13	5.4 ± 1.4	0.959	19 ± 5.6	0.83 ± 0.13	**0.962**	8.7 ± 1.4	-0.65 ± 0.18	0.53 ± 0.033	0.928
166	**4.5**	0.82 ± 0.039	12 ± 2.8	0.996	7.7 ± 1.7	0.96 ± 0.039	0.995	-1.6 ± 8.6	14 ± 10	0.45 ± 0.189	**0.998**
	6.5	0.70 ± 0.031	7.6 ± 0.84	0.994	13 ± 1.4	0.77 ± 0.035	0.991	8.8 ± 1.3	-0.29 ± 0.11	0.68 ± 0.044	**0.996**
	7.4	0.83 ± 0.027	3.9 ± 0.12	0.991	25 ± 0.76	0.87 ± 0.031	**0.993**	6.4 ± 0.32	-0.37 ± 0.017	0.58 ± 0.008	0.954
48	**4.5**	0.83 ± 0.011	13 ± 1.4	0.996	6.9 ± 0.75	0.95 ± 0.019	**0.999**	23 ± 2.6	-1.8 ± 0.23	0.51 ± 0.021	0.910
	6.5	0.63 ± 0.046	8.4 ± 0.63	**0.999**	11 ± 0.99	0.69 ± 0.052	0.998	9.9 ± 0.045	-0.47 ± 0.029	0.59 ± 0.010	0.995
	7.4	0.84 ± 0.015	3.8 ± 0.42	0.987	26 ± 3.1	0.88 ± 0.012	**0.989**	6.2 ± 0.79	-0.38 ± 0.082	0.56 ± 0.021	0.955

DOX release from *O*-HTCC NPs was expected to show a similar profile to chitosan due to the similarity between both polymer structures. However, the presence of the ammonium quaternary group in *O*-HTCC may affect not only its behavior to pH but also its interaction with DOX and

consequently its release. Table 7.5 shows the obtained data from fitting experimental results of DOX release from *O*-HTCC NPs. In a first analysis, some differences can be found with the increase of molecular weight, although *b* constant is below 1 for all cases, indicating a mixture between Fickian diffusion and Case II mechanism. The higher and lower molecular weights show similar DOX release profiles to chitosan in the same molecular weights. In both cases, either Weibull or Korsmeyer-Peppas models are well fitted, will almost no differences between both adjusted coefficients of determination. Moreover, exponent *n* from Korsmeyer-Peppas model is below 0.85 for all cases, indicating anomalous or non-Fickian diffusion where the diffusion rate is equal to the relaxation rate. This is correlated to the values of exponent *m*, which is higher than 0.43. The intermediate molecular weights show some different release profiles. In these cases, Peppas-Sahlin is the model with the best fitting. At pH 4.5 an inversion of the k_1 and k_2 constants occur, i.e., k_2 is higher than k_1, indicating that DOX release occurs mainly due to the relaxation of the polymer chains rather than by Fickian diffusion. In these intermediate molecular weights the presence of the ammonium quaternary group in *O*-HTCC appears to affect DOX release, greater than in the higher and lower molecular weights.

7.3.6.2. DOX release from CS Fe_3O_4 and *O*-HTCC Fe_3O_4 NPs

After analyzing the mechanism of DOX release from chitosan and *O*-HTCC nanoparticles, it is important to access the influence that the presence of Fe_3O_4 nanoparticles have in the mechanism of DOX release from CS Fe_3O_4 NPs.

Table 7.6 shows the obtained results from fitting the selected mathematical models to DOX release from CS NPs of 38 kDa incorporated with four types of Fe_3O_4 NPs: pristine Fe_3O_4, Fe_3O_4 TC 10 mM, Fe_3O_4 OA 64 mM, and Fe_3O_4 TD. Starting with CS pristine Fe_3O_4 NPs, the experimental data is well fitted by the three models since the adjusted coefficient of determination is very similar between the three models. For Korsmeyer-Peppas model, exponent *n* is between 0.43 and 0.85, indicating a combinatory mechanism of release between Fickian diffusion and relaxation of the polymer chain. Constant *b* of Weibull model shows some differences between different pH. At pH 4.5 and 6.5, constant *b* has a value below 0.75, corresponding to a drug release by Fickian diffusion. As the pH increases to 7.4, the Case II mechanism also plays an important role in drug release. Finally, Peppas-Sahlin parameters corroborate with the other models' parameters. Exponent *m* has a value around 0.53, indicating an anomalous transport. Similarly to what happened to chitosan nanoparticles alone, k_1 constant is much higher than k_2.

Table 7.6. DOX release profile from freeze-dried CS NPs (38 kDa) with pristine Fe_3O_4, Fe_3O_4 TC 10 mM, Fe_3O_4 OA 64 mM and Fe_3O_4 TD: parameters values and R^2_{adj}obtained from fitting the mathematical models to experimental data.

Fe_3O_4 type	pH	Korsmeyer-Peppas			Weibull			Peppas-Sahlin			
		n	K	R^2_{adj}	a	b	R^2_{adj}	k_1	k_2	m	R^2_{adj}
Pristine Fe_3O_4	**4.5**	0.51 ± 0.015	18 ± 1.8	0.968	5.3 ± 0.59	0.64 ± 0.040	0.982	20 ± 2.9	-1.3 ± 0.34	0.52 ± 0.026	**0.985**
	6.5	0.51 ± 0.018	17 ± 0.60	**0.998**	5.3 ± 0.20	0.61 ± 0.028	0.992	20 ± 1.1	-1.3 ± 0.089	0.53 ± 0.002	0.992
	7.4	0.75 ± 0.033	6.4 ± 0.51	0.986	15 ± 1.3	0.80 ± 0.034	**0.989**	10 ± 0.62	-0.71 ± 0.079	0.53 ± 0.010	0.945
Fe_3O_4 TC 10mM	**4.5**	0.55 ± 0.014	19 ± 3.4	0.962	5.0 ± 0.90	0.70 ± 0.023	**0.979**	23 ± 4.7	-1.6 ± 0.58	0.51 ± 0.018	0.976
	6.5	0.55 ± 0.028	17 ± 1.9	**0.996**	5.2 ± 0.64	0.64 ± 0.043	0.991	21 ± 3.1	-1.3 ± 0.30	0.54 ± 0.014	0.985
	7.4	0.72 ± 0.044	7.6 ± 0.61	0.991	13 ± 1.1	0.78 ± 0.049	**0.993**	11 ± 0.75	-0.82 ± 0.054	0.53 ± 0.007	0.946
Fe_3O_4 OA 64mM	**4.5**	0.83 ± 0.047	18 ± 2.8	0.993	5.0 ± 0.85	1.0 ± 0.034	**0.999**	30 ± 3.4	-2.5 ± 0.41	0.50 ± 0.011	0.912
	6.5	0.47 ± 0.021	19 ± 2.7	**0.998**	4.8 ± 0.80	0.54 ± 0.021	0.995	23 ± 3.7	-1.9 ± 0.55	0.48 ± 0.033	0.983
	7.4	0.77 ± 0.006	7.6 ± 0.29	0.993	12 ± 0.50	0.83 ± 0.005	**0.995**	12 ± 0.41	-0.97 ± 0.067	0.51 ± 0.009	0.928
Fe_3O_4 TD	**4.5**	0.65 ± 0.046	6.6 ± 1.6	0.976	16 ± 4.1	0.70 ± 0.053	0.980	8.2 ± 2.3	-0.42 ± 0.27	0.59 ± 0.069	**0.981**
	6.5	0.64 ± 0.022	10 ± 0.53	0.998	9.3 ± 0.52	0.70 ± 0.03	**0.999**	14 ± 0.91	-1.2 ± 0.027	0.48 ± 0.011	0.955
	7.4	0.85 ± 0.11	3.0 ± 1.4	0.991	38 ± 14	0.87 ± 0.11	**0.992**	5.0 ± 1.9	-0.34 ± 0.22	0.56 ± 0.057	0.937

Moreover, k_1 is lower at pH 7.4, indicating a lower contribution of Fickian diffusion at this pH. Taking these results into consideration, the incorporation of pristine Fe_3O_4 in chitosan nanoparticles does not clearly affects DOX releasing mechanism. Similar to what was observed in the DOX release curves, incorporation of Fe_3O_4 TC 10 mM, Fe_3O_4 OA 64 mM and Fe_3O_4 TD NPs into CS NPs has the same effect as the incorporation of pristine Fe_3O_4. Consequently, drug release mechanisms are similar between the three samples. As such, it can be concluded that the stabilization of iron oxide nanoparticles with tri-sodium citrate and oleic acid does not influence the drug release application of DOX-loaded CS Fe_3O_4 NPs. Moreover, the method of iron oxide nanoparticles synthesis also does not influence the mechanism of DOX release.

Succeeding, the amount of pristine Fe_3O_4 NPs incorporated into CS NPs will be further analyzed. In the drug release curves, the total amount of DOX released decreases with the increase of Fe_3O_4 amount. Table 7.7 show the results of fitting experimental data of DOX release from CS NPs of 469 kDa incorporated with 0.5 mg, 1.5 mg and 6 mg of pristine Fe_3O_4, at pH 4.5, 6.5 and 7.4. All the samples are well fitted by both Korsmeyer-Peppas and Weibull mode, with slight differences between the adjusted coefficients of determination. In Korsmeyer-Peppas model, exponent *n* increases with the increase of pH, crossing the boundary of 0.85 at pH 7.4 from an anomalous transport to Super-case II. The same happens with constant *b* from Weibull model, which increase with the increase of pH. At pH 4.5 and 6.5 it indicates a mixed mechanism between Fickian and case II. At pH 7.4 constant *b* is higher than 1, indicating a complex release mechanism. Peppas-Sahlin parameters have the same profile as for DOX release from CS NPs. Comparison between different amounts of Fe_3O_4 NPs shows no significant differences between 0.5 mg, 1.5 mg and 6 mg. As such, the amount of pristine Fe_3O_4 NPs incorporated into CS NPs does not affect the mechanism of DOX release, although it significantly reduces the total amount of released DOX.

Similar to chitosan, the effect on DOX release of the incorporation of Fe_3O_4 NPs into *O*-HTCC NPs was also accessed.

Table 7.8 displays the results of fitting the three selected models to DOX release experimental data from *O*-HTCC NPs incorporated with four types of Fe_3O_4 NPs: pristine Fe_3O_4, Fe_3O_4 TC 10 mM, Fe_3O_4 OA 64 mM, and Fe_3O_4 TD. An overall analysis shows a small difference between the adjusted coefficients of determination, indicating that the three models fitted well to the experimental data. Furthermore, DOX release from *O*-HTCC pristine Fe_3O_4 show similar results to *O*-HTCC NPs. Exponent *n* from Korsmeyer-Peppas model has a value below 0.85, which correlates to the exponent *m* of Peppas-Sahlin model, which has an average value of 0.5. Both of them indicate an anomalous release mechanism. Moreover, constant k_1 is higher than k_2, similarly to

O-HTCC NPs, indicating a predominance of Fickian diffusion. Finally, constant *b* correlates with the later mechanism, showing a value below 0.75 for almost all cases.

Table 7.7. DOX release profile from freeze-dried CS NPs (469 kDa) with different amounts of pristine Fe_3O_4 NPs (0.5 mg, 1.5 mg, and 6 mg): parameters values and R^2_{adj} obtained from fitting the mathematical models to experimental data.

mg (Fe_3O_4)	pH	Korsmeyer-Peppas			Weibull			Peppas-Sahlin			
		n	K	R^2_{adj}	a	b	R^2_{adj}	k_1	k_2	m	R^2_{adj}
0.5	**4.5**	0.63 ± 0.064	19 ± 4.3	0.975	5.0 ± 1.4	0.73 ± 0.058	**0.984**	24 ± 5.8	-2.26 ± 1.2	0.48 ± 0.049	0.948
	6.5	0.93 ± 0.16	7.6 ± 4.0	**0.998**	16 ± 9.0	1.0 ± 0.15	**0.998**	15 ± 5.2	-1.1 ± 0.57	0.53 ± 0.042	0.883
	7.4	1.3 ± 0.068	9.1 ± 2.1	**0.998**	11 ± 3.0	1.4± 0.053	0.997	19 ± 2.8	-1.9 ± 0.40	0.48 ± 0.018	0.830
1.5	**4.5**	0.56 ± 0.081	23 ± 9.9	0.963	4.3 ± 2.2	0.66 ± 0.065	**0.975**	29 ± 2.5	-3.5 ± 2.7	0.43 ± 0.064	0.934
	6.5	0.58 ± 0.026	8.4 ± 0.37	**0.999**	11 ± 0.53	0.62 ± 0.028	0.998	11 ± 0.31	-0.96 ± 0.052	0.48 ± 0.008	0.949
	7.4	0.99 ± 0.017	10 ± 0.52	**0.984**	9.3 ± 0.49	1.0 ± 0.019	0.982	16 ± 1.4	-1.9 ± 0.084	0.43 ± 0.018	0.828
6	**4.5**	0.51 ± 0.13	4.5 ± 2.2	0.982	25 ± 9.9	0.54 ± 0.14	**0.984**	5.1 ± 2.6	-0.32 ± 0.12	0.53 ± 0.088	0.991
	6.5	0.50 ± 0.066	17 ± 2.3	0.982	5.2 ± 0.84	0.55 ± 0.077	**0.985**	22 ± 2.5	-2.5 ± 0.42	0.42 ± 0.018	0.946
	7.4	1.3 ± 0.14	1.7 ± 0.97	0.902	80 ± 56	1.3 ± 0.13	**0.904**	3.1 ± 1.9	-0.25 ± 0.2	0.52 ± 0.057	0.867

Again, similarly to DOX release from CS NPs, the incorporation of pristine Fe_3O_4, Fe_3O_4 TC 10 mM and Fe_3O_4 TD into *O*-HTCC NPs have the same effect in DOX release profile. This point out that DOX release profile from *O*-HTCC NPs is not influenced by the synthesis method nor by the stabilization with tri-sodium citrate. For *O*-HTCC Fe_3O_4 OA 64 mM NPs the only significant difference is that constant *b* from Weibull model shows higher values, crossing the boundary

of 0.75, and consequently shifting the predominant release mechanism from Fickian diffusion to a mixed mechanism between Fickian diffusion and Case II.

Table 7.8. DOX release profile from freeze-dried *O*-HTCC NPs (48 kDa) with pristine Fe_3O_4, Fe_3O_4 TC 10 mM and Fe_3O_4 OA 64 mM: parameters values and R^2_{adj} obtained from fitting the mathematical models to experimental data.

Fe_3O_4 type	**pH**	**Korsmeyer-Peppas**			**Weibull**			**Peppas-Sahlin**			
		n	**K**	**R^2_{adj}**	**a**	**b**	**R^2_{adj}**	**k_1**	**k_2**	**m**	**R^2_{adj}**
Pristine Fe_3O_4	**4.5**	0.58 ± 0.052	10 ± 1.4	0.977	9.5 ± 1.5	0.65 ± 0.056	0.983	11 ± 1.3	-0.55 ± 0.099	0.58 ± 0.019	**0.992**
	6.5	0.68 ± 0.026	11 ± 0.44	**0.996**	8.3 ± 0.39	0.78 ± 0.034	0.993	16 ± 1.0	-0.91 ± 0.17	0.56 ± 0.023	0.976
	7.4	0.65 ± 0.019	7.6 ± 0.43	**0.994**	13 ± 0.73	0.68 ± 0.020	0.993	10 ± 0.72	-1.0 ± 0.10	0.46 ± 0.005	0.945
Fe_3O_4 TC 10mM	**4.5**	0.59 ± 0.061	9.6 ± 1.4	0.970	10 ± 1.6	0.67 ± 0.077	0.976	11 ± 2.0	-0.57 ± 0.14	0.58 ± 0.033	**0.988**
	6.5	0.65 ± 0.032	12 ± 0.53	**0.999**	8.1 ± 0.37	0.73 ± 0.042	0.998	16 ± 1.2	-0.99 ± 0.14	0.55 ± 0.016	0.973
	7.4	0.55 ± 0.040	8.6 ± 0.90	**0.989**	11 ± 1.2	0.58 ± 0.040	0.987	11 ± 0.84	-1.2 ± 0.24	0.44 ± 0.033	0.953
Fe_3O_4 OA 64mM	**4.5**	0.75 ± 0.031	22 ± 4.3	0.986	4.1 ± 0.87	0.86 ± 0.031	**0.991**	30 ± 4.9	-3.7 ± 0.83	0.41 ± 0.013	0.869
	6.5	0.57 ± 0.021	13 ± 1.6	**0.998**	7.2 ± 1.1	0.62 ± 0.028	0.997	18 ± 2.8	-1.7 ± 0.37	0.46 ± 0.013	0.943
	7.4	0.76 ± 0.020	8.2 ± 1.5	0.983	12 ± 2.0	0.81 ± 0.022	**0.986**	13 ± 1.7	-1.2 ± 0.32	0.47 ± 0.032	0.892
Fe_3O_4 TD	**4.5**	0.55 ± 0.016	12 ± 1.2	0.969	8.1 ± 0.87	0.63 ± 0.022	0.977	14 ± 1.5	-0.89 ± 0.14	0.51 ± 0.005	**0.980**
	6.5	0.66 ± 0.031	10 ± 0.67	**0.999**	9.1 ± 0.59	0.74 ± 0.046	**0.999**	14 ± 1.4	-0.89 ± 0.092	0.54 ± 0.011	0.976
	7.4	0.68 ± 0.062	3.3 ± 0.84	0.983	31 ± 9.1	0.70 ± 0.060	**0.985**	4.6 ± 1.1	-0.34 ± 0.12	0.53 ± 0.035	0.964

Table 7.9. DOX release profile from freeze-dried *O*-HTCC NPs (469 kDa) with different amounts of pristine Fe_3O_4 NPs (0.5 mg, 1.5 mg and 6 mg): parameters values and R^2_{adj} obtained from fitting the mathematical models to experimental data.

mg (Fe_3O_4)	**pH**	**Korsmeyer-Peppas**			**Weibull**			**Peppas-Sahlin**			
		n	**K**	**R^2_{adj}**	**a**	**b**	**R^2_{adj}**	**k_1**	**k_2**	**m**	**R^2_{adj}**
0.5	**4.5**	0.97 ± 0.067	53 ± 7.0	0.997	1.4 ± 0.28	1.2 ± 0.11	**0.999**	59 ± 2.1	-8.8 ± 0.75	0.37 ± 0.014	0.807
	6.5	0.78 ± 0.023	16 ± 0.82	**0.996**	5.8 ± 0.35	0.92 ± 0.033	0.995	25 ± 1.3	-2.1 ± 0.17	0.50 ± 0.010	0.923
	7.4	0.84 ± 0.182	7.8 ± 1.3	**0.980**	13 ± 2.4	0.87 ± 0.19	0.978	12 ± 2.0	-1.3 ± 0.24	0.45 ± 0.025	0.888
1.5	**4.5**	0.51 ± 0.017	19 ± 0.76	0.951	4.8 ± 0.22	0.61 ± 0.024	0.964	22 ± 0.94	-1.6 ± 0.19	0.50 ± 0.027	**0.981**
	6.5	0.64 ± 0.104	11 ± 0.95	**0.991**	8.4 ± 0.72	0.70 ± 0.11	0.988	16 ± 0.71	-1.4 ± 0.15	0.47 ± 0.029	0.935
	7.4	0.93 ± 0.072	8.5 ± 0.39	**0.998**	11 ± 0.51	0.98 ± 0.075	**0.998**	13 ± 0.32	-1.4 ± 0.040	0.44 ± 0.002	0.867
6	**4.5**	0.54 ± 0.004	14 ± 1.4	0.980	6.6 ± 0.72	0.63 ± 0.006	0.986	16 ± 2.2	-0.95 ± 0.25	0.55 ± 0.019	**0.992**
	6.5	0.59 ± 0.012	11 ± 0.81	**0.998**	8.1 ± 0.61	0.65 ± 0.009	**0.998**	16 ± 1.2	-1.3 ± 0.21	0.48 ± 0.018	0.955
	7.4	0.80 ± 0.060	6.1 ± 0.36	0.978	16 ± 0.94	0.84 ± 0.064	**0.980**	9.2 ± 0.41	-0.93 ± 0.034	0.44 ± 0.009	0.882

Finally, the amount of pristine Fe_3O_4 NPs incorporated into *O*-HTCC NPs was also evaluated (Table 7.9). In the same way to the previous results, the adjusted coefficient of determination is analogous between the three models. Exponent *n* and exponent *m* have values between 0.43 and 0.85 for almost all cases, indicating equilibrium between Fickian diffusion and relaxation rate of the polymer chain. In these exponents, no difference was found with the increase of Fe_3O_4 amount. On the other hand, constant *b* decreases with the increase of Fe_3O_4 amount, shifting from values above 0.75 (mixed mechanism) to values below 0.75 (Fickian diffusion) at pH 4.5. At pH

7.4 constant *b* values are fixed between 0.75 and 1, without variation with the increase in Fe_3O_4 amount. The later correlates with the results of constant k_1 from Peppas-Sahlin model, which decreases with the increase of Fe_3O_4 weight at pH 4.5, but no significant shift is observed at pH 7.4. Accordingly, the amount of Fe_3O_4 weight incorporated into *O*-HTCC NPs only has effect at lower pH; at physiological pH (7.4) no significant effect was found. At pH 4.5 the increase of Fe_3O_4 amount seams to facilitate DOX release by Fickian diffusion, probably due to an increased relaxation in the polymer chains.

7.4. Summary

When constructing a drug delivery system the main purpose is to obtain a drug release in a predictable and controllable rate. Achieving such a drug delivery system, not only increases drug safety but also improves its performance. Doxorubicin is a perfect candidate to be incorporated in drug delivery systems, since it is a widely used drug for several types of cancer but has severe side effects, such as cardiotoxicity.

Chitosan is a biopolymer widely used as a drug delivery system. Drug delivery from chitosan is dependent upon its swelling behavior and drug-chitosan interactions, which are influenced by pH of the medium. As such, drug release from chitosan' structure may be highly controllable. Furthermore, ionically cross-linked chitosan NPs are mainly used for drug delivery applications due to the higher versatility of cross-linking, leading to higher swelling, and consequently, higher pH-sensitivity [33].

The main purpose of the present work was to develop DOX delivery systems based on chitosan. For that, the previously studied nanoparticles in Chapter 3 and Chapter 4 were used. As such, DOX was encapsulated in chitosan and *O*-HTCC nanoparticles with different molecular weights, with and without iron oxide nanoparticles. Furthermore, release profiles were studied at physiological temperature at three different pH: 4.5 (lysosomal pH), 6.5 (tumor microenvironment) and 7.4 (physiological pH). Finally, mathematical models suitable for drug release systems were applied to the experimental data.

Optimization of DOX encapsulation into chitosan nanoparticles led to an encapsulation efficiency above 70%. DOX encapsulation into *O*-HTCC is not so effective, probably due to the increase of charge repulsion between polymer and drug. Still, an encapsulation efficiency of about 50 % was achieved. On the other hand, incorporation of Fe_3O_4 NPs into polymeric NPs did not significantly

affected DOX encapsulation. Moreover, polymer molecular weight does not affect DOX encapsulation efficiency, within the tested range.

DOX release profiles from chitosan nanoparticles show a pH-sensitive release. In more acidic pH, DOX release is enhanced. In contrast, at physiological pH drug release is minimal (around 20% in most cases). However, in the majority of the studied samples, DOX release profile show a burst effect within the first hour of experiment, reaching a plateau after 8-10 h, in some cases extended to 24 h. The initial burst effect is often associated with release of hydrophilic molecules from polymeric carriers, followed by a phase of very slow drug release [51]. Burst effect may occur due to immediate dissolution of DOX present at the surface of the NPs. Incorporation of Fe_3O_4 NPs into polymeric NPs increases DOX release in the same experimental conditions. However, the incorporation of higher amounts of Fe_3O_4 NPs into polymeric NPs led to a negative effect, i.e., total amount of DOX release was smaller.

To understand the underlying mechanisms of DOX release from CS and *O*-HTCC NPs, three mathematical models were fitted to the experimental data: Korsmeyer-Peppas, Weibull and Peppas-Sahlin model. In the majority of the samples, both Korsmeyer-Peppas and Weibull fitted well to the experimental data, with slight differences between their adjusted coefficients of determination. These models lead to a concordant mechanism for most of the samples, indicating an anomalous release at pH 4.5 and 7.4 where both Fickian diffusion and polymer relaxation contributes to the drug release mechanism. These results are in concordance with chitosan swelling behavior described in literature [34, 35]. DOX release at pH 6.5 should be further analyzed, since it is a transitory pH of CS and more complex drug release mechanism may be present at this pH.

The present work gives a great contribution in understanding the release of a widely used chemotherapeutic drug from a widely used polymeric drug delivery system. Knowledge of the mechanisms of DOX release is a first step to the application of such drug delivery system in order to reduce DOX side effects and improve its effectiveness in treating several tumors.

Moreover, the incorporation of iron oxide nanoparticles into this polymeric system extends its application. In this regard, these types of composite nanoparticles can be used for magnetic hyperthermia combined with drug release. Furthermore, the presence of iron oxide nanoparticles may also be useful to detect the composite inside the body by magnetic resonance image, thus allowing diagnostic and treatment simultaneously. Consequently, the studied polymeric nanoparticles incorporated with inorganic ones have a huge potential as theranostic agents.

7.5. References

1. W. H. De Jong, P. J. Borm, Drug delivery and nanoparticles:applications and hazards, Int J Nanomedicine, 3 (2008), 133-149.

2. T. L. Doane, C. Burda, The unique role of nanoparticles in nanomedicine: imaging, drug delivery and therapy, Chemical Society reviews, 41 (2012), 2885-2911.

3. S. Parveen, R. Misra, S. K. Sahoo, Nanoparticles: a boon to drugdelivery, therapeutics, diagnostics and imaging, Nanomedicine: Nanotechnology, Biology and Medicine, 8 (2012), 147–166.

4. S. M. Swain, F. S. Whaley, M. S. Ewer, Congestive heart failure in patients treated with doxorubicin: a retrospective analysis of three trials, Cancer, 97 (2003), 2869-2879.

5. G. Minotti, P. Menna, E. Salvatorelli, G. Cairo, L. Gianni, Anthracyclines: molecular advances and pharmacologic developments in antitumor activity and cardiotoxicity, Pharmacol Rev, 56 (2004), 185-229.

6. H. Brockmann, [Anthracyclinones and Anthracyclines. (Rhodomycinone, Pyrromycinone and Their Glycosides)], Fortschritte der Chemie organischer Naturstoffe = Progress in the chemistry of organic natural products. Progres dans la chimie des substances organiques naturelles, 21 (1963), 121-182.

7. M. Al-Hajj, M. S. Wicha, A. Benito-Hernandez, S. J. Morrison, M. F. Clarke, Prospective identification of tumorigenic breast cancer cells, Proc Natl Acad Sci U S A, 100 (2003), 3983-3988.

8. C. Monneret, Invited review Recent developments in the field of antitumour anthracyclines, European Journal of Medicinal Chemistry, 36 (2001), 483-493.

9. D. A. Gewirtz, A critical evaluation of the mechanisms of action proposed for the antitumor effects of the anthracycline antibiotics adriamycin and daunorubicin, Biochem Pharmacol, 57 (1999), 727-741.

10. D. B. Sawyer, X. Peng, B. Chen, L. Pentassuglia, C. C. Lim, Mechanisms of anthracycline cardiac injury: can we identify strategies for cardioprotection?, Prog Cardiovasc Dis, 53 (2010), 105-113.

11. C. A. Geisberg, D. B. Sawyer, Mechanisms of anthracycline cardiotoxicity and strategies to decrease cardiac damage, Curr Hypertens Rep, 12 (2010), 404-410.

12. C. d. L. Davies, Radiation Improves the Distribution and Uptake of Liposomal Doxorubicin (Caelyx) in Human Osteosarcoma Xenografts, Cancer Research, 64 (2004), 547-553.

13. European Medicines Agency - European Public Assessment reports - Myocet, http://www.ema.europa.eu/ema/index.jsp?curl=pages/medicines/human/medicines/000297/human_med_000916.jsp&murl=menus/medicines/medicines.jsp&mid=WC0b01ac058001d125&jsenabled=true, accessed on August 15, 2015

14. M. L. Tan, A. M. Friedhuber, D. E. Dunstan, P. F. Choong, C. R. Dass, The performance of doxorubicin encapsulated in chitosan-dextran sulphate microparticles in an osteosarcoma model, Biomaterials, 31 (2010), 541-551.

15. T. Betancourt, B. Brown, L. Brannon-Peppas, Doxorubicin-loaded PLGA nanoparticles by nanoprecipitation: preparation, characterization and in vitro evaluation, Nanomedicine (Lond), 2 (2007), 219-232.

16. K. A. Janes, M. P. Fresneau, A. Marazuela, A. Fabra, M. J. Alonso, Chitosan nanoparticles as delivery systems for doxorubicin, J Control Release, 73 (2001), 255-267.

17. S. Bisht, A. Maitra, Dextran-doxorubicin/chitosan nanoparticles for solid tumor therapy, Wiley Interdiscip Rev Nanomed Nanobiotechnol, 1 (2009), 415-425.

18. M. Susa, A. K. Iyer, K. Ryu, F. J. Hornicek, H. Mankin, M. M. Amiji, Z. Duan, Doxorubicin loaded Polymeric Nanoparticulate Delivery System to overcome drug resistance in osteosarcoma, BMC cancer, 9 (2009), 399.

19. F. Wang, Y. C. Wang, S. Dou, M. H. Xiong, T. M. Sun, J. Wang, Doxorubicin-tethered responsive gold nanoparticles facilitate intracellular drug delivery for overcoming multidrug resistance in cancer cells, ACS Nano, 5 (2011), 3679-3692.

20. D. Lorusso, A. Di Stefano, V. Carone, A. Fagotti, S. Pisconti, G. Scambia, Pegylated liposomal doxorubicin-related palmar-plantar erythrodysesthesia ('hand-foot' syndrome), Annals of oncology : official journal of the European Society for Medical Oncology / ESMO, 18 (2007), 1159-1164.

21. L. E. van Vlerken, T. K. Vyas, M. M. Amiji, Poly(ethylene glycol)-modified nanocarriers for tumor-targeted and intracellular delivery, Pharm Res, 24 (2007), 1405-1414.

22. M. Salerno, E. Cenni, C. Fotia, S. Avnet, D. Granchi, F. Castelli, D. Micieli, R. Pignatello, M. Capulli, N. Rucci, A. Angelucci, A. Del Fattore, A. Teti, N. Zini, A. Giunti, N. Baldini, Bone-targeted doxorubicin-loaded nanoparticles as a tool for the treatment of skeletal metastases, Current cancer drug targets, 10 (2010), 649-659.

23. K. J. Widder, A. E. Senyel, G. D. Scarpelli, Magnetic microspheres: a model system of site specific drug delivery in vivo, Proc Soc Exp Biol Med, 158 (1978), 141-146.

24. K. Akiyoshi, I. Taniguchi, H. Fukui, J. Sunamoto, Hydrogel nanoparticle formed by self-assembly of hydrophobized polysaccharide, stabilization of adriamycin by complexation, European journal of pharmaceutics and biopharmaceutics, 42 (1996), 286-290.

25. P. Couvreur, B. Kante, L. Grislain, M. Roland, P. Speiser, Toxicity of polyalkylcyanoacrylate nanoparticles II: Doxorubicin-loaded nanoparticles, J Pharm Sci, 71 (1982), 790-792.

26. C. Cuvier, L. Roblot-Treupel, J. M. Millot, G. Lizard, S. Chevillard, M. Manfait, P. Couvreur, M. F. Poupon, Doxorubicin-loaded nanospheres bypass tumor cell multidrug resistance, Biochem Pharmacol, 44 (1992), 509-517.

27. C. C. Berry, Progress in functionalization of magnetic nanoparticles for applications in biomedicine, Journal of Physics D: Applied Physics, 42 (2009), 224003.

28. S. Wada, L. Yue, K. Tazawa, I. Furuta, H. Nagae, S. Takemori, T. Minamimura, New local hyperthermia using dextran magnetite complex (DM) for oral cavity: experimental study in normal hamster tongue, Oral diseases, 7 (2001), 192-195.

29. M. Rinaudo, Chitin and chitosan: Properties and applications, Progress in Polymer Science, 31 (2006), 603-632.

30. Q. Yuan, J. Shah, S. Hein, R. D. Misra, Controlled and extended drug release behavior of chitosan-based nanoparticle carrier, Acta Biomater, 6 (2010), 1140-1148.

31. P. C. McDonald, J. Y. Winum, C. T. Supuran, S. Dedhar, Recent developments in targeting carbonic anhydrase IX for cancer therapeutics, Oncotarget, 3 (2012), 84-97.

32. G. Unsoy, R. Khodadust, S. Yalcin, P. Mutlu, U. Gunduz, Synthesis of Doxorubicin loaded magnetic chitosan nanoparticles for pH responsive targeted drug delivery, Eur J Pharm Sci, 62 (2014), 243-250.

33. J. Berger, M. Reist, J. M. Mayer, O. Felt, N. A. Peppas, R. Gurny, Structure and interactions in covalently and ionically crosslinked chitosan hydrogels for biomedical applications, Eur J Pharm Biopharm, 57 (2004), 19-34.

34. S. A. Agnihotri, N. N. Mallikarjuna, T. M. Aminabhavi, Recent advances on chitosan-based micro- and nanoparticles in drug delivery, J Control Release, 100 (2004), 5-28.

35. P. He, Chitosan microspheres prepared by spray drying, International journal of pharmaceutics, 187 (1999), 53-65.

36. J. Siepmann, F. Siepmann, Mathematical modeling of drug delivery, Int J Pharm, 364 (2008), 328-343.

37. A. Javid, S. Ahmadian, A. A. Saboury, S. M. Kalantar, S. Rezaei-Zarchi, Chitosan-coated superparamagnetic iron oxide nanoparticles for doxorubicin delivery: synthesis and anticancer effect against human ovarian cancer cells, Chemical biology & drug design, 82 (2013), 296-306.

38. T. Higuchi, Rate of release of medicaments from ointment bases containing drugs in suspension, J Pharm Sci, 50 (1961), 874-875.

39. C. Raman, C. Berkland, K. Kim, D. W. Pack, Modeling small-molecule release from PLG microspheres: effects of polymer degradation and nonuniform drug distribution, J Control Release, 103 (2005), 149-158.

40. G. Frenning, U. Brohede, M. Stromme, Finite element analysis of the release of slowly dissolving drugs from cylindrical matrix systems, J Control Release, 107 (2005), 320-329.

41. Y. Fu, W. J. Kao, Drug release kinetics and transport mechanisms of non-degradable and degradable polymeric delivery systems, Expert opinion on drug delivery, 7 (2010), 429-444.

42. N. A. Peppas, P. Bures, W. Leobandung, H. Ichikawa, Hydrogels in pharmaceutical formulations, Eur J Pharm Biopharm, 50 (2000), 27-46.

43. S. Dash, P. N. Murthy, L. Nath, P. Chowdhury, Kinetic modeling on drug release from controlled drug delivery systems, Acta poloniae pharmaceutica, 67 (2010), 217-223.

44. P. Costa, J. M. Sousa Lobo, Modeling and comparison of dissolution profiles, Eur J Pharm Sci, 13 (2001), 123-133.

45. R. W. Korsmeyer, R. Gurny, E. Doelker, P. Buri, N. A. Peppas, Mechanisms of solute release from porous hydrophilic polymers, International journal of pharmaceutics, 15 (1983), 25-35.

46. P. L. Ritger, N. A. Peppas, A simple equation for description of solute release II. Fickian and anomalous release from swellable devices, Journal of Controlled Release, 5 (1987), 37-42.

47. R. Chouhan, A. Bajpai, Real time in vitro studies of doxorubicin release from PHEMA nanoparticles, J Nanobiotechnology, 7 (2009), 5.

48. N. A. Peppas, Analysis of Fickian and non-Fickian drug release from polymers, Pharmaceutica acta Helvetiae, 60 (1985), 110-111.

49. H. H. B, Controlled Release from Erodible Slabs, Cylinders, and Spheres, in: Controlled Release Polymeric Formulations, AMERICAN CHEMICAL SOCIETY, 1976, pp. 26-32.

50. N. A. Peppas, J. J. Sahlin, A simple equation for the description of solute release. III. Coupling of diffusion and relaxation, International journal of pharmaceutics, 57 (1989), 169-172.

51. D. Y. Arifin, L. Y. Lee, C. H. Wang, Mathematical modeling and simulation of drug release from microspheres: Implications to drug delivery systems, Adv Drug Deliv Rev, 58 (2006), 1274-1325.

52. V. Papadopoulou, K. Kosmidis, M. Vlachou, P. Macheras, On the use of the Weibull function for the discernment of drug release mechanisms, Int J Pharm, 309 (2006), 44-50.

53. C. Fang, F. M. Kievit, O. Veiseh, Z. R. Stephen, T. Wang, D. Lee, R. G. Ellenbogen, M. Zhang, Fabrication of magnetic nanoparticles with controllable drug loading and release through a simple assembly approach, J Control Release, 162 (2012), 233-241.

54. F. M. Kievit, F. Y. Wang, C. Fang, H. Mok, K. Wang, J. R. Silber, R. G. Ellenbogen, M. Zhang, Doxorubicin loaded iron oxide nanoparticles overcome multidrug resistance in cancer in vitro, J Control Release, 152 (2011), 76-83.

55. R. S. Tığlı Aydın, M. Pulat, 5-Fluorouracil Encapsulated Chitosan Nanoparticles for pH-Stimulated Drug Delivery: Evaluation of Controlled Release Kinetics, Journal of Nanomaterials, 2012 (2012), 1-10.

56. M. Talelli, C. J. Rijcken, T. Lammers, P. R. Seevinck, G. Storm, C. F. van Nostrum, W. E. Hennink, Superparamagnetic iron oxide nanoparticles encapsulated in biodegradable thermosensitive polymeric micelles: toward a targeted nanomedicine suitable for image-guided drug delivery, Langmuir, 25 (2009), 2060-2067.

57. B. Manocha, A. Margaritis, Controlled Release of Doxorubicin from Doxorubicin/γ-Polyglutamic Acid Ionic Complex, Journal of Nanomaterials, 2010 (2010), 1-9.

58. S. Mitra, U. Gaur, P. C. Ghosh, A. N. Maitra, Tumour targeted delivery of encapsulated dextran-doxorubicin conjugate using chitosan nanoparticles as carrier, J Control Release, 74 (2001), 317-323.

59. A. Rampino, M. Borgogna, P. Blasi, B. Bellich, A. Cesaro, Chitosan nanoparticles: preparation, size evolution and stability, Int J Pharm, 455 (2013), 219-228.

60. Y. Zhang, M. Huo, J. Zhou, A. Zou, W. Li, C. Yao, S. Xie, DDSolver: an add-in program for modeling and comparison of drug dissolution profiles, AAPS J, 12 (2010), 263-271.

61. H. K. Shaikh, R. V. Kshirsagar, S. G. Patil, Mathematical models for drug release characterization: a review World Journal of Pharmacy and Pharmaceutical Sciences 4(2015), 324-338.

– This page is intentionally blank –

Chapter 8. Conclusions and Future Perspectives

In this chapter, the main findings of this PhD thesis are presented, comparing the key results with the literature. Future work is also proposed and discussed.

8.1. Thesis findings

The main objective of this PhD thesis, as presented in Chapter 1, was to develop a theranostic system composed of a magnetic core and a chitosan-based coating. This system was expected to achieve several functions: act as a drug delivery platform for doxorubicin; sensitize and/or destroy cancer cells by magnetic hyperthermia; to allow diagnostic and/or treatment monitoring by magnetic resonance imaging; and finally, to do it all in a highly specific manner due to the presence of a monoclonal antibody specific for a transmembranar protein present in several solid tumors. To achieve these objectives, four tasks were proposed at the beginning of this PhD thesis:

1. Production and characterization of superparamagnetic iron oxide nanoparticles with diameters in the nanometric range, stable in physiological conditions and able to generate heat by the application of an alternating external magnetic field.

2. Production and characterization of chitosan and *O*-HTCC nanoparticles with diameters in the nanometric range, stable in physiological conditions. Further, both polymers are used to coat iron oxide nanoparticles produced in task 1.

3. Production of a highly specific monoclonal antibody for CA IX (a glycoprotein over expressed in osteosarcoma).

4. Study the suitability of the produced nanoparticles for application in magnetic hyperthermia, as a contrast agent for magnetic resonance image, and as a drug delivery system.

Accordingly, task 1 results are presented and discussed in Chapter 3, task 2 in Chapter 4, task 3 in Chapter 5, and finally the results of task 4 are presented and discussed in Chapter 6 and Chapter 7. The main conclusions of each task will be further presented.

8.1.1. Production and characterization of iron oxide nanoparticles

The theranostic system developed in this PhD thesis is expected to have a magnetic core. Iron oxide nanoparticles were selected as the most advantageous magnetic nanoparticles for the required functions. There are several techniques available to synthetize this type of nanoparticles, from which chemical precipitation and thermal decomposition were selected. Iron oxide nanoparticles produced by chemical precipitation were the main focus of this study due to the easiness of methodology and low cost production.

The produced iron oxide nanoparticles by either chemical precipitation or thermal decomposition are composed of magnetite with an average crystallite size of 9 nm. However, the iron oxide nanoparticles produced by chemical precipitation are often unstable in aqueous suspensions, thus invalidating its application in the biomedical field. To remove this drawback, the stabilization effect of three surfactants was studied: tri-sodium citrate, oleic acid, and triton X-100. Both morphological and physicochemical analysis revealed that none of the surfactants used affect the properties of the nanoparticles. Triton X-100 was the one with the worst performance for the stabilization of iron oxide nanoparticles. An optimal concentration for the stabilization effect was found for both oleic acid and tri-sodium citrate: 64 mM and 10 mM, respectively. Tri-sodium citrate showed the best performance for long-term stability (up to 8 weeks), while oleic acid was the best for short-term stability (24 hours).

Magnetic characterization confirmed the superparamagnetic behavior of the produced iron oxide nanoparticles, even in the presence of the surfactants. The saturation magnetization of pristine iron oxide nanoparticles at 320 K obtained was 58 $emu.g^{-1}$, which decreases to 45 $emu.g^{-1}$ in the presence of oleic acid 64 mM.

Oleic acid forms a bilayer on the iron oxide nanoparticles contributing to maximum stabilization in water solution. That was confirmed by a zeta potential of -120 mV at physiological pH.

The produced iron oxide nanoparticles met the requirements for the magnetic core of the theranostic system proposed in this PhD thesis.

8.1.2. Production and characterization of chitosan and *O*-HTCC coating

The development of the chitosan-based coating was first obtained by depolymerized of chitosan in a simple and rapid procedure. Five different molecular weight chitosan were successful obtained. Using chitosan of different molecular weights, *O*-HTCC was synthesized. Then, both chitosan and *O*-HTCC were used to produce polymeric nanoparticles. The optimized polymeric nanoparticles obtained have an average hydrodynamic diameter within the range of 100-200 nm. This is ideal size for intravenous administration since it evades being retained in the spleen, or being removed from the circulation by extravasation and renal clearance, improving the blood circulation time. Zeta potential measurements confirmed that the produced polymeric nanoparticles have a positive charge and are stable in aqueous solution.

The incorporation of iron oxide nanoparticles in the polymeric ones demonstrated that the hydrodynamic diameter of coated nanoparticles increases, being dependent on the polymer molecular weight. Iron oxide nanoparticles coated with low molecular weight chitosan show an average hydrodynamic diameter of around 250 nm, which may cause the retention of these nanoparticles in the spleen. As such, the production of chitosan-coated iron oxide nanoparticles should be further optimized.

8.1.3. Production of monoclonal antibody anti-CA IX

This aimed the achievement of highly specific target theranostic system. The presence of CA IX was demonstrated in two cell lines of solid tumors: osteosarcoma and breast cancer. Although it is a preliminary conclusion, the developed multifunctional system is not only suitable for osteosarcoma theranostic, but also for theranostic of other solid tumors such as breast cancer.

At least one hybridoma producing monoclonal antibodies anti-CA IX from each immunization was obtained: whole protein, central peptide, and N-terminal peptide. Recloning and purification steps are still required before attaching the produced monoclonal antibody to the theranostic system developed.

8.1.4. Suitability as theranostic agents

The developed parts were tested for the functions that the theranostic system is expected to fulfil. As such, iron oxide nanoparticles with and without polymeric coating were tested as magnetic hyperthermia agents, and as contrast agents for magnetic resonance imaging. Polymeric nanoparticles with and without iron oxide were studied as drug delivery systems for doxorubicin. Finally, cytotoxicity assays were performed for all samples.

Magnetic hyperthermia tests revealed that pristine Fe_3O_4 NPs have a SAR of 100 $W.g^{-1}$ for an iron concentration of 125 mM at 24 $kA.m^{-1}$ of the AC magnetic field strength and frequency of 418.5 kHz. Stabilization with tri-sodium citrate at 10 mM reduces SAR value to 50 $W.g^{-1}$, while oleic acid at 64 mM causes a reduction even higher, to 20 $W.g^{-1}$. To better understand these differences, Brownian and Néel relaxation times were calculated in water and agar dispersions. The obtained conclusion is that both pristine and tri-sodium citrate stabilized Fe_3O_4 nanoparticles have a large contribution of the Brownian movements for the heat generation, when in water dispersions. Oleic acid forms a bilayer that entraps the iron oxide nanoparticles, thus limiting their movements. Consequently, the generated heat in the latter case is only due to the Néel relaxation, thus SAR value being smaller. The same behavior is observed when polymer-coated iron oxide nanoparticles are subjected to the AC magnetic field, leading to the conclusion that chitosan entraps the nanoparticles and limits their movements.

NMR measurements where performed for the most stable iron oxide nanoparticles produced, the ones stabilized with 96% of oleic acid. The promising results showed that the longitudinal relaxation time is slightly altered, while the transverse relaxation time remarkably increases. As such, these nanoparticles have potential as negative contrast agents for magnetic resonance imaging, although further tests are required to define the working conditions and reliability.

Drug delivery studies were performed in polymeric nanoparticles with and without iron oxide nanoparticles incorporated. Optimization of the experimental parameters led to a doxorubicin encapsulation above 70% in chitosan nanoparticles and 50% in *O*-HTCC nanoparticles. The incorporation of iron oxide nanoparticles in the polymeric ones did not change the encapsulation efficiency of doxorubicin. The release of doxorubicin from polymeric nanoparticles has a burst effect in the first hours, reaching a plateau after 8 h-10 h, in some cases extended to 24 h. Moreover, doxorubicin release in pH-sensitive: at pH 4.5 doxorubicin release in enhanced, while at physiological pH the release is slower. Incorporation of small amounts of iron oxide nanoparticles into polymeric ones enhances doxorubicin release; however, higher amounts (6 mg) of iron oxide nanoparticles have the opposite effect.

Fitting mathematical models to experimental data of doxorubicin release some differences between samples were found. Doxorubicin release occurs by an anomalous release mechanism, although the diffusion mechanism dominates in not freeze-dried polymeric samples. In freeze-dried samples of chitosan nanoparticles, both Fickian diffusion and polymer relaxation have an important contribution to DOX release mechanism. The incorporation of iron oxide nanoparticles does not clearly change the doxorubicin release mechanism. However, it has influence in the polymer relaxation, thus facilitating drug release by Fickian diffusion. The incorporation of a

higher amount of iron oxide nanoparticles has an opposite effect, decreasing the contribution of Fickian diffusion for doxorubicin release from the polymer matrix. The protonation of chitosan' amino groups at pH 4.5 (below its pka) also facilitate doxorubicin release by Fickian diffusion, although polymer relaxation also plays an important role in the release mechanism.

Cytotoxic assays *in vitro* demonstrated that pristine and tri-sodium citrate iron oxide nanoparticles are not cytotoxic in the tested range of concentrations. Oleic acid-coated iron oxide nanoparticles cause a reduction in cell viability for concentrations above 250 $\mu g.ml^{-1}$. Polymeric nanoparticles also did not show significant cytotoxicity in the tested range of concentration, for both Vero and SaOs-2 cell lines.

The integration of all components is the great novelty of this work. Overall, the results led to conclude that to construct a theranostic system for magnetic hyperthermia, magnetic resonance imaging, and drug delivery might contain:

- Superparamagnetic iron oxide nanoparticles produced by either chemical precipitation or thermal decomposition techniques with an average diameter of 9 nm and saturation magnetization of 58 $emu.g^{-1}$;
- Coating the iron oxide nanoparticles with either chitosan or *O*-HTCC, preferably of low molecular weight, having the coated nanoparticle an average hydrodynamic diameter of 250 nm;
- Encapsulation of doxorubicin into polymer-coated iron oxide nanoparticles with a maximum encapsulation efficiency of about 95%.

The theranostic system produced in the above-described conditions is able to release 31% of the encapsulated doxorubicin in physiological pH (e.g. blood), 74% in the tumor microenvironment (pH 6.5) and 82% if the system is internalized by tumor cells (pH 4.5, lysosomes). These conditions are set using chitosan as the coating. If instead the coating chosen is *O*-HTCC, the released DOX is lower: 25% at pH 7.4, 67% at pH 6.5, and 59 % at pH 4.5.

These theranostic systems are also able to generate heat by the application of an external alternating magnetic field. The efficiency of the system depends upon the used coating and the core. Thus, specific absorption rate (SAR) values vary from 6 to 86 $W.g^{-1}$, using an iron concentration of 6.3 mM.

Table 8.1 and Table 8.2 resume the optimal conditions obtained for the theranostic core, and for the theranostic system, respectively.

To confirm the functionality and define precisely its working conditions future work needs to be performed.

Table 8.1.Optimal conditions obtained from the experimental word during this PhD thesis for the theranostic core: average diameter measured by transmission electron microscopy (TEM), saturation magnetization (M_S), total amount of doxorubicin (DOX) released over 72 h; specific absorption rate (SAR) obtained from magnetic hyperthermia measurements; and relaxation times T1 and T2 obtained from nuclear magnetic resonance measurements.

Properties		**Core composition**				
		Pristine Fe_3O_4	**Fe_3O_4 TC**	**Fe_3O_4 OA**	**Fe_3O_4 TX**	**Fe_3O_4 TD**
Average diameter	**TEM (nm)**	8.5	9.1	8.5	8.6	8.0
Magnetic properties	**M_S (emu.g^{-1})**	58	61	45	60	61
	Superparamagnetic			yes		
DOX release (%, 72 h)	**pH 4.5**	96	94	96	N/A	N/A
	pH 6.5	58	55	39		
	pH 7.4	24	31	32		
SAR (W.g^{-1})[1]		93	64	5		3
NMR[2]	**T1 (mMs)$^{-1}$**	N/A	N/A	0.05		N/A
	T2 (mMs)$^{-1}$			88.4		

N/A – data not available.
[1]SAR values were obtained using the following conditions: field intensity of 24 kA.m^{-1}; frequency of 418.5 kHz; 10 minutes of field application; 1 ml of samples; and average iron concentration of 60 mM.
[2]NMR measurements were performed in the most stable sample; iron oxide nanoparticles obtained from chemical precipitation technique and stabilized with 96% of oleic acid, with respect to Fe_3O_4 nanoparticles mass, at physiological pH, 7.4.

Table 8.2. Optimal conditions obtained from the experimental word during this PhD thesis for the theranostic system: average hydrodynamic diameter (D_H) measured by dynamic light scattering, total amount of doxorubicin (DOX) released over 72 h; and specific absorption rate (SAR) obtained from magnetic hyperthermia measurements.

Coating composition		**Chitosan 39 KDa**					***O*-HTCC 48 KDa**				
Core composition		**-**	**Pristine Fe_3O_4**	**Fe_3O_4 TC**	**Fe_3O_4 OA**	**Fe_3O_4 TD**	**-**	**Pristine Fe_3O_4**	**Fe_3O_4 TC**	**Fe_3O_4 OA**	**Fe_3O_4 TD**
Average diameter	**D_H (nm)**	104	259	N/A	N/A	270	91	N/A	N/A	N/A	N/A
DOX release (%,72 h)	**pH 4.5**	66	82	84	81	35	66	59	56	56	59
	pH 6.5	62	74	78	65	43	52	67	61	44	54
	pH 7.4	13	31	36	33	18	23	25	26	30	15
SAR ($W.g^{-1}$)[1]		N/A	41	52	63	6	N/A	77	86	14	35

N/A – data not available.
[1]SAR values were obtained using the following conditions: field intensity of 24 $kA.m^{-1}$; frequency of 418.5 kHz; 10 minutes of field application; 1 ml of samples; and iron concentration of 6.3 mM (the same iron concentration used in drug release studies).

8.2. Future work

The work presented in this PhD thesis is just the beginning of a larger amount of work that still has to be done defined the applicability and suitability of this technology in cancer treatment. This section will start with the future work related to each part of the theranostic system and ends with future to the final theranostic system.

8.2.1. Core of the theranostic system

In this PhD thesis, iron oxide nanoparticles were synthetized and characterized as the core of the proposed theranostic system. However, some improvements can be performed in this regard:

- **Adoption and optimization of other synthesis methods of iron oxide nanoparticles.**

Several methods for the synthesis of iron oxide nanoparticles are described in the literature. In this PhD thesis, only two methods were used. Chemical precipitation technique was optimized to obtain stable and superparamagnetic nanoparticles, while thermal decomposition was not so extensively evaluated. The later one is very useful to produce monodisperse and highly stable nanoparticles. Similarly, other available methods have been described to produce stable and superparamagnetic nanoparticles.

- **Incorporation of other materials in the core of the theranostic system.**

Magnetic nanoparticles may have different compositions other than iron oxide. Materials such as iron in combination to iron oxides have shown a remarkably similar spinel structure to magnetite, with similar or improved magnetic properties.

On the other hand, non-magnetic materials can be incorporated into the theranostic system' core to improve its performance. For example, conjugation of gadolinium with iron oxide has demonstrated synergetic effects in magnetic resonance imaging

8.2.2. Chitosan-based coating

The development of an ideal coating for a theranostic system needs to be adapted for the required applications. In this case, chitosan and *O*-HTCC were studied as possible coatings for iron oxide nanoparticles. Although the production of chitosan-based nanoparticles was optimized, additional studies need to be made:

- **Improve the core incorporation into the polymeric nanoparticle.**

Incorporation of iron oxide nanoparticles into chitosan-based nanoparticles was successful. However, in this work is lacking different characterizations to confirm this successful incorporation. Furthermore, the obtained coated nanoparticles have an average hydrodynamic diameter of at least 250 nm for the lowest molecular weight tested. Considering that this system still lacks the monoclonal antibody and the drug, the obtained size is too large for intravenous administration. As such, other methods should be tested to optimize the size of coated nanoparticles.

- **Study the feasibility of other chitosan-based coatings.**

In this work, only chitosan and *O*-HTCC were tested as coatings for the theranostic system. In Chapter 4 some chitosan derivatives were described, which have different properties than chitosan

or *O*-HTCC. As such, some of these derivatives could be tested as alternative coatings for the theranostic system.

In addition, chitosan is often used as a grafting into other polymers with specific properties. For example, chitosan has been used in combination with poly(N-isopropylacrylamide) (PNIPAAm) to incorporate iron oxide nanoparticles into PNIPAAm microgels. These microgels are able to maintain the thermosensitivity of PNIPAAm combined with the properties of magnetic properties, making them appropriate for magnetic hyperthermia or magnetic resonance imaging.

8.2.3. Theranostic system

The proposed theranostic system in this PhD thesis is composed of four basic components: a magnetic core, a chitosan-based coating, a monoclonal antibody, and an incorporated drug. Although each one of these parts was extensively studied and evaluated for the proposed functions, the complete system was not assembled. Still much work is needed in this regard.

- Assemble the complete theranostic system and evaluate its functionality.

The complete assemble of the theranostic system is by itself a challenge. Grafting the monoclonal antibody to the polymeric coating by covalent bonds while maintain the nanoparticle structure may be hard to accomplish. Furthermore, the complete assemble of the system can influence the properties of the individual parts. As such, after complete assembling, the most important properties such as hydrodynamic size, superparamagnetism, ability to generate heat by the application of an external magnetic fields or to enhance contrast in magnetic resonance imaging, must be evaluated.

- Evaluate the *in vitro* lyse capacity of the theranostic system

After complete assembling of the theranostic system and confirmation of its reliability, still is needed to confirm its functionality to kill cancer cells *in vitro*. For that, the interaction of the system with tumoral and non-tumoral cells has to be accessed before naming the system specific for cancer cells.

Moreover, application of magnetic hyperthermia *in vitro* was performed in this PhD thesis as a preliminary study. As such, further studies need to be performed.

- Evaluate the *in vivo* biodistribution and anti-tumoral activity

When the theranostic system is fully characterized and proved to be effective *in vitro*, biodistribution and in vivo anti-tumoral activity tests can be performed. In this final stage, the four main

functionalities of the proposed theranostic systems are to be evaluated: high specificity for solid tumors such as breast cancer or osteosarcoma; drug delivery system; magnetic hyperthermia agents; and contrast agent for magnetic resonance imaging. Although this final task is still far of being concretized, it should be the main target of future work.

8.3. Summary

The development of theranostic systems has been a growing research topic due to its possible great ability to selectively kill cancer cells. The research developed during this PhD thesis aimed to contribute to a step forward in this field. The obtained results and the main conclusions provide the basis for the development of the final theranostic system. Furthermore, the suggested future work allows attaining the final theranostic construct for osteosarcoma theranostic. An important conclusion to retain from this PhD work is the multifunctionality of the developed theranostic system. Although the purpose was osteosarcoma, this system can be applied for other solid tumors with proper adjustments.

Cancer theranostic is currently a hot topic and clinical application of these systems should be coming soon.